

PLANET MIGRATION INDUCED BY GRAVITATIONAL INSTABILITIES

Scott Michael

Submitted to the faculty of the University Graduate School
in partial fulfillment of the requirements
for the degree
Doctor of Philosophy
in the Department of Astronomy,
Indiana University
April 2011

Accepted by the Graduate Faculty, Indiana University, in partial fulfillment of the requirements for the degree of Doctor of Philosophy.

Richard H. Durisen, Ph.D.

Stuart L. Mufson, Ph.D.

Haldan N. Cohn, Ph.D.

Charles J. Horowitz, Ph.D.

April 1, 2011

Copyright © 2011
Scott Michael

For Rhonda
my one true love

Acknowledgements

As with any great endeavor in one's life, this dissertation has taken a great deal of time and effort, and I have poured a great deal of myself into it. Along the way I've had the honor and privilege to help, and be helped by a variety of wonderful people. It is nearly impossible to thank everyone who impacted me in a positive way throughout this eight year process, so if I've left you out please do not feel insulted. To all of those who have helped me along on this journey, I appreciate you more than you will ever know.

I must start by thanking God, throughout this sojourn there have been many times when I felt that I would not be able to finish this work. But each time, His inspiration and grace encouraged me to continue on until, finally, the work was completed. "He brought me up out of the pit of destruction, out of the miry clay, And He set my feet upon a rock making my footsteps firm." (Psalm 40:1)

I must also thank my beautiful wife Rhonda, who has always been by my side through this sometimes difficult journey. Throughout our marriage, which began only a few days before my graduate studies, she has encouraged me in all of my endeavors, while gently nudging me to keep my focus on what was important. In those times when I hit a dead end in my studies and would begin to despair, she would always be there to rouse me from my despondency and inspire me to continue to press forward. In addition to being an emotional support through this process, Rhonda has been a material support, whether working to support us financially, or staying at home to care for our son, she has always done everything with grace and

humility. Rhonda, I have never thanked you enough for everything you have done for me during this time, and I probably never could. Needless to say, without you this work would never have been accomplished. Thank you for always believing in me.

Of course, my interest and passion for science, in general, and astrophysics, specifically, would never have flourished without the guidance of my parents, Patrick and Susan Michael. Their hard work and dedication in raising me has made me what I am today. They always encouraged me to pursue my interests, no matter how far-fetched or impractical they were. Mom and Dad, I know that I was, at times, a difficult child and young adult; it was your compassion and steadfastness that made this possible.

It would be difficult, if not impossible, to complete a dissertation in computational astrophysics without a good deal of computational resources. In this regard, I have been particularly fortunate throughout my studies. Indiana University's Data Capacitor, which I have used to great effect, is a singular resource. Stephen Simms, the manager of the Data Capacitor, and his team have been instrumental in providing access to the simulation data generated in the course of this work, and have helped to greatly simplify and streamline the process of data analysis. In the course of doing the research for, and writing this work, the members of the Data Capacitor team and I have become good friends. I thank you all for your friendship, it will endure beyond the Data Capacitor, and, when possible, I will always "Choose Lustre".

There are many more resource providers to be thanked, the National Science Foundation, the TeraGrid, NASA, and Indiana University's Information and Technology Services. Specifically, I would like to thank the management and staff of the

NASA Advanced Supercomputing Division, the National Center for Supercomputing Applications, and the Pittsburgh Supercomputing Center. Thank you for investing in, maintaining, and making available to the public some of the world's finest shared memory machines. I would also like to thank the system administrators of Indiana University's supercomputing resources, Big Red and Quarry. In particular, George Turner has done an excellent job of maintaining the Quarry cluster at Indiana University. It has been an absolutely essential resource for the data analysis and reduction tasks contained in this work.

For the past two years, while completing this work, I have worked as employee of the High Performance Applications group in University Information and Technology Services. My manager Robert Henschel has been more supportive of this work than I could have ever have hoped. Robert, thank you for your consideration throughout this process.

Last, but certainly not least, I must thank my advisor, and friend throughout this process, Richard Durisen. Dick has been a most excellent mentor through all of my studies at Indiana University, but particularly for my dissertation work. He was always willing to let me try new ideas and approaches, but somehow prevented me from ever straying too far off of the path. But most of all, Dick has been a great friend. Whenever the stresses of research threatened to overwhelm me Dick was there with a reassuring word, or a diversion to relieve the pressure. Dick, I thank you for the investment you have made into my career, and the sacrifices accompanying it. I know that our friendship and collaboration will continue to be enjoyable and fruitful for many years to come.

Scott Michael

**PLANET MIGRATION INDUCED BY GRAVITATIONAL
INSTABILITIES**

ABSTRACT: The study of gravitational instabilities (GIs) and their effects on protoplanetary disks has been an area of active research for over a decade. Although some studies have indicated that GIs cannot form gas giant planets directly, it is clear that they can have a significant effect on protoplanetary disk evolution. In this dissertation, I present several areas where GIs may play a key role in the evolution of a protoplanetary disk. These studies are carried out using three dimensional numerical simulations. I have carried out and analyzed twenty simulations with varying initial conditions, resolutions, and physical effects. Although all indications from these simulations are that GIs cannot form gas giant planets directly at radii smaller than 40 AU, they have shown that GIs can have a dramatic effect on protoplanetary disk structure and planets embedded in a protoplanetary disk.

I present several key results including: the effects of a varied initial surface density profile, azimuthal resolution, the amplitude of the initial random perturbation, and the adiabatic index used on the onset, strength and general evolution of GIs in protoplanetary disks. Additionally, I give results from studies of the interaction of the instabilities with the central star when it is allowed to move freely in response to the action of the GIs. Finally, I expound on several results regarding the interaction of embedded massive planets and GI active disks. I find that the presence of massive planets can have a dramatic effect on the evolution of GIs in an active disk, and the GIs can also dramatically effect the migration of the embedded planet. In fact, the action of the GIs may cause planets to migrate outward, contrary to the standard theory of the planet migration in laminar disks.



Contents

1	Introduction	1
1.1	Protostars and Protoplanetary Disk Systems	2
1.2	Gas Giant Formation Theories	3
1.2.1	The Nucleated Instability Theory	4
1.2.2	The Disk Instability Theory	7
1.3	Other Effects of Gravitational Instabilities	9
1.3.1	Understanding the Impact of Numerical and Physical Effects on GIs	10
1.3.2	Stellar Motion Caused by GIs	11
1.3.3	Planet Migration	11
1.4	This Work	18
2	Numerical Methods	20
2.1	Standard IUHG Algorithms	20
2.2	Cooling Algorithms	26
2.2.1	Constant Cooling Time	26
2.2.2	Cai/Mejía Radiative Routine	27
2.2.3	Boley Radiative Routine	27
2.3	Indirect Potential	28
2.4	Planet Integration	30
2.4.1	Leapfrog Integrator	30
2.4.2	Determination of Accelerations	33
2.5	Computational Resources	35
3	Comparative Study of Conditions	36
3.1	Analysis Procedures	38
3.1.1	Global Fourier Components	39
3.1.2	Periodicity of Coherent Modes	40

3.1.3	Mass Transport in Protoplanetary Disks	41
3.1.4	Gravitational Torques from Global Instabilities	45
3.1.5	Effective α	48
3.2	The Simulations	50
3.3	Variation of Initial Surface Density Profile	52
3.3.1	Overall Evolution	53
3.3.2	The Burst Phase	57
3.3.3	The Asymptotic Phase	62
3.3.4	Conclusions	64
3.4	Variation of Azimuthal Resolution	66
3.5	Variation of γ in the Equation of State	78
3.6	Variation of the Initial Perturbation	82
3.7	Conclusions	89
4	Stellar Motion	93
4.1	General Comparisons	94
4.2	Detailed Motion	99
4.3	Disk Analysis	107
4.3.1	One-armed Structure	107
4.3.2	Disk/Star Interaction	109
4.4	Conclusions	116
5	Planet Migration	119
5.1	Planet Simulations	119
5.1.1	Inserting Planets Into the Disk	121
5.2	Migration in Laminar Disks	124
5.3	The BASELINE Simulation	129
5.4	The Asymptotic Phase Simulations	137
5.4.1	Effects in the Disk	140
5.4.2	Planet Motions	153
5.5	The Initial Disk Simulations	161
5.5.1	Effects in the Disk	162
5.5.2	Planet Motions	170
5.6	Conclusions	174

6 Conclusion	175
6.1 Key Findings	176
6.1.1 Physical and Numerical Conditions	177
6.1.2 Stellar Motion	178
6.1.3 Planetary Migration	179
6.2 Future Work	180
6.3 Final Remarks	181
References	183

List of Tables

2.1	Algorithms used for different types of simulations	22
3.1	Disk initial conditions	52
3.2	Minimum Q values for different initial surface density profiles	61
3.3	Time averaged A_m , Toomre Q and α for several azimuthal resolutions.	70
4.1	Pattern speeds of periodogram features	112
5.1	$\langle A_m \rangle$ values for the asymptotic phase simulations	145

List of Figures

1.1	Figures from Pollack et al. (1996)	6
1.2	Examples of an object that does not form a gap and one that does . .	15
3.1	Time series of midplane and meridional densities for G1.7TC2P0.5 disk	54
3.2	Time series of midplane and meridional densities for G1.7TC2P1 disk	55
3.3	Time series of midplane and meridional densities for G1.7TC2P1.5 disk	56
3.4	Fourier components as a function of time for different initial surface density profiles	58
3.5	Fourier reconstructed midplane densities	59
3.6	Burst mass accretion rates for different initial surface density profiles	63
3.7	Surface density, Toomre Q , and entropy for the end of simulations with varying initial surface density profiles	65
3.8	$\langle A_m \rangle$ values for the comparison of initial surface density profiles . . .	67
3.9	Final midplane and meridional densities for varied azimuthal resolutions	69
3.10	$\langle A_m \rangle$ values for the comparison of azimuthal resolution	73
3.11	Comparison of $l_{max} = 128$ and 512 run asymptotic torque profiles. . .	74
3.12	Comparison of α profiles for varying azimuthal resolution	76
3.13	Final midplane and meridional densities of fragmenting disks	81
3.14	The $t_{cool}\Omega$ curves for fragmenting simulations	83
3.15	Fourier components as a function of time for different initial random perturbation amplitudes	84
3.16	Midplane and meridional densities for varying initial random pertur- bation amplitudes	86
3.17	Surface density and Toomre Q for the simulations with varying initial random perturbations at 4 ORPs	88
3.18	Surface density and Toomre Q for the simulations with varying initial random perturbations at 15 ORPs	90
4.1	Comparison of indirect and fixed run final midplane densities	96

4.2	Comparison of indirect and fixed run final surface densities	97
4.3	Comparison of Toomre Q for indirect and fixed simulations.	98
4.4	Comparison of indirect and fixed asymptotic $\langle A_m \rangle$ values	100
4.5	Comparison of indirect and fixed run mass transport rates for the burst and asymptotic phases	101
4.6	Position of the system center of mass (COM) and its radial excursion.	103
4.7	COM periodogram for radius and random sample	105
4.8	COM periodogram for x and y coordinates	106
4.9	Angular momentum and torque on central star	108
4.10	Indirect simulation periodograms for $m = 1 - 4$	110
4.11	Fixed simulation periodograms for $m = 1 - 4$	111
4.12	Comparison of indirect and fixed run asymptotic torque profiles.	113
4.13	Difference of indirect and fixed run asymptotic torque profiles.	115
4.14	Comparison of indirect and fixed run α profiles	117
5.1	Comparison of midplane and meridional densities for constant t_{cool} and BASELINE runs	128
5.2	Toomre Q and cooling times for several intervals of the BASELINE simulation	131
5.3	Time series of midplane and meridional densities for BASELINE disk	132
5.4	A_m values for the BASELINE simulation	134
5.5	Internal energy of the BASELINE simulation	135
5.6	Torque and α measurement for the asymptotic phase of the BASE- LINE simulation	136
5.7	BASELINE disk periodograms	138
5.8	BASELINE mass transport rates	139
5.9	Time series of midplane and meridional densities for 0.3JUP10ORP disk	141
5.10	Time series of midplane and meridional densities for 1JUP10ORP disk	142
5.11	Time series of midplane and meridional densities for 3JUP10ORP disk	143
5.12	Toomre Q and cooling times for several intervals of the 3JUP10ORP simulation	146
5.13	Comparison of internal energy for the BASELINE and asymptotic phase simulations	147

5.14 Comparison of disk torque for the BASELINE and asymptotic phase simulations	149
5.15 Comparison of effective α for the BASELINE and asymptotic phase simulations	150
5.16 3JUP10ORP disk periodograms	152
5.17 Planet radial positions for the asymptotic phase simulations	154
5.18 1JUP10ORP disk periodograms	157
5.19 Planet eccentricities for the asymptotic phase simulations	159
5.20 Instantaneous migration timescales for the planets in the asymptotic phase simulations	160
5.21 Time series of midplane and meridional densities for 0.3JUP0ORP disk	163
5.22 Time series of midplane and meridional densities for 1JUP0ORP disk	164
5.23 Time series of midplane and meridional densities for 3JUP0ORP disk	165
5.24 Fourier components as a function of time for different planet masses inserted at $t = 0$	167
5.25 Disk torque for the initial disk simulations averaged from 6 to 10 ORPs	169
5.26 Planet radial positions for the initial disk simulations	172
5.27 Planet eccentricities for the asymptotic phase simulations	173

Chapter 1

Introduction

*The White Rabbit put on his spectacles.
“Where shall I begin, please your Majesty?” he asked.
“Begin at the beginning,” the King said gravely,
“and go on till you come to the end: then stop.”*
– Alice’s Adventures in Wonderland, Chapter 12

This work was born of the endeavor to answer the overarching question “How do gas giant planets form?” The interest in this question was driven, in large part, by the discovery of the first extrasolar gas giant planet by [Mayor & Queloz \(1995\)](#). This discovery was soon followed by others and currently there are nearly 500 known extrasolar planets, or exoplanets. Few of these planets are terrestrial in nature, the vast majority are either gas or ice giant planets. The ubiquity of these objects reinforces the original question “How do gas giant planets form?”

It has been theorized for over two centuries ([Kant & Jaki 1981](#)) that planets form from a disk surrounding a protostar. Modern treatments of this theory conclude that the formation of a star/disk system is a natural consequence of the collapse of a protostellar cloud ([Cassen & Moosman 1981](#); [Yorke et al. 1993](#); [Vorobyov & Basu 2006](#)). In fact, direct observations of circumstellar disks have existed for over a decade ([Padgett et al. 1999](#)). Clearly planets form from the gas and dust contained in the nebula, or protoplanetary disk; the point of debate now is the formation mechanism.

1.1 Protostars and Protoplanetary Disk Systems

A protoplanetary disk is not an isolated system; it is instead a part of a forming stellar system. These systems are generally termed young stellar objects (YSOs), which include the protostar, the protoplanetary disk, and the infalling envelope. Such objects are generally divided into three groups based on the infrared and millimeter excesses in their spectral energy distributions (Adams et al. 1987; Kenyon & Hartmann 1987; Greene et al. 1994); they are Class I, II, and III YSOs. Class I YSOs have large infrared excesses due to the fact that they are young embedded stars surrounded by a dusty disk and infalling envelope. Once the envelope has dissipated and only the disk remains, the YSO is characterized by moderate infrared excess and has become a Class II object. Class III YSOs have little infrared excess and are in a late phase of the formation process. Class III objects have either no disk or a very tenuous one, which produces little infrared emission. In addition to the Class I, II, and III objects, researchers have suggested a Class 0 phase, in which the star is so deeply embedded in the envelope that optical emission from the star is not visible (Andre et al. 1993). Others have argued that proposed Class 0 objects may actually be Class I objects that have formed in a denser environment and therefore have more substantial envelopes (Jayawardhana et al. 2001).

Much of this work is applicable to T Tauri stars, a class of variable stars named after their prototype T Tauri. They are pre-main sequence stars found near molecular clouds and identified by their optical variability and strong chromospheric lines, and are typically surrounded by a circumstellar accretion disk. T Tauri stars are classified into two categories: classical T Tauri stars (CTTS), which have excess

infrared emission, strong line emission, and an active accretion disk, and weak line T Tauri stars (WTTS), which have little infrared excess, weak line emission, and a mostly dissipated disk. CTTS are considered to be Class I or II objects while WTTS are Class III objects. YSOs are thought to follow an evolutionary sequence through the different Classes, and therefore transition from CTTS to WTTS. Although there are some indications that the Class I to II transition can occur in ~ 1 Myr (Eisner & Carpenter 2006), firm estimates on the duration of each of the phases are not well known, and probably vary from one system to another.

1.2 Gas Giant Formation Theories

There are two major theories of gas giant planet formation that are currently being considered – core accretion, or nucleated instability, and disk instability. The nucleated instability theory, first discussed by Safronov & Zvjagina (1969) and later improved by Mizuno (1980), has come to be considered the standard theory of gas giant planet formation. It states that a rocky core builds up via accretion of solids in the protoplanetary disk. When this core is massive enough, it will accrete the surrounding gas until it clears a gap within the disk. The disk instability theory first proffered by Kuiper (1951) and later revisited by Boss (1997) postulates that protoplanetary disks susceptible to gravitational instabilities (GIs) could form gravitationally bound clumps, which would eventually contract to become gas giant planets.

Each of the theories has advantages and challenges; in the next sections, I will highlight some of them. It should be noted that hybrids of the two theories have been proposed (see §1.2.2) where the nucleated instability is accelerated by the action of

GIs.

1.2.1 The Nucleated Instability Theory

In the nucleated instability picture, a large solid core must first build up through the collision of rocky materials (Safronov & Zvjagina 1969). When this core grows to several Earth masses, it gravitationally attracts the surrounding gas to form a gas giant planet (Mizuno 1980). Observational estimates of disk lifetimes range from 0.1 to 10 Myr, (Haisch et al. 2001; Chen & Kamp 2004). Simulations by Pollack et al. (1996) found that core accretion could produce a gas giant planet ~ 8 Myr after kilometer-sized planetesimals have formed. In addition, Pollack et al. (1996) found that the formation time is highly dependent on the initial protoplanetary disk surface density. Figure 1.1 reproduces portions of Figure 1 and Figure 2 from (Pollack et al. 1996) and shows the dramatic variation of formation time with initial surface density. However, the core masses (M_{core}) of the planets produced by these simulations ($\sim 15M_{\oplus}$) are outside the range of Jupiter’s core mass (0–11 M_{\oplus}) inferred from the Jovian gravitational moments and detailed equation of state calculations (Saumon & Guillot 2004). The large range of possible M_{core} is due to uncertainties in the equation of state (EOS) of hydrogen and helium at megabar pressures. Saumon & Guillot (2004) found the most likely values of M_{core} to be $\leq 5M_{\oplus}$. However, new simulations by Militzer et al. (2008) predict a Jupiter core mass of 14–18 M_{\oplus} . The results of Saumon & Guillot (2004) allow for several possibilities: (1) Core accretion can occur for $M_{core} \leq 5M_{\oplus}$, (2) Jupiter formed with a more massive core which was then dispersed into Jupiter’s outer layers, or (3) Jupiter did not form via core

accretion. More recent work by [Hubickyj et al. \(2005\)](#) and [Papaloizou & Nelson \(2005\)](#) have addressed the first point by demonstrating that a gas giant planet can form via core accretion with $M_{core} = 5M_{\oplus}$ in 4.5 Myr and 3 Myr, respectively. However, for these simulations, the authors used dust grain opacities of 2% and 1% of the interstellar value. When the dust grain opacity is set to the interstellar value, gas giants form in 95 Myr and 30 Myr ([Hubickyj et al. 2005](#)). The critical uncertainty in determining these timescales is the growth time of the protoplanet's envelope. [Ida & Lin \(2008\)](#) recast the equation for the growth timescale of a protoplanet's envelope $\tau_e = M(dM_e/dt)^{-1}$ to

$$\tau_e = k_1 \left(\frac{M_p}{M_{\oplus}} \right)^{-k_2} \text{ yr}, \quad (1.1)$$

where M_p is the planetary mass, including the envelope, and M_{\oplus} is an Earth mass. k_1 and k_2 are parameters which have strong dependence on several factors, including the envelope opacity. Values for the [Pollack et al. \(1996\)](#) simulations are $k_1 = 10^{10}$ and $k_2 = 3$.

Forming kilometer-sized planetesimals needed to build the cores may be difficult due the effects of migration. Planetesimals must grow from small dust grains in the gas disk which is accreting onto the central star. Since the particles are strongly affected by gas drag until they reach sizes of tens of meters ([Weidenschilling 1977](#)), they must grow to this size quickly or be accreted into the star. See §1.3.3 for a further discussion on the effects of migration.

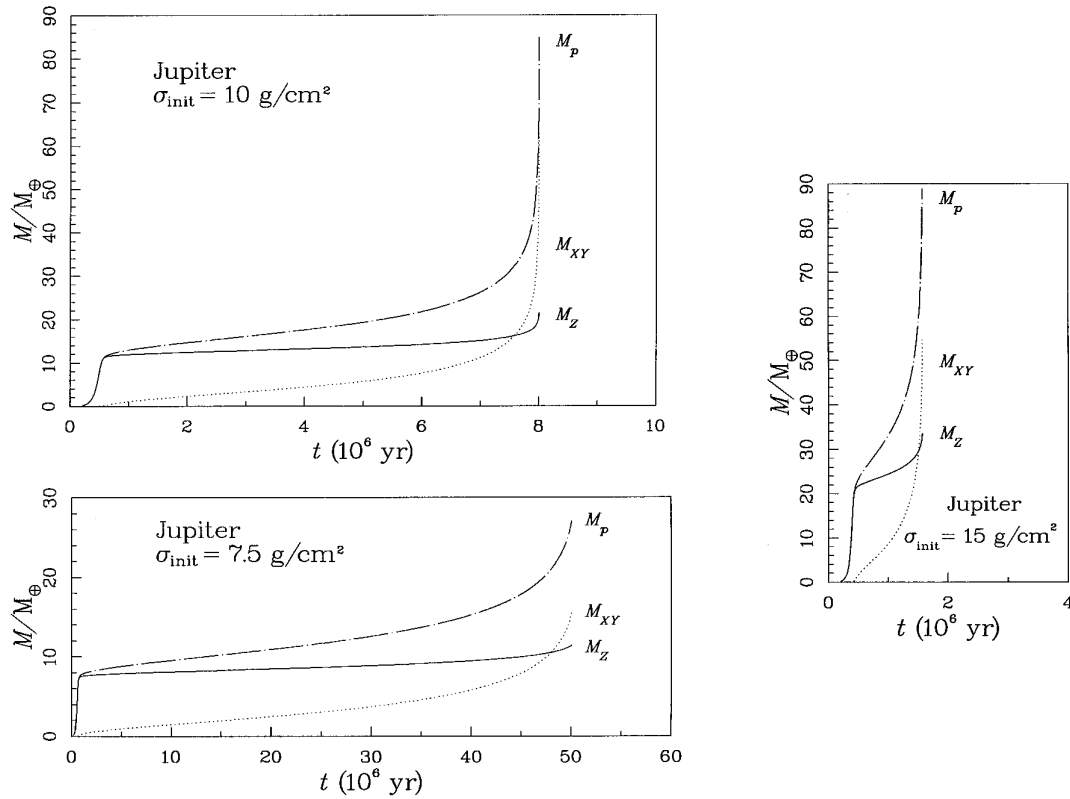


Figure 1.1: Panels from Figures 1 and 2 of [Pollack et al. \(1996\)](#). Each panel represents the growth of a gas giant planet via the nucleated instability. The solid line represents the growth of solids, the dotted line the accretion of hydrogen and helium, and the dashed line represents the total mass. Three simulations are shown with the principle difference being the surface density of solids at Jupiter's radius, which varies between 7.5 g/cm^2 and 15 g/cm^2 . Clearly the surface density of solids has a strong effect on growth time. Figure reproduced with permission of co-author Olenka Hubickyj.

1.2.2 The Disk Instability Theory

On the other hand, disk instability (Kuiper 1951; Cameron 1978; Boss 1997; Durisen et al. 2007) can form dense clumps via GIs in times comparable to the dynamic time of the disk ($\lesssim 10^3$ yr). According to the theory, these clumps are the self-gravitating precursors to gas giant planets. As the clump contracts, the solids contained in the gas will rain out to form a core (Slattery et al. 1980; Helled et al. 2008; Helled & Schubert 2008); the clump can also capture more solids from the surrounding disk (Helled et al. 2006; Guillot 2010). A protoplanetary disk must meet three main requirements to form gas giant planets via disk instability: (1) GIs must occur in the disk, (2) the GIs must cause the disk to fragment into dense clumps, and (3) these clumps must survive long enough to become gravitationally bound.

To parameterize the susceptibility of a disk to instability, consider the Toomre Q parameter (Toomre 1964), where

$$Q = \frac{c_s \kappa}{\pi G \Sigma}. \quad (1.2)$$

Here, c_s is the sound speed, κ is the epicyclic frequency, where κ is calculated by $\kappa = \sqrt{rd\Omega^2/dr + 4\Omega^2}$ using azimuthally averaged midplane values of Ω , and Σ is the gas surface density. The factors in equation (1.2) represent stabilizing and destabilizing influences in the disk. The local pressure, represented by c_s , acts to stabilize short wavelengths while the disk rotation, represented by κ , acts to stabilize long wavelengths. Disk self-gravity, represented by $\pi G \Sigma$, acts to destabilize the disk. For $Q \leq 1$, a disk is highly unstable to an axisymmetric ring instability (Toomre 1964), and spiral instabilities set in at somewhat higher Q -values. Numerical simulations

generally show that disks with Q -values ~ 1.5 to 1.7 are marginally unstable (Boss 2000; Pickett et al. 2003; Durisen et al. 2007).

Even though spiral disturbances due to GIs may exist in a disk, the disk may not fragment into dense clumps. Whether a disk will fragment is largely controlled by the cooling time. Isothermal calculations of low- Q disks, representing instantaneous cooling, tend to form many fragments (Boss 2000; Pickett et al. 2003). Simulations using parameterized cooling find that the cooling times, with an adiabatic index, i.e. the ratio of specific heats, $\gamma = 5/3$ for the gas, must be less than about one half to one orbit period for fragments to appear (Gammie 2001; Rice et al. 2003b; Mejía et al. 2005). For a $\gamma = 7/5$ gas, fragmentation occurs for cooling times as long as two to four disk orbit periods (Rice et al. 2005; Clarke et al. 2007). Regardless of the EOS, simulations using more realistic radiative physics find that cooling times are too long to form fragments in protoplanetary disks inside about 40 AU (Cai et al. 2006, 2008; Boley et al. 2006, 2007a; Boley & Durisen 2008; Stamatellos & Whitworth 2008; Forgan et al. 2009). Although there are some dissenters (Boss 2007; Mayer et al. 2007), the failure of realistically cooled disks to fragment inside 40 AU is strongly supported by analytic arguments (Rafikov 2005, 2007). On the other hand, recent analytic or semi-analytic work (Clarke 2009; Rafikov 2009; Dodson-Robinson et al. 2009) and simulations (Stamatellos & Whitworth 2009; Boley 2009; Boley et al. 2010) indicate that disk fragmentation and gas giant protoplanet formation may indeed occur in real disks outside 100 AU.

Once fragments form, they must survive long enough to become bound by self-gravity. Although many clump forming simulations have found clump lifetimes of multiple disk orbits (Boss 2003; Rice et al. 2003b; Mayer et al. 2004), other simula-

tions find that the clumps are destroyed by the shearing motion of the disk (Pickett et al. 2003; Mejía et al. 2005). Although some of this discrepancy may be due to different numerical methods (Pickett & Durisen 2007), simulations using the same code show clump destruction and survival also depend on the physical conditions in the disk. Obviously the particulars of a disk (EOS, mass, temperature, opacity, location, etc.) play a pivotal role in all aspects of the disk instability theory. Given the existing difficulties with both theories, some authors have proposed hybrid theories where GIs assist planetesimal formation and accelerate core accretion (Haghighipour & Boss 2003b; Rice et al. 2004, 2006; Durisen et al. 2005).

1.3 Other Effects of Gravitational Instabilities

Regardless of whether planets typically form via disk instability, nucleated instability, or some combination, gravitational instabilities can play a key role in various aspects of protoplanetary disk evolution. Although there are convincing analytical arguments (Rafikov 2005, 2007) and simulation results (Nelson et al. 2000a; Cai et al. 2006; Boley et al. 2006, 2007a; Stamatellos & Whitworth 2008; Boley & Durisen 2008) showing that protoplanetary disks cannot undergo fragmentation via gravitational instability at radii $\lesssim 40\text{AU}$, analytical arguments and theoretical modeling have shown that GIs can be active for a range of disk parameters over a large range of radii (Vorobyov & Basu 2008; Vorobyov 2009; Rafikov 2009; Zhu et al. 2009). Indeed, it is generally accepted that Class I objects are massive enough CTTS to be GI active; additionally GIs could influence FU Orionis outbursts in this stage of evolution (Armitage et al. 2001; Vorobyov & Basu 2006; Boley & Durisen 2008; Zhu et al. 2009). However,

this may not be the only phase in disk evolution when GIs can play a major role (c.f., [Zhu et al. 2010](#)), since GIs are not only strongly affected by mass, but also by disk energetics. This makes auxiliary effects of GIs particularly interesting since they may be ubiquitous. In non-fragmenting disks, GIs can play an important role in mass and energy transport, the migration of embedded massive objects, and the motion of the central star. I will explore each of these throughout this work.

1.3.1 Understanding the Impact of Numerical and Physical Effects on GIs

To date, much effort has been devoted to understanding when and how GIs can cause a disk to fragment. Less emphasis has been placed on understanding how various disk properties might change the initiation of GI activity and what effect such properties might have on the basic characteristics of the instabilities. Key questions such as “What are the primary factors that determine the dominant unstable mode in a GI active disk?” or “How do physical quantities in the disk (e.g. surface density profile, composition, equation of state) affect the onset and growth of GIs?” still have no definitive answer. These questions and their corollaries are important when considering effects of GIs beyond direct planet formation. In chapter 3 I address some of these issues, by varying both physical and numerical parameters for several simulations. Analysis of these disks provides insight into physical and numerical factors that can dramatically alter the character of GIs. Specifically, I study the effectiveness of GIs as a mass transport mechanism and attempt to determine whether angular momentum transport in a GI active disk is a local or global process ([Balbus & Papaloizou 1999](#); [Vorobyov 2010](#)).

1.3.2 Stellar Motion Caused by GIs

[Adams et al. \(1989\)](#) proposed that a $m = 1$ pattern in a circumstellar disk could grow via interaction with the central star. This amplification, termed Stimulation by the Long-range Interaction of Newtonian Gravity, or SLING, acts when an $m = 1$ mode is stimulated and reflects from the outer disk edge. When reflected, trailing waves become leading waves and vice versa. The amplification occurs if the reflected waves have the same phase as those generated by resonant forcing of the central star ([Shu et al. 1990](#)). Even if SLING amplification is not acting, $m = 1$ patterns can develop from the interaction of higher-order modes. This second-order effect can still be substantial if the interacting modes are highly nonlinear. Some numerical work has been done to study the possibility of stellar motion caused by waves created from GIs, but it has either focused on fragmenting disks ([Boss 1998a](#)) or been dominated by local modes ([Rice et al. 2003a](#)). In chapter 4, I examine the effect of GI activity on stellar motion.

1.3.3 Planet Migration

Regardless of how a gas giant planet forms, whether by core accretion, gravitational instability, or a hybrid of the two, an interesting question is what happens to a protoplanet after it has formed and before the disk dissipates. Linear analysis ([Ward 1997](#); [Tanaka et al. 2002](#)) as well as numerical simulations ([Nelson & Papaloizou 2003, 2004](#)) indicate that in a laminar disk, or a disk dominated by MHD turbulence, planets tend to migrate inward via type I or type II migration and may be accreted onto the central star. The distinction between type I and type II migration

is whether or not the planet can open a gap in the disk. If no gap forms, the planet undergoes type I migration where the planet and disk exchange angular momentum via gravitational torques. In the case of type II migration, a gap forms and the planet migrates inward due to the overall disk evolution caused by viscous stresses. Type III migration occurs for objects in the transition between type I and type II migration, i.e., bodies massive enough to create a dip or gap in the surface density profile locally but not massive enough to completely clear a gap. In the case of type III migration, fluid elements follow horseshoe streamlines in the vicinity of the planet. When the fluid elements execute a U-turn at the end of the streamlines, they can gain or lose angular momentum from the planet, resulting in a coorbital corotation torque (Masset & Papaloizou 2003). Because this is a transitional case, and the streamlines that give rise to the coorbital torque are too complex and on too small of a scale to model accurately with a global fixed grid, I do not consider type III migration in my investigations. The preceding description is included for completeness.

1.3.3.1 Gap Formation

The gravitational torque exerted by an embedded object on the disk is

$$T_g = \zeta r_p^4 \Omega^2 \left(\frac{r_p}{\Delta r} \right)^3 \left(\frac{m_p}{M_\star} \right)^2. \quad (1.3)$$

Here r_p is the orbital radius of the planet, Ω the orbital frequency, m_p the planet mass, M_\star the star mass, Δr is the larger of the disk scale height, H , and the Hill radius of the planet, and ζ is a numerically determined factor ~ 0.25 (Lin & Papaloizou

1979a,b; Goldreich & Tremaine 1980; Lin & Papaloizou 1986). An object's Hill radius defines the region in which its gravitational field dominates the motion of a small mass orbiting the object. It is defined as $R_H = r \left(\frac{m_p}{3M_\star} \right)^{1/3}$. This torque acts to transfer angular momentum from the planet to the disk at $r_p + \Delta r$ and to transfer angular momentum from the disk to the planet at $r_p - \Delta r$. This causes material at larger radii to gain angular momentum and move outwards while material inside the planet's orbit will lose angular momentum and move inwards. The net effect is for a gap to open in the disk at the planet's orbital radius. This may be counterbalanced by other mechanisms which act as viscous stresses. The viscous torque exerted on material outside r by material inside r in a keplerian disk is (Lynden-Bell & Pringle 1974),

$$T_v = 3\pi\Sigma\nu\Omega r^2. \quad (1.4)$$

Here ν represents the disk kinematic viscosity. This torque acts to transfer angular momentum outward and mass inward. If it is greater than the gravitational torque at $r + \Delta r$, then material will move inward and gap formation will be halted. So the condition for gap formation is $T_g > T_v$.

If one adopts the α -disk prescription described by Shakura & Syunyaev (1973) (see §3.1.5) and assumes $\nu = \alpha c_s H$ where α is a parameter and c_s is the isothermal sound speed, then the torque inequality implies that

$$\left(\frac{m_p}{M_\star} \right)^2 \gtrsim 3\pi\zeta\alpha \left(\frac{H}{r} \right)^5 \quad (1.5)$$

must be satisfied to form a gap if $H > R_H$. If $H < R_H$ then the criterion becomes,

$$\frac{R_H}{r} \gtrsim \zeta \alpha. \quad (1.6)$$

See Figure 1.2 for a comparison between a gap forming planet and a non-gap forming planet.

1.3.3.2 Type I Migration

In the case of type I migration, the protoplanet is not massive enough to open a gap in the disk and migrates inward by exchanging angular momentum with the disk via gravitational torques. Typically in type I migration, the mass of the planet is small enough that its gravitational perturbations do not have a large effect on the structure of the surrounding disk. However, for a given spiral mode the planet can couple strongly to the disk at the inner and outer Lindblad resonances (Papaloizou et al. 2007). The planet potential can be Fourier decomposed in the azimuthal direction. Each component can be thought of as a perturbing potential $\Phi_m(r, \phi)$, which has azimuthal mode number m and rotates with pattern frequency Ω_p . In this case, angular momentum is exchanged with the disk whenever $m(\Omega - \Omega_p)$ equals either 0 or $\pm\kappa$. For a Keplerian disk $\kappa \equiv \Omega$ so this occurs at the corotation resonance, when $\Omega = \Omega_p$. It also occurs at the inner Lindblad resonance, when $\Omega = \Omega_p + \Omega/m$, and the outer Lindblad resonance, when $\Omega = \Omega_p - \Omega/m$. Spiral density waves are launched at the Lindblad resonances and transfer angular momentum throughout the disk. The waves at the outer Lindblad resonance produce a negative torque (i.e., transfer angular momentum from the planet to the disk), while waves at the inner

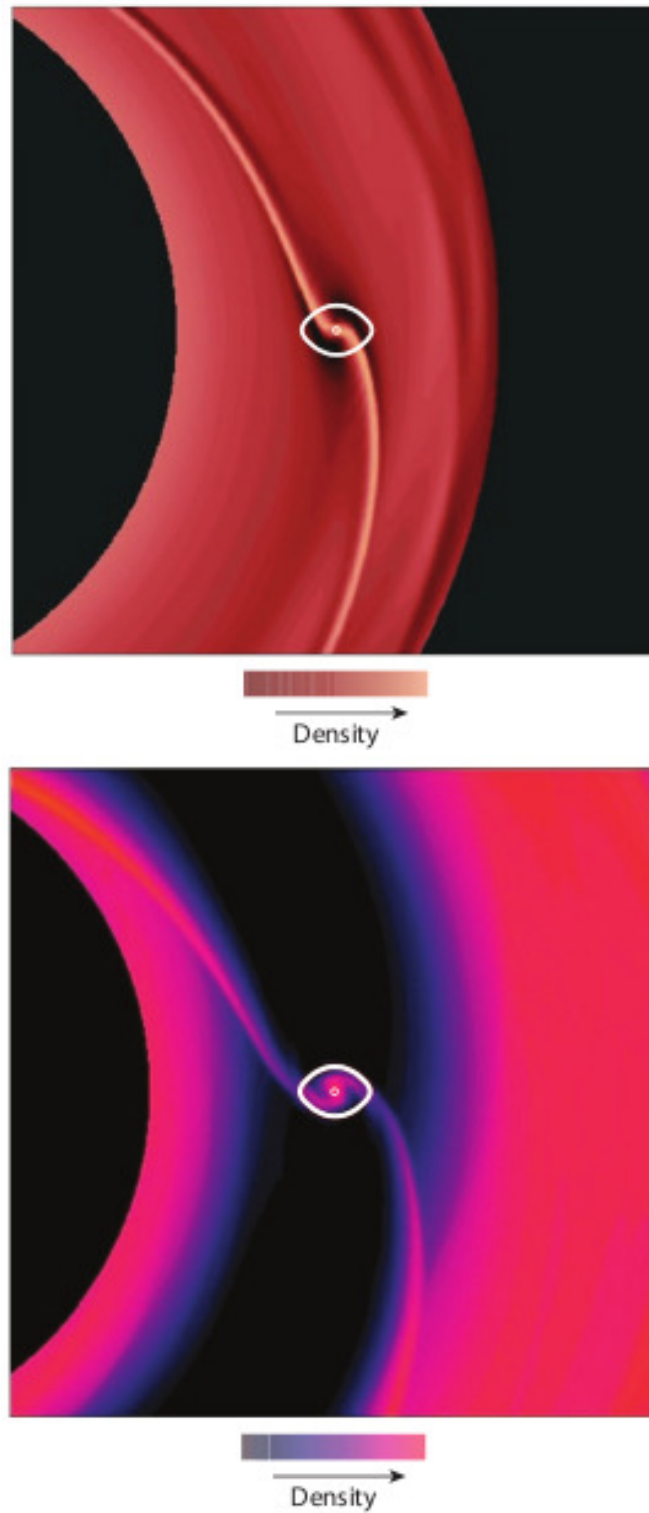


Figure 1.2: *These images taken from [Chambers \(2009\)](#) show examples of numerical simulations that contain an object that does form a gap (bottom) and one that does not (top). Figure reproduced with permission of author Pawel Artymowicz.*

Lindblad resonance produce a positive torque (i.e., transfer angular momentum from the disk to the planet). In general, these torques are not equal, partly due to the fact that the outer Lindblad resonance lies closer to the planet than the inner one. The result is a net decrease of angular momentum for the planet (Papaloizou et al. 2007). This, in turn, leads to the inward migration of the planet.

For type I migration, the timescale for the protoplanet to migrate into the central star can be less than a few $\times 10^5$ years, short compared to disk lifetimes. In an isothermal disk, the migration rate is approximately,

$$\frac{dr_p}{dt} \approx -(2.7 + 1.1q) \left(\frac{M_p}{M_\star} \right) \left(\frac{\Sigma r_p^2}{M_\star} \right) \left(\frac{c_s}{r_p \Omega_p} \right)^{-2} \Omega_p. \quad (1.7)$$

Here, the gas surface density $\Sigma \propto r^{-q}$, Ω_p is the angular orbital velocity of the disk at the planet radius, and c_s is the isothermal sound speed (Tanaka et al. 2002). This result, derived using linear analysis, has been confirmed via numerical simulations for planet masses less than a few times M_\oplus (D'Angelo et al. 2003; D'Angelo & Lubow 2008).

Although this rapid migration timescale is problematic for the survival of growing gas giant planet cores, there are many factors that can alter type I migration. Investigations into how type I migration might proceed differently and factors that might change the migration rate have had some success. For example, most work done on type I migration assumes a vertically isothermal disk structure, but recent work has shown that type I migration may be altered substantially for a non-isothermal disk (Paardekooper & Mellema 2006; Kley & Crida 2008). In fact, under certain disk conditions, planet cores may migrate *outward* (Kley & Crida 2008). Additionally, as

I will show in this dissertation, if the disk is gravitationally unstable, the instabilities may slow inward migration, or even cause the protoplanet to move outward. These effects may help to explain how embryos, cores, and protoplanets can survive in a protoplanetary disk after they form as well as provide insight into their distributions in multiple planet systems, more than fifty of which have already been discovered. So far, migration in gravitationally unstable disks has only been studied in the context of fragmented disks (Mayer et al. 2004; Boss 2005).

1.3.3.3 Type II Migration

With type II migration, the protoplanet is massive enough to open a gap and then migrates with the motion of the surrounding disk. Once the gap has been opened, the planet's migration rate is tied to the viscous evolution of the disk. The planet migrates inward at the same rate as the gas inflow rate due to viscosity. This rate is

$$\frac{dr_p}{dt} = -\frac{3\nu}{2r_p}, \quad (1.8)$$

where ν is the kinematic viscosity of the disk.

If the planet moves toward the inner or outer edge of the gap, the resulting torque imbalance acts to restore its position to the middle of the gap. Although the timescale for the viscous evolution of the disk is generally longer than the type I migration timescale, it is still sufficiently short to pose problems for planet survivability. Very massive planets undergo migration at a reduced rate compared to equation (1.8) due to the fact that there is a maximum torque that can be exerted by the disk from its viscous evolution. When the planet mass $M_p \gtrsim \pi r_p^2 \Sigma$, the migration rate depends

on $\Sigma r_p^2/M_p$ instead of depending solely on the viscosity.

1.4 This Work

In this thesis, I investigate several of the aforementioned phenomena caused by GIs in protoplanetary disks through three dimensional radiative hydrodynamic simulations. By varying several different parameters and simulating new physical mechanisms, I explore the effects of varied conditions on GIs. I also study how GIs can impact stellar motion and planetary migration. In all, I am seeking to answer the following questions:

- How do the following affect GI onset and evolution:
 - Surface density
 - Azimuthal resolution
 - Equation of state
 - Initial random perturbation
- What is the interplay between GI activity and stellar motion?
- How do GIs affect planet migration?
- Can planets or protoplanets trigger GIs?
- How does the presence of a planet or protoplanet affect the onset or characteristics of GIs?

In chapter 2, I discuss the various aspects and features of the hydrodynamic codes used. Specifically, I describe the inclusion of the indirect potential method and the Verlet integration method to include stellar motion and planetary companions. Chapter 3 looks at the ramifications of varying several physical and numerical parameters in disk simulations, including initial surface density profile, equation of state, initial density perturbation, and numerical resolution. Detailed analysis of disk dynamics, mass transport rates, and GI characteristics are performed. In chapter 4, the outcome of allowing the central star to move in a GI active disk is examined and compared to the fixed star case. Chapter 5 studies the effect of GIs on planetary migration and also examines how the presence of a planet can impact the onset of GIs. Finally, in chapter, 6 I summarize the key results.

Chapter 2

Numerical Methods

*The best laid schemes of Mice and Men
oft go awry,
And leave us nothing but grief and pain,
For promised joy!*
– Robert Burns, *To a Mouse*

Several different versions of the Indiana University Hydrodynamics Group (IUHG) code have been used to carry out the studies being presented. This chapter describes their design and presents the addition of several new algorithms used to account for stellar motion and to follow the motion of a planet in a GI-active protoplanetary disk I also present results from tests to evaluate the accuracy and efficiency of these new algorithms.

2.1 Standard IUHG Algorithms

The standard version of the IUHG code is an Eulerian scheme which is second-order in both space and time. The evolution is carried out in cylindrical coordinates (ϖ, ϕ, z) on an evenly spaced three dimensional grid. The rotation axis of the disk is aligned with the z -axis. The (ϖ, ϕ, z) -directions will hereafter be referred to as the radial, azimuthal, and vertical directions. The disk is treated as having reflection symmetry about the midplane in order to reduce computation time. Poisson's equation is solved

via Fourier decomposition and cyclic reduction (Tohline 1980). Shock heating is modeled via artificial viscosity (Pickett 1995) and cooling can be treated in various ways. For this study, three particular cooling methods are of interest, an *ad hoc* constant cooling time prescription, the Cai/Mejía radiative algorithm (Mejía 2004; Cai 2006), and the Boley radiative algorithm (Boley et al. 2007a). (See §2.2 below for details on the cooling algorithms.)

The equations of hydrodynamics and self-gravity are:

$$\frac{\partial \rho}{\partial t} + \nabla \cdot \rho \mathbf{v} = 0, \quad (2.1)$$

$$\frac{\partial \rho \mathbf{v}}{\partial t} + \nabla \cdot \rho \mathbf{v} \mathbf{v} = -\nabla p - \rho \nabla \Phi_{\text{tot}} - \nabla \cdot (\rho \mathbf{Q}), \quad (2.2)$$

$$\frac{\partial \epsilon}{\partial t} + \nabla \cdot \mathbf{v} \epsilon = -p \nabla \cdot \mathbf{v} + \Gamma - \Lambda, \quad (2.3)$$

$$\nabla^2 \Phi_{\text{disk}} = 4\pi G \rho. \quad (2.4)$$

These are the mass continuity equation (2.1), the equations of motion (2.2), the internal energy equation (2.3), and Poisson’s equation (2.4). Here ρ is the mass density, \mathbf{v} represents the gas velocity, p is the gas pressure, \mathbf{Q} is the artificial viscosity tensor, ϵ is the internal energy density, Γ represents heating due to artificial viscosity, Λ represents net cooling due to energy transport via radiation or other mechanisms, and Φ_{tot} and Φ_{disk} are the total and disk gravitational potentials, respectively. (See §2.3 and §2.4.2 for the determination of the total potential.)

Artificial viscosity is treated using a von Neumann-type scheme (Norman & Winkler 1986) in which the off-diagonal terms of the artificial viscosity tensor are set to zero and the heating due to artificial viscosity is given by $\Gamma = \rho(\mathbf{Q}_{\varpi\varpi} \partial_{\varpi} v_{\varpi} + \mathbf{Q}_{\phi\phi} r^{-1} \partial_{\phi} v_{\phi} + \mathbf{Q}_{zz} \partial_z v_z)$. Previous versions of the code have used a constant ratio of

Simulation Type	EOS	Cooling	Central Star	Planet
Initial Conditions	γ	t_{cool}	Fixed	No
Indirect Comparison	γ	t_{cool}	Indirect	No
Planet Baseline	H_2	Radiative	Indirect	No
Planet Comparisons	H_2	Radiative	Indirect	Yes

Table 2.1: Each column indicates the treatment of all physical effects for each suite of simulations. The equation of state (EOS) is treated as a fixed γ or full H_2 EOS, the cooling algorithm is a constant cooling time or the Boley radiative routine, the central star is treated as a fixed potential or allowed to move via the indirect potential, and some simulations include planets.

specific heats γ and an ideal gas equation of state to define the pressure

$$p = (\gamma - 1)\epsilon. \quad (2.5)$$

This allows one to rewrite the energy equation (2.3) in conservative form,

$$\frac{\partial \epsilon^{1/\gamma}}{\partial t} + \nabla \cdot \mathbf{v} \epsilon^{1/\gamma} = \frac{\epsilon^{1/\gamma-1}}{\gamma} (\Gamma - \Lambda). \quad (2.6)$$

This version of the energy equation was first included in the IUHG code by [Pickett \(1995\)](#) and was found to produce better energy conservation than direct implementation of equation (2.3). Equation (2.6) is used for those simulations which use a constant γ equation of state. However, other simulations use a more realistic equation of state for H_2 which takes into account its translational, rotational and vibrational states ([Boley et al. 2007b](#)). See table 2.1 for details of algorithms used for each type of simulation.

The code evolves several state variables, namely the mass density ρ , internal energy density ϵ and momentum densities $\rho \mathbf{v}$. Each component of the momentum is evolved independently. Expansion of equation (2.2) yields three equations for the

momentum, namely,

$$\frac{\partial S}{\partial t} + \nabla \cdot S\mathbf{v} = -\rho \frac{\partial p}{\partial \varpi} - \rho \frac{\partial \Phi_{\text{tot}}}{\partial \varpi} - \frac{\partial \varpi \rho \mathbf{Q}_{\varpi\varpi}}{\varpi \partial \varpi} + \frac{A^2}{\rho \varpi^3}, \quad (2.7)$$

$$\frac{\partial A}{\partial t} + \nabla \cdot A\mathbf{v} = -\rho \frac{\partial p}{\partial \phi} - \rho \frac{\partial \Phi_{\text{tot}}}{\partial \phi} - \frac{\partial \rho \mathbf{Q}_{\phi\phi}}{\partial \phi}, \text{ and} \quad (2.8)$$

$$\frac{\partial T}{\partial t} + \nabla \cdot T\mathbf{v} = -\rho \frac{\partial p}{\partial z} - \rho \frac{\partial \Phi_{\text{tot}}}{\partial z} - \frac{\partial \rho \mathbf{Q}_{zz}}{\partial z}. \quad (2.9)$$

This gives three momentum density arrays S , T , and A , which are the radial $\rho\mathbf{v}_\varpi$, vertical $\rho\mathbf{v}_z$ and angular momentum densities $\rho\varpi\mathbf{v}_\phi$, respectively. The momentum density arrays along with the mass density ρ updated according to equation (2.1) and the internal energy density ϵ updated according to either equation (2.3) or (2.6), depending on the type of EOS used, define the five state variable arrays evolved by the code.

The five state variables are updated in time via a two-step process achieved through operator splitting, which has been shown to reduce numerical noise (Williams 1988; Yang 1992). The equations are written in a conservative form, except for the energy equation in the cases in which the H_2 equation of state is used. The two steps are known as *sourcing* and *fluxing*. In the source step, the dynamic variables are accelerated by the pressure force, the centrifugal force, and gravity. Also, heating and cooling due to artificial viscosity and the cooling prescription are accounted for by updating the internal energy. In the fluxing step, the variables are fluxed by calculating the flow through the surfaces of the grid cells. All of the surfaces at the grid boundaries use outflow boundary conditions. As described by Yang (1992), the fluxing is accomplished by using a second-order van Leer monotonic advection (van Leer 1979). Yang (1992) found that by calculating the S and T values at the centers

of their respective cell faces and the ρ , A , and ϵ arrays at the cell centers greater stability was achieved over calculating all the values at the cell centers. For more details on the specifics of the differencing schemes see [Pickett \(1995\)](#).

In order to achieve second-order accuracy in time, the dynamical quantities are advanced a half step, the half-sourced values are transported a full step, and finally the source terms are updated and the final distribution is sourced for the second half step. Since the potential distribution is calculated from the density, which has no source terms, it only needs to be calculated once per step. For a flow chart of these steps see [Mejía \(2004\)](#) or [Boley \(2007\)](#).

The potential used to source the state variables is made up of several components namely, the disk component, the stellar component, the indirect component, and the planet component. So

$$\Phi_{\text{tot}} = \Phi_{\text{disk}} + \Phi_{\text{star}} + \Phi_{\text{ind}} + \Phi_{\text{planet}}. \quad (2.10)$$

The indirect component contains two pieces — due to the disk Φ_{ind} (disk) and the planet Φ_{ind} (planet). Each of the terms in equation (2.10) is calculated differently. The Φ_{disk} component comes from the solution to equation (2.4). The disk potential is calculated by first determining the boundary potential by multipole expansion of spherical harmonics using $l = |m| = 10$. Once the boundary conditions have been obtained, the density data is Fourier transformed in the ϕ -direction. Each of the Fourier components yields a 2D boundary value problem which can be cast into a block-tridiagonal matrix and is then solved using cyclic reduction. The solution in Fourier space is then transformed back into real space.

The star’s potential has been calculated in two different ways. Initial equilibrium models are generated using a self-consistent field algorithm which produces a star/disk model (Pickett 1995). In order to avoid overly small time steps the central star is removed (Pickett et al. 2003). The gravitational effect of the removed material can be calculated from the mass distribution removed. This potential data is then saved and can be applied to the simulation as long as the mass inside the hole is assumed to be stationary. Tests have shown that approximating the evacuated mass as a point mass in the midplane on the z -axis makes a negligible difference to the potential, so most recent simulations have used this approximation. Making such an approximation is beneficial because the star’s potential can now be recalculated if it moves from the grid center. However, there are more computationally efficient and elegant ways of treating stellar motion besides moving the star directly (e.g., §2.3). In all but one of the Initial Conditions runs (see table 2.1), the central star is treated as a point mass fixed at the grid center in an inertial frame. All simulations in chapters 4 and 5 employ the indirect potential method described in §2.3 to account for accelerations of the frame centered on the star due to interactions with the disk and planet. In all cases, except for one in chapter 3, the star remains fixed at the grid center and is treated as a point mass so that

$$\Phi_{\text{star}} = -\frac{GM_{\text{star}}}{r}. \quad (2.11)$$

There are two terms which go into the calculation of Φ_{ind} , specifically the disk’s indirect contribution and the indirect contribution of the planet. The treatment of the planet potential is described in §2.4.2.

2.2 Cooling Algorithms

Several different cooling routines were used in the simulations contained in this study. I will briefly outline the key characteristics of these algorithms, but interested readers can consult [Mejía \(2004\)](#), [Cai \(2006\)](#), and [Boley \(2007\)](#) for more details. The three cooling types I will focus on are constant cooling time, the Cai/Mejía radiative routine, and the Boley radiative routine.

2.2.1 Constant Cooling Time

The constant cooling time algorithm is the simplest of the cooling algorithms, and although it is the least physically accurate, it does provide insight when comparing the effect of other parameters on the strength and character of GIs. It also executes the fastest, and this allows for more efficient sampling of parameter space. The volumetric cooling rate in equation (2.3) is determined according to

$$\Lambda = \epsilon/t_{cool}, \tag{2.12}$$

where the cooling time t_{cool} is a constant parameter that is set at the beginning of a simulation. The energy is removed from every cell with a density greater than the negligible background density, also determined at the beginning of a simulation. The cooling time is generally specified in Outer Rotation Periods (ORPs) which is the initial rotation period at radial zone 200 (≈ 33 AU) for the original Mejía disk with a $\varpi^{-1/2}$ surface density profile. In all simulations in this dissertation, the ORP is roughly 180 years. See Table 3.1 for more precise values.

2.2.2 Cai/Mejía Radiative Routine

One of the first algorithms treating realistic radiative cooling to be used in the IUHG code was developed by Mejía (2004) and uses flux-limited diffusion in all directions wherever the Rosseland mean optical depth integrated vertically downward is $\tau > 2/3$. For these regions, the cooling term Λ is $\nabla \cdot F$, where F is the diffusive radiative energy flux. At the disk photosphere ($\tau = 2/3$), the disk interior is coupled to the disk atmosphere by applying an Eddington-like fit which determines the flux leaving the disk. The atmosphere is heated by this flux and in turn radiates according to its emissivity. Half of the emitted radiation is assumed to be lost, and half is radiated back down to the photosphere. This algorithm does not allow for the exchange of radiation between cells in the atmosphere. Cai (2006) updated and improved these routines by smoothing the boundary flux over two vertical cells and allowing for the addition of incoming radiative flux from an envelope or the surrounding disk. One of the drawbacks of this scheme is that there is always a sharp temperature drop of tens of percent at $\tau = 2/3$ due to the fact that cell-to-cell coupling is not treated properly in the atmosphere (Boley et al. 2006, 2007a).

2.2.3 Boley Radiative Routine

In order to address this shortcoming, Boley et al. (2007a) implemented a new radiative scheme, where the transport of energy by radiation in the vertical direction is computed using the method of discrete ordinates (Chandrasekhar 1960). Here each vertical column is considered to be a separate plane parallel structure, and the transfer is calculated using a single upward ray at $\mu = 1/\sqrt{3}$ to the vertical and a single

downward ray at $\mu = -1/\sqrt{3}$, where μ is the cosine of the angle between the ray and the disk vertical. For optical depths greater than $\tau = 1/\sqrt{3}$, transport in the ϖ and ϕ directions is treated using flux-limited diffusion. No transport is modeled in the ϖ and ϕ directions for $\tau < 1/\sqrt{3}$. The advantage of this scheme is that the vertical transport is modeled explicitly, no fitting of the atmosphere is required and cell-to-cell coupling is included explicitly for all τ . Tests of this algorithm yield qualitatively similar results to the Cai/Mejía scheme (Boley et al. 2007a). However, the Boley scheme removes the temperature discontinuity at the photosphere seen in the Cai/Mejía scheme, so the atmosphere is hotter. For more details on the implementation of the algorithm, see Boley (2007). All of the simulations including radiative transport in this work use the Boley scheme. The Cai/Mejía scheme is described for completeness.

2.3 Indirect Potential

One major concern in previous simulations has been the spurious growth or suppression of one-armed spirals once GIs set in due to the fact that the central mass remained fixed at the grid center. When the central star is not allowed to move, forces that would normally be exerted on the star by one-armed spirals are effectively ignored. One way to determine the magnitude of this effect is to track the position of the disk center of mass. If the disk is centered very near the star's position, the star's motion should be small. Constant cooling runs using a fixed central potential show that the disk's center of mass was at most a few cells away from the grid center. However, this method only takes into account what the disk's effect

would be on the star if the star were fixed at the grid center. It does not capture the full interaction between star and disk and, more importantly, the possible feedback between stellar motion and growth of one-armed modes (Adams et al. 1989; Shu et al. 1990). The only way to measure the effect of GIs on stellar motion and the effect of stellar motion on GIs is to model it explicitly.

I chose to use the indirect potential method (Nelson et al. 2000b) to model the motion of the central star. With this treatment, the grid is considered to be an accelerated frame, not an inertial frame. This scheme has the practical benefit that the star remains fixed at the grid center. The acceleration of the star-centered reference frame due to gravitational forces can be included into the pre-existing equation of motion (2.2) as an additional potential, termed the *indirect potential*. In this case the potential at some point in the disk is given by,

$$\Phi = -\frac{GM_*}{r} + G \int_{V'} \frac{dm(\mathbf{r}')}{r'^3} \mathbf{r} \cdot \mathbf{r}' + \Phi_{\text{disk}}, \quad (2.13)$$

where Φ_{disk} is the disk potential calculated from equation (2.4) as described in §2.1. The first term is the standard potential from a central point mass Φ_{star} and the second term is Φ_{ind} (disk), the indirect potential due the acceleration of the star by the disk. In practice, I compute

$$\int_{V'} \frac{dm(\mathbf{r}')}{r'^3} \mathbf{r}' \quad (2.14)$$

and then compute

$$G\mathbf{r} \cdot \int_{V'} \frac{dm(\mathbf{r}')}{r'^3} \mathbf{r}' \quad (2.15)$$

for each cell. This turns out to be much less computational burden than computing the entire integral in equation (2.13) for each cell. In chapter 4 I detail the effect of adding stellar motion to GI-active simulations and compare the results to previous fixed star simulations and indirect potential simulations performed by other authors.

2.4 Planet Integration

2.4.1 Leapfrog Integrator

In order to model the effect of GIs on the migration of protoplanets and planets, I have added routines to the standard version of the code to follow the motion of massive particles in a GI-active background. I determined that the simplest second-order accurate scheme to implement was the leapfrog scheme, sometimes known as the Verlet method. It has been shown to be the simplest example of a symplectic integrator (Channell & Scovel 1990; Yoshida 1990) and produces high accuracy and stability when compared with other second-order integrators such as Runge-Kutta methods. Generally the equations are written in a time-interleaved fashion with the positions and accelerations specified on the integer time steps and the velocities specified on the half-integer steps as in

$$r_1 = r_0 + v_{1/2}\Delta t \quad (2.16a)$$

$$\text{and } v_{3/2} = v_{1/2} + a_1\Delta t. \quad (2.16b)$$

Note that the displacement of v with respect to r and a is time symmetric, preventing the accumulation of error in the energy over time. However, it is more convenient

to write the equations such that all necessary quantities are defined on integer time steps:

$$r_1 = r_0 + v_0 \Delta t + \frac{1}{2} a_0 (\Delta t)^2, \quad (2.17a)$$

$$v_1 = v_0 + \frac{1}{2} (a_0 + a_1) \Delta t. \quad (2.17b)$$

Starting at time step $t = 0$ with variables r_0 , v_0 and a_0 defined, one first computes r_1 based on these values. Next one computes $a_1(r_1)$ by calculating the forces from both the disk and the central star. This step is done *after* the potential is updated following the full hydrodynamic flux step so that the integration of the planet is in phase with the integration of the disk hydrodynamics. Finally, with a_0 and a_1 in hand, v_1 is calculated. Although equation (2.17) may appear to have lost its time symmetry, it is, in fact, equivalent to equation (2.16), which can be verified by direct substitution (Barnes & Hut 1989; Tuckerman et al. 1992).

Another concern with the leapfrog scheme is that the time symmetry of the integrator is lost when variable step sizes are used. Unfortunately, variable step sizes are an intrinsic part of the main hydrodynamics code, where the time step is set by either the Courant time or the local heating or cooling time, whichever is the smallest, and is allowed to vary as the disk evolves. Indeed, when GIs set in and begin to generate strong shocks, the Courant time, heating times and cooling times can sometimes decrease dramatically. Hut et al. (1995) describe a method by which time symmetry can be recovered by determining the time step in such a way as to guarantee symmetry to the desired accuracy. The implicit form of their

time-symmetrized scheme can be written as follows:

$$\varsigma_1 = f(\varsigma_0, \delta t), \quad (2.18a)$$

$$\delta t = \frac{1}{2}[h(\varsigma_0) + h(\varsigma_1)]. \quad (2.18b)$$

Here ς is the two dimensional phase space vector composed of the planet's position \mathbf{r} and velocity \mathbf{v} , the function f is defined by equation (2.17), and h is the time step criterion. As [Hut et al. \(1995\)](#) note, while there are many possibilities for this criterion; they use the minimum overall particle pairs of interparticle encounters and free-fall times. Although these criteria are perfectly reasonable for an N-body code, they are not well suited to my purposes. A more fitting criterion would be some fraction of the Keplerian orbit period divided by the azimuthal resolution, or perhaps some fraction of the free-fall time. In lieu of adding an additional time step limitation to the existing code, I compared the typical Courant time to the Keplerian orbit period at 5 AU. Based on this comparison I surmised that typical Courant times for the hydrodynamics should be sufficiently small to insure an adequate level of time symmetry and limit the growth of errors.

In order to test this hypothesis, a simulation was performed in which the integration time step of the planet was set by the Courant time of a background disk undergoing a full hydrodynamic evolution. The planet and the disk were not allowed to interact. The only information used from the disk in the planet's evolution was the time step. The planet was given an initial velocity consistent with a circular orbit at 20 AU. After completing seven orbits, the orbital energy was conserved to one part in 10^4 , and the orbital angular momentum was conserved to one part in

10^{12} . Based on these findings, I determined that the time steps set by the Courant time were sufficiently small to ensure an acceptable level of time symmetry.

2.4.2 Determination of Accelerations

There are basically three components of the planet's acceleration which need to be determined at each time step from equations (2.17). These are: the acceleration due to the central star, the acceleration due to the reference frame and the acceleration due to the protoplanetary disk. The planet's equation of motion in the frame of the star can be written as:

$$\frac{d\mathbf{r}_p^2}{dt^2} = -\frac{G(M_* + m_p)}{r_p^3}\mathbf{r}_p - a_{\text{disk}} - a_{\text{ind}}(\text{disk}). \quad (2.19)$$

The first term contains the acceleration due to the central star as well as the contribution of the planet to the indirect term. These accelerations are calculated straightforwardly at each time step.

The other complicating factor in adding the planet integration is an accurate determination of the planet's acceleration due to the force exerted on the planet by the disk. This complication arises due to the fact that the disk potentials are only computed at cell centers by the Poisson solver employed in the IUHG code. However, we require the force (i.e., potential derivatives) to be determined wherever the planet might be, which will generally not be at a cell center or face center. In order to calculate the force due to the disk at any position, a linear interpolation is used. The simplifying assumption is made that the planet is formed in the disk midplane with zero vertical velocity. Since we use reflection symmetry about the midplane, the z

component of the acceleration is always zero. Forces are first calculated at cell faces in the ϖ and ϕ directions and are then averaged to find the forces at the vertices of the cell containing the planet. A set of two linear interpolations is then performed for each component to determine the force.

In order to test the implementation of the interpolation routines and integrator, simulations were performed in which an initial axisymmetric disk was held fixed while a planet orbited in its potential. Since the mass distribution of the protoplanetary disk used is not a simple one, results could not be compared to analytic solutions. However the z component of the angular momentum was conserved to one part in 10^{13} and the expected rosette pattern was observed in the orbit, which maintained nearly constant apapse and periapse radii.

Once the planet's new position has been determined via the leapfrog integrator, its potential is added into the overall potential determining the evolution of the hydrodynamics. There are two parts to the planet's contribution, the direct and indirect components. Φ_{planet} is given by

$$\Phi_{\text{planet}} = -\frac{Gm_p}{\sqrt{\varpi^2 + \varpi_p^2 - 2\varpi\varpi_p \cos(\phi - \phi_p) + \varepsilon}}, \quad (2.20)$$

where m_p , ϖ_p and ϕ_p are the planet's mass, radial position and azimuthal position, respectively. ε is a smoothing parameter which is set to be some fraction of the planet's Hill radius. In this case,

$$\varepsilon = b\varpi_p^3 \sqrt{\frac{m_p}{3M_*}} \quad (2.21)$$

where I have set the fraction $b = 0.2$ in all cases. The indirect portion of the planet's potential can be written as:

$$\frac{Gm_p}{\varpi_p^3} \mathbf{r} \cdot \mathbf{r}_p. \quad (2.22)$$

Once Φ_{planet} and Φ_{ind} (planet) have been calculated, they are added into the total potential.

2.5 Computational Resources

To perform simulations in a reasonable time frame on typical grids (1 –20 million computational cells), the code must be executed in a parallel fashion. If the code were to be executed in serial I estimate that a simulation with a resolution of (512,512,64) would take more than six months of CPU time to complete. Historically, the code has been developed with OpenMP parallelism, and for this reason requires a shared memory machine, with a single system image containing 64 or more cores, to execute effectively. The simulations described in this work have been carried out on a variety of machines, with the most computationally demanding (i.e., highest resolution) being executed on SGI's Altix 4700 architecture. Even with the massive shared memory architecture of the Altix 4700, typical simulations including planets and radiative transport, like those in chapter 5, required approximately 200,000 core hours of computational time to complete a 20 ORP run. When exploiting the parallelism of the problem by using 64 computational cores, this translates to 3,125 wall clock hours (4.3 months).

Chapter 3

Comparative Study of Physical and Numerical Conditions

... the steady motion was unstable for large disturbances long before the critical velocity was reached, a fact which agreed with the full-blown manner in which the eddies appeared
– O. Reynolds, 1883

To obtain a better understanding of the effects of various physical and numerical parameters in the standard version of the IUHG code described in §2.1, I performed a series of simulations with varied physical and numerical specifications. In this chapter, I describe the outcome of altering the following: initial surface density profile, azimuthal resolution, adiabatic index in the equation of state, and the amplitude of the initial random perturbation. I investigate the effect of varying each parameter on GI unstable disks in general, as well as examining some effects specific to each of the parameters.

For the initial surface density profile study, I looked at three different disk models with initial surface density profiles $\Sigma \sim \varpi^{-p}$, where $p = 0.5, 1, \text{ and } 1.5$. For each simulation I started from an equilibrium disk and evolved the disk for several thousand years. The impetus behind this study is to understand how varying the initial surface profile affects several aspects of disk evolution in an unstable disk. I analyzed whether this changed the timing or onset of each of the phases in the prototypical

evolution of a unstable disk. I also studied the effect on some of the primary characteristics of the GIs, that is, the dominant unstable mode, the torques generated by the GIs, and the resulting mass transport. Finally, I looked at the surface density profile after a few thousand years of evolution in the asymptotic phase to gain insight into how GIs reorder disk structure.

An important question when interpreting results from any fixed grid simulation is whether the grid resolution is influencing the phenomenon being studied. If so, numerical artifacts may either be masking the phenomenon or masquerading as a physical effect. To determine the resolution needed for numerical convergence in the simulations, I interpolated one of the initial surface density profile comparison disks to several different azimuthal resolutions near the beginning of the asymptotic phase of the disk evolution. I tested the convergence of several physical phenomena including GI amplitude, the strength of torques generated by GIs, and the dominant unstable mode.

To study the effects of altering the adiabatic index for the ideal gas equation of state, I performed simulations with $\gamma = 7/5$ and additional simulations with $\gamma = 5/3$, and compared them to a disk from the initial surface density profile comparison. I analyzed these disks to see if the different equation of state would alter the strength of the GIs. I performed simulations with both $\gamma = 5/3$ and $\gamma = 7/5$ to characterize the fragmentation limit for each of the adiabatic indices. The fragmentation limit is the volumetric cooling time at which a disk will fragment, $t_{cool}(crit)$. Each of these additional simulations were started from an equilibrium disk model used in the initial surface density profile comparison.

Each of the initial equilibrium disks is typically seeded with a random perturba-

tion to allow the GIs to grow from noise. In most simulations, the amplitude of the perturbation used is rather small; however, there are astrophysical situations where an external perturbation could be more substantial. For example, the infall rate from the envelope surrounding a protoplanetary disk could fluctuate in both time and space. To study how a stronger initial perturbation can affect disk evolution, I performed simulations with an initial random perturbation using three different amplitudes.

Understanding the importance of each of these effects allowed me to make a more informed decision on the types of disks to simulate in subsequent studies where I examined more complicated physical effects. This chapter begins with a description of the various analysis techniques used in studying and comparing the disks. These techniques include computing the amplitude of the global Fourier amplitude A_m for different numbers of spiral arms, determining the periodicity of discrete spiral modes, and calculating the gravitational torque due to the spiral structure generated by the GIs. The description of the methods is followed by discussion of some relevant background information on current debates as to the nature and importance of GIs and their effects.

3.1 Analysis Procedures

In this section I describe the tools used to compare and contrast various disk simulations. There are several trivially simple analyses performed, such as computation of the surface density profile, Toomre Q , midplane and meridional density maps, etc. which I will not elucidate here. In addition to these straightforward tasks, I

used several more complex techniques to gain insight into the disk evolution, such as measuring the amplitude of the global Fourier components of the GIs, calculating the periodicity of the Fourier modes based on Fourier phase information, and computing global gravitational torques due to spiral structures induced by GIs.

3.1.1 Global Fourier Components

In order to quantify the global amplitude of non-axisymmetric structure, I use the quantity A_m defined by [Imamura et al. \(2000\)](#),

$$A_m = \frac{(a_m^2 + b_m^2)^{1/2}}{\pi \int \rho_0 \varpi d\varpi dz}. \quad (3.1)$$

Here,

$$a_m = \int_V \rho \cos(m\phi) \varpi d\varpi dz d\phi \quad (3.2a)$$

and

$$b_m = \int_V \rho \sin(m\phi) \varpi d\varpi dz d\phi, \quad (3.2b)$$

are the Fourier components and ρ_0 is the axisymmetric component of the density, and is defined as $\frac{1}{2\pi} \int_{-\pi}^{\pi} \rho d\phi$. The volume integrals are over the entire simulation volume. This analysis, by design, neglects the phase information in the density variations. Values of A_m are computed up to $m = l_{max}/2$, where l_{max} is the azimuthal resolution. Higher m -values violate the Nyquist-Shannon theorem ([Shannon 1984](#)). Due to the

fact that the simulations have assumed a fixed central potential, which is not allowed to move in response to non-axisymmetric structures in the disk, the $m = 1$ Fourier component should not be considered to be an accurate measurement for any of the simulations considered in this chapter. Fixing the central star could, in principle, suppress the growth of a $m = 1$ mode via SLING amplification (see section 4.3.1 for a more detailed discussion of the SLING mechanism). However, simulations considered in chapters 4 and 5 have included the indirect potential, which takes into account the motion of the central star. In these cases, the $m = 1$ modes are accurately reflected in all the analyses. Throughout this work, I refer to the A_m values as modes; however, it should be noted that this analysis measures the amplitude of a particular m -valued Fourier component, which may or may not be a true eigenmode of the disk. Frequently, the A_m values are computed for many snapshots of disk evolution and then time-averaged so as to remove fluctuations on small temporal scales. When referring to A_m values, it is understood that I am referring to the value of a snapshot, while $\langle A_m \rangle$ refers to the time-averaged quantity. Another relevant quantity is the sum of the time-averaged values over all m -values, which is denoted as $\langle A_\Sigma \rangle$.

3.1.2 Periodicity of Coherent Modes

Another powerful tool in examining structure caused by GI activity is the periodogram. As in the A_m analysis, I Fourier decompose the non-axisymmetric density fluctuations locally in $\cos(m\phi + \phi_m)$. In this case ϕ_m contains the phase information for a m -armed structure. The midplane density structures are decomposed giving

the Fourier components as a function of ϖ . After constructing a time series of these Fourier components from the density files saved throughout a simulation, I search for any coherent pattern frequencies by constructing a Lomb-Scargle periodogram (Scargle 1982; Horne & Baliunas 1986) of $\cos(m\phi)$ at each radius. For each m -value, I then construct a map of the periodic structures in the phase angle as a function of radius and frequency. When a period exhibits a large power relative to the background and spans a large radial range in this plot, it indicates the presence of coherent global GI modes or waves. I also identify the corotation radii and inner and outer Lindblad resonances associated with each of these m -values (see §1.3.3.2 for an explanation of Lindblad resonances). Typically I investigate the periodicity of low-order modes only, as higher-order modes tend to be plagued by small scale noise.

3.1.3 Mass Transport in Protoplanetary Disks

In order for mass transport to occur in a protoplanetary disk, material must either lose angular momentum, and be accreted inward, or gain angular momentum, and be accelerated outward. The transport of angular momentum must be facilitated by some form of torque. Hartmann (1998) provides a review of several possible mechanisms for angular momentum transport in accretion disks. For physical parameters in protoplanetary disks, molecular viscosity is far too small to play a significant role in mass accretion. Another possibility that has been considered is turbulent convection. However, several detailed studies (Ryu & Goodman 1992; Cabot & Pollock 1992; Stone & Balbus 1996) indicate that this mechanism will act to transport angular momentum inward, resulting in outward mass transport. Another possi-

ble mechanism is the magnetorotational instability (MRI) (Balbus & Hawley 1997), which acts to drive magnetohydrodynamic (MHD) turbulence. The MRI is a robust instability that can develop in disks with a vanishingly small initial magnetic field.

The basic idea behind the instability is as follows. Initially a magnetic field line radially connects two adjacent annuli. If the disk has a Keplerian rotation profile, then the inner annulus will have a larger angular velocity than the outer annulus. This causes the field lines to stretch, which is opposed by the magnetic field. This, in turn, will accelerate the outer annulus with respect to the inner annulus as the field lines attempt to return to equilibrium. As angular momentum is transferred outward, the inner annulus will move further inward and the outer annulus will move further outward exacerbating the imbalance. As the field lines are stretched further and material is transferred over an increasing radial extent, turbulent motions develop (Hawley et al. 1995). Even with a vanishing small magnetic field, the instability will grow because the initial stretching of the magnetic field amplifies the field, i.e., the instability exhibits a dynamo effect (Hawley et al. 1996).

However, there are a few constraints on the system in order for the MRI to be active and effective. Because the instability is driven by the shearing of the magnetic field, the field cannot be too strong. If the field is strong enough to enforce the corotation of neighboring annuli, then the field lines will not be stretched and the instability will not develop. Additionally, the field must be able to couple effectively to the gas disk. The field itself interacts with charged particles, which are plentiful in many astrophysical settings. However, in a cold disk, shielded from external irradiation by dust grains, the number of ions in the gas can become very small. This can lead to *dead zones* in the disk, areas where the magnetic field cannot

effectively couple to the disk and therefore the MRI cannot grow. The MRI may be active near the surface of the disk where irradiation can keep the ionization fraction large enough. In such cases, disks may undergo layered accretion where MRI-driven turbulence causes accretion near the disk surface but there is no accretion in the dead zone near the disk midplane (Gammie 1996).

Much work has been done to characterize the magnitude of angular momentum transport caused by the MRI in protoplanetary disks. Early works by Hawley et al. (1995) and Brandenburg et al. (1995) indicated that the effective α (Shakura & Syun-yaev 1973) produced by the MRI could range from 0.001 to 0.1 depending on the particulars of the field geometry. However, recent studies have shown the importance of numerical dissipation (Fromang & Papaloizou 2007), viscous and resistive dissipation (Lesur & Longaretti 2007), and field geometry (Simon & Hawley 2009). At present these quantities are not well known for protoplanetary disk environments, and so the effective α produced by the MRI in protoplanetary disks in locations where it can act is poorly quantified.

Gravitational instabilities can also facilitate the transport of angular momentum. For Toomre $Q \lesssim 1.7$ (Durisen et al. 2007), gravitational interactions produce spiral waves. If these spiral waves are trailing waves and can be sustained by the instability despite the effects of shear, then a concentration of mass will build in a trailing spiral arm. The leading and trailing portions of the arm will be gravitationally attracted to each other causing the trailing portion (or outer radii) to experience a positive torque. As in the MRI, attraction between inner and outer annuli attempts to force the disk into solid body rotation and transfers angular momentum outward. The chief difference is that the MRI is driven by magnetic attraction while GIs are driven

by gravitational attraction.

Another key difference is the conditions under which each of the instabilities will develop. As discussed above, the MRI is a fairly robust instability that will develop in the presence of a vanishingly small magnetic field given that the disk is able to couple to the field effectively. On the other hand, GIs require a Toomre $Q \lesssim 1.7$ to develop. As outlined in §1.2.2, three factors in the disk determine the Toomre Q parameter. The local pressure and rotation act to stabilize the disk against short and long wavelength instabilities, respectively. The destabilizing force is gravity. Therefore, the conditions are right for GIs when there is rapid cooling, large mass concentrations, and little rotational support. Typically, this occurs in the cold outer regions of a massive protoplanetary disk.

If the condition $Q \lesssim 1.7$ is satisfied, this does not in itself mean that GIs will be effective in transporting angular momentum. The two major characteristics that determine the effectiveness of angular momentum transport, or the magnitude of the gravitational torque, are the strength of the GIs and the coherence of the structures produced by the instability. These can be measured by the analyses described in the preceding sections. The strength of the GIs can be quantified by looking at the A_m values because it is a measure of the mass in non-axisymmetric m -armed structures. Additionally, one can look at A_Σ as a measure of the total strength of GIs for all m -values in the disk.

The other factor that determines how effectively GIs can transport angular momentum is the coherence of the patterns produced by the instability. It is possible, for example, for a given m -value to have a large measured A_m but, since the A_m measure does not take phase information into account, the amplitude could be phased

differently at different radii. In an extreme case, if the amplitude at different radii were phased properly, the net torque could be negligible over a large radial extent in the disk. To determine the coherence of structures, I use the periodogram, described in §3.1.2, to look for stripes of power that have the same pattern speed over a large range of radii. In addition to determining their pattern speed, I can determine where they are most effective in transporting angular momentum by looking at the corotation and inner and outer Lindblad resonances of these structures. It should be noted that the A_m method for determining the strength of GIs and the periodogram method for determining coherence are independent, that is, the A_m measures only the amplitude and has no information on the coherence while the periodogram measures only the coherence and has no information of the amplitude of the pattern. In principle, it would be possible to have a strong incoherent pattern *and* a weak coherent pattern that could be misinterpreted as a single strong coherent pattern. However, this is unlikely and in all cases I look at other time varying quantities that link these two measures, such as net torques.

3.1.4 Gravitational Torques from Global Instabilities

A coherent structure with a large density enhancement will produce a gravitational torque and, in the case of a trailing spiral, cause angular momentum to be transferred outward. As in Lynden-Bell & Kalnajs (1972), by taking a cylindrical surface at some radius \mathbf{r} , one can calculate the torque couple C of the portion of the disk at radii greater than \mathbf{r} on the portion of the disk inside \mathbf{r} by integrating the stress tensor T over the surface of the cylinder,

$$C = \int \mathbf{r} \times T \cdot dS. \quad (3.3)$$

In a protoplanetary disk, the chief contributions to the stress tensor, in the absence of a magnetic field, come from the Reynolds stress and gravitational stress. The relevant component of the Reynolds stress tensor is

$$T_{\varpi\phi}^{Reyn} = \rho \delta v_{\varpi} \delta v_{\phi} \quad (3.4)$$

where ρ is the gas density, δv_{ϖ} is the velocity fluctuation of the fluid from the mean flow in the ϖ -direction, and δv_{ϕ} is the velocity fluctuation of the fluid from the mean flow in the ϕ -direction. The torque that arises from this stress can then be computed by

$$C_z^{Reyn}(\varpi) = \varpi^2 \int_0^{2\pi} \int_{-\infty}^{\infty} T_{\varpi\phi}^{Reyn} d\phi dz. \quad (3.5)$$

However, in order to determine the components of the Reynolds stress accurately, one must first define a mean flow and measure the fluctuations about that flow. In a GI-active disk dominated by nonlinear gravitational interactions, defining a mean flow can be difficult. Although some researchers have found the Reynolds stresses to be comparable to the gravitational stresses in local simulations (e.g., [Gammie 2001](#)), in instances where our group and some others have attempted to quantify the Reynolds stress in global simulations, it has been found to be relatively small in comparison with the gravitational stress in GI active regions ([Lodato & Rice 2004](#); [Boley et al. 2006](#); [Boley 2007](#)). For this reason, I will focus on the torque due to the gravitational stress.

Instead of integrating the gravitational stress tensor over the cylindrical surface, one may replace the surface integral with a volume integral

$$C = \int \rho \mathbf{r} \times \nabla \Phi dV, \quad (3.6)$$

where Φ is the gravitational potential. As in [Boley et al. \(2006\)](#), I am only interested in the torque about the z -axis. So,

$$C_z(\varpi) = \int_{V(\varpi)} \rho \frac{\partial \Phi}{\partial \phi} dV. \quad (3.7)$$

This allows me to compute the torque of the outer disk on the inner disk as a function of ϖ by integrating over the entire volume $V(\varpi)$ enclosed by a cylinder of radius ϖ . Each value of ϖ represents the computation with new cylindrical radius, yielding a plot of the torque versus ϖ .

In addition, I use the Fourier coefficients to construct a density distribution with only m -armed structure. The density can be reconstructed from the Fourier coefficients c_m and s_m given by,

$$c_m = \frac{1}{\pi} \int_{-\pi}^{\pi} \rho \cos(m\phi) d\phi, \quad m \geq 0 \quad (3.8a)$$

and

$$s_m = \frac{1}{\pi} \int_{-\pi}^{\pi} \rho \sin(m\phi) d\phi, \quad m \geq 1 \quad (3.8b)$$

by combining them so that

$$\rho = \frac{c_0}{2} + \sum_{m=1}^N [c_m \cos(m\phi) + s_m \sin(m\phi)]. \quad (3.9)$$

I can then construct the density from a single m -valued by

$$\rho_m = c_m \cos(m\phi) + s_m \sin(m\phi). \quad (3.10)$$

Once these density maps have been created, I compute the torque due to each of the m -armed structures and can thereby measure the relative importance of each of the modes in transporting angular momentum.

3.1.5 Effective α

[Shakura & Syunyaev \(1973\)](#) first parametrized the viscosity in a steady-state disk with the α parameter. Although their original work applied to X-ray bright accretion disks around black holes, their approach has proved fruitful in many astrophysical situations. In the α -disk formalism, the effective kinematic viscosity ν can be written as

$$\nu = \alpha c_s H, \quad (3.11)$$

where c_s is the sound speed and H is the disk scale height. With this formalism, when the accretion rate \dot{M} is constant in both time and radius, $\dot{M} = 3\pi\nu\Sigma = 3\pi\alpha c_s^2\Sigma/\Omega$, where Σ is the surface density and Ω the rotational frequency. The steady-state α -disk formalism makes no assumption about the nature of the angular momentum transport, except that it resembles viscosity and hence, in a steady-state, heating

and cooling balance locally. [Gammie \(2001\)](#) envisioned a razor thin gravitationally unstable disk where the heating due to local turbulent dissipation caused by GIs was balanced by the local cooling rate. Assuming a local cooling time t_{cool} , [Gammie](#) found that

$$\alpha = [\Gamma(\Gamma - 1)\frac{9}{4}\Omega t_{cool}]^{-1}, \quad (3.12)$$

where Γ is the two-dimensional adiabatic index. The two-dimensional index relates to the three-dimensional index γ by $\Gamma = (3\gamma - 1)/(\gamma + 1)$ for a non-self-gravitating disk and $\Gamma = 3 - 2/\gamma$ for a strongly self-gravitating disk.

A key question in the evolution of GI-active protoplanetary disks is whether the GIs dissipate energy locally (i.e. as $t_{cool}\Omega = \text{const.}$) or globally (i.e. as $t_{cool} = \text{const.}$). Following [Lodato & Rice \(2004\)](#), to compare the effective α in my simulations to [Gammie's](#) prediction, I compute α from stresses in the disk,

$$\alpha(\varpi) = \left| \frac{d \ln \Omega}{d \ln \varpi} \right|^{-1} \frac{\mathcal{T}_{\varpi\phi}^{grav} + \mathcal{T}_{\varpi\phi}^{Reyn}}{\int_z \rho c_s^2 dz}. \quad (3.13)$$

Here Ω is the azimuthally averaged rotation speed, \mathcal{T} the vertically integrated, azimuthally averaged stress tensor, ρ the density, and c_s the local sound speed. Due to the fact that most of the disks I consider are substantially extended in the z direction, it is unclear whether using the midplane sound speed with vertically integrated quantities, such as Σ (as [Lodato & Rice \(2004\)](#) do), will produce accurate results. Furthermore, due to numerical uncertainties in the determination of the Reynolds stress and its small magnitude compared to the gravitational stress, I neglect the Reynolds stress. The gravitational torque from equation (3.7) can be used to determine the vertically integrated and azimuthally averaged gravitational stress tensor

by

$$\begin{aligned}\mathcal{T}_{\varpi\phi}^{grav}(\varpi) &= \frac{1}{2\pi\varpi^2} C_z^{grav} \\ &= -\frac{1}{2\pi\varpi^2} \int_{V(\varpi)} \rho \frac{\partial\Phi}{\partial\phi} dV.\end{aligned}\tag{3.14}$$

One should note, however, that this analysis produces an *effective* α caused by gravitational stresses. Strictly speaking, a gravitationally unstable disk is not in a steady state with \dot{M} constant in both time and radius. Calculating the effective α allows one to measure the efficacy of the angular momentum transport. Note that most MRI simulations predict an $\alpha \gtrsim 0.01$, with the precise value depending on the numerical resolution and assumptions about dissipation, stratification and ionization (Hartmann et al. 1998; Fromang & Papaloizou 2007; Guan et al. 2009; Davis et al. 2009).

3.2 The Simulations

All the models considered in this chapter have a disk to star mass ratio of $\approx 0.14 - 0.15$. The initial models were generated using a grid-based self-consistent field (SCF) scheme (Hachisu 1986; Pickett et al. 1996, 2003) that is able to generate a disk with an arbitrary power law for the surface density, $\Sigma = \Sigma_0 \varpi^{-p}$.

The volumetric cooling rate is constant everywhere in the disk and is defined by the parameter

$$t_{cool} = \epsilon/\Lambda = \text{const},\tag{3.15}$$

where ϵ is the internal energy density and Λ is the volumetric cooling rate. Here

t_{cool} is given in outer rotation periods (ORPs) where 1 ORP is chosen arbitrarily (Mejía et al. 2005) to be the rotation period at radial zone 200 (≈ 33 AU) and is approximately 180 years for the G1.7TC2P0.5 disk (see table 3.1). Although the assumption of $t_{cool} = \text{const.}$ is not particularly realistic, it allows for a much more extensive search of parameter space because the computations are less expensive than those with more realistic radiative physics. Because of variations in the initial models, the value of the ORP in physical units varies. However, the variation is no more than 25%.

Each of the disks have a $1.0M_{\odot}$ central star, which is either treated as a point mass or a mass distribution and fixed to the center of the grid. The disks initially range from between 1.8 – 2.3 AU to 40 AU in extent. For chapter 3, all disks have an initial resolution of $(r, \phi, z) = (256, 128, 32)$ which gives $\approx 1/6$ AU cell widths in the r and z direction. Each of the initial disks has $1.4 \leq Q_{\min} \leq 2.0$ making them marginally unstable.

Overall, I studied eight different initial disk models, which I will refer to by their γ , t_{cool} , and initial surface density profile (e.g., G1.7TC2P1 is a disk with $\gamma = 1.7$, $t_{cool} = 2$, and $\Sigma = \Sigma_0 \varpi^{-1}$). The axisymmetric disk models are all seeded with an initial random cell-to-cell perturbation in density. Typically the amplitude of this perturbation is small, most models have a density perturbation amplitude of $\xi = 0.0001$ (see §3.6). The RAND indicator at the end of a run name identifies those runs which did not use the standard $\xi = 0.0001$ initial perturbation but instead used some larger amplitude. The number following RAND represents the amplitude of initial density perturbation used to seed the GIs. For those simulations with a number, the number represents the percent perturbation (e.g., RAND5 means

Model	p	ORP (yr)	M_{disk}/M_*	l_{max}
G1.7TC2P0.5	0.445	179	0.141	128
G1.7TC2P1	0.931	214	0.153	64,128,256,512
G1.7TC2P1.5	1.485	171	0.141	128
G1.7TC0.6P1	0.931	214	0.153	512
G1.4TC1P1	0.931	214	0.153	512
G1.4TC2P1	0.931	214	0.153	512
G1.4TC3P1	0.931	214	0.153	256
G1.7TC2P1RAND1	0.931	214	0.153	128
G1.7TC2P1RAND5	0.931	214	0.153	128

Table 3.1: Initial conditions for each of the disk simulations discussed in this chapter.

$\xi = 0.05$).

3.3 Variation of Initial Surface Density Profile

To study the effect of the initial surface density profile on the onset and outcome of GIs, I analyzed three disk simulations G1.7TC2P0.5, G1.7TC2P1, and G1.7TC2P1.5. All three disks use the volumetric cooling in equation (3.15) with $t_{\text{cool}} = 2$ ORPs. The SCF scheme described by Pickett et al. (1996) was used to generate equilibrium models with surface density profiles that followed $\Sigma \sim \varpi^{-p}$ for p of 1/2, 1, and 3/2. Due to numerical inaccuracies in the determination of the equilibrium state, the surface density profiles produced were not exact. The actual surface density profile produced by the SCF scheme was measured by using a linear least squares fit for p . Those values can be found in table 3.1. The numerical inaccuracies in the SCF code also introduced a slight variation in the disk to star mass ratio between models.

Additionally, these variations cause a small difference in the physical value of the ORP. All of these variations are minor compared to the drastic difference in initial surface density profile.

3.3.1 Overall Evolution

As in [Mejía et al. \(2005\)](#), the disks begin in an axisymmetric phase, experience a burst of spiral activity, and transition to an asymptotic phase where the disk cooling is roughly balanced by heating due to shocks and gravitational contraction. In this last phase, average quantities are changing slowly, even though the detailed structure can change on a dynamic timescale. Mass transport is generally the strongest during the onset of the gravitational instabilities. During this initial burst of activity, the overall disk structure can change dramatically. Although all three of the disks seem to follow this general trend, there are some significant variations. Figures [3.1](#), [3.2](#), and [3.3](#) show several snapshots of the midplane and a meridional cut of the density for the three simulations. The times given in each panel are in ORPs and range from the initial axisymmetric disk to the end of the simulations around 18 ORPs. The disk cools in the axisymmetric phase from 0 – 2 ORPs for the G1.7TC2P0.5 and G1.7TC2P1 disks. This is followed by a burst of GI activity initiated in the low Q region, seen in the next three panels from 2 – 6 ORPs. The burst transitions from strong GI activity to a quasi-steady state with $1.5 \lesssim Q \lesssim 2.0$. The transition phase occurs from 6 – 12 ORPs and is followed by the asymptotic phase, which lasts through the end of the simulation. The G1.7TC2P1.5 disk displays much different behavior. It remains nearly axisymmetric until 4 ORPs, and then undergoes a burst

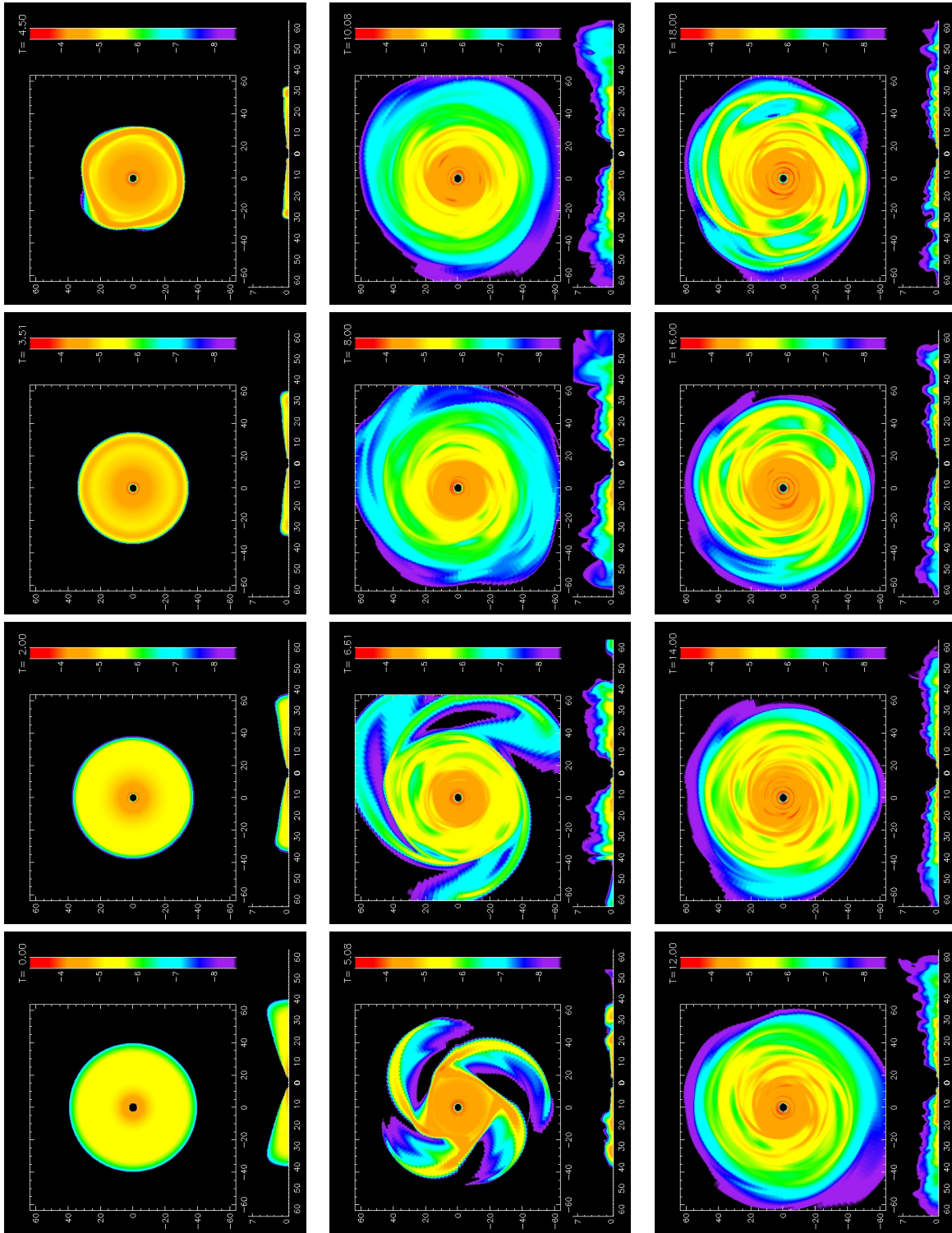


Figure 3.1: Midplane and meridional densities in logarithmic scale for several times in the G1.7TC2P0.5 simulation. The axes have units of AU and the time is given in ORPs in the upper right of each panel. The series starts at $t = 0$ ORPs and proceeds left to right and top to bottom to the end of the simulation at ≈ 18 ORPs.

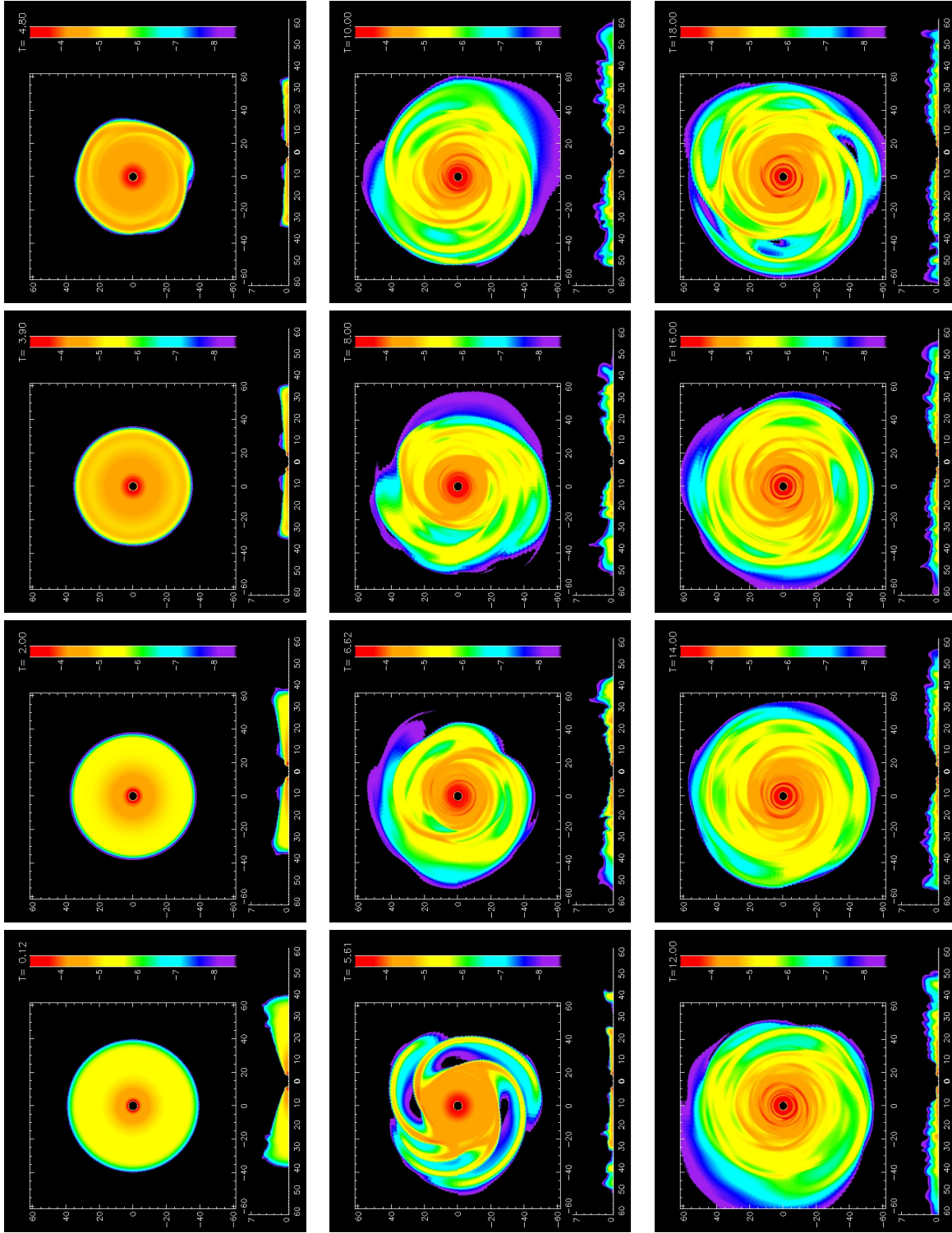


Figure 3.2: Midplane and meridional densities in logarithmic scale for several times in the G1.7TC2P1 simulation. The axes have units of AU and the time is given in ORPs in the upper right of each panel. The series starts at $t = 0$ ORPs and proceeds left to right and top to bottom to the end of the simulation at ≈ 18 ORPs.

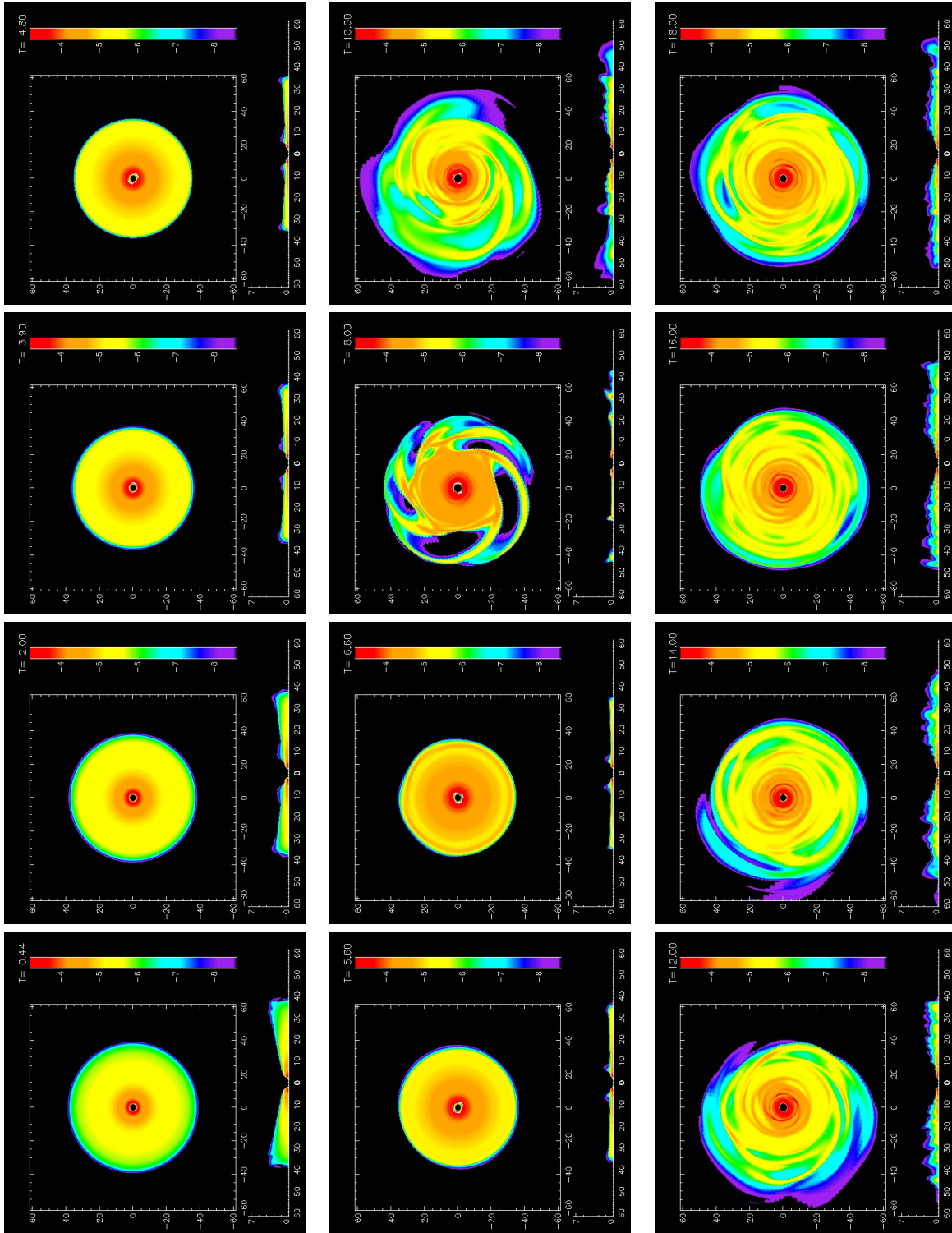


Figure 3.3: Midplane and meridional densities in logarithmic scale for several times in the G1.7TC2P1.5 simulation. The axes have units of AU and the time is given in ORPs in the upper right of each panel. The series starts at $t = 0$ ORPs and proceeds left to right and top to bottom to the end of the simulation at ≈ 18 ORPs.

from 4 – 9 ORPs.

A similar behavior can also be seen in the Fourier amplitudes. Figure 3.4 shows A_m as a function of time for each of the disks through the burst phase and into the asymptotic phase. The amplitudes plotted in figure 3.4 show only contributions from radii greater than 25 AU due to $m = 1$ signal contamination at small radii. One can see that for the G1.7TC2P0.5 and G1.7TC2P1 disks the amplitudes begin to grow exponentially near 2 ORPs and reach a peak amplitude between 5 and 6 ORPs; this is the burst phase. Density structures for $m = 1 - 5$ are shown for the burst onset in the G1.7TC2P1 disk in figure 3.5. The decomposed density structures are shown with an additional axisymmetric background to avoid display issues with the logarithmic scale. One can see in both the A_m plots (figure 3.4) and the density decompositions (figure 3.5) that strong $m = 3, 4,$ and 5 patterns are present in the burst. After the burst phase, the amplitudes remain high through the asymptotic phase.

The G1.7TC2P1.5 disk shows very different behavior. Here, the amplitude growth does not begin until somewhere around 4 ORPs, and the peak amplitude is reached between 8 and 9 ORPs. Since the amplitudes grow more slowly in the G1.7TC2P1.5 disk, the burst is less pronounced, the disk does not expand as much, and less mass is transported through the disk (see figure 3.6).

3.3.2 The Burst Phase

The burst phase is clearly seen in the $t = 4 - 6$ ORPs panels of figures 3.1 and 3.2 and in the $t = 6 - 8$ ORPs panels of figure 3.3. These figures also illustrate the dominant

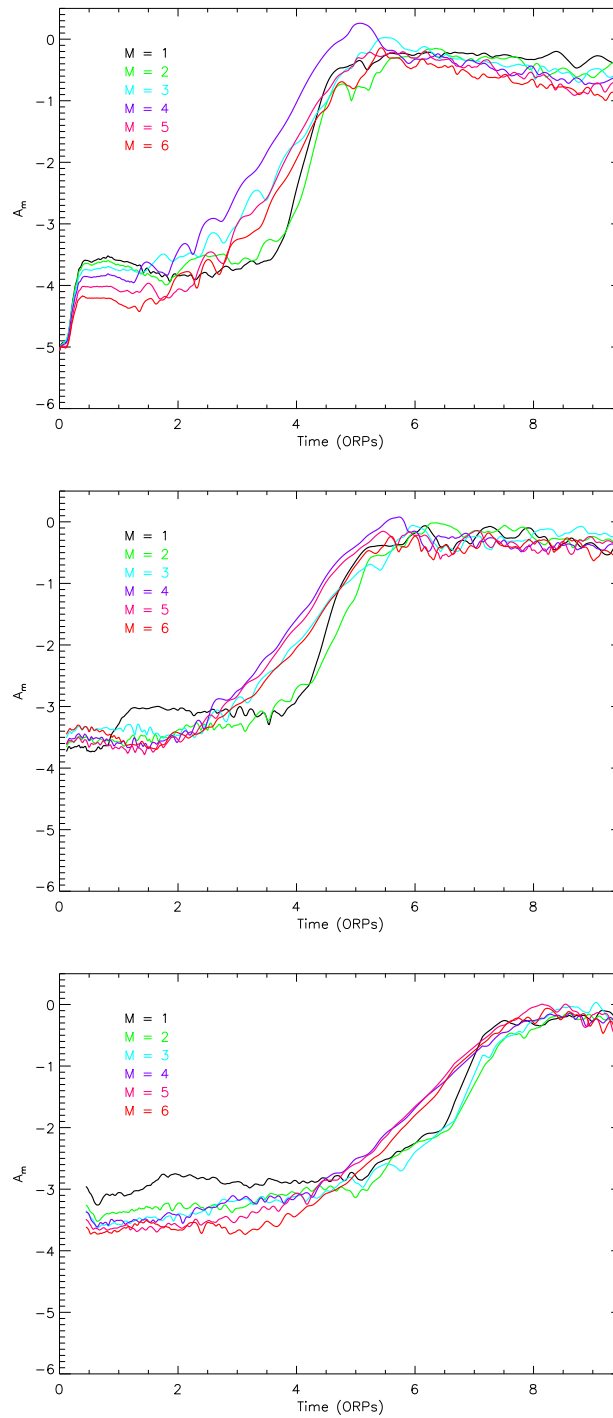


Figure 3.4: Each panel shows the Fourier components A_m as a function of time for $m = 1-6$. The *G1.7TC2P0.5*, *G1.7TC2P1*, and *G1.7TC2P1.5* simulations are shown from top to bottom. The amplitudes are shown from the initial models through the asymptotic phase. Contribution to the A_m components is only calculated for $\varpi > 25$ AU due to contamination from a spurious $m = 1$ signal. Note the protracted burst, which occurs later, and the dominance of the $m = 5$ and 6 modes in the *G1.7TC2P1.5* simulation.

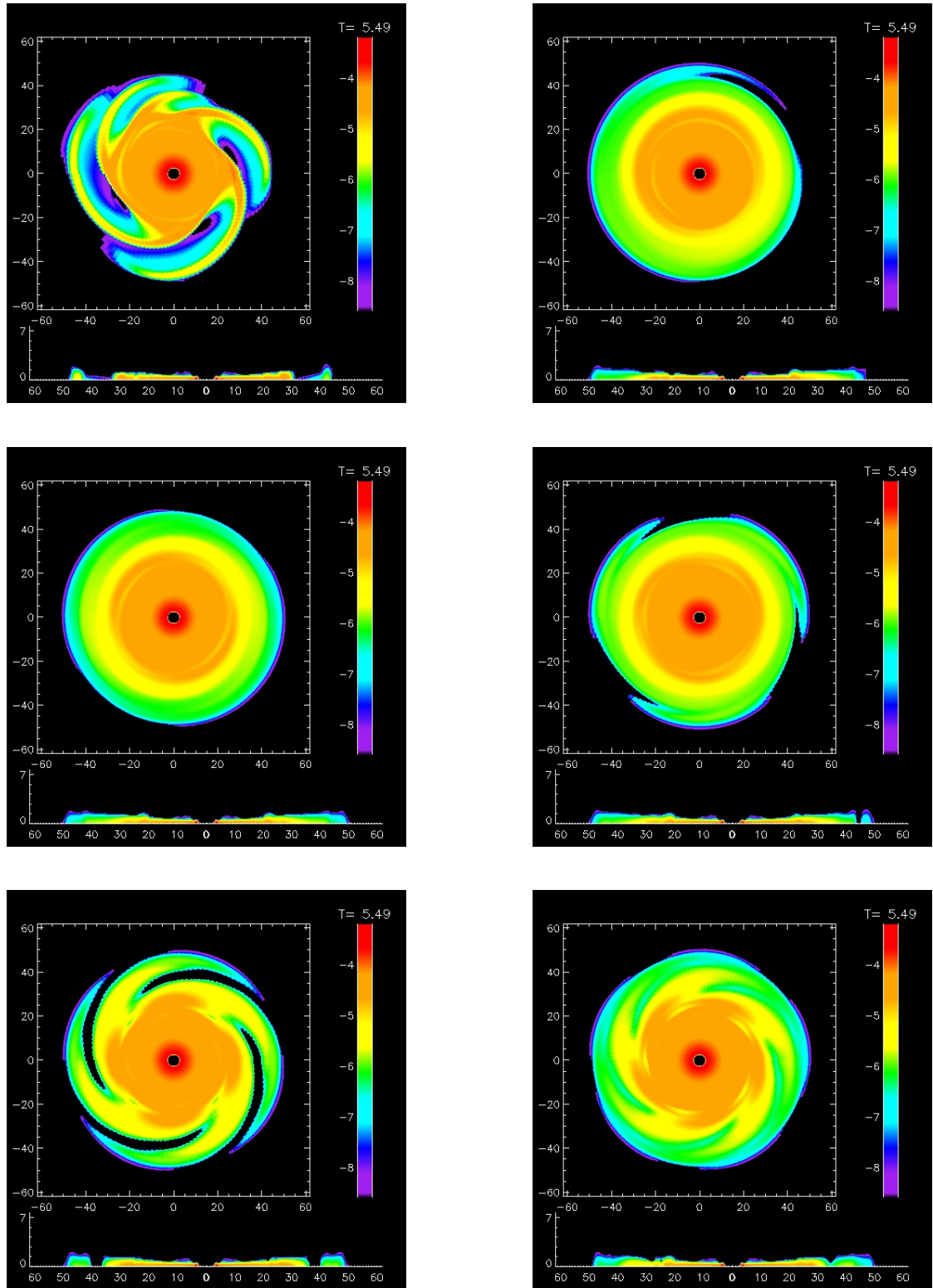


Figure 3.5: Panels showing the midplane and meridional densities of the Fourier decomposed m -values for the G1.7TC2P1 disk during the burst phase at $t = 5.5$ ORPs. The top left panel is the full density structure. Proceeding left to right and top to bottom $m = 1, 2, 3, 4,$ and 5 are shown superimposed on the underlying axisymmetric structure, $m = 0$. Densities are given in code units using a logarithmic scale.

m -armed spirals in the burst phase, $m = 4$ and 5 for G1.7TC2P0.5 and G1.7TC2P1 and $m = 5$ and 6 for G1.7TC2P1.5. The burst phase and dominant modes can also be seen in the steep rise in A_m in figure 3.4. The burst can be defined by the time period between the onset of linear growth of the low-order modes and the peak of the growth as measured by eye from figure 3.4. Using this definition, the burst was determined to be from 2.1 to 5.5 ORPs for the G.17TC2P0.5 disk, from 2.0 to 6.0 ORPs for the G1.7TC2P1 disk, and from 4.0 to 8.8 ORPs for the G1.7TC2P1.5 disk.

The shift in dominant mode is due to the shortening of the most unstable wavelength as the surface density decreases at the radius of the minimum Q . The most unstable wavelength is given by

$$\lambda = \frac{2\pi^2 G \Sigma}{\kappa^2} \quad (3.16)$$

(Toomre 1981), here κ is determined primarily by the mass of central star, which remains constant. Since the instabilities initiate at radii near the minimum Toomre Q , which are the same for all three disks, and the G1.7TC2P0.5 disk has a significantly larger Σ at these radii, one would expect the most unstable wavelength to be longer for the G1.7TC2P0.5 disk. This, in turn, should result in lower-order m -values being dominant when the instabilities are initiated, which is what is seen in figure 3.4.

Table 3.2 gives the minimum Toomre Q value near the time when the amplitudes begin to grow, and the radius at which Q is smallest. The minimum Q tends to be at the same radius for all three disks, due to the fact that the initial Q profile is similar for all the disks. Another factor is the global cooling time which tends to bias the cooling to the outer disk, i.e., $t_{cool} = 2$ represents a cooling time of two rotational

Model	Q_{min}	Q_{min} Radius (AU)	Time (ORPs)
G1.7TC2P0.5	1.0	33	2.1
G1.7TC2P1	1.3	34	1.9
G1.7TC2P1.5	1.1	33	4.2

Table 3.2: *Minimum Q values and their positions near the time when non-axisymmetric amplitudes begin to grow.*

periods at 33 AU and 10 rotational periods at 11 AU.

Because all three disks have similar minimum Q values at similar radii, the key difference is the amount of mass involved in this initial burst. For the G1.7TC2P1.5 case, there is less disk mass at radii $\gtrsim 30$ AU than in the G1.7TC2P1 and G1.7TC2P0.5 disks. The protracted burst seen in the G1.7TC2P1.5 disk is most likely due to the fact that there is less mass in the region where the disk first becomes unstable. In fact, the G1.7TC2P1.5 disk appears to burst in radial stages as opposed to globally as in the G1.7TC2P1 and G1.7TC2P0.5 disks. In the G1.7TC2P1 and G1.7TC2P0.5 disks, Q drops to its minimum and then GIs erupt strongly heating the disk over a range of radii (i.e., 15 AU to 40 AU). In the G1.7TC2P1.5 case, the heating is much more localized to the area around the Q minimum. Regions of the disk interior to the Q minimum continue to cool until they become unstable at some later time. Due to the lack of mass in the outer disk, the initial instability in the G1.7TC2P1.5 disk is too weak to cause shock heating over a large radial range.

One of the consequences of weaker GI activity and higher-order modes playing more of a role in the burst is that the mass transport rates differ dramatically for the different surface density profiles. As figure 3.6 shows, the peak mass transport rate in the G.17TC2P0.5 disk is about a factor of five greater than the peak mass

transport rate in the G1.7TC2P1.5 disk. Here the burst is defined by the time period determined by eye from figure 3.4, as explained earlier in this section. Another interesting fact to note from figure 3.6 is that the integrated mass transport is much larger for the G.17TC2P0.5 disk since mass is being transported over a larger radial range.

3.3.3 The Asymptotic Phase

In order to predict the outcome of the reordering of the disk due to the burst phase, consider a disk in the asymptotic phase where heating and cooling are roughly balanced. This state, termed “gravitoturbulence” by Gammie (2001), forces the Toomre Q parameter to a marginally unstable value which is typically constant throughout the GI-active region (see figure 3.7). Boley & Durisen (2008) showed that for an axisymmetric disk with constant γ , a Keplerian rotation profile, and negligible self-gravity,

$$\Sigma(\varpi) = \pi^{-(3\gamma+1)/4} \left(\frac{2}{\gamma-1} \left\{ \frac{\Gamma[\gamma/(\gamma-1)]}{\Gamma[(3\gamma-1)/(2\gamma-1)]} \right\}^2 \right)^{(1-\gamma)/4} \quad (3.17)$$

$$\times [\gamma K(\varpi)]^{1/2} [GQ(\varpi)]^{-(\gamma+1)/2} \Omega(\varpi)^\gamma.$$

Here γ is the polytropic constant and K is the entropy constant in the equation of state (i.e., $P = K\rho^\gamma$). With roughly constant Q and K , as in figure 3.7, equation (3.17) predicts that $p = 5/2$. When a least squares fit for p is performed on the final surface density profiles, I find that $p = 2.3$, 2.7, and 2.4 for the G.17TC2P0.5, G1.7TC2P1, and G1.7TC2P1.5 disks, respectively. In all cases p was measured in

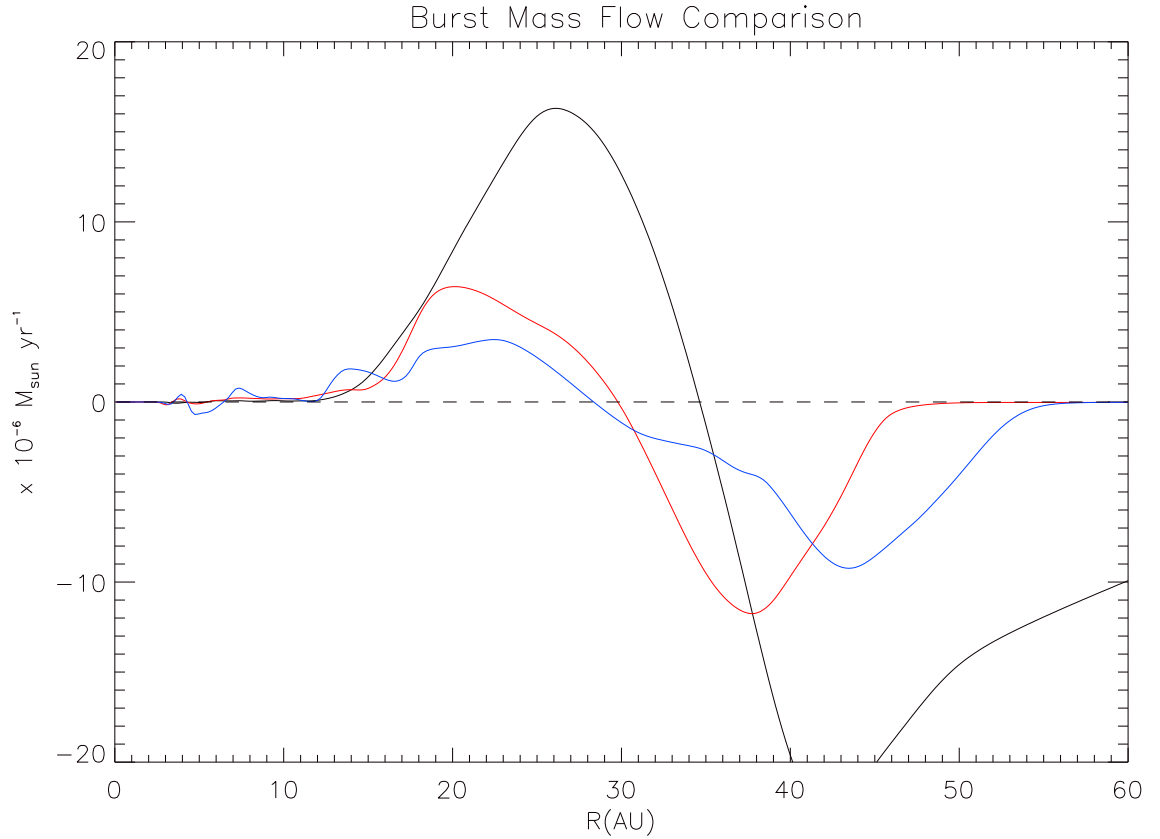


Figure 3.6: The radial mass accretion rates are shown in solar masses per year for the G1.7TC2P0.5 (black), G1.7TC2P1 (red), and G1.7TC2P1.5 (blue). These rates are measured during the burst phase of each of the simulations. The time period encompassing the burst is different for each of the simulations. The burst is measured from 2.1 – 5.5 ORPs for the G1.7TC2P0.5 disk, 2.0 – 6.0 ORPs for the G1.7TC2P1 disk, and 4.0 – 8.8 ORPs for the G1.7TC2P1.5 disk. The dashed line represents no mass flow.

the regions where the Toomre Q and the entropy parameter K were determined to be relatively constant. These determinations were made by eye and cover the ranges of 12 to 48 AU, 12 to 49 AU, and 11 to 45 AU for the G.17TC2P0.5, G1.7TC2P1, and G1.7TC2P1.5 disks, respectively. Considering their initial disparity in $\Sigma(\varpi)$, the final surface density profiles are remarkably similar and also remarkably close to the predicted value.

To determine the strength of GI activity in the asymptotic phase, I measured A_m for $m = 1-64$ from 13 to 19 ORPs for each of the disks. The average $\langle A_m \rangle$ values over these time intervals are plotted in figure 3.8. The error bars in this plot represent the RMS fluctuations about the mean for the time interval from 13 to 19 ORPs. Another measure of total non-axisymmetry is the $\langle A_\Sigma \rangle$ value (see §3.1.1), these values are 2.8, 2.3, and 1.8 for the G1.7TC2P0.5, G1.7TC2P1, and G1.7TC2P1.5 disks, respectively. Although the shape of the $\langle A_m \rangle$ spectrum remains the same for the three cases, the non-axisymmetric power decreases as the initial surface density steepens.

3.3.4 Conclusions

Three main conclusions come from the comparison of the simulations with different initial surface density profiles. First, varying the initial surface density profile makes almost no qualitative difference in the onset and evolution of GI activity. The disks all go through the same evolutionary phases at nearly the same times, and the outcome of the GI activity is very similar in terms of final surface density profile and asymptotic $\langle A_m \rangle$. There are, however, measurable differences. As the initial surface density profile steepens, the onset and peak of the burst, as measured by the peak

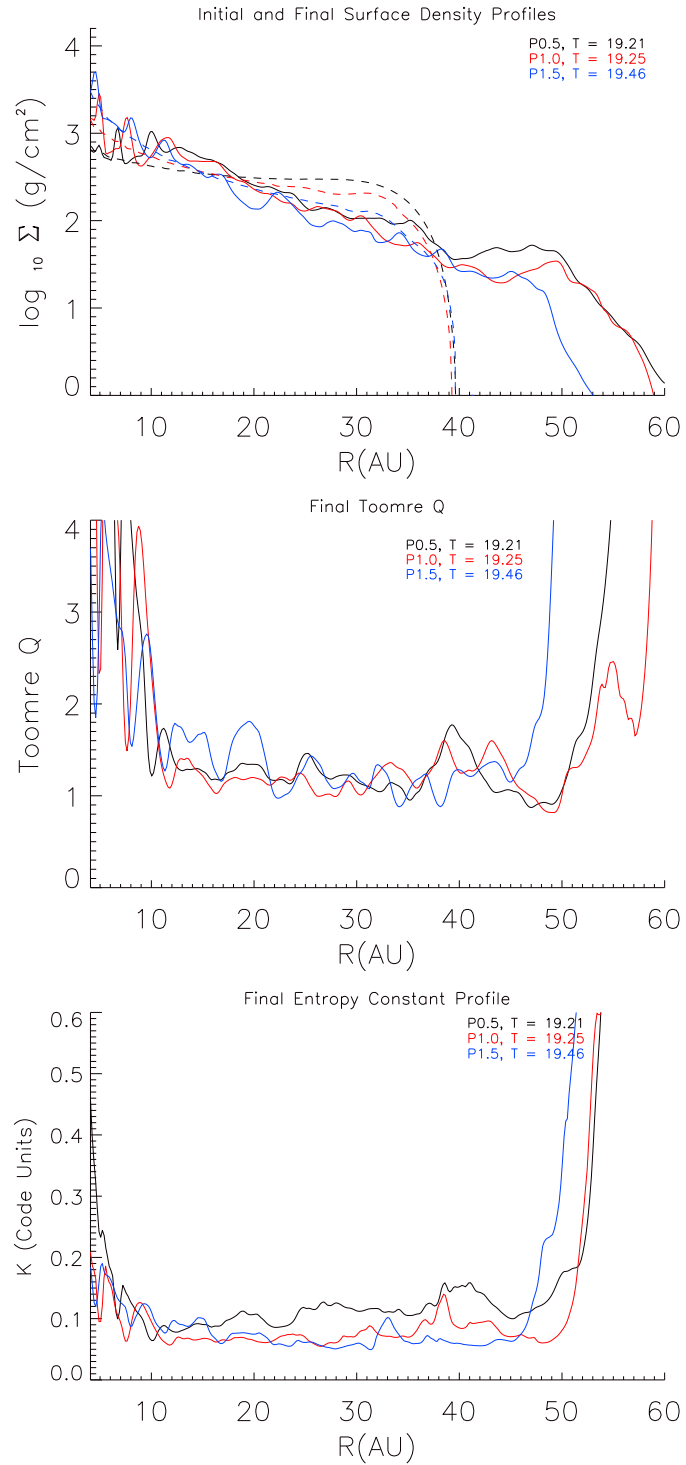


Figure 3.7: Plots show the final surface density profile (top), Toomre Q distribution (middle), and entropy parameter K (bottom) versus radius for each of the three disks. The G1.7TC2P0.5 disk is shown in black, G1.7TC2P1 is shown in red, and G1.7TC2P1.5 is shown in blue. The surface density is plotted logarithmically, and initial surface density profiles are presented in dashed lines for comparison. The final entropy profiles are given in code units. The time of measurement is given in ORPs.

A_m amplitudes, is delayed. Additionally, the mass transport rates during the burst decrease, and the $\langle A_m \rangle$ amplitudes during the asymptotic phase decrease slightly as well.

3.4 Variation of Azimuthal Resolution

To understand the relationship between azimuthal resolution and the outcome of GIs, I performed four disk simulations, which are all variations of the G1.7TC2P1 simulation. For this study, I concentrated on the effect of resolution on gravitational torques and the effective α in the asymptotic phase of the simulations. Since the computational burden of running all four simulations from the axisymmetric phase is rather high, the $l_{max} = 128$ was run through the axisymmetric, burst and transition phases. The other simulations all began by interpolating the $l_{max} = 128$ simulation to higher or lower azimuthal resolution at 9.6 ORPs, near the end of the transition phase. Although this strategy saved a large amount of computational time, it limits the scope of the analysis to the asymptotic phase. The four resolutions used are $l_{max} = 64, 128, 256,$ and 512 . After interpolation, the GIs in the disk have additional or fewer degrees of freedom, and so it takes some time for the disk to transition to the new resolution. I evolved the disk from 9.6 to 12 ORPs before making any comparisons so that the disk could relax to the asymptotic state. All four disks use a volumetric cooling rate as in equation (2.12) with $t_{cool} = 2$. Figure 3.9 compares the four different resolutions at 18 ORPs near the end of the simulations. One can clearly see that the lower resolution simulations had more clearly defined spiral structures with greater density contrast at larger radii. The density structures of the higher

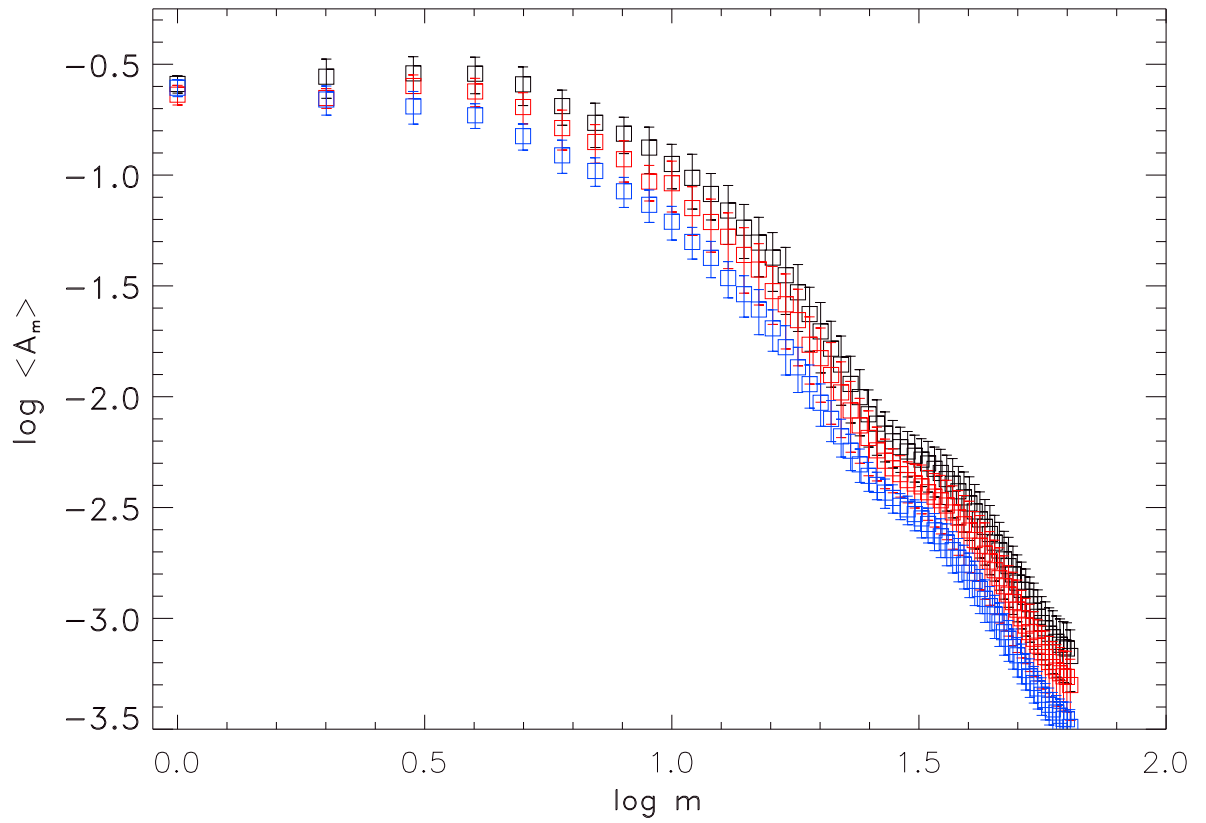


Figure 3.8: Time-averaged values of A_m for each of the three simulations with varied initial surface density profiles. *G1.7TC2P0.5* is shown in black, *G1.7TC2P1* is shown in red, and *G1.7TC2P1.5* is shown in blue. The A_m values are averaged over the interval 13 – 19 ORPs. The “error bars” on each m -value represent the RMS fluctuations about the time-averaged mean. The plot depicts m -values from 1 to 64 on a logarithmic scale.

resolution simulations were more washed out and are not dominated by low-order structures. This resulted in larger non-axisymmetric amplitudes for low-order modes and larger torques for the simulations with smaller azimuthal resolutions (see figures 3.10 and 3.11).

Azimuthal resolution is particularly important because it allows GI power to spread to higher-order modes (i.e., modes with more arms) that behave more like local turbulence. I test this by examining the amplitude in various modes to see how they are affected by the choice of grid. Figure 3.10 shows the $\langle A_m \rangle$ values averaged from 12 to 19 ORPs for the different resolutions. For each simulation, I computed $\langle A_m \rangle$ values up to $m = l_{max}/2$. This represents the smallest wavelength for which I can reliably measure the GI amplitudes (Shannon 1984). Clearly, as l_{max} is increased, the amplitude increases in modes with a larger m -value. Additionally, the amplitudes of low-order m -modes is decreased. This is most likely due to the fact that, as l_{max} is increased, the degrees of freedom available for the non-axisymmetric structure increase as well, so power is naturally spread from low-order to high-order m -values. Table 3.3 lists the time-averaged $\langle A_m \rangle$ summed over $m = 2$ to $l_{max}/2$ for each of the resolutions. This total non-axisymmetric amplitude $\langle A_\Sigma \rangle$ varies by at most 7% for the different values of l_{max} , with $l_{max} = 256$ being the most significant outlier. The $m = 1$ mode is not included in the integrated $\langle A_\Sigma \rangle$ value because the central star is artificially fixed to the grid center in these simulations (see chapter 4).

I identify $m = 2 - 7$ as the low-order modes that are considered to be global modes, with $m = 1$ again excluded due to the fixed central star. This determination was made by considering the radial range over which the mode is most effective in transporting angular momentum, i.e., from the inner Lindblad resonance to the outer

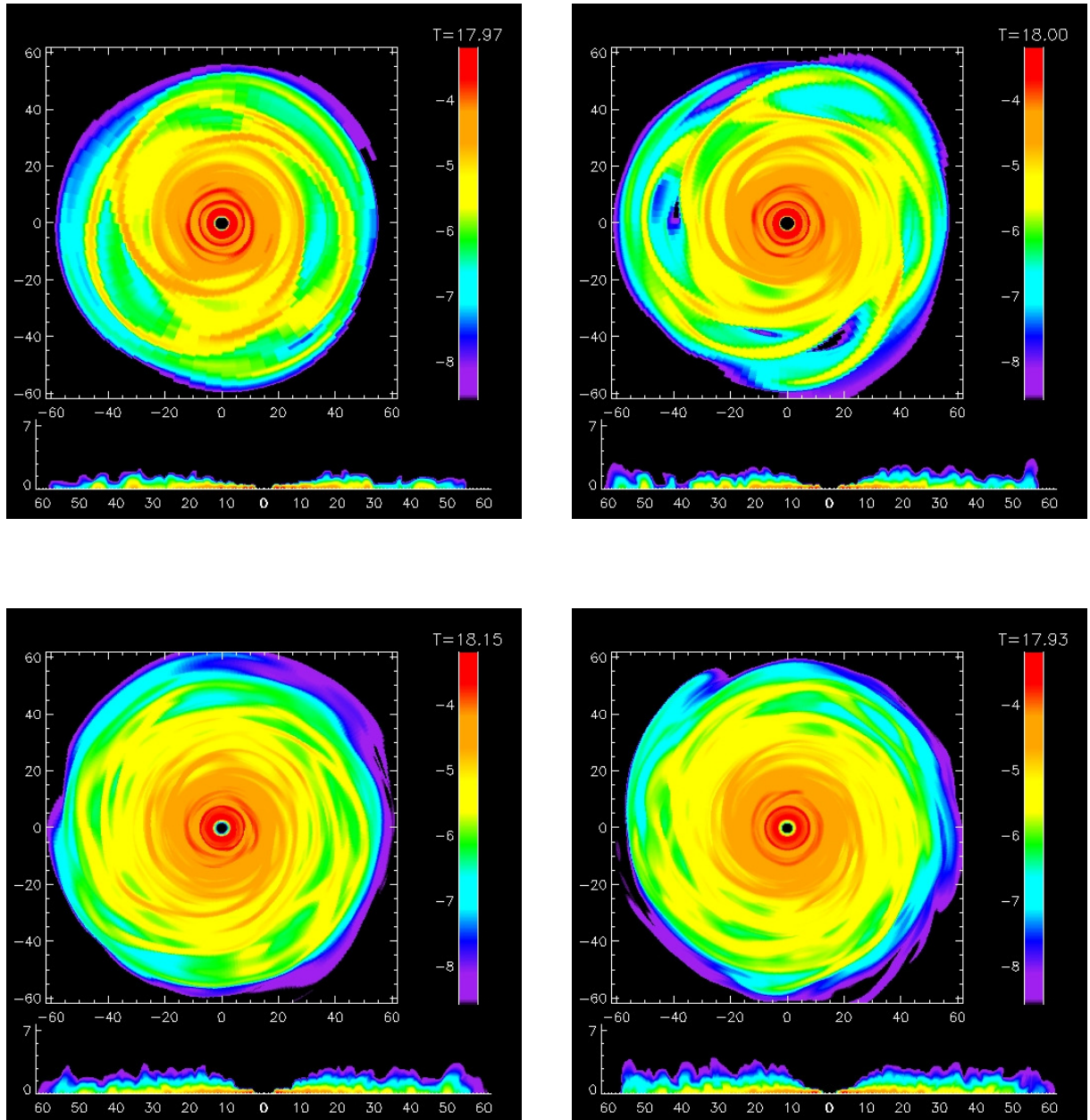


Figure 3.9: The midplane and meridional density contours are shown for each of the four azimuthal resolutions considered. From the top left going clockwise these are $l_{max} = 64$, 128, 512, and 256. Densities are plotted in code units on a logarithmic scale. This snapshot is taken near the end of the simulations at ≈ 18 ORPs.

l_{max}	Q_{avg}	$\langle A_{\Sigma} \rangle$	$\langle A_{2-7} \rangle / \langle A_{\Sigma} \rangle$	α_{avg}
64	1.26	1.96	0.76	0.069
128	1.24	1.91	0.62	0.044
256	1.39	1.83	0.54	0.026
512	1.48	1.95	0.49	0.020

Table 3.3: Temporally and spatially averaged quantities for several values of l_{max} . All values are averaged over the time interval from 12 to 19 ORPs. The Toomre Q quantities and the α quantities are averaged in radius from 10 to 40 AU. The $\langle A_m \rangle$ quantities are averaged from 2 AU to the outer edge of the grid.

Lindblad resonance, and comparing it to the disk scale height. These quantities are roughly equal for $m = 7$. For lower-order modes, the radial range exceeds the scale height. Table 3.3 shows that the amount of power present in these low-order modes represents a much smaller fraction of the total power as the azimuthal resolution increases. This fraction systematically decreases as l_{max} increases, with the difference between the lowest resolution and the highest resolution being a factor of 1.6. As l_{max} increases, the percentage change from one resolution to another changes as well. For example, when l_{max} was increased from 64 to 128 $\langle A_{2-7} \rangle / \langle A_{\Sigma} \rangle$ decreases by 18%. However, when l_{max} was increased from 256 to 512 $\langle A_{2-7} \rangle / \langle A_{\Sigma} \rangle$ decreases by only 9%. Ideally, if the simulations were totally converged, the fraction of non-axisymmetric amplitude would not change with an increase in l_{max} , however the $l_{max} = 512$ simulation is clearly very close to convergence.

The total amount of non-axisymmetric power, represented by $\langle A_{\Sigma} \rangle$, is related to the strength of GI activity and stayed roughly constant with changing azimuthal resolution. This is due to the fact that the amplitude of non-axisymmetric structures is strongly dependent on the local cooling time (Cossins et al. 2009), which was the same for all of the simulations. Cossins et al. (2009) find that $\langle A_{\Sigma} \rangle^2 \approx 1/t_{cool}$. This

results in the Q values being similar for all of the simulations because the strength of the instability (parameterized by Q) is directly related to the amplitude of the non-axisymmetric structure. The Toomre Q values presented in table 3.3 for each of the resolutions are averaged over the time interval 12 to 19 ORPs, and from 10 to 40 AU, the region of the disk that is gravitationally unstable. Like $\langle A_\Sigma \rangle$ the time averaged Toomre Q values varied by a relatively small amount as the resolution increased, with the maximum difference being 15% between $l_{max} = 128$ and 512. Some of the difference may have been due to the nonlinear and chaotic behavior of the GIs. Additionally, differences in the time sampling may have resulted in minor differences in the time-averaged values. Since the Courant time $\sim \Delta x/v_x$, as the resolution increases, the time step decreases, resulting in a larger number of time samples for the higher-resolution studies, and greater accuracy in the temporal integration.

Naturally, one would expect as the non-axisymmetric amplitude is transferred from lower-order modes to higher-order modes that the gravitational torques in the disk should decrease. This is due to the fact that low-order modes have a longer wavelength and, if coherent in radius, have a longer lever arm to produce torques. On the other hand, high-order modes have relatively short wavelengths and so produce more localized effects and smaller net torques. These modes tend to produce pockets of local GI activity, whose torques can cancel each other out over the whole disk. Figure 3.11 compares the torque profiles for the $l_{max} = 128$ and 512 simulations. Contributions to the torque from the $m = 1$ pattern, the sum of $m = 1$ and 2, the sum of $m = 1, 2$ and 3, and the sum of $m = 1, 2, 3$ and 4 are included in addition to the total torque. As the azimuthal resolution was increased from $l_{max} = 64$ to 512, the total torque decreased monotonically. The comparison between $l_{max} = 128$

and 512 is shown as an example of the general trend. Although the general shape of the torque profile is consistent between the two resolutions, there are some minor variations, primarily due to differences in the torque from $m \geq 4$.

Figure 3.12 shows the effective α for the four different grid resolutions, time-averaged from 12 to 19 ORPs. For comparison, the predicted values from Gammie's (2001) equation (3.12) are shown for the strongly self-gravitating limit (lower curve) and the non-self-gravitating limit (upper curve). Note that predictions from Gammie (2001) are based upon a thin disk approximation, where the local balance of heating and cooling dominates the energetics.

In an α -disk formalism, the mechanism giving rise to the transport of angular momentum also acts to dissipate energy. Based on simulations using a local cooling prescription, i.e., $t_{cool}\Omega = \text{const.}$, Lodato & Rice (2005) concluded that a disk in a state of gravitoturbulence would have locally balanced heating and cooling rates. If the heating were due to local dissipation, then α and t_{cool} are related by

$$\alpha = \left| \frac{d \ln \Omega}{d \ln R} \right|^{-2} \frac{1}{\gamma(\gamma - 1)t_{cool}\Omega}. \quad (3.18)$$

Rice et al. (2005) concluded that for a given $t_{cool}\Omega$ there exists some maximum stress α_{max} , which if exceeded would cause a disk to fragment. The horizontal dot-dashed line in figure 3.12 indicates the $\alpha_{max} \approx 0.06$ found by Rice et al. (2005). Clarke et al. (2007) have revised this limit to $\alpha_{max} = 0.12$ for cases where t_{cool} varies with time, but, because the t_{cool} used in these simulations is constant with time, I display the α_{max} presented by Rice et al.. It is interesting to note that at higher resolution the disks did not reach this critical α and did not fragment. However, the lower

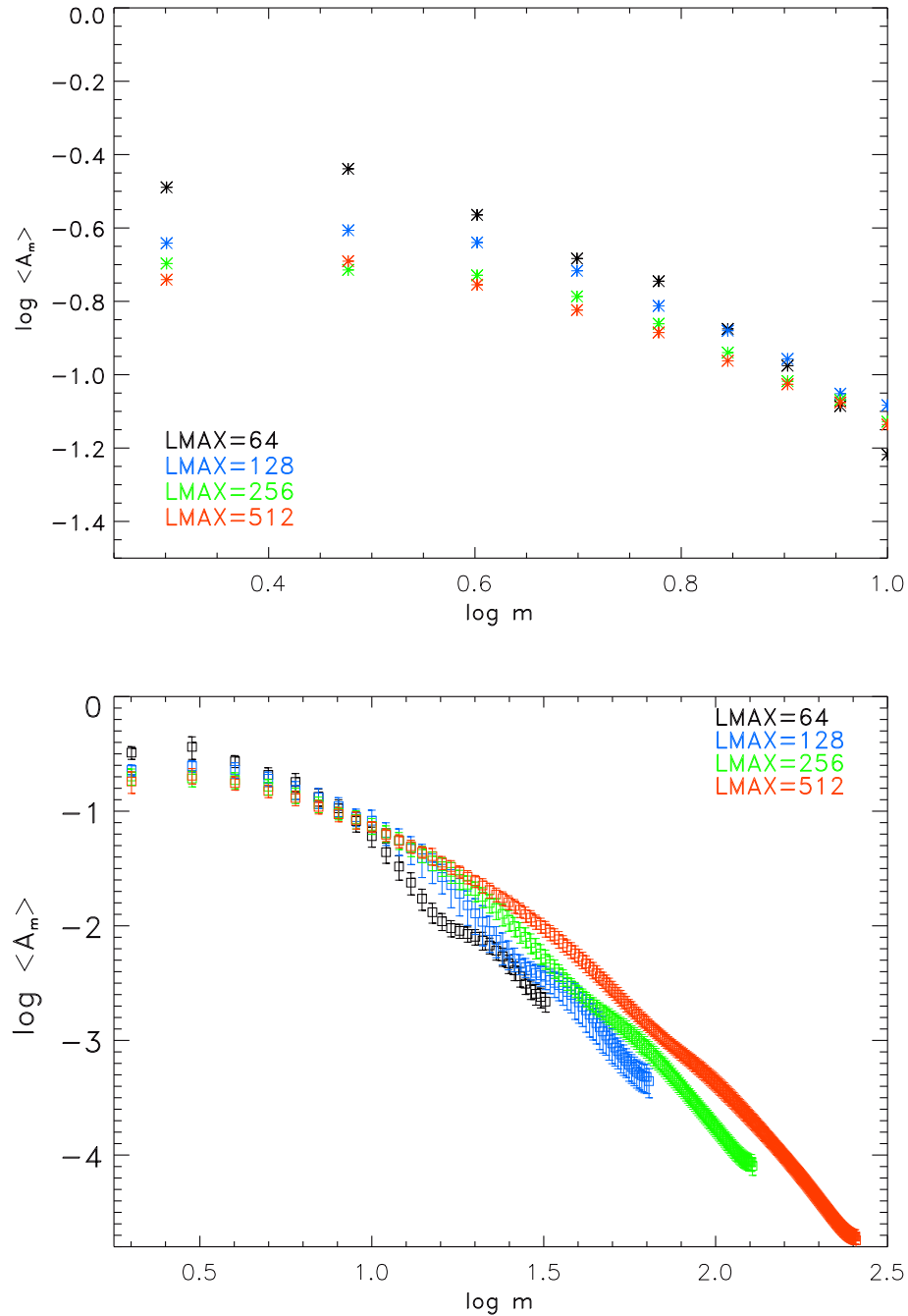


Figure 3.10: Time averaged values of A_m for each of the three simulations with varied azimuthal resolution. The $l_{max} = 64$ simulation is shown in black, $l_{max} = 128$ is shown in blue, $l_{max} = 256$ is shown in green, and $l_{max} = 512$ is shown in red. The A_m values are averaged of the interval from 12 – 19 ORPs. The “error bars” in the lower plot on each m value represent the RMS fluctuations about the time averaged mean. The top plot depicts a zoomed in region for $m = 2 - 10$, it is shown without “error bars” for clarity. The plots depict m -values from 2 to $l_{max}/2$ on a logarithmic scale.

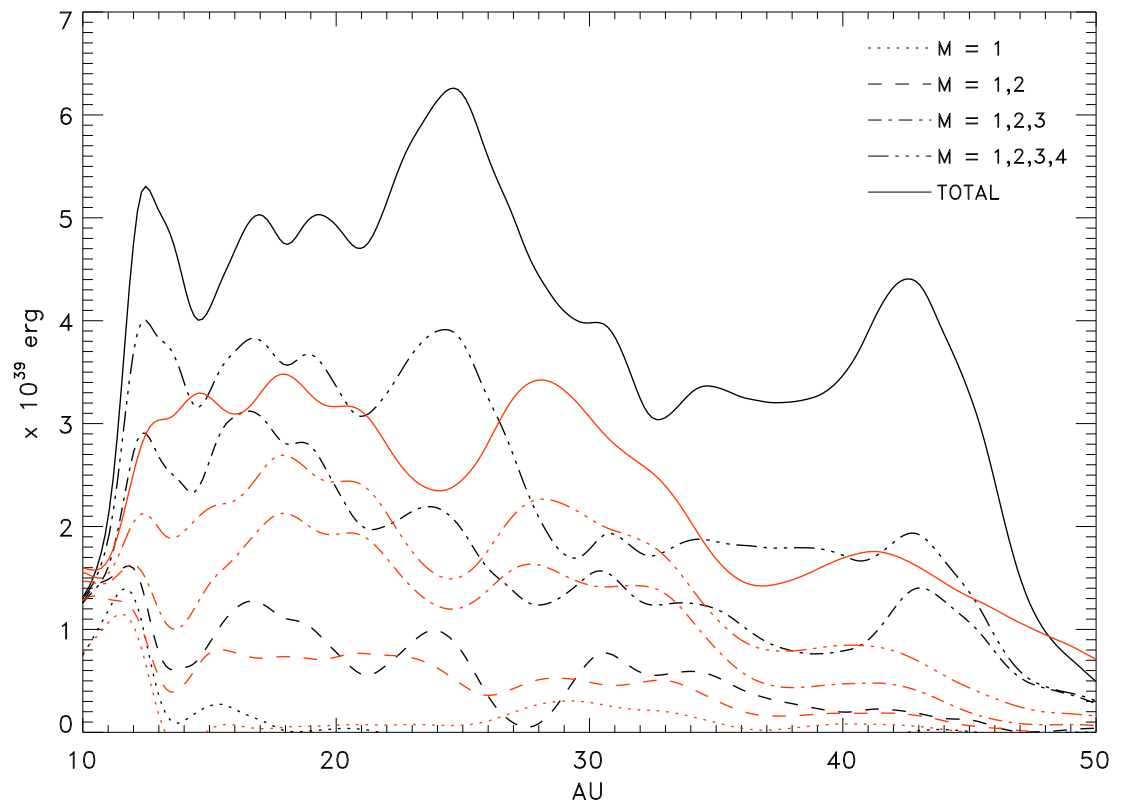


Figure 3.11: Torque profiles averaged from 12 to 19 ORPs for the $l_{max} = 512$ (red) and $l_{max} = 128$ (black) simulations. Total torques are shown as well as contributions from sums of various m -values.

resolution disks that exceeded this threshold did not fragment either. This could be due to suppression of fragmentation at lower resolution because there is insufficient resolution to follow the fragments as they form.

As the azimuthal resolution increases, the effective α in the GI active region decreases. This is due to the decrease in the total gravitational torque, as illustrated in figure 3.11. This decrease in gravitational torque is due, in turn, to the shift of non-axisymmetric amplitude from low-order global modes, which produce large torques, to high-order local modes, which tend to cancel each other out when integrated over the whole disk. In fact, the decrease in the ratio of low-order amplitude to the total amplitude $\langle A_{2-7} \rangle / \langle A_{\Sigma} \rangle$ closely tracks the decrease in the time-averaged α averaged from 10 to 40 AU, as seen in table 3.3. Although the average α values have not converged to a single value for my highest two resolutions, the percentage change decreased as l_{max} increased. In addition, figure 3.12 shows that the $l_{max} = 256$ and 512 simulations have qualitatively similar time averaged α profiles over a large range of disk radii. These profiles also fall midway between the predicted **Gammie** curves. Indeed the α_{avg} value of 0.020 for the $l_{max} = 512$ simulation is squarely between the α_{avg} values for the **Gammie** curves 0.014 (strongly self-gravitating) and 0.027 (non-self-gravitating).

Clearly, azimuthal resolution plays an important role in accurately quantifying the key mass transport mechanisms in global simulations of gravitationally unstable disks. Although I have not conclusively shown numerical convergence at a resolution of $l_{max} = 512$, there are strong indications that this resolution is adequate to appropriately quantify the magnitude of gravitational torques and an effective gravitational α resulting from GI activity. The percent change in α_{avg} between $l_{max} = 256$

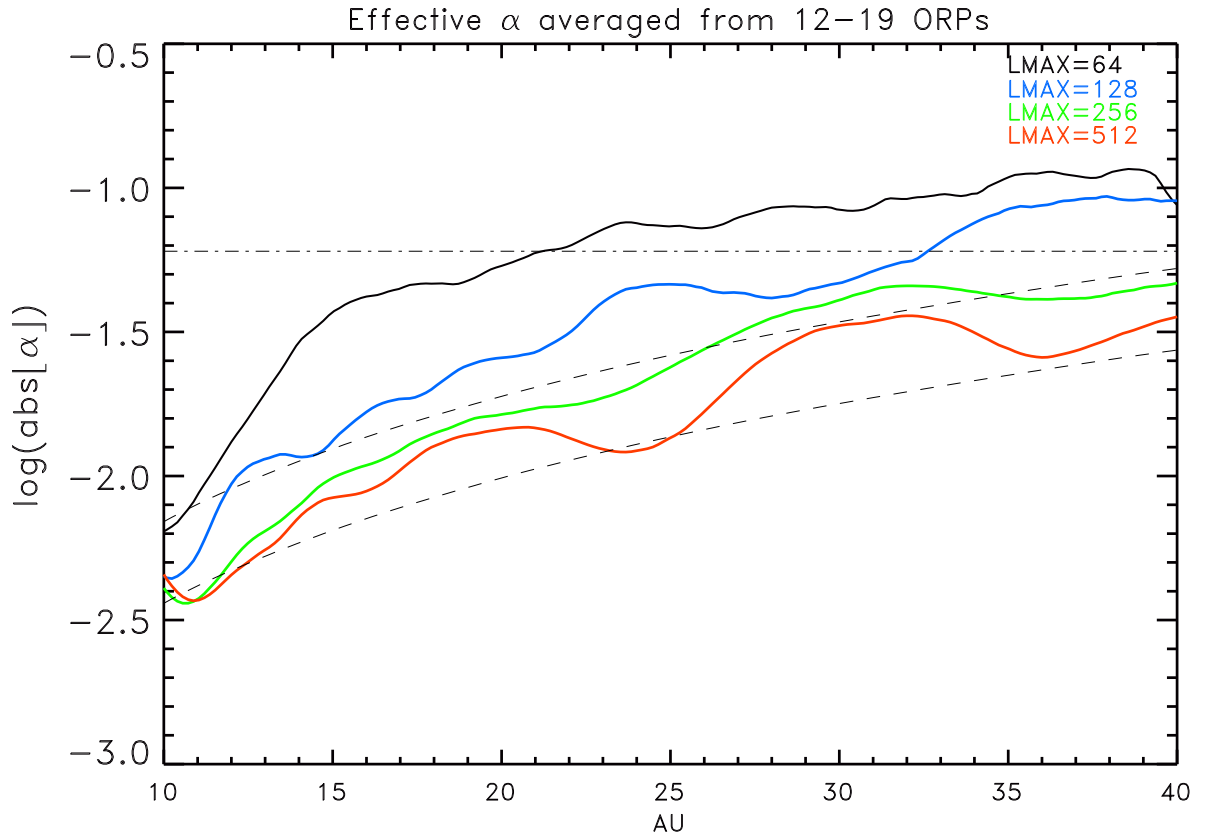


Figure 3.12: *Effective Shakura-Sunyaev α -values computed for the $l_{max} = 64$ (black), 128 (blue), 256 (green), and 512 (red) simulations averaged over the asymptotic phase from 12 to 19 ORPs. Shown for comparison are curves predicted by Gammie with $t_{cool} = 2$ ORPs. The upper curve assumes a self-gravitating disk; the lower curve assumes gravity is due to the star alone. The dot-dash line indicates the critical α found by Rice et al. (2005) for fragmentation.*

and 512 is the lowest of any resolution increase, and although it is a $\sim 20\%$ difference the qualitative difference between the $l_{max} = 256$ and 512 α_{avg} curves is rather small. Of course, to determine convergence conclusively would require another simulation with a l_{max} of 1024, but the computational cost is prohibitive for this case at the present time.

In addition, the α curve for $l_{max} = 512$ falls squarely between the [Gammie](#) predicted curves. Gammie's prediction is based on the assumption is a local balance of cooling, in this case from the t_{cool} prescription, and heating from GI activity. If the heating from GI activity is localized then the local balance of heating and cooling assumption should be valid for these disks. However, it should be noted that Gammie's predictions are not correct on all counts (see below), and are only valid when the quantities considered are averaged over long time periods and considered over a large radial range. If one were to use the parametrization predicted by Gammie's formula in simulations, much of the detailed structure would be missed. Such local, rapidly varying structure can play an important role in many disk processes (see, for example, planet migration in [chapter 5](#)). In addition, to correctly predict the α in a disk using Gammie's formula, one must know the disk cooling time, which, in the case of a disk with realistic radiative cooling, is not known *a priori*.

Although the effective α curves do correspond roughly to the [Gammie](#) prediction, the results from these simulations differ from [Gammie's](#) in one significant way. The local shearing box simulations performed by [Gammie \(2001\)](#) show that the total effective α is composed of a gravitational stress component and a Reynolds stress component that are nearly equal, see [Gammie \(2001, figure 3\)](#). On the other hand, [Lodato & Rice \(2004\)](#) reported similar small Reynolds stresses for several of their

simulations (see their figure 5). All of the analyses presented here only consider the gravitational stress. When I attempt to measure the Reynolds stress, I find it is quite small compared to the gravitational stress. As noted previously, the Reynolds stress is very hard to determine in global simulations. However, the prediction made by [Gammie](#) relies only on the idea that heating from GI activity balances cooling. So the exact mix of stresses contributing to the total amount of heating could be different depending on the type of simulation, the physics considered in the simulation, and the simulation parameters.

The requirement of $l_{max} = 512$ as a minimum azimuthal resolution for accurate computation of GI effects does not necessarily apply to all possible disk analyses. This study focused primarily on the accurate determination of non-axisymmetric structure, gravitational torques, and effective gravitational α . Another aspect where azimuthal resolution is known to be important is disk fragmentation ([Pickett et al. 2003](#)). However, comparative studies, such as the one presented in §3.3, still produce valid results at lower azimuthal resolutions.

3.5 Variation of γ in the Equation of State

All the simulations discussed in this chapter used an ideal gas equation of state as outlined in chapter 2. The pressure is determined by the internal energy ϵ and the adiabatic index γ as in (2.3). As the adiabatic index decreases, so does the pressure for a given ϵ , and this is typically referred to as a “softer” equation of state because the fluid is more compressible. Authors who use an ideal gas equation of state with fixed γ have employed both $\gamma = 7/5$, because it mimics molecular hydrogen with

excited rotation states (Boss 1998b), and $\gamma = 5/3$, because it represents a monatomic ideal gas (Pickett et al. 1998). In fact, molecular hydrogen H_2 can behave like a $\gamma = 7/5$ or $\gamma = 5/3$ ideal gas depending on the composition and temperature. If one disregards dissociation and ionization, H_2 typically behaves like a $\gamma = 5/3$ ideal gas for $T < 100K$ and like a $\gamma = 7/5$ ideal gas for $T > 300K$ (Decampoli et al. 1978). The precise temperature range over which this transition takes place depends on the ratio of ortho-hydrogen (parallel proton spins) to para-hydrogen (antiparallel proton spins) (Boley et al. 2007b).

Naturally, one would assume that a lower γ , and thus a more compressible fluid, would lead to a protoplanetary disk that is more susceptible to fragmentation. Indeed, in a series of Smoothed Particle Hydrodynamic (SPH) simulations, Rice et al. (2005) found that disks with $\gamma = 7/5$ were susceptible to fragmentation at larger $t_{cool}\Omega$ than disks with $\gamma = 5/3$; specifically, the fragmentation limit was $t_{cool}\Omega = 12 - 13$ for $\gamma = 7/5$ and $t_{cool}\Omega = 6 - 7$ for $\gamma = 5/3$.

To confirm the findings of Rice et al., and to test the applicability for fixed grid simulations with global cooling times, I performed four simulations in addition to those already discussed. These are G1.6TC0.6P1, G1.4TC3P1, G1.4TC2P1, and G1.4TC1P1. To produce initial equilibrium disk models for the $\gamma = 7/5$ simulations, I modified the initial axisymmetric equilibrium models used as initial models for the $\gamma = 5/3$ simulations. To maintain the pressure balance, and the hydrostatic equilibrium of the initial disk, I changed the internal energy density, ϵ , of each cell according to equation (2.5) so that,

$$\epsilon_{7/5} = 5/3\epsilon_{5/3}. \quad (3.19)$$

Here $\epsilon_{5/3}$ and $\epsilon_{7/5}$ are the internal energy densities of the disks with $\gamma = 5/3$ and $7/5$, respectively. Although this change of only the internal energy density maintains pressure equilibrium, it introduces an entropy gradient that is dynamically unstable. However, the fluid re-equilibrates rapidly (in < 1 ORP) and stability is quickly restored.

It has been shown that the primary factor that governs the strength of GIs in a disk is the cooling rate (Gammie 2001; Mejía et al. 2005). For $\gamma = 5/3$, Gammie (2001) found that a disk should fragment if $t_{cool}\Omega \lesssim 3$ and Mejía et al. (2005) found that a disk will fragment for a global cooling rate $t_{cool} \lesssim 0.5$ ORP, provided the simulation is carried out at high enough resolution. The procedure I employed was to perform a simulation using a cooling rate that would not cause the disk to fragment, and then run subsequent simulations, decreasing the cooling rate until the disk fragmented. For a $\gamma = 5/3$ gas, I found that a disk will fragment with a global cooling rate of $t_{cool} = 0.6$ ORPs, consistent with Mejía et al. (2005). With a $\gamma = 7/5$, gas I found that a global cooling rate of $t_{cool} = 1$ ORPs will cause strong fragmentation. When $t_{cool} = 2$ ORPs and the adiabatic index is $7/5$, I found that the disk is on the verge of fragmentation. Fragments form, but are quickly destroyed by Keplerian shear, see bottom panel of figure 3.13 for an example. All four simulations were identical to the G1.7TC2P1 simulation except for the adiabatic index, cooling rate, and in the case of fragmenting disks, the azimuthal resolution. Both fragmenting disks, G1.7TC0.6P1 and G1.4TC2P1, and the borderline case, G1.4TC2P1, were simulated with $l_{max} = 512$.

Figure 3.13 shows midplane and meridional densities for the two strongly fragmenting simulations, G1.7TC0.6P1 and G1.4TC1P1. Both disks produce many

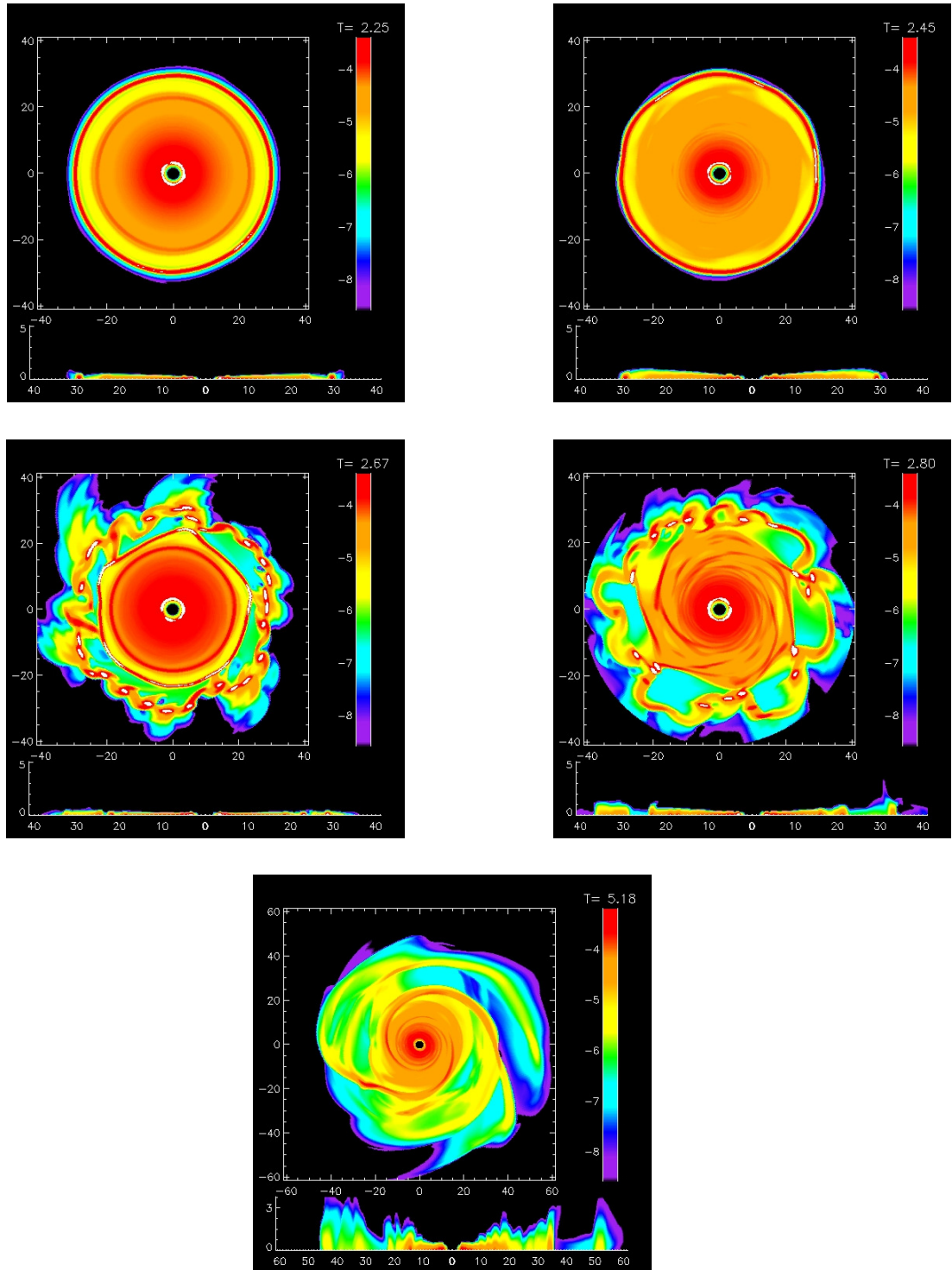


Figure 3.13: Midplane and meridional densities are plotted in code units on a logarithmic scale for the G1.7TC0.6P1 (left) and G1.4TC1P1 (right) simulations. The top panels show both simulations just before fragmentation, a dense ring has formed as a precursor to fragmentation. The second row of panels show the simulations just after the disk has fragmented, measurement of the fragments positions determines the $t_{\text{cool}}\Omega$ at which each disk fragments. The bottom panel shows an example of a tenuous fragment that forms in the G1.4TC2P1 simulation. This fragment is subsequently destroyed by Keplerian shear.

tightly bound clumps, but the disk with a softer equation of state does so with a longer cooling time. Although the determination of the fragmentation threshold is not precise, it does set a maximum global $t_{cool}(crit)$ that will cause fragmentation in the disk. Additionally, by examining the location in the disk where the fragmentation occurs, I can convert the global $t_{cool}(crit)$ to a local $t_{cool}\Omega(crit)$. In both of the fragmenting cases, a dense ring forms at the radius where the fragmentation occurs, shortly before the disk breaks apart into fragments. The dense ring can be seen forming in the top panels of figure 3.13, the middle panels show the time when clumps first appear. By measuring the average Ω at the radius where clumps appear, I can determine the value of $t_{cool}\Omega(crit)$ for which the fragmentation occurs.

Figure 3.14 shows $t_{cool}\Omega$ plotted as a function of radius for the G1.7TC0.6P1 and G1.4TC1P1 simulations. The simulation with $\gamma = 7/5$ is shown in red, while the $\gamma = 5/3$ simulation is shown in black. The dashed lines indicate the fragmentation criteria as a function of $t_{cool}\Omega$ presented by Rice et al. (2005) as $t_{cool}\Omega(crit) = 12 - 13$ for $\gamma = 7/5$ and $t_{cool}\Omega(crit) = 6 - 7$ for $\gamma = 5/3$. The minimum radius where fragmentation occurs in each of the simulations is shown with a hash mark. I find fragmentation criteria of about $t_{cool}\Omega(crit) = 5.5$ and 11 for $\gamma = 5/3$ and $7/5$, respectively. These numbers are in rough agreement with those found by Rice et al..

3.6 Variation of the Initial Perturbation

In order to seed the non-axisymmetric structure that will eventually grow to a non-linear amplitude, a small initial random density perturbation is introduced into the axisymmetric equilibrium models used to begin a simulation. Typically, this pertur-

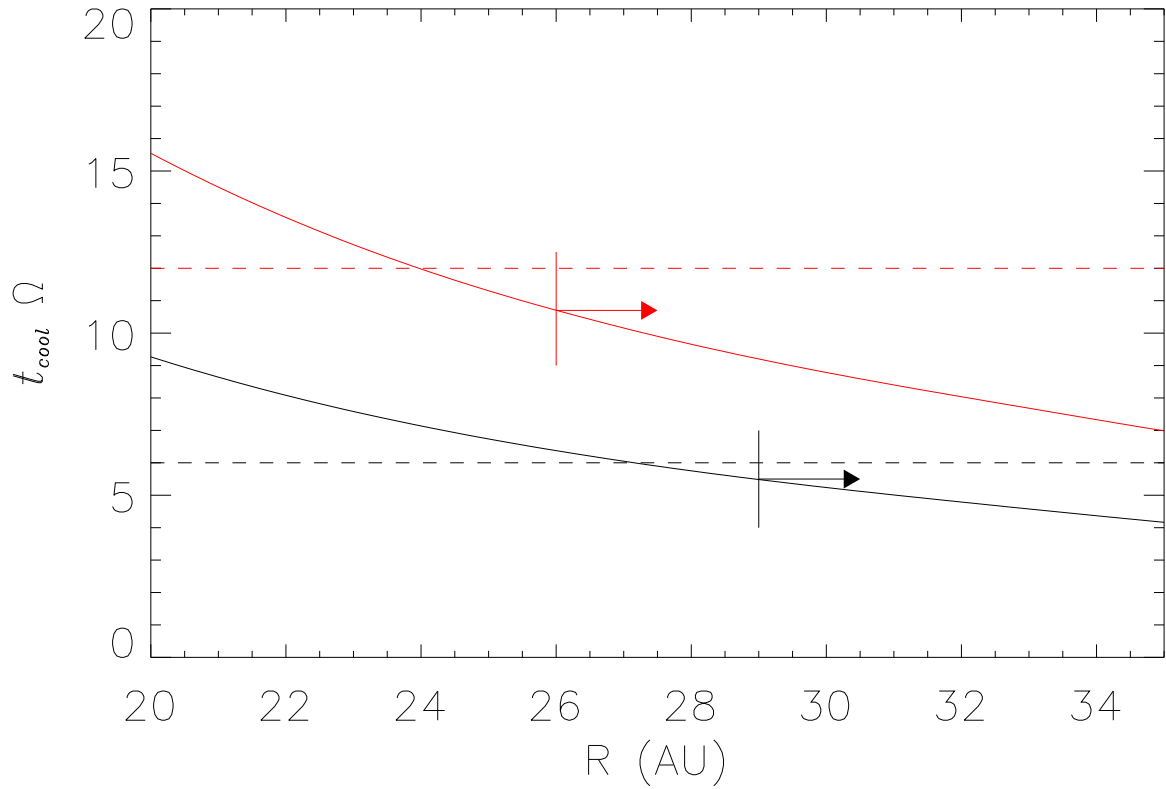


Figure 3.14: The $t_{cool}\Omega$ curves are plotted versus radius for the G1.4TC1P1 (red) and G1.7TC0.6P1 (black) simulations. For comparison the $t_{cool}(crit)\Omega$ lines from Rice et al. (2005) are plotted for $\gamma = 7/5$ and $5/3$. The vertical hash mark represents the radius at which fragments first form in each of the simulations.

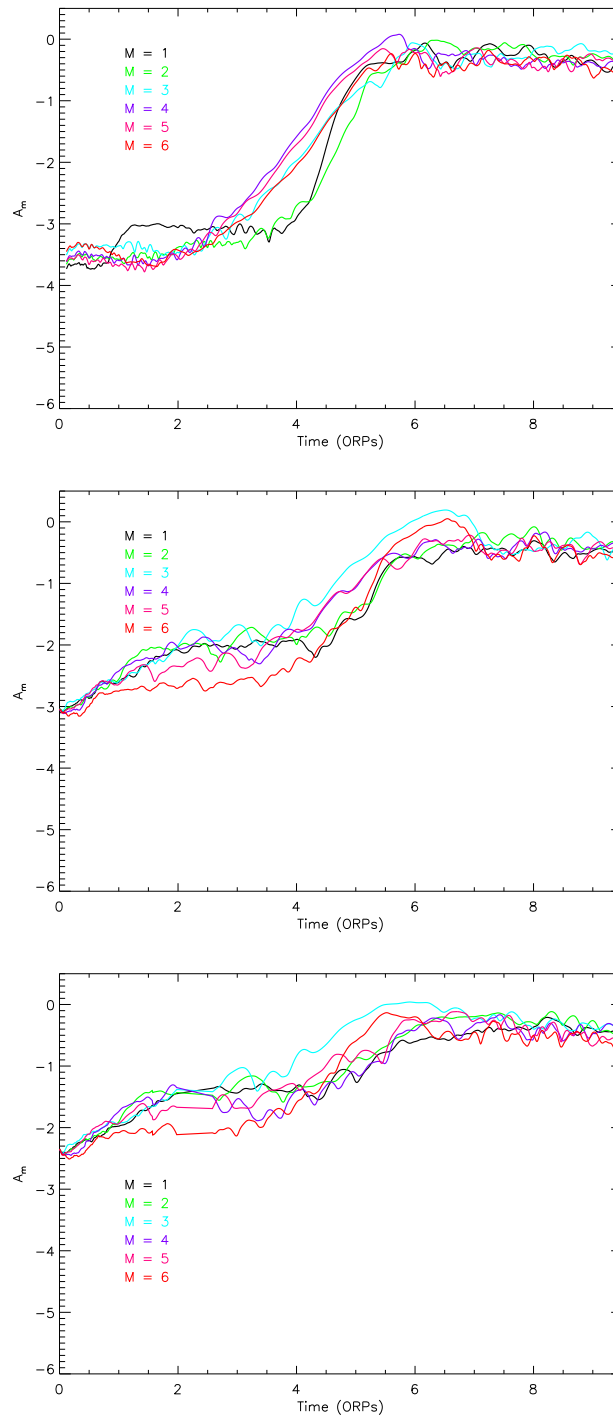


Figure 3.15: Each panel shows the Fourier components, A_m , as a function of time for $m = 1 - 6$. The $\xi = 0.0001, 0.01$, and 0.05 simulations are shown from top to bottom. The amplitudes are shown from the initial models through the nonlinear saturation in the burst phase. Contribution to the A_m components is only calculated for $\varpi > 25$ AU due to contamination from a spurious $m = 1$ signal.

bation is rather small with the amplitude being $\xi = 0.0001$, i.e., $\Delta\rho/\rho = \xi R$, where R is a random number between -1 and 1 . The perturbation $\Delta\rho/\rho$ is calculated for each cell and R is uncorrelated from cell to cell. This value of ξ is used for all simulations discussed in this work other than those in this section. In order to investigate the effect this random perturbation has on the onset of GIs, I performed two additional simulations by giving the G1.7TC2P1 initial axisymmetric equilibrium disk random perturbations with amplitude $\xi = 0.01$ and $\xi = 0.05$. These simulations were run through the burst phase using $l_{max} = 128$.

Figure 3.15 shows the evolution of the A_m values over time for $m = 1 - 6$ for each of the three simulations. As in figure 3.4, only material at $\varpi > 25$ AU contributes to the measurement of A_m . As the value of ξ is increased, the initial A_m amplitudes increase as well. However, this change also results in a more subtle effect. For larger ξ , the growth in amplitude begins almost immediately, but at a somewhat slower rate. Eventually, the growth steepens, but less and less so as ξ gets larger. The net effect is that the A_m values saturate somewhat sooner with the *smallest* value of ξ .

This phenomenon can be explained in a fairly straightforward manner. The larger the value of ξ , the larger the initial A_m amplitudes. This means that significant coherent non-axisymmetric structures appear very early in the simulations when ξ is large. Figure 3.16 shows the midplane and meridional densities of each of the three simulations at 4.25 ORPs. In the simulations with $\xi = 0.01$ and 0.05 one can see non-axisymmetric structure, while the simulation with $\xi = 0.0001$ remains nearly axisymmetric. This non-axisymmetric structure acts to heat the disk and thereby prevents Q from dropping rapidly. The axisymmetric ring that grows as a precursor to the burst of GI activity in the $\xi = 0.0001$ simulations is disrupted by the non-

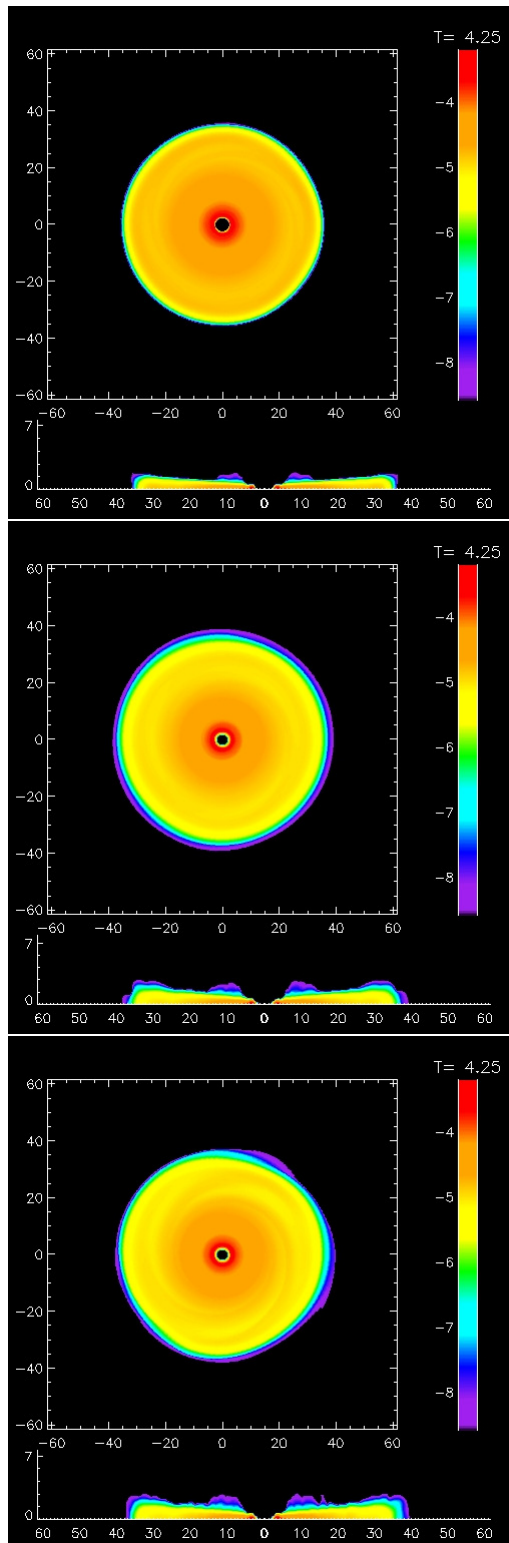


Figure 3.16: *Midplane and meridional densities are shown in code units on a logarithmic scale for the $\xi = 0.0001$ (top), 0.01 (middle), and 0.05 (bottom) simulations. Densities are shown at 4.25 ORPs in the middle of the A_m growth, when non-axisymmetric structure is just beginning to be visible. Note the lack of non-axisymmetric structure in the $\xi = 0.0001$ simulation.*

axisymmetric structures present earlier in the $\xi = 0.01$ and 0.05 simulations, and so the amplitude continues to grow at a slower rate. When the axisymmetric ring forms in the $\xi = 0.0001$ simulation, Q becomes very small, in some regions less than 1, and so a strong burst of GI activity is initiated at the radius where the ring forms. Figure 3.17 shows the surface density profiles and Toomre Q profiles for the three disks near the same time as the density snapshots in 3.16. The surface density is presented in linear scale to highlight the differences where the dense ring forms. This ring has an inner radius near 25 AU and is centered around 30 AU. It is most prominent in the simulation with $\xi = 0.0001$ and decreases in mass as ξ increases. As figure 3.17 shows, this overdensity can be correlated to a decrease in the Toomre Q . The Q profile changes slope near 24 AU for the $\xi = 0.0001$ simulation corresponding to the inner radius of the ring. The change in slope is less pronounced for the $\xi = 0.01$ simulation and is not noticeable for the $\xi = 0.05$ simulation. As the additional mass in the ring forces Q to smaller values, the GI activity increases. This, in turn, appears as rapid growth in the A_m amplitudes.

Another interesting difference between the simulations with small and large ξ values is the fastest growing mode. For both $\xi = 0.01$ and 0.05 , $m = 3$ is the dominate mode while the modes are growing, as shown in figure 3.15. The $m = 2$ mode is also more prominent than in the small ξ simulation. For $\xi = 0.0001$, $m = 4$ and 5 dominate. This may be due to the fact that, when an axisymmetric ring is allowed to form, Q is at its minimum over a smaller radial extent, which may bias the disk towards the growth of modes with shorter wavelengths. However, when non-axisymmetric structures are present over a large radial extent and Q is roughly the same over this range, modes of any wavelength can grow.

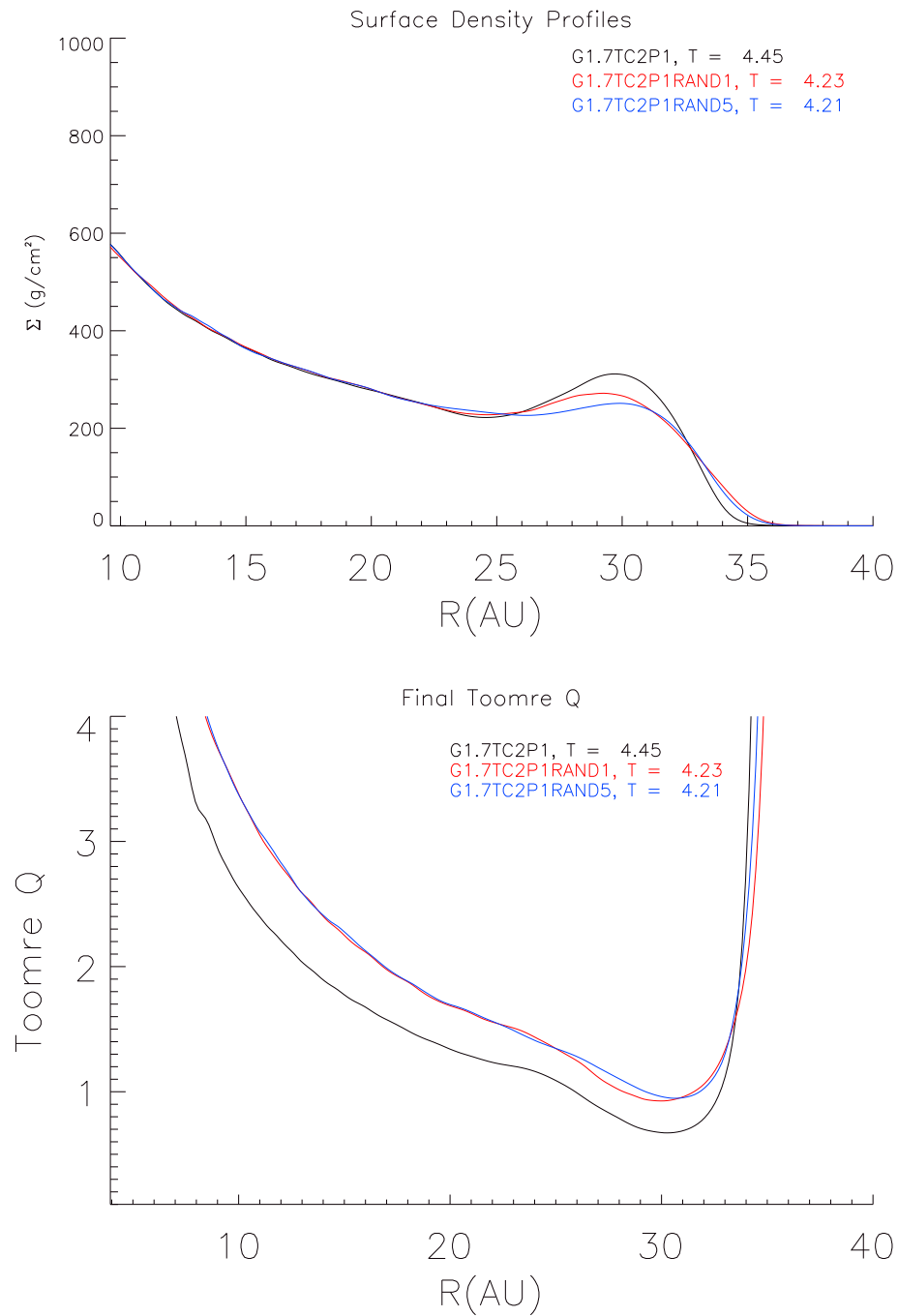


Figure 3.17: Plots show the final surface density profile (top) and Toomre Q distribution (bottom) versus radius for each of the three disks. The G1.7TC2P1 disk is shown in black, G1.7TC2P1RAND1 is shown in red, and G1.7TC2P1RAND5 is shown in blue. The time of measurement is given in ORPs.

Although a variation of perturbation amplitudes did cause significant differences in the burst phase, the early asymptotic phase is largely unaffected. In figure 3.18 one can see the surface density profile and Toomre Q profile of each of the disks at ≈ 15 ORPs. There is some minor variation in the inner disk at radii < 10 AU with different surface density enhancements, but the inner disk, specifically the radius at which the disk transitions from being GI active to inactive, is very chaotic. For radii > 15 AU there is very little difference between the disks in either surface density or Q value.

3.7 Conclusions

In this chapter, I have explored how varying both initial conditions and simulation parameters can affect the onset and outcome of gravitational instabilities in protoplanetary disks. In a disk with a constant global cooling time, the onset of GIs occurred at approximately the same radius; so, for a steeper initial surface density profile, less mass was present in the GI-active region. This means that the burst of GI activity took longer to occur and was less effective at transporting mass inward. Nevertheless, the overall disk evolution was largely unchanged. All disks followed the same pattern of evolutionary phases, and, when they reached the asymptotic phase, they had all converged to similar configurations, namely, a GI active protoplanetary disk with roughly constant Q , constant specific entropy, and a surface density profile of $\Sigma \propto \varpi^{-5/2}$.

When considering the effect of azimuthal resolution on the asymptotic behavior of a GI unstable disk, I found that, without sufficient azimuthal resolution ($l_{max} \leq 256$),

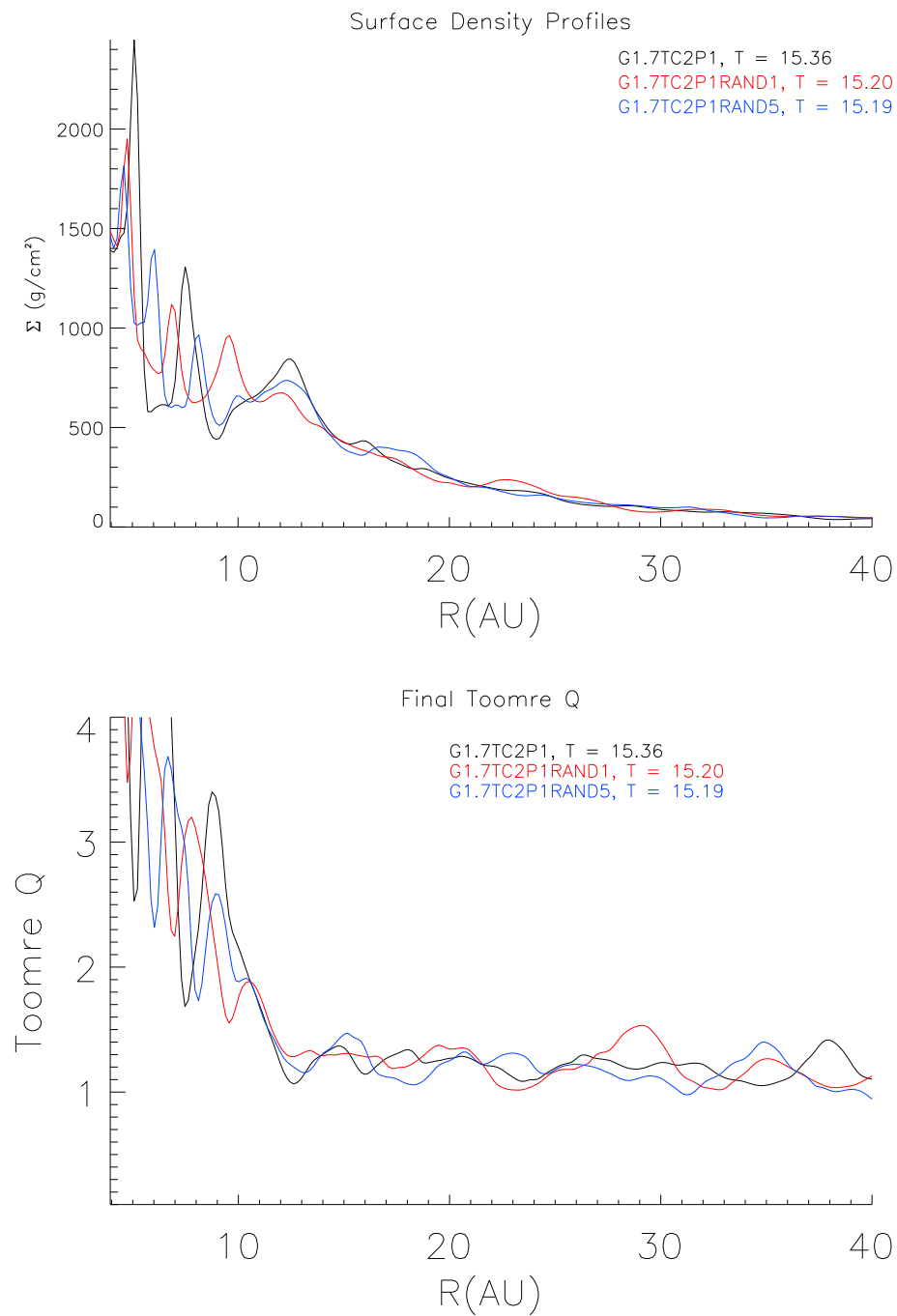


Figure 3.18: Plots show the final surface density profile (top) and Toomre Q distribution (bottom) versus radius for each of the three disks. The G1.7TC2P1 disk is shown in black, G1.7TC2P1RAND1 is shown in red, and G1.7TC2P1RAND5 is shown in blue. The time of measurement is given in ORPs.

gravitational torques and the effective gravitational α were underestimated for disks with a constant global cooling time. I also found that, at higher resolutions, non-axisymmetric amplitude shifted to higher-order modes, and the amplitude of low-order modes decreased. This resulted in a decrease of the gravitational torque and effective gravitational α . For $l_{max} = 512$, the effective gravitational α was in very good agreement with the prediction of [Gammie \(2001\)](#), which follows from an argument of local balance of GI heating and cooling. However, his detailed simulations found that the torques and heating in the disk were due in equal parts to gravitational stresses and Reynolds stresses. This is in contrast to my measurements where only gravitational stresses were significant, in rough agreement with [Lodato & Rice \(2004\)](#).

I also found agreement with [Rice et al. \(2005\)](#) on the $t_{cool}\Omega(crit)$ fragmentation criteria for disks with adiabatic indices of $\gamma = 5/3$ and $7/5$. The key finding was that the trend found by [Rice et al.](#) for constant $t_{cool}\Omega$ cooling also applies for a constant global cooling time. Perhaps not surprisingly, the more compressible $\gamma = 7/5$ equation of state led to fragmentation at longer cooling times, twice as long as for a disk composed of a $\gamma = 5/3$ gas.

Finally, my simulations studying the amplitude of the initial random perturbation showed that the extremely small amplitudes used in most simulations allow disks with constant global cooling rates to develop dense axisymmetric rings before a burst of GI activity. For the large variety of environments in which a protoplanetary disk may be found, it is likely that protoplanetary disks have a variety of initial perturbations. A disk with a $\gtrsim 1\%$ amplitude for random density perturbations avoids the artificially low Q values found in the axisymmetric ring. It should be noted that disks with larger

perturbations still followed the same basic phases of evolution, but the initial growth of the instability was not as dramatic as in simulations with small perturbations. In addition, the primary spiral modes seen in the burst phase were affected by the amplitude of the initial perturbation.

Chapter 4

Stellar Motion

When it is darkest, men see the stars.
– Ralph Waldo Emerson

As described in §2.3 a concern with previous simulations using an artificially fixed central potential is that one-armed spirals could be modeled improperly since stellar motion and subsequent feedback into the spiral structure is explicitly suppressed. In these cases, keeping the star fixed means SLING amplification (Adams et al. 1989; Shu et al. 1990) of spiral structures would be impossible. Other authors have approached this problem in different ways. For most SPH implementations (Rice et al. 2003b; Mayer et al. 2004), the stellar motion is included automatically by treating the star as a central sink particle that is smoothed differently from the rest of the SPH particles. However, simulations such as those by Rice et al. (2003a) exhibit a large initial accretion rate onto the central object. How the transfer of angular momentum from the disk material to the central object is handled could be quite important to the object’s motion. Other Eulerian grid-based hydrodynamic schemes use either the indirect potential method or some type of integration of the stellar equation of motion. For the latter approach, accurately determining the force on the central star can be somewhat challenging depending on the method used to calculate the disk potential. To avoid explicitly integrating the stellar equation

of motion, [Boss \(2000\)](#) allows the central protostar “to wobble in response to the growth of nonaxisymmetry in the disk, thereby preserving the location of the center of mass of the star/disk system.” Unfortunately, this method does not fully capture the protostar/disk interaction since the protostar’s equation of motion is not being integrated properly. In order to explore the effect of the protostar/disk interaction, I implemented the indirect potential described in detail in [§2.3](#). In this chapter, I present the results of that simulation and compare it to previous results using a fixed central star. In [§4.1](#) an overall qualitative comparison is made, in [§4.2](#) I look at the stellar motion in more detail and corresponding behaviors in the disk and in [§4.3](#) I compare the detailed torques, α s and periodograms.

4.1 General Comparisons

For this comparison I used the G1.7TC2P0.5 disk, hereafter referred to as the fixed simulation, described in [§3.2](#). After changes were made to the code to include the indirect potential, I started the run from the initial disk with the same 2 ORP cooling time and 0.01% amplitude of initial random hit. I also used the same $1 M_{\odot}$ star and $0.14 M_{\odot}$ disk. Overall the outcome was fairly similar. The disk with the indirect potential included went through the same phases as the fixed star disk. The onset of the burst phase occurred around 4.5 ORPs with the initial burst being predominately five-armed and transitioning to a predominately three-armed structure. The transition phase began near 7.0 ORPs and continued through the asymptotic phase which began around 11.0 ORPs. The simulation continued to 19.5 ORPs; see the right panels of [figure 4.1](#) for a comparison of the final midplane densities of each of

the disks.

In this comparison, one can see that the structures in the indirect simulations appear to be a bit less well defined, probably owing to weaker GI activity as measured by integrated Fourier amplitudes. One can also see that the system center of mass, indicated by the white x in figure 4.1 has not moved very far from the center of the grid. So allowing the star to move did not result in a large motion of the center of mass. Additionally, as can be seen in figure 4.2, the final azimuthally-averaged surface density profiles showed very little difference. Assuming the surface density profile is a power law $\Sigma \propto \varpi^{-p}$, a least squares fit for p between 15 and 40 AU gave 2.33 and 2.31 for the indirect and fixed cases, respectively. Also, the Toomre Q values, plotted for several different times for both disks in figure 4.3, are similar for each of the simulations with $1.5 > Q > 1$ in the asymptotic phase. Overall Q -values may have been slightly smaller for the indirect simulation.

Despite the similarities there were some noticeable differences. First, the burst in the indirect disk was weaker than that of the fixed disk. This can be seen in the Fourier amplitudes, when A_m is summed over m from 1 to 64. For the time period between 4.5 and 11 ORPs, the maximum summed amplitude was 5.8 in the indirect case as opposed to 7.6 in the fixed case. The mean of the summed amplitudes over this time interval was also lower at 2.1 compared to 2.7 in the fixed case. Additionally, as can be seen in the left panels of figure 4.1, the mode dominating the midplane density structure is a five-armed spiral instead of a four-armed spiral.

This trend continued throughout the asymptotic phase with the mean value of the summed amplitudes being 2.2 in the indirect case compared to 2.7 in the fixed case averaged over the interval from 12 to 19.5 ORPs. Figure 4.4 shows the full range

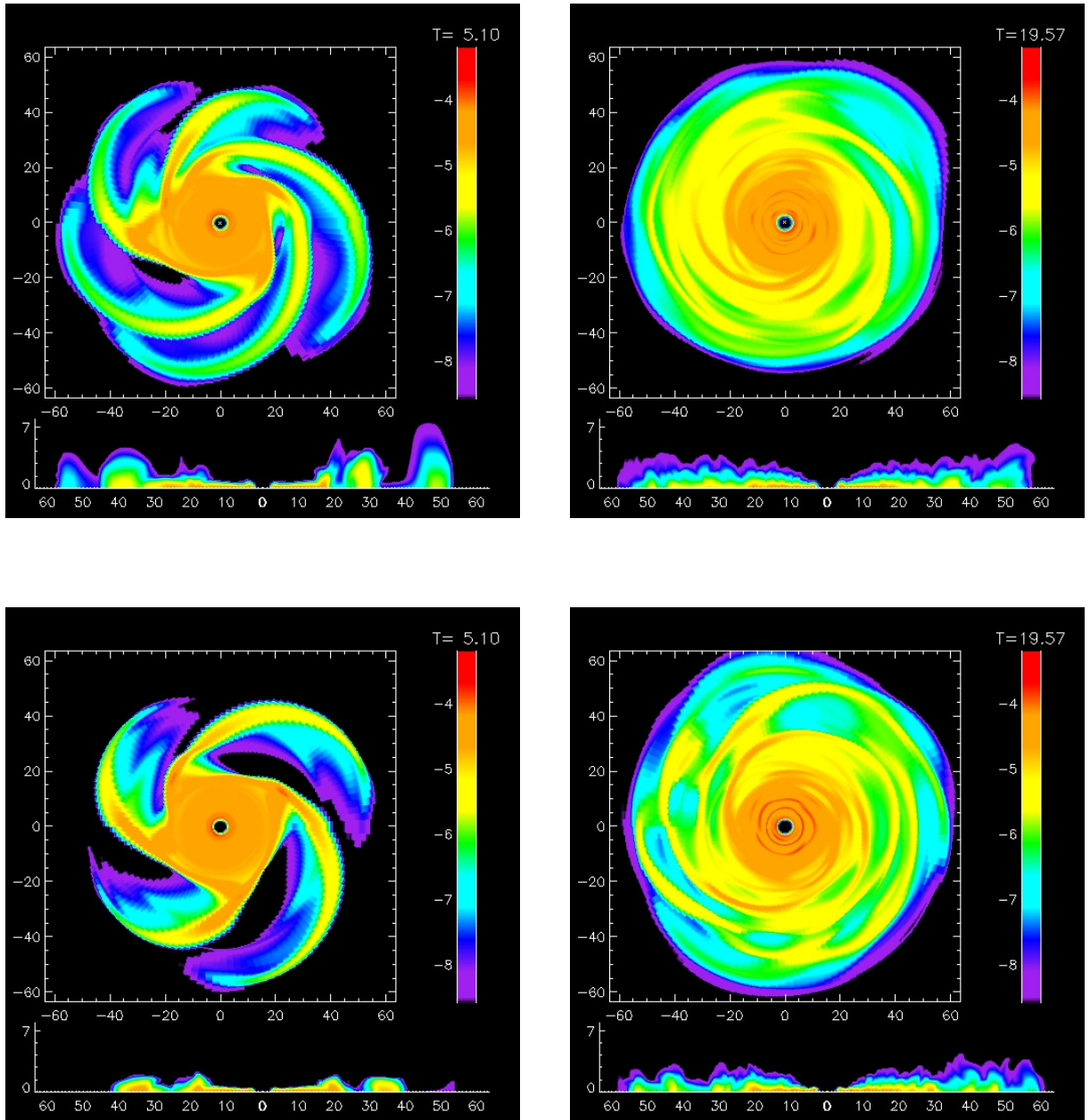


Figure 4.1: *Midplane densities in logarithmic scale of the indirect (top) and fixed (bottom) simulations. The axes have units of AU and the time is given in ORPs. The small white x in the indirect panel is the position of the system center of mass (disk plus star). In both panels the star is at the center of the grid. The left-hand panels show the saturation of the initial growth in the burst phase. The right-hand panels are representative of the asymptotic behavior.*

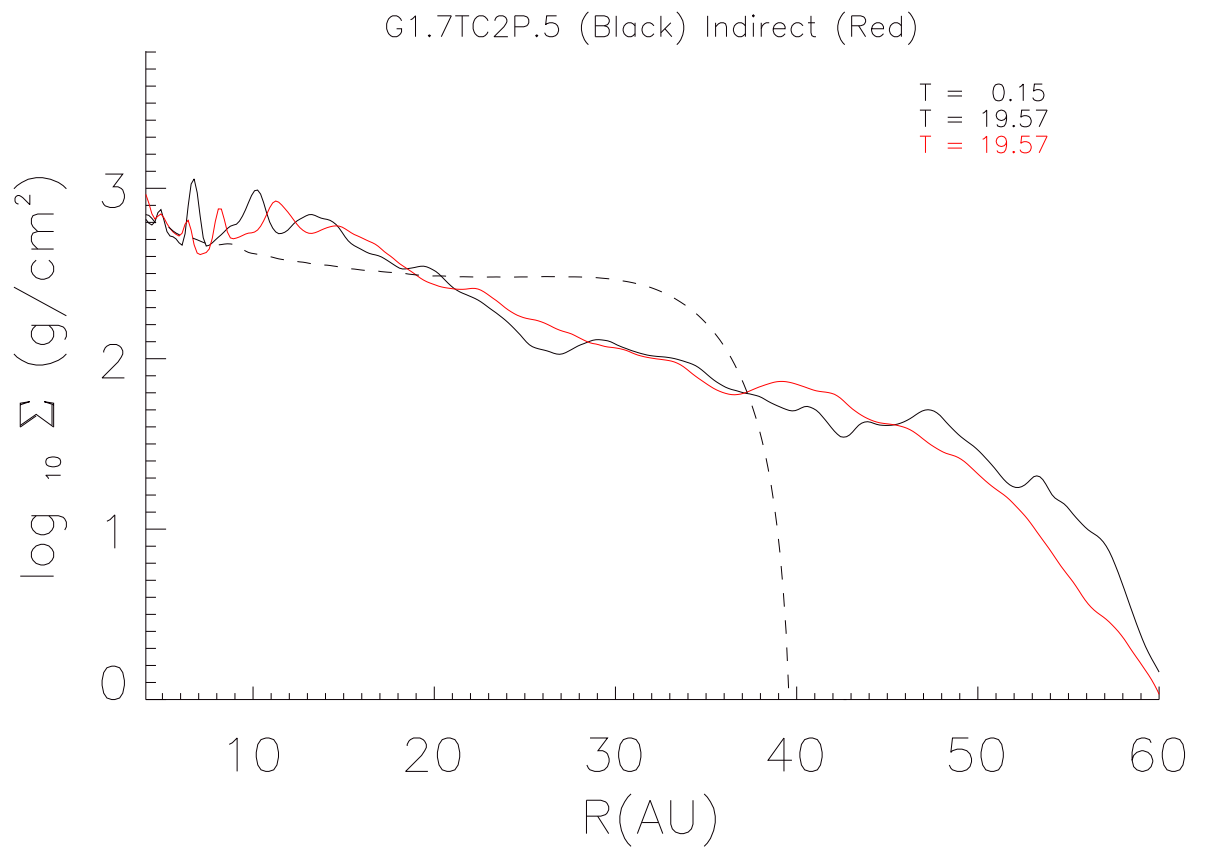


Figure 4.2: Surface densities in logarithmic scale of the indirect (red) and fixed (black) simulations. Times are measured in ORPs.

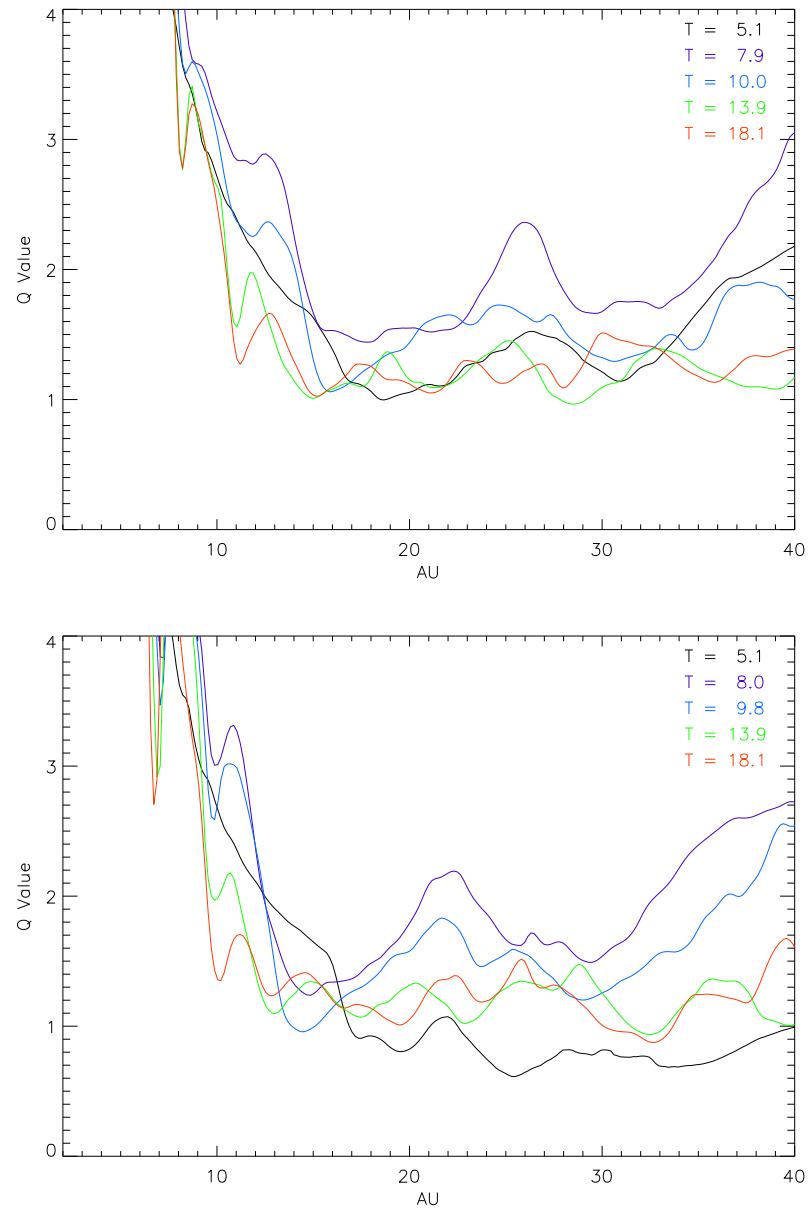


Figure 4.3: Toomre Q for the indirect (top) and fixed (bottom) simulations plotted at several times. Q values are shown at approximately $t = 5, 8, 10, 14$ and 18 ORPs. Overall the indirect simulations exhibit slightly higher Q values, indicating weaker GI activity.

of m values over this time. The “error bars” on each of the points indicate the RMS fluctuations over the sampling interval. It should be noted that the number of data points used to compute the averages, as well as the RMS fluctuations were different for each of the runs. In the indirect case 801 files were used while in the fixed case 504 files were used. This was mainly due to the difference in time step length and is not thought to cause major differences in the RMS fluctuations.

Figure 4.5 compares the mass transport during both the burst phase and the asymptotic phase. Overall, the addition of stellar motion did not affect the general outcome of GI activity, although it did produce a measurable weakening of the GIs.

4.2 Detailed Motion

Due to my treatment of the stellar motion via the indirect potential, the motion of the star was not calculated explicitly in the simulation. In fact, by definition the star remained at the center of the grid because the simulation is performed in its frame. By looking at the system center of mass (COM), one sees the inverse of the stellar motion. Figure 4.6 shows both the motion of the system COM for the duration of the simulation, as well as the COM radial motion versus time. I calculated the maximum radial excursion of the center of mass to be 0.24 AU and its mean distance from the star to be 0.11 AU for the time period between 4 and 19.5 ORPs.

This result is somewhat striking because it is at odds with previous simulations performed by Rice et al. (2003a), hereafter RABB, who found a maximum radial excursion of $\sim 5 \times 10^{-3}$ AU. There are several key differences in my simulations

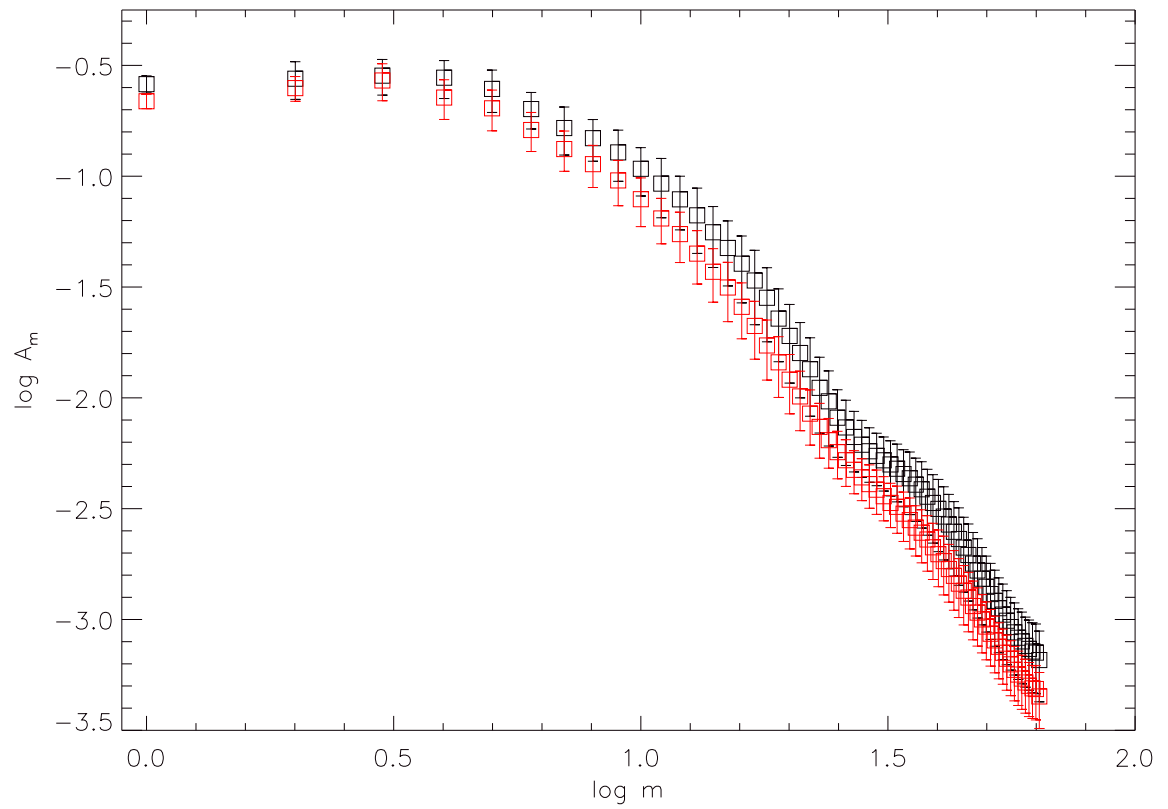


Figure 4.4: Comparison of indirect (red) and fixed (black) $\langle A_m \rangle$ values for each m averaged from 12 to 19.5 ORPs. The error bars represent the RMS of the fluctuations over this time period.

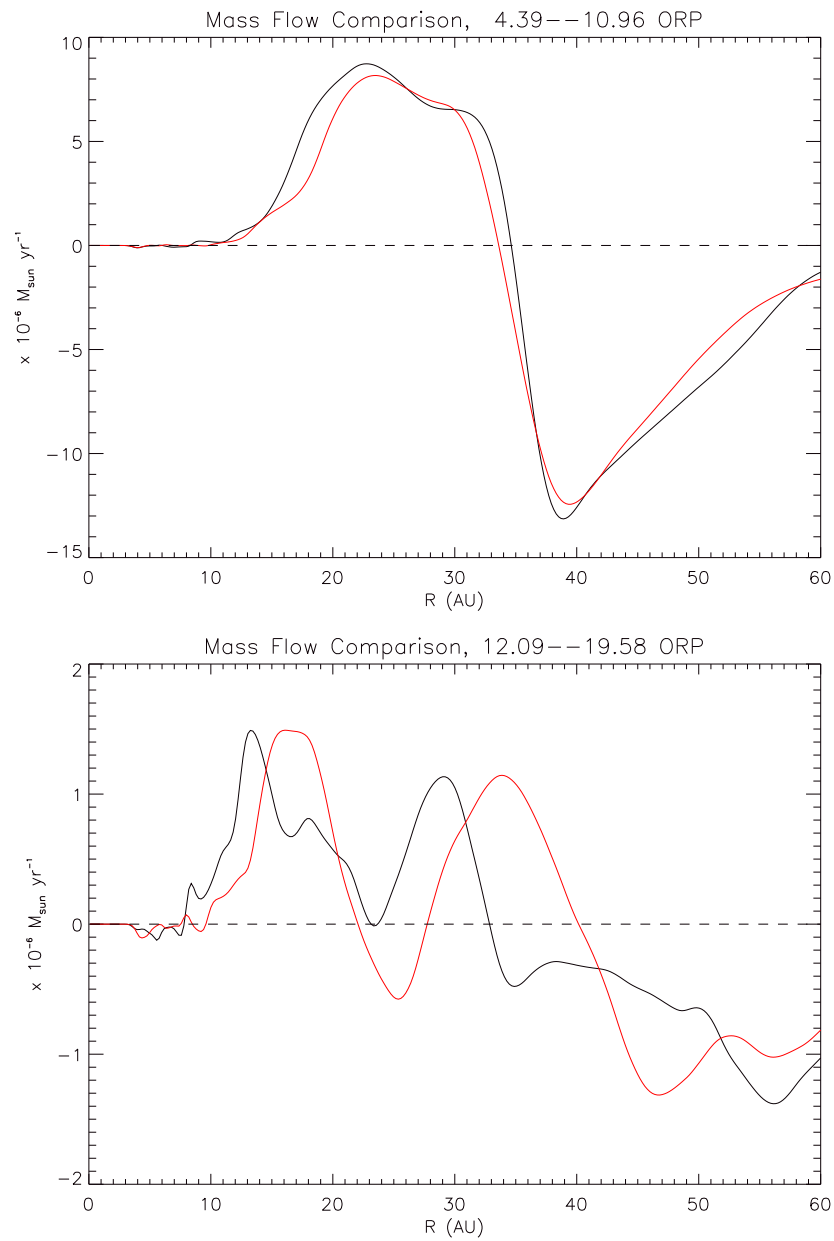


Figure 4.5: Mass transport rates in solar masses per year plotted during the burst (top) and asymptotic (bottom) phases. The red curve represents the indirect simulation, the black curve is the fixed simulation and the dashed line represents no mass flow.

and those of RABB. First, my simulations were carried out on a Eulerian grid, while RABB's used SPH. Another key difference is that instead of using a global cooling time which applied to the entire disk, RABB used a local cooling time which is tied to the local orbital speed, in their case, $t_{\text{cool}} = 5\Omega^{-1}$ or $t_{\text{cool}} = 10\Omega^{-1}$. Using this cooling prescription has the effect of shortening the cooling time with decreasing radius. Due to this, the innermost parts of the RABB disks had extremely short cooling times and were violently GI unstable. This drove large accretion rates causing the inner 2 AU of mass to be accreted onto the central star. The outcome of this transport could vary significantly depending on the treatment of the linear and angular momentum of the material as it is added to the star.

My simulation did not exhibit a large accretion rate onto the central body because, like other constant cooling time simulations, the inner disk stayed gravitationally stable. Figure 4.6 shows the COM motion from 0 to 12 ORPs in black and 12 to 19.5 ORPs in red. The black depicts the COM motion starting at $t = 0$ through the burst and transition phases, while the red shows the asymptotic phase. In the burst phase, one can see that the COM went through its largest excursion from the origin. This may, in fact, have been transient SLING behavior. However once the disk entered the asymptotic phase the COM excursion decreased in amplitude but remained non-negligible. From 12 to 19.5 ORPs the mean distance from the star was 0.09 AU. By constructing a Lomb-Scargle periodogram (Lomb 1975; Scargle 1982) of the COM positions, I determined the periodicity of the stellar motion. Figure 4.7(a) shows the Lomb-Scargle periodogram power of the radial motion measured between 12 and 19.5 ORPs. If I assume that the most powerful signal is due to the star's primary orbit, I arrive at a pattern speed of 0.72 ORP. If such a system were

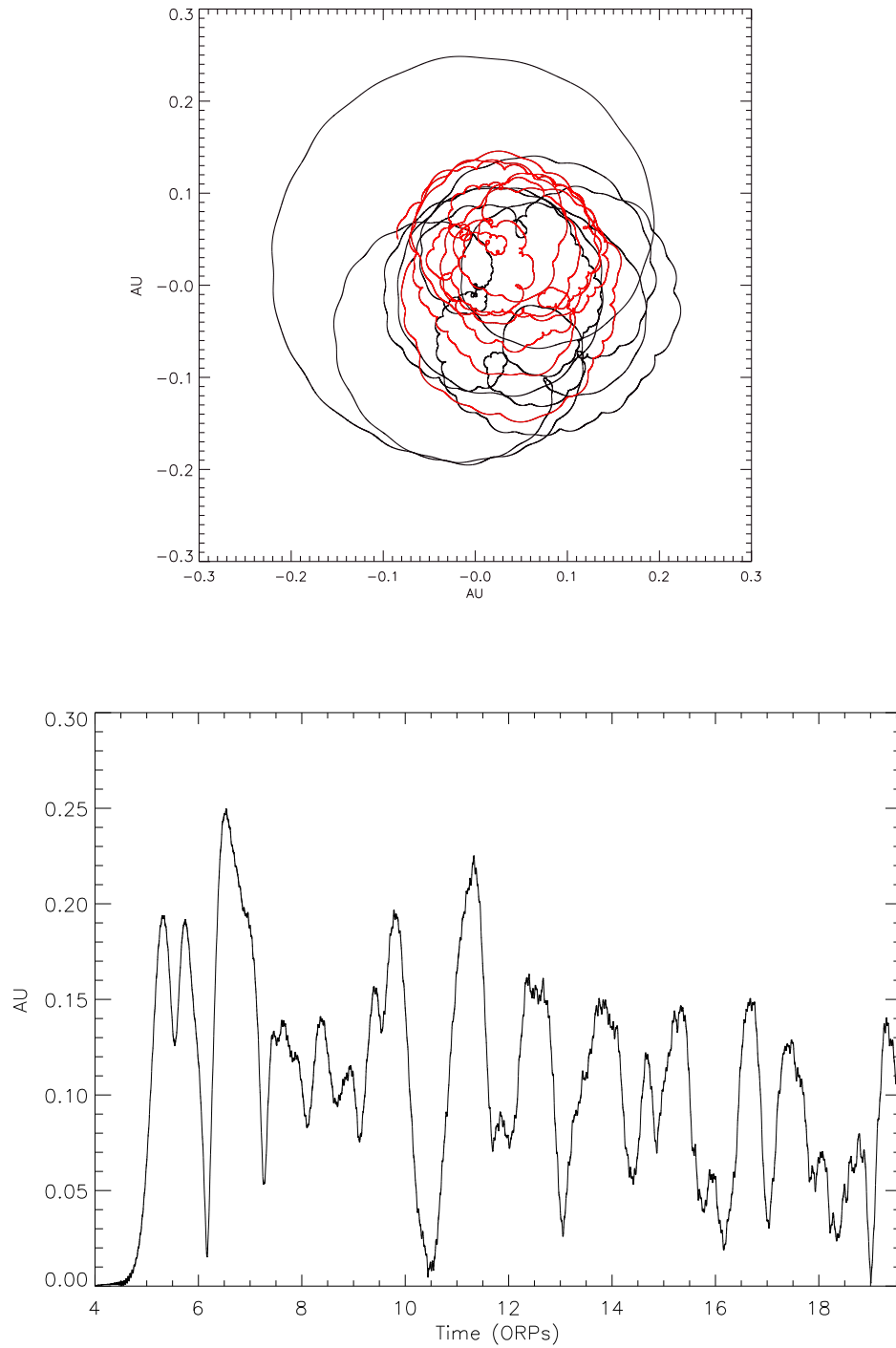
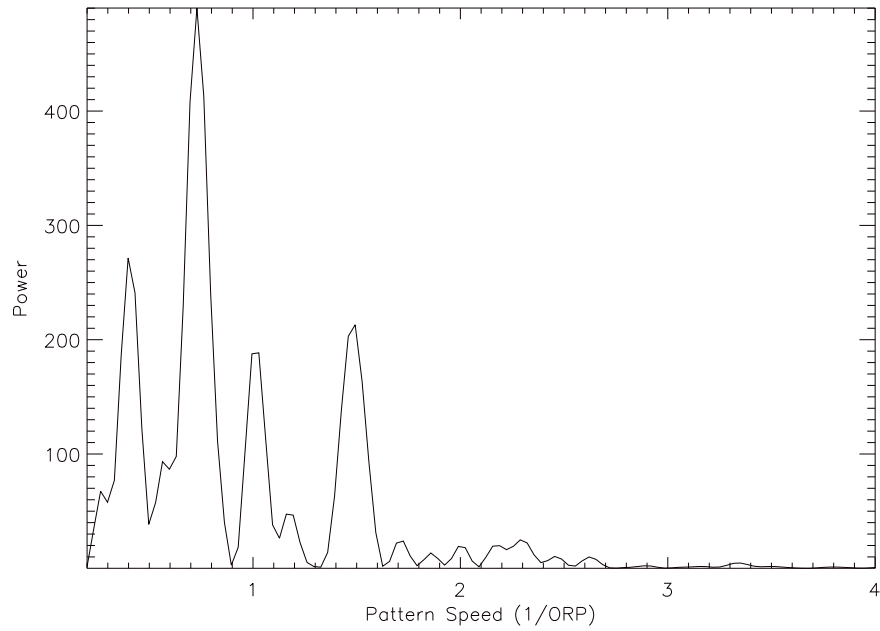


Figure 4.6: Plot of the system COM motion in the x - y plane (top), both axes are labelled in AU, and system COM radial excursion (bottom) for the duration of the simulation, the radial excursion is labelled in AU and time in ORPs.

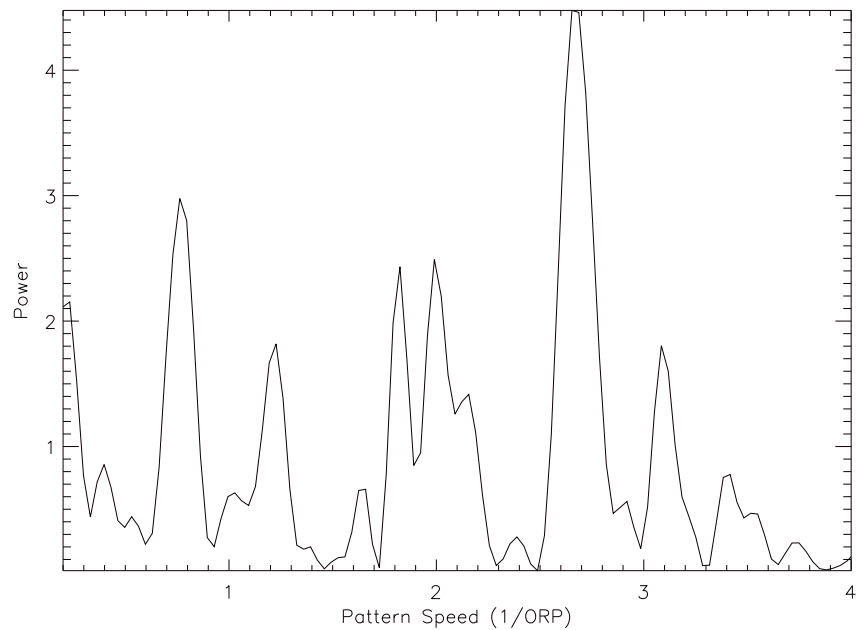
located at a distance of 100 pc, this would yield a proper motion of $\sim 16\mu\text{as/yr}$. To confirm the presence of this signal, I performed several tests. I sampled the data at several different rates, although I stored the data for each time step. Calculating a periodogram from the full 250,000 time step data set proved to be too compute intensive. I sampled the data at 50, 200, 500, and 1000 time step intervals and found the same pattern in each. As I increased the sampling frequency the features became sharper and more well defined as expected. Figure 4.7(a) shows results from the 50 time step sampling.

I also tested for a signal in a random rearrangement of the data. I took the data which produced the signal in figure 4.7(a) and randomly reassigned the radius values to a time step. I then produced a periodogram which is presented in figure 4.7(b). One can see that there is no clear signal. I also obtained periodograms for the x and y motion of the COM as shown in figure 4.8. They exhibit a periodicity similar to the ϖ motion. For each of these cases, I also calculated the false alarm probability, F , (Horne & Baliunas 1986) where the quantity $1 - F$ is the probability that the data contain a signal. For the r , x , and y motions $1 - F$ was $\gg .99999$. For the random resampling of the r data $1 - F$ was 0.24.

From the large motions exhibited by the system COM and therefore by the star in the inertial frame, one can clearly see that there was an appreciable amount of angular momentum transferred between the disk and the star. Figure 4.9 shows the star's angular momentum and torque produced by the star/disk interaction. These quantities are calculated by taking a five point numerical derivative in time of the system COM values. This gives system COM velocities which were used to compute the star's angular momentum. I then computed another five point derivative of the



(a) Lomb-Scargle periodogram of radial motion.



(b) Lomb-Scargle periodogram of randomized radial motion.

Figure 4.7: *Lomb-Scargle periodogram power of the radial motion of the COM. The power scale in this case is arbitrary, only relative power is important. These periodograms have been generated using data from 12 to 19.5 ORPs.*

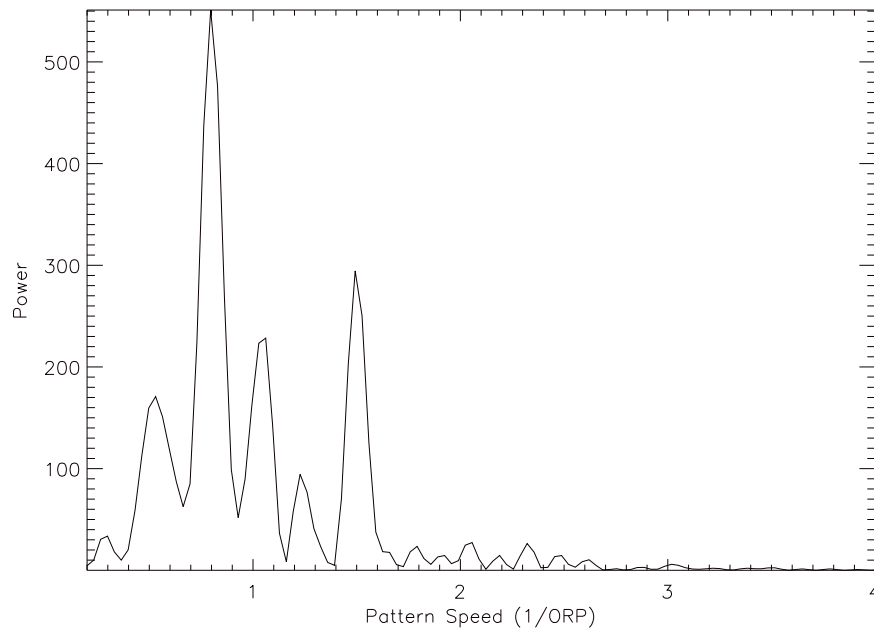
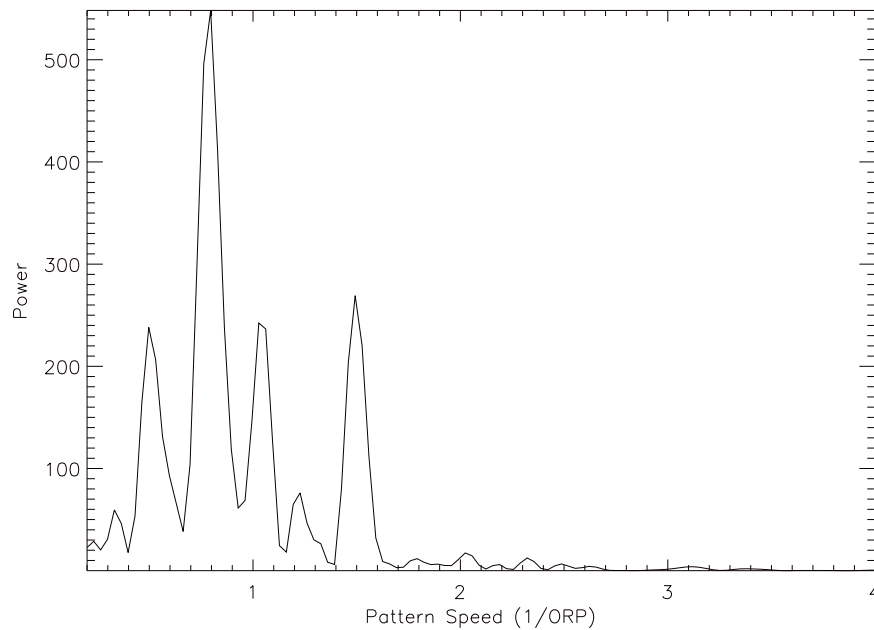
(a) Lomb-Scargle periodogram of x motion.(b) Lomb-Scargle periodogram of y motion.

Figure 4.8: Lomb-Scargle periodogram power of the x and y motion of the COM. The power scale in this case is arbitrary, only relative power is important. This periodogram has been generated using data from 12 to 19.5 ORPs.

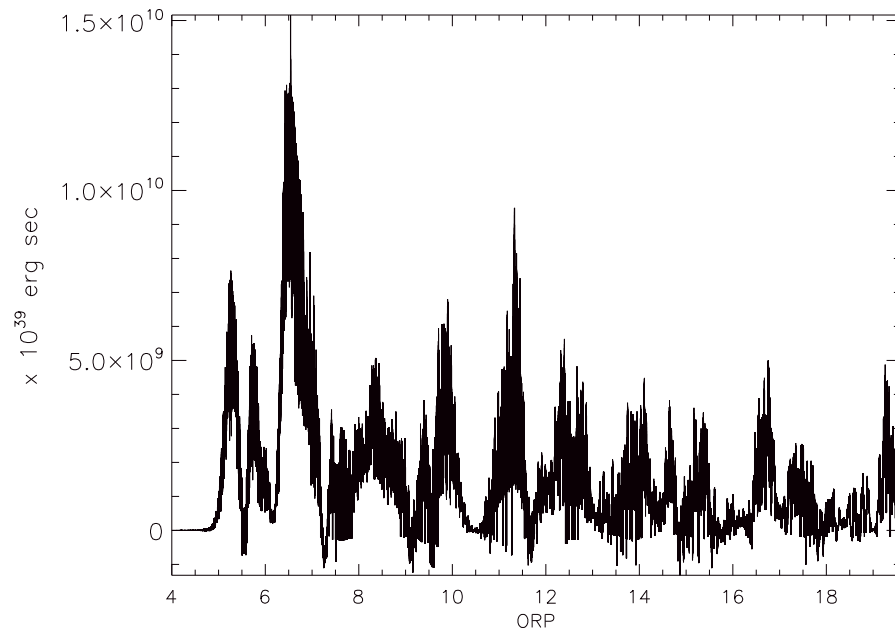
angular momentum to produce the torque. Clearly transfer of angular momentum caused the star's orbit to change in radius. Additionally, the torques measured are comparable to the gravitational torques measured in the disk (see §4.3 and figure 4.12). Although the instantaneous torques can be 10^3 larger in magnitude than the average disk gravitational torques, averaging the torque from 12 to 19.5 ORPs gives a value of 5.1×10^{38} ergs, which is the same order of magnitude as the average gravitational torques measured in the disk (figure 4.12). Since these torques were comparable, it would appear that the stellar motion should not be neglected.

4.3 Disk Analysis

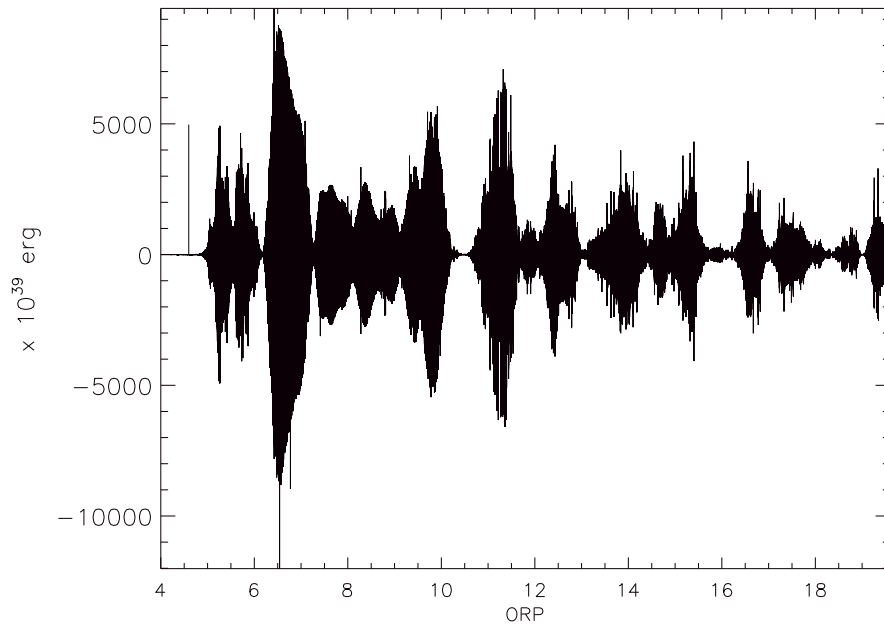
Although the general characteristics of the two simulations were similar, detailed analysis of the disk dynamics revealed that there were measurable differences between the two cases. Figure 4.4 shows that the Fourier amplitudes in the indirect simulation were smaller than the fixed star simulation. Another important characteristic of an m -armed spiral structure is the coherence of the pattern.

4.3.1 One-armed Structure

I first examined the $m = 1$ patterns in the indirect simulation. In this case, $m = 1$ is important because interactions between the star and $m = 1$ structure can amplify the $m = 1$ pattern via the SLING mechanism (Adams et al. 1989; Shu et al. 1990). Figure 4.10 shows the periodograms for $m = 1 - 4$ for the indirect simulation, while figure 4.11 shows them for the fixed simulation. It does not seem that $m = 1$ had any stronger radially coherent patterns in the indirect simulation. This indicates that



(a) Stellar angular momentum as a function of time.



(b) Torque exerted on the star as a function of time.

Figure 4.9: Plot of the stellar angular momentum and torque as a function of time, measured using the motion of the system COM.

sustained SLING amplification was not present during the asymptotic phase of the indirect simulation. Additional evidence to support this claim may be found in figure 4.12, which divides the contribution to the disk torque into its various components. One can see that the contribution from the $m = 1$ component is negligible. I may not have seen evidence of SLING amplification due to the fact that even though it is a dynamic effect, SLING has a rather long growth time, and the integration times may have been too short to detect its growth. However, it is also possible that SLING was simply not operating, due to the fact that our disk was fairly low mass compared to those considered by Adams et al. (1989). These findings confirm the conclusions of Noh et al. (1992), who found that for low-mass disks the growth of $m = 1$ patterns was due mainly to swing amplification and contributions from the indirect potential.

Although there was no sustained growth of an $m = 1$ pattern due to SLING amplification, it is possible that a transient episode of SLING took place during the burst phase. As can be seen in figure 4.6, the most rapid growth of radial motion occurred during the burst and transition phases from 4.5 to 11.0 ORPs. Indeed, the black curve in figure 4.6 shows the great looping excursions from the origin which occurred during the burst phase.

4.3.2 Disk/Star Interaction

Although the motion of the star did not induce sustained $m = 1$ growth, the star apparently did have a strong interaction with the disk. The first clues of this interaction come from comparing strong periods in the COM x and y periodograms and

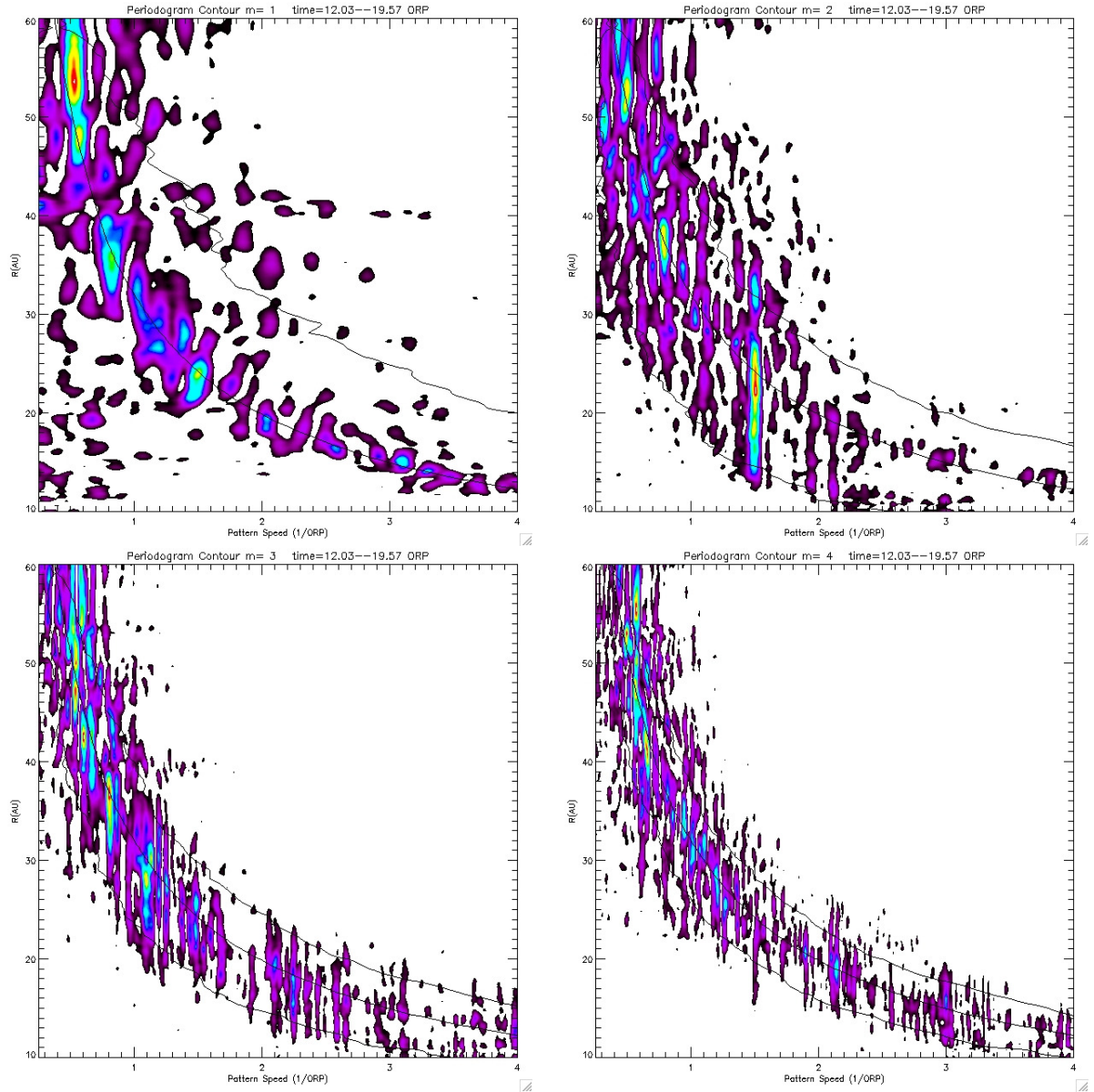


Figure 4.10: *Periodograms for the indirect simulation measured using data from 12 to 19.5 ORPs, $m = 1 - 4$ are presented here. The color scale represents relative power with purple being the smallest and red/white being the largest, in this case the relative power is the important measure as opposed to the absolute numbers. The solid lines represent the outer Lindblad resonance, corotation, and inner Lindblad resonance radii, from top to bottom, for each m -value.*

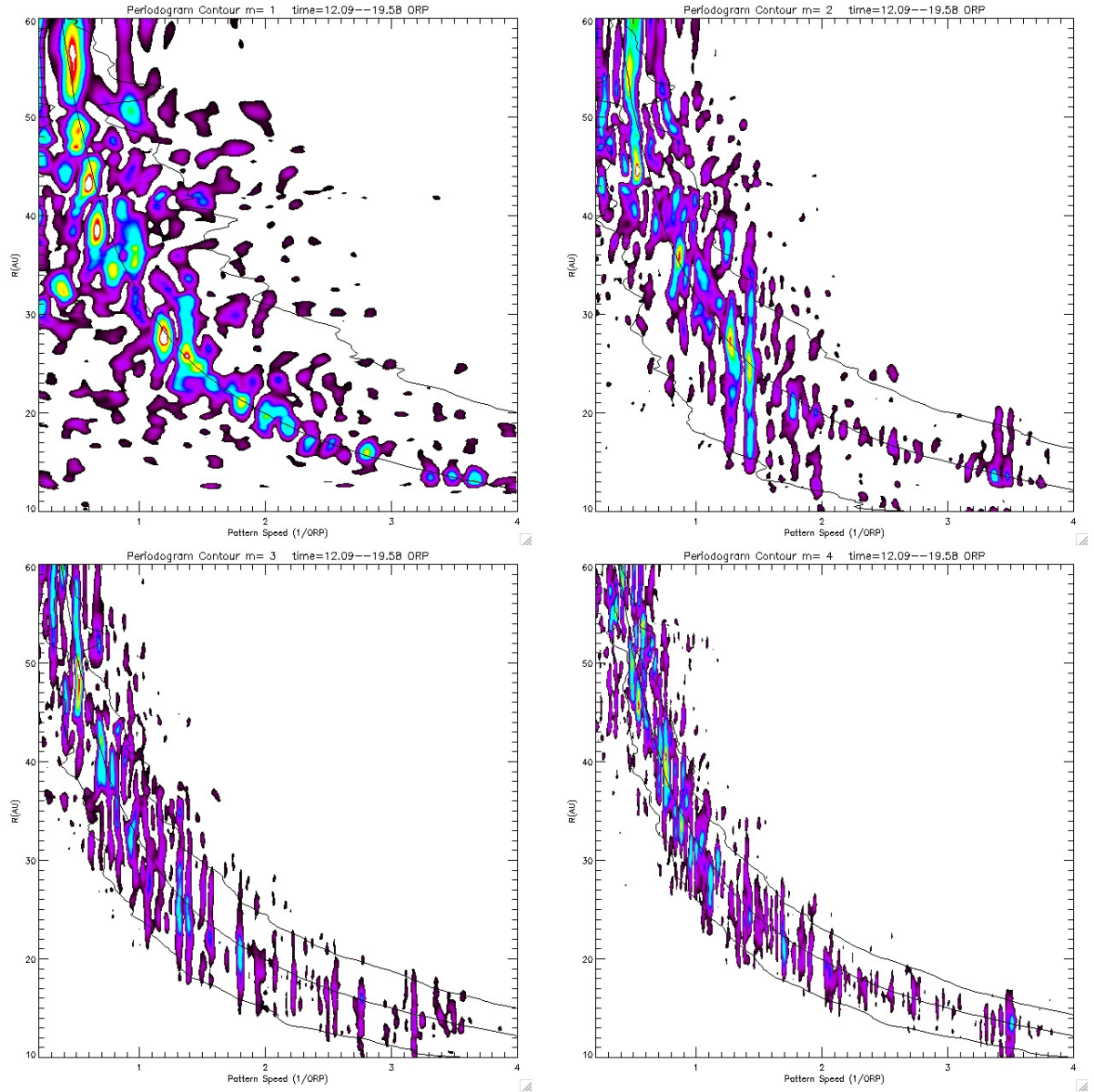


Figure 4.11: *Periodograms for the fixed simulation measured using data from 12 to 19.5 ORPs, $m = 1 - 4$ are presented here. The color scale represents relative power with purple being the smallest and red/white being the largest, in this case the relative power is the important measure as opposed to the absolute numbers. The solid lines represent the outer Lindblad resonance, corotation, and inner Lindblad resonance radii, from top to bottom, for each m -value.*

Table 4.1: *Pattern speeds of prominent periodogram features.*

Signal Measured	Pattern Speeds (1/ORP)			
COM x -motion	0.55	0.80	1.05	1.50
COM y -motion	0.51	0.80	1.02	1.50
$m = 1$ Pattern	0.65	0.85	—	1.50
$m = 2$ Pattern	0.50	0.80	—	1.50
$m = 3$ Pattern	0.59	0.80	1.05	1.50

strong stripes of power in the disk periodograms. Table 4.1 compares the pattern speeds of the most prominent features in each of these periodograms. One can see that the periodicity in the x and y COM motion corresponds to coherent patterns in $m = 1, 2, 3$ at pattern speeds of 0.5, 0.8, and 1.50/ORP. The most striking of these features in the $m = 2$ and 3 periodograms is the one at a pattern speed of 1.50/ORP. It also has the best agreement among all the measured signals. The effects of this star/disk interaction can be seen in the disk torque as well. Figure 4.12 compares the gravitational torque of the disk on itself for several m -values. Clearly, the disk torque is decreased in the indirect simulation when compared to the fixed simulation. Specifically we see a sharp decrease at 23.5 AU which corresponds to the corotation radius of a pattern with pattern speed 1.50/ORP. One can also observe the torque maximum at 19AU, which is particularly prominent in all m values corresponds to the inner Lindblad resonance of a $m = 3$ pattern with pattern speed 1.50/ORP.

The structure of the torque profile is clearly different from the fixed simulation in that it is weaker overall and significantly weaker at the corotation of major $m = 2$ and 3 features which share a periodicity with the COM motion. The decrease in disk torque was most certainly due to the disk/star interaction as is evidenced by the strong periodicity at the torque minimum seen in the periodograms of figure 4.10.

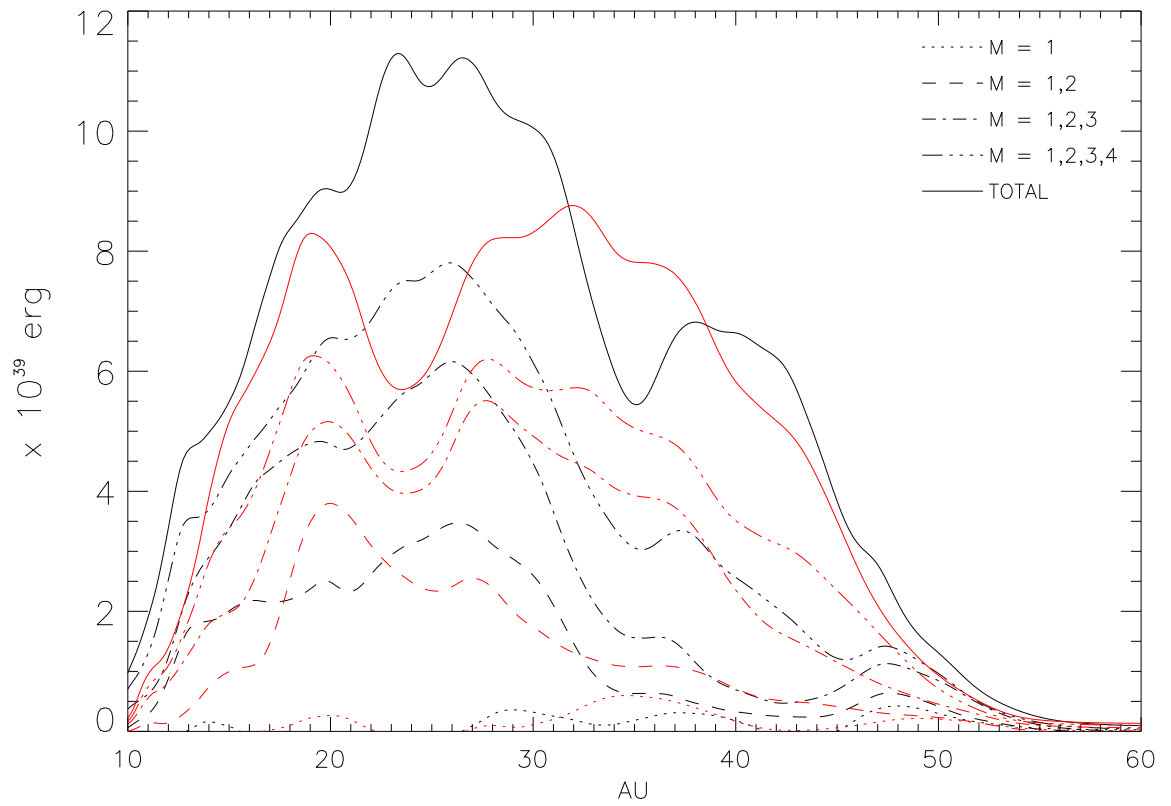


Figure 4.12: Torque profiles averaged from 12 to 19.5 ORPs for the indirect (red) and fixed (black) simulations.

All $m > 1$ values in figure 4.10 show a significant stripe of power which intersects corotation at 24 AU, corresponding to the torque minimum. Additionally, when examining the difference in torque between the indirect and fixed cases, one finds that the decrease in disk torque is comparable to the torque on the star as measured in figure 4.9(b). Figure 4.13 shows the difference of the disk torques in the fixed star and indirect simulations. In fact, the time averaged torque from 12 to 19.5 ORPs on the star was 5.1×10^{38} ergs, while the difference in disk torques averaged over the same time interval and averaged from 10 to 60 AU was 9.0×10^{38} ergs. Apparently, some of the torque, which was confined to the disk in the fixed star case, was transferred to the star when the star was allowed to move.

Even though the differences in disk structure introduced by the star’s motion were measurable in the torque profiles and periodograms, the overall mass transport in the disk was largely unaffected as can be seen in the mass transport rates in figure 4.5. Another metric of mass transport is the effective gravitational α , which is plotted for both the fixed and indirect simulations in figure 4.14. Figure 4.14 also shows the predicted Gammie (2001) curves for a fully self-gravitating and non-self-gravitating disk for $t_{cool} = 2$. Although the indirect potential α was smaller than the fixed-star α , it followed the overall trend of the fixed-star α . The decrease in α is consistent with the decrease in torque. One can notice that the inclusion of stellar motion brought the measured α somewhat closer to the predicted Gammie α . Perhaps the combination of stellar motion and increased angular resolution, which also acts to decrease the measured α (see §3.4), would bring the measured α into further agreement with Gammie’s prediction. However, as noted in §3.4, one cannot accurately predict the detailed disk structure based on an α model, nor can one

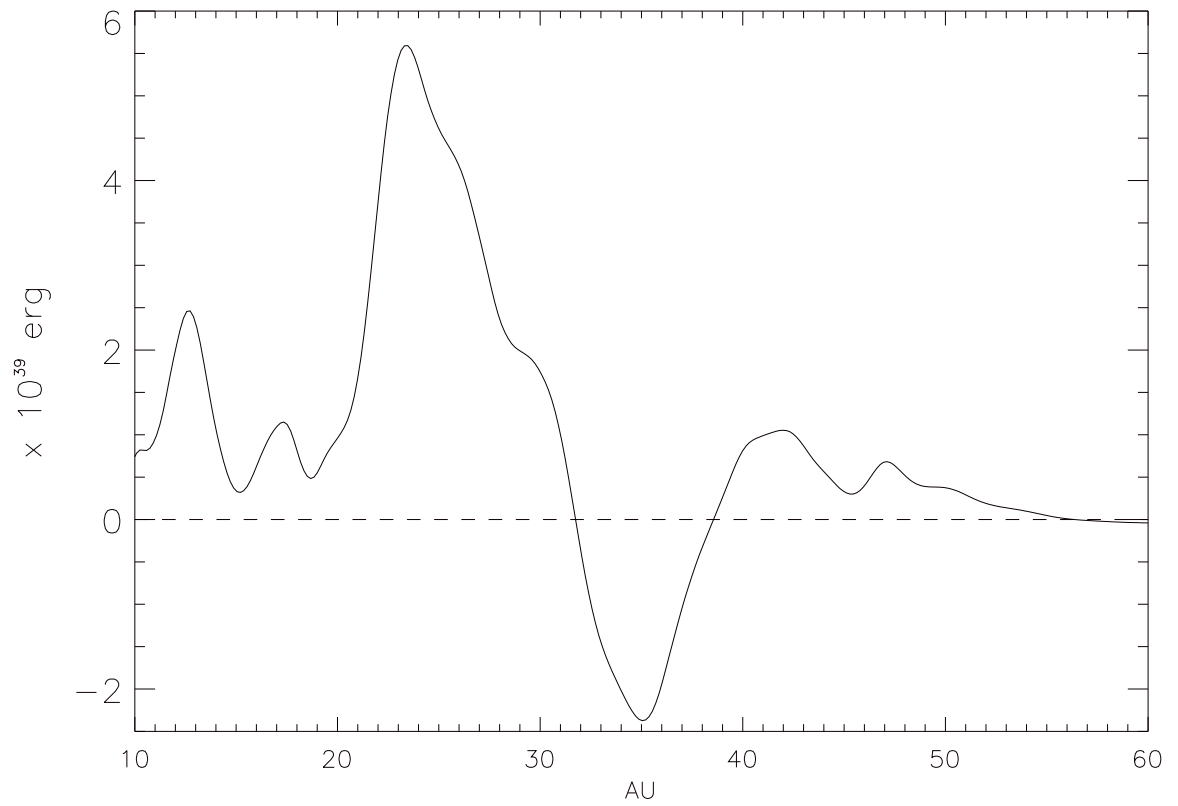


Figure 4.13: *The difference (fixed – indirect) between the torque profiles averaged from 12 to 19.5 ORPs for the indirect and fixed simulations.*

predict the asymptotic phase t_{cool} in a fully radiative disk based on initial conditions (see also [Johnson & Gammie \(2003\)](#)).

4.4 Conclusions

In this chapter I have shown that the inclusion of stellar motion in our three dimensional radiative hydrodynamic simulations has a measurable, but not drastic, effect on the structure of a gravitationally unstable protoplanetary disk. Although the gross features such as surface density profile, midplane density structure, $\langle A_m \rangle$ values, and mass transport rates remained largely unchanged in this comparison, one can see that the motion of the central star was not negligible, as previously reported by [Rice et al. \(2003a\)](#), and there is a relationship between changes in the disk self-torque and the star/disk interaction. Clearly, there is a strong correlation between the periodic motion of the star caused by torque exerted by the disk and the periodicity in the spiral patterns for $m = 1 - 4$, which can be seen by studying Figures [4.8\(a\)](#), [4.8\(b\)](#), [4.10](#), and [4.11](#) as well as table [4.1](#). There is certainly a complex interaction and feedback between the disk and star which gives rise to this correlation. Further study is required to determine the nature of this feedback and its sensitivity to various simulation parameters such as cooling time (and thereby GI strength), initial surface density profile, and star to disk mass ratio.

Overall the net effect of the star/disk interaction is to introduce a new degree of freedom to the system which allows some of the force that previously went into disk self-torque to be applied to the star/disk torque. This, in turn, slightly lowers the strength of the $\langle A_m \rangle$ values, disk torques, and α . Additionally, the star/disk torque

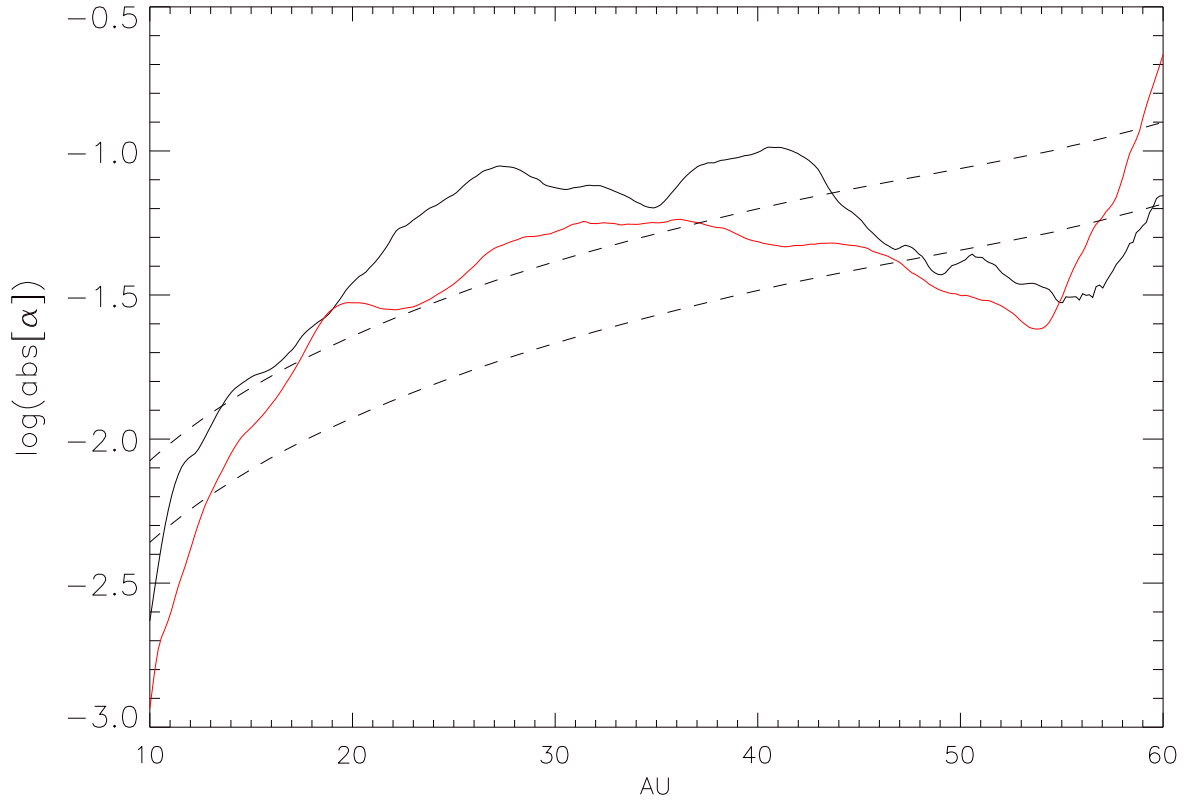


Figure 4.14: Effective Shakura-Sunyaev α -values computed for the fixed star (black curve) and indirect (red curve) simulations averaged over the asymptotic phase from 12.5 to 19 ORPs. Shown for comparison are curves predicted by *Gammie* with $t_{\text{cool}} = 2$ ORP. The upper curve assumes a self-gravitating disk; the lower curve assumes gravity is due to the star alone. For $Q \approx 1.3$, we expect the disk to be significantly self-gravitating.

increases the stellar angular momentum and, since we assume it is all converted to orbital angular momentum, changes the star's orbit substantially.

Chapter 5

Planet-Disk Interactions and Planet Migration

*I am a leaf on the wind.
Watch how I soar.*

– Hoban 'Wash' Washburn, *Serenity*

To extend the work presented in chapters 3 and 4, I performed a series of simulations that explore the interplay between a GI active disk and a massive planet. In this chapter, using algorithms described and tested in §2.4, I explore the effect a massive planet can have on the onset of GIs, and how GI activity in a protoplanetary disk can affect the migration of the planet. I also investigated how the planet's mass affects the interaction by simulating several planet masses.

5.1 Planet Simulations

Overall I considered seven simulations in the planet-disk interaction study: a fiducial run with no planet, which I will refer to as the BASELINE, three calculations with a planet included in the initial disk, and three calculations where a planet was inserted into the disk after GI activity was underway. All cases started with a resolution of $(\varpi, \phi, z) = (256, 512, 32)$; the ϖ and z grid dimensions were doubled to expand the grid when the disks went through the burst phase so that mass was not lost from the grid.

The BASELINE simulation used an initial disk identical to the G1.7TC2P0.5 disk from chapter 3 (see table 3.1), except that the disk material inside 5 AU was removed. The ≈ 2 AU hole was expanded to 5 AU because the Boley radiative routines are subject to numerical instabilities when the disk is poorly resolved in the vertical direction (Boley et al. 2007a). Since the initial disk has an aspect ratio of $H/\varpi \approx 0.1$, by increasing the radius of the inner hole, the vertical resolution at the inner edge was increased as well. The removal of this material had very little effect on the total disk mass; it represented a decrease of only 3%.

In addition to the small change in the initial disk, the BASELINE disk and the disks including planets were evolved using several different physics algorithms from the simulations in chapters 3 and 4 (see table 2.1). All simulations in this chapter received an initial perturbation with an amplitude of $\xi = 0.0001$ and used the indirect potential, described in §2.3 and chapter 4. In detail, the major differences are as follows. The disks in this chapter used the Boley radiative routines, outlined in §2.2.3 and described in detail by Boley et al. (2007a), to compute the cooling of a particular cell, while simulations from previous chapters used the constant cooling approximation from §2.2.1. A maximum grain size of 1 micron was used to determine the opacities; see Cai et al. (2006) for a discussion on the effects of maximum grain size on the evolution of GIs. The disks were also evolved using a more realistic H_2 equation of state instead of the ideal gas equation of state with fixed ratio of specific heats from equation (2.5) that was used in the simulations from chapters 3 and 4. As discussed in §3.5, simulations using a fixed γ used either $\gamma = 7/5$ or $5/3$. However, fixing the adiabatic index to one of these values may gloss over important phenomena, especially near regions in the temperature range where the first adiabatic index of

the gas, Γ_1 , is transitioning from $\Gamma_1 = 7/5$ to $5/3$. Of particular interest is the Γ_1 in regions affected by shock induced heating from GIs.

[Boley et al. \(2007b\)](#) describe in detail some of the potential inaccuracies in different treatments of the H_2 equation of state, and propose a method for accurately representing it. This approach was used for the simulations in this chapter. One of the difficulties with this approach is determining the appropriate mixture of ortho-hydrogen to para-hydrogen. Figure 1 of [Boley et al. \(2007b\)](#) shows the dramatic variation of Γ_1 for different choices of the ortho/para ratio. The appropriate value to use for a typical protoplanetary disk is not well known, although the ratio has been studied for various astrophysical conditions ([Osterbrock 1962](#); [Decampli et al. 1978](#); [Flower & Watt 1984](#); [Sternberg & Neufeld 1999](#); [Fuente et al. 1999](#); [Flower et al. 2006](#)). An approximate timescale for ortho- and para-hydrogen species to equilibrate is ≈ 300 yr ([Boley et al. 2007b](#)). This is longer than the dynamical timescale throughout the disk (1 ORP ≈ 180 yr), so it is unlikely that the ortho/para ratio is an equilibrium mix. For these simulations, I adopted a fixed ortho/para ratio of 3:1 because this is the statistical ratio with which H_2 is assumed to form on cold grains ([Flower et al. 2006](#)).

5.1.1 Inserting Planets Into the Disk

To study how GIs affect planet migration in an active disk, I performed three simulations with planets of varying masses. These planets were inserted at 10.5 ORPs after the initial burst of GI activity had subsided and GIs appeared to be in a quasi-steady state. In order to study the maximal interaction between GIs and the planet, I at-

tempted to place the planet at the corotation radius of the dominant global $m = 2$ mode. Analysis of the disks from chapter 3 coupled with preliminary findings from the BASELINE simulation indicated that the corotation radius of the $m = 2$ mode in a disk without a planet was ≈ 25 AU.

I inserted planets with masses of 0.3, 1, and 3 M_J , where M_J is one Jupiter mass, at a cylindrical radius of 25 AU at the time of 10.5 ORP in the BASELINE calculation. The planets were inserted in the disk midplane, and, because the simulations have reflection symmetry about the midplane, the vertical force on the planet is always zero. The planets were given an initial circular velocity determined by treating the star plus the disk mass at $\varpi < 25$ AU as a point mass at the grid center. I carried out each of these simulations to > 20 ORPs, resulting in ≈ 1800 yr of simulation time with the planets included. I will refer to each of the simulations by the planet mass and the time of planet insertion (e.g. 0.3JUP10ORP refers to the simulation including a planet of 0.3 M_J added at 10.5 ORP).

In addition to inserting planets into disks which were already GI active, I performed three simulations where I inserted planets into the initial equilibrium disk. Using these simulations I was able to explore how the presence of a planet affected the onset of GIs. As in the asymptotic phase simulations, I performed three simulations with planets of varying mass. The planets were again inserted at a cylindrical radius of 25 AU in the disk midplane with a circular velocity calculated in the same manner as the simulations with planets inserted at 10.5 ORPs. As with the $t = 0$ disks, I will refer to each of the simulations by the planet mass and the time of planet insertion (e.g. 0.3JUP0ORP refers to the simulation including a planet of 0.3 M_J added at 0 ORP). I will refer to the cases in which the planet was inserted

into the initial equilibrium disk as the initial disk simulations collectively, while the simulations where the planet was inserted at 10.5 ORPs will be referred to as the asymptotic phase simulations.

The planets were treated as smoothed point masses, see equation (2.20), and do not accrete mass from the surrounding disk. The smoothing length was set to 20% of the planet's Hill radius for all simulations. Accretion from a planetary disk to a planet is a complex process in a laminar disk where disk material entering the Hill sphere of the planet is expected to form a circumplanetary disk and to accrete onto the planet through this disk. The accretion rate through the circumplanetary disk and the rate at which material can accrete onto the planet are determined by local disk properties. Additionally, it is unclear whether a circumplanetary disk can form in a GI-active region.

The assumption of a non-accreting planet can be explained by two possible physical scenarios. The GI-active disk environment in which the planet is embedded is not, strictly speaking, in hydrostatic equilibrium, so material inside the Hill sphere may be forced outside of it by the action of the GIs. Although some material is sure to become gravitationally bound, it may be an extremely small amount due to the turbulent behavior of the surrounding disk. Another known possibility is that the Kelvin-Helmholtz time of the atmosphere surrounding the planet is longer than the migration time (Helled et al. 2006). In this case, the planet cannot accrete additional material from the surrounding disk since the atmosphere cannot contract rapidly enough. This may be the case if the atmosphere is built up while the central planet maintains a low luminosity, which could be caused by large opacity (Hubickyj et al. 2005). In accreting and non-accreting comparison simulations performed by

Nelson et al. (2000b), the non-accreting planet migrated inward more rapidly during an initial gap forming phase but slowed after a couple thousand orbit periods (see figure 4 from Nelson et al. (2000b)).

5.2 Migration in Laminar Disks

As described in §1.3.3, when an object in a protoplanetary disk becomes massive enough that forces due to gas drag are negligible, it may migrate in a laminar disk by type I, type II, or type III migration. Although the mechanisms driving each of these types of migration vary, the characteristic that determines which type of migration will occur is the ability of the object to form a gap in the protoplanetary disk. Besides the criterion that tidal torques exceed viscous torques for gap formation (see equations (1.5) and (1.6)), another possibility for gap opening is that the disk response to tidal forcing from the embedded object becomes nonlinear. A sufficient condition for nonlinearity through shock formation is (Korycansky 1999)

$$\frac{m_p}{M_\star} > \left(\frac{H}{\varpi}\right)^3. \quad (5.1)$$

Although none of the disks I considered are laminar because they are all susceptible to GIs, one can consider whether the inserted planets would form a gap if the disks were laminar. The $3 M_J$ planet is most likely to open a gap; its Hill radius is 2.5 AU, which is roughly equal to the disk scale height at 25 AU. As this is a borderline case, either equation (1.5) or equation (1.6) might apply. For equation (1.5) we have,

$$0.4 \gtrsim \alpha. \quad (5.2)$$

Estimates for α in protoplanetary disks vary widely, but most researchers agree on an effective $\alpha \leq 0.1$, which would mean that the $3 M_J$ planet should open a gap if the disk scale height is greater than the planet's Hill radius. On the other hand, if the disk scale height is less than the planet's Hill radius, the criterion becomes

$$\frac{R_H}{\varpi} \gtrsim \zeta \alpha. \quad (5.3)$$

This is most likely not the case as $\zeta \sim 0.25$ and $\alpha \leq 0.1$. However, the nonlinearity criterion of equation (5.1) is probably met since $\frac{m_p}{M_\star} = 0.003$ and $\frac{H}{\varpi} \approx 0.1$. In any case, the $3 M_J$ planet is near the gap forming limit but slightly above, the $1 M_J$ planet is right on the borderline, and the $0.3 M_J$ planet is near the limit but slightly below for a laminar disk. However, the analysis performed for laminar disks probably does not hold for GI active disks, as the viscous torque in a GI active disk is not properly described by equation (1.4), because of large spatial and temporal fluctuations in the gravitational torque driven by the GIs.

As outlined in §1.3.3, migration rates can vary dramatically depending on the type of migration an object is undergoing. To review briefly, type I migration occurs when no gap is opened in the disk, type II occurs when the object clears a gap in the disk, and type III occurs when a gap is only partially opened. Although the type I and type II migration mechanisms produce a more or less steady migration rate in a laminar disk, type III migration is a self-sustaining mechanism that results in runaway migration rates. Type III migration, first introduced by [Masset & Papaloizou \(2003\)](#), is highly dependent on the details of the flow inside the Hill radius of the embedded object but tends to have short migration timescales of order a few

hundred orbits. In type III migration, the embedded object opens a partial gap, and disk material that flows across the object’s orbit executes U-turns at the end of horseshoe orbits. As the orbital radius of the disk material changes, a torque is imparted to the embedded object that is proportional to its migration rate. This rate changes due to the torque and is increased in proportion to the co-orbital mass deficit δm (see equation (21) from [Masset & Papaloizou \(2003\)](#)), further accelerating the object’s inward migration. Since type III migration rates are determined by a nonlinear interaction between the disk, embedded object, and inter-gap flows, it is very difficult to predict migration rates. Simulations have been performed by [Lin & Papaloizou \(2010\)](#) and [Pepliński et al. \(2008a,b,c\)](#), who show that type III migration is a rapid, runaway process. At any rate, it is likely that the simulations presented in this chapter lack the radial and azimuthal resolution to accurately resolve the corotation torques and horseshoe orbits that drive type III migration.

If the mass of the embedded object is less than or comparable to the mass of the surrounding disk material that it is interacting with gravitationally, then type II migration rates can be estimated by looking at the timescale for the viscous evolution of the disk. In a steady state disk, the viscous migration timescale is given by,

$$\tau_{mig} \sim \frac{2\varpi_p^2}{3\nu}. \quad (5.4)$$

Here ϖ_p is the radius of the embedded object and ν represents the kinematic viscosity. Although there are no viscosity terms explicitly included in the code, if one uses the standard α prescription ([Shakura & Syunyaev 1973](#)), then one can write $\nu = \alpha H c_s$. However, it should be noted that it is important to consider the nature

of the effective viscosity. Although, in all likelihood, GIs do not produce an effective viscosity or effective α that is compatible with all of the assumptions made by [Shakura & Syunyaev](#), the effective α s determined in chapter 3 and 4 can be used to estimate the migration timescale crudely. Assuming $\alpha \approx 0.02$ (see figure 5.6) and $c_s = H\Omega$, and inserting into equation (5.4) results in a migration timescale of $\tau_{mig} \approx 2200$ ORPs (471,000 years) for a planet at a radius of 25 AU in a Keplerian disk.

If the embedded object is not massive enough to open a gap or partial gap, then type I migration will take place. Type I migration rates have been estimated for isothermal disks by [Tanaka et al. \(2002\)](#) and more recently for adiabatic disks by [Paardekooper et al. \(2010\)](#). [Paardekooper et al.](#) present the total torque on an embedded object in a non-isothermal disk as being composed of a Lindblad torque and a corotation, or horseshoe drag, torque. They present an analytical formula (equation (14) of their paper) for the Lindblad torque that approximately agrees with [Tanaka et al. \(2002\)](#). The formula for the corotation torque is quite complex, but mainly depends on the local entropy and vortensity gradients. In addition, results from [Paardekooper et al.](#) assume unsaturated torques and low-mass planets. Because it is unclear whether the corotation torques are modelled accurately by my simulations and calculation of the vortensity gradient is problematic, I will use the formula from [Tanaka et al. \(2002\)](#) to obtain a ballpark estimate of the timescale for type I migration.

Equation (70) of [Tanaka et al. \(2002\)](#) gives the type I migration timescale as

$$\tau_{mig} = (2.7 + 1.1q)^{-1} \frac{M_\star}{m_p} \frac{M_\star}{\Sigma_p \varpi_p^2} \left(\frac{c_s}{\varpi_p \Omega_p} \right)^2 \Omega_p^{-1}. \quad (5.5)$$

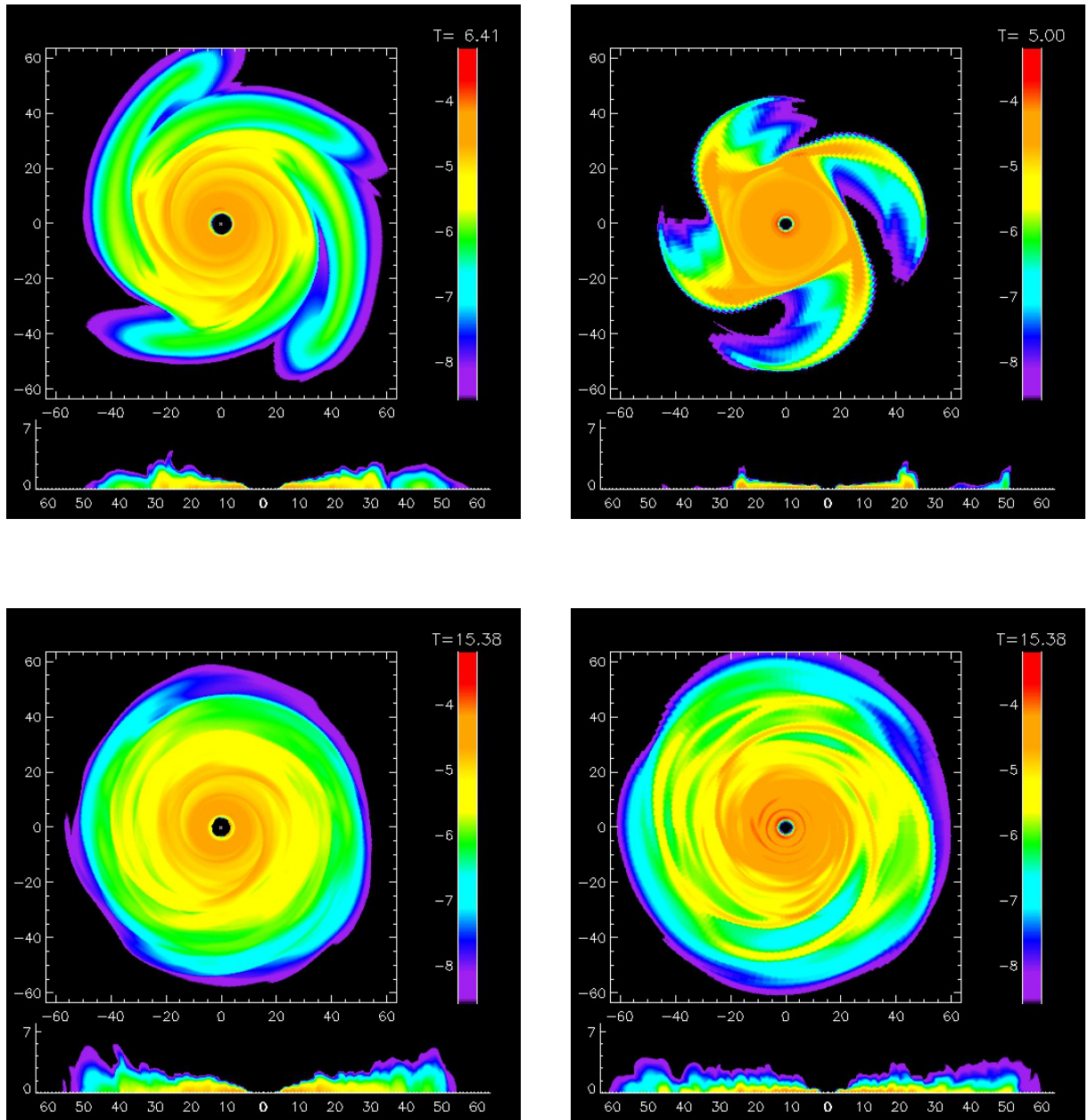


Figure 5.1: The midplane and meridional density contours are shown for both the *G1.7TC2P0.5* and *BASELINE* runs at two different times. The burst phase comparison, chosen at the burst peak, can be seen in the top two panels and the asymptotic phase comparison can be seen in the bottom two panels. The *BASELINE* run is on the left and *G1.7TC2P0.5* is on the right. Densities are plotted in code units on a logarithmic scale.

Here ϖ_p is the object radius, Σ_p is the surface density at that radius, Ω_p is the rotational frequency, c_s is the sound speed, and q is the index for the power law of the surface density distribution, i.e., $\Sigma = \Sigma_0 \varpi^{-q}$. Using values measured from the initial G1.7TC2P0.5 disk described in §3.2, I find that the migration timescale for a $1 M_J$ object at 25 AU is ≈ 20 ORPs (4,280 years). I also measured these values in the disk at 10.5 ORPs and found that the migration timescale for a $1 M_J$ object at 25 AU is $\approx 28.2/(2.7 + 1.1q)$ ORPs. The GI activity at this time made it difficult to accurately measure the power law index of the surface density distribution near 25 AU. However, if one assumes that $0.5 < q < 2.5$, this yields a range for the migration timescale of 5.2 – 8.7 ORPs (1,113 – 1,862 years). Estimates for the migration time scale inversely with the planet mass. In §5.4.2 and §5.5.2, I compare these estimates to migration timescales measured in the simulations.

5.3 The BASELINE Simulation

The BASELINE simulation was qualitatively similar to the G1.7TC2P0.5 simulation from chapter 3. The major differences between the setup of the simulations were the azimuthal resolution, the cooling algorithm, and the equation of state; the latter two are discussed in detail in §5.1. One can also find a detailed discussion about the effects of different cooling algorithms in Boley et al. (2006). Figure 5.1 shows, although qualitatively similar, that the density structures were measurably different in the burst and asymptotic phases. This section provides detailed analysis of the BASELINE run, as it is the fiducial run for comparison to the subsequent simulations with planets included. Where applicable, I provide comparisons to the constant

cooling case, G1.7TC2P0.5.

Clearly, when compared to the G1.7TC2P0.5 disk, the BASELINE disk had much more extended spiral arms and was more extended in the z direction at the onset of the burst. This, along with a slightly later burst onset, was due to the cooling time being longer when the cooling time is determined by using the radiative routines instead of setting a constant global cooling time (Boley et al. 2006). Figure 5.2 shows the column-wise cooling times for the BASELINE disk during the burst phase, the time period of 6 – 8 ORPs. One can see that, for the radial range from 10 – 30 AU, the cooling times are typically 3 – 4 ORPs, and that, only beyond 30 AU, do the cooling times drop to ≈ 2 ORPs. In addition, much of the structure was not as sharply defined (i.e., there was not as much density contrast in the spiral structures). This was also due to the typically longer cooling times seen when using radiative physics. Additionally, the increased azimuthal resolution tended to weaken low-order modes in favor of high-order ones (see chapter 3).

Figure 5.3 shows several midplane density snapshots of the BASELINE simulation. As in previous simulations, the disk began in the axisymmetric phase, underwent a burst of GI activity, and then transitioned to a quasi-steady state, the asymptotic phase. The burst was dominated by $m = 4$ and 5 which can be seen in the density structures in figure 5.3 and the time evolution of the non-axisymmetric amplitudes A_m in the top panel of figure 5.4.

For the purposes of analyses of the asymptotic phase, I use a time interval of 14 – 21 ORPs. During the asymptotic phase, the disk is evolving slowly in a quasi-steady state. By examining the internal energy in figure 5.5, one can see that the internal energy dropped during the axisymmetric phase, then increased during the

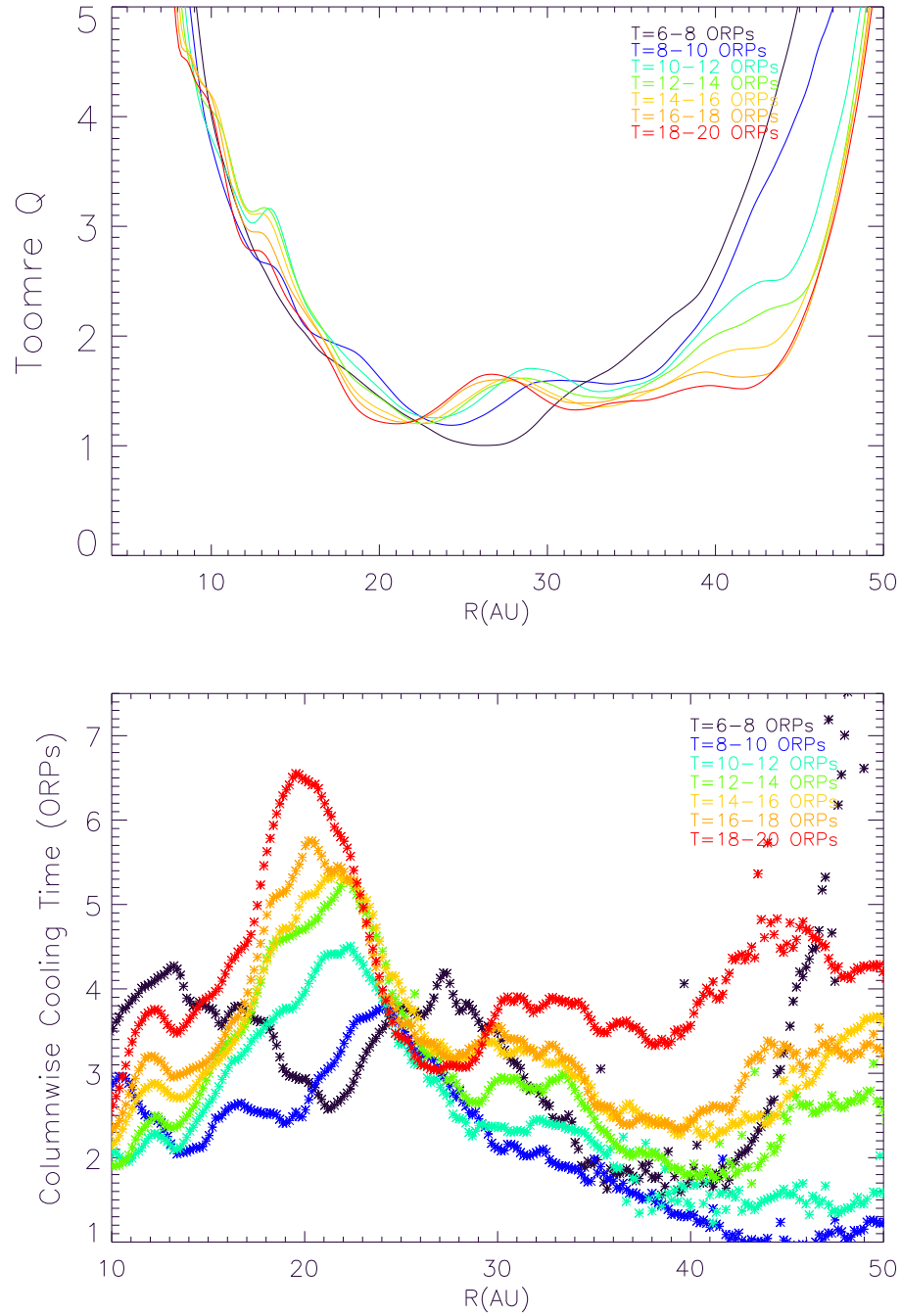


Figure 5.2: Plots show the azimuthally averaged midplane Toomre Q distribution (top) and column-wise cooling times (bottom) for a range of times throughout the asymptotic phase of the BASELINE simulation. Cooling times are calculated using equation (5.6). Values are averaged over several 2 ORP intervals.

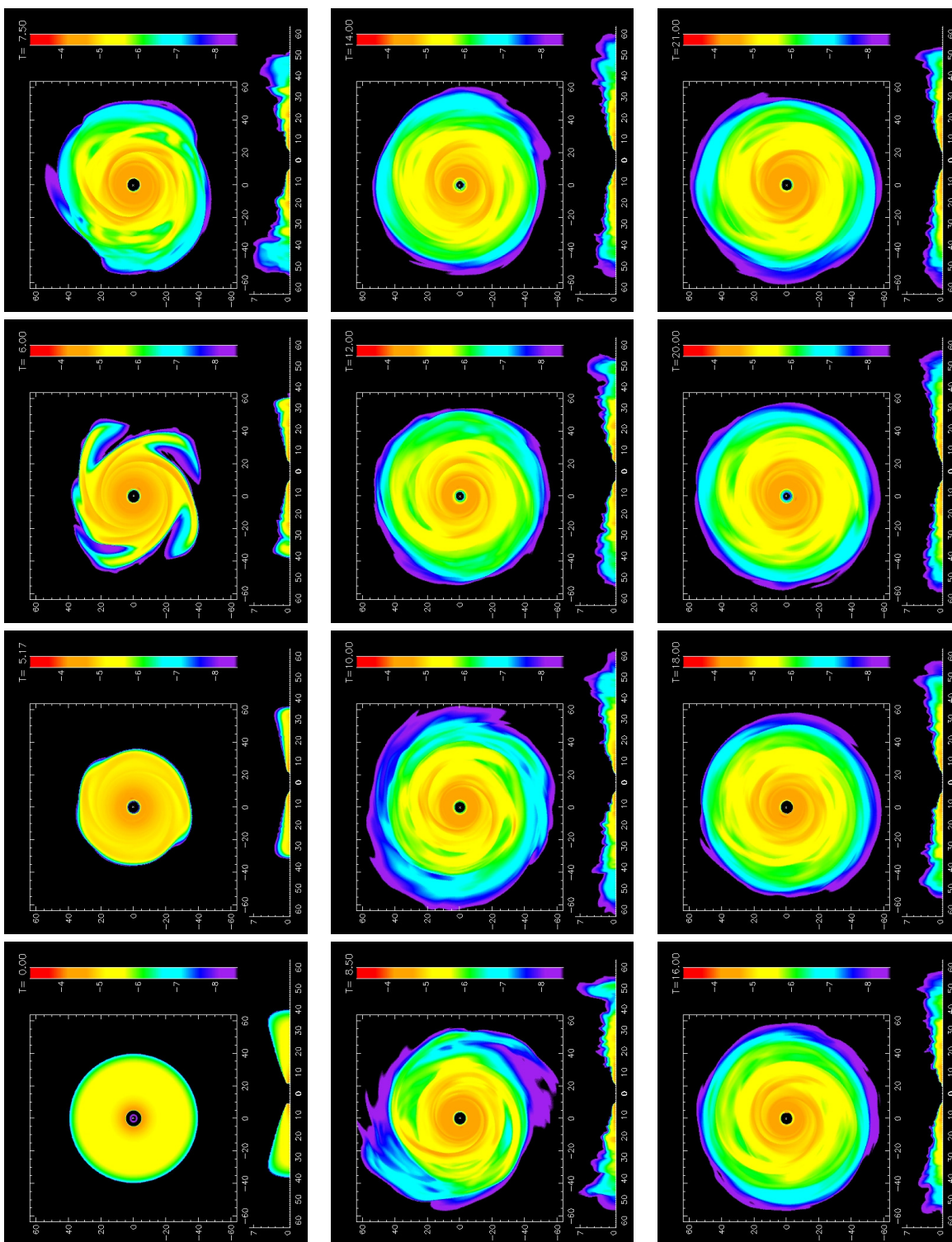


Figure 5.3: Midplane and meridional densities in logarithmic scale for several times in the BASELINE simulation. The axes have units of AU and the time is given in ORPs in the upper right of each panel. The series starts at $t = 0$ ORPs and proceeds left to right and top to bottom to the end of the simulation at ≈ 21 ORPs.

burst phase and varied a bit during the transition phase. Here the internal energy was calculated by simply summing the ϵ of all of the cells in the disk. By 14 ORPs it had settled down but continued to evolve slowly. The top panel of figure 5.2 shows the azimuthally averaged Toomre Q values averaged over 2 ORP intervals. As with previous Toomre Q plots, I assumed $\kappa = \Omega$. By looking at the Toomre Q values in figure 5.2, one can see that the Toomre Q has settled into a roughly steady state by 14 ORPs.

The asymptotic phase of the BASELINE run was dominated by low-order modes. The $\langle A_m \rangle$ values, averaged from 14 to 21 ORPs, are displayed in figure 5.4. These values show the typical spectrum of amplitudes, with fairly small rms deviations. The summed value of the amplitudes $\langle A_\Sigma \rangle = 1.43$ (see table 5.1), which is slightly smaller than the values seen in the simulations from §3.4. This is most likely due to the difference in cooling algorithms used. The top panel of figure 5.6 shows the torque profile of the disk as a function of radius averaged from 14 to 21 ORPs. The torque was dominated by low-order modes ($m = 1 - 4$), which is similar to the analysis of previous disks. The torque shows a particularly strong peak near 23 AU. This is mirrored in the α plot in the bottom panel of figure 5.6. The bottom panel of figure 5.2 shows column-wise cooling times averaged over 2 ORP intervals for several intervals. The cooling time for a column was determined by summing the total internal energy of an annulus and dividing by the flux lost from that annulus. that is

$$t_{cool} = \frac{\int_0^\infty \int_0^{2\pi} \epsilon \, d\phi \, dz}{\int_0^\infty \int_0^{2\pi} \nabla \cdot \mathbf{F} \, d\phi \, dz}. \quad (5.6)$$

It is interesting to note that, at the region where the torque peaks, ~ 23 AU,

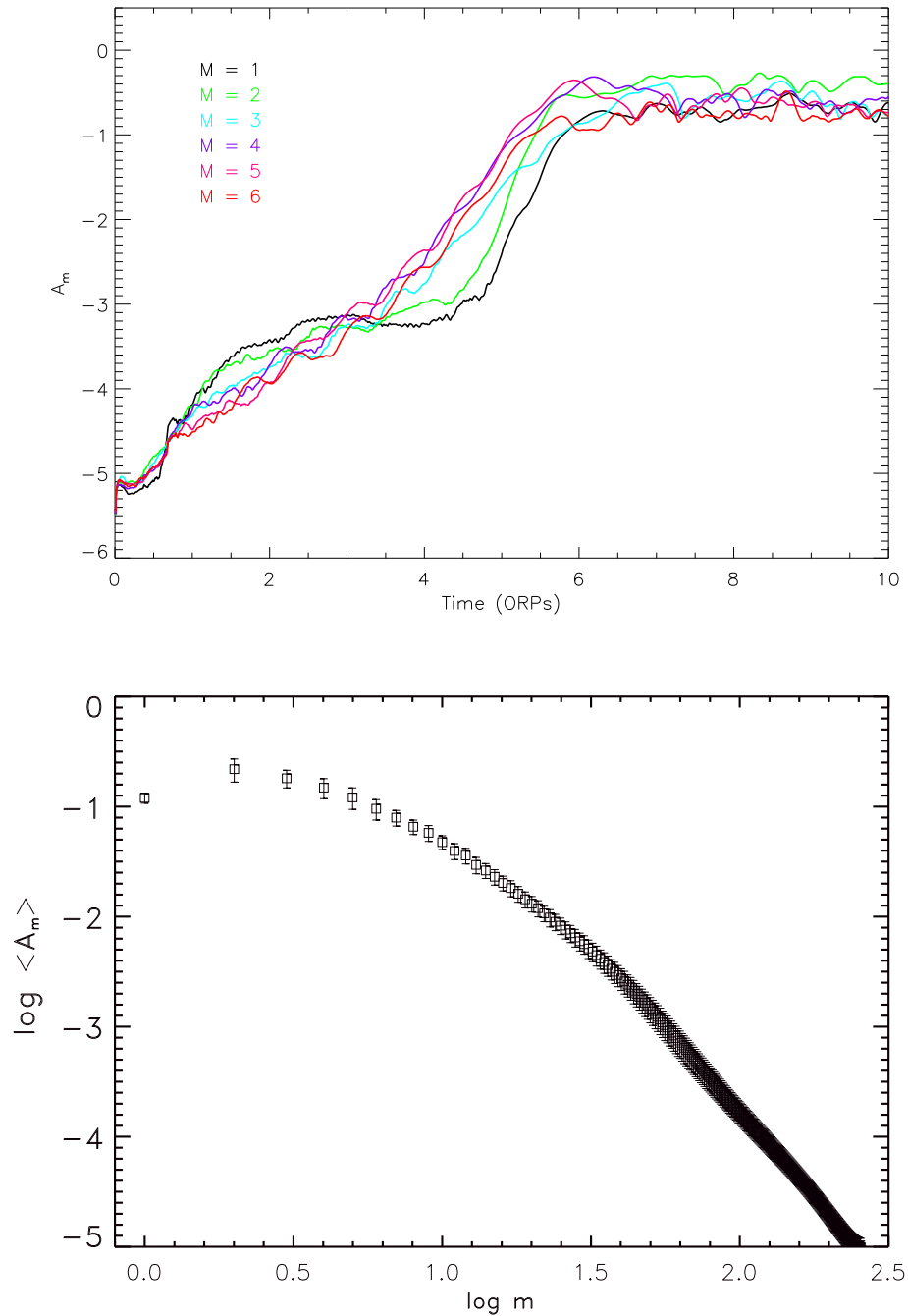


Figure 5.4: (Top) Fourier components A_m as a function of time for $m = 1 - 6$. The amplitudes are shown from the initial models through the asymptotic phase. Contribution to the A_m components is only calculated for $\varpi > 15\text{AU}$ due to contamination from a spurious $m = 1$ signal. (Bottom) Values of $\langle A_m \rangle$ for the BASELINE simulation. The $\langle A_m \rangle$ values are averaged over the interval 14 – 21 ORPs. Contribution to the $\langle A_m \rangle$ components is calculated for the entire disk. The “error bars” on each m -value represent the RMS fluctuations about the time-averaged mean. The plot depicts m -values from 1 to 256 on a logarithmic scale.

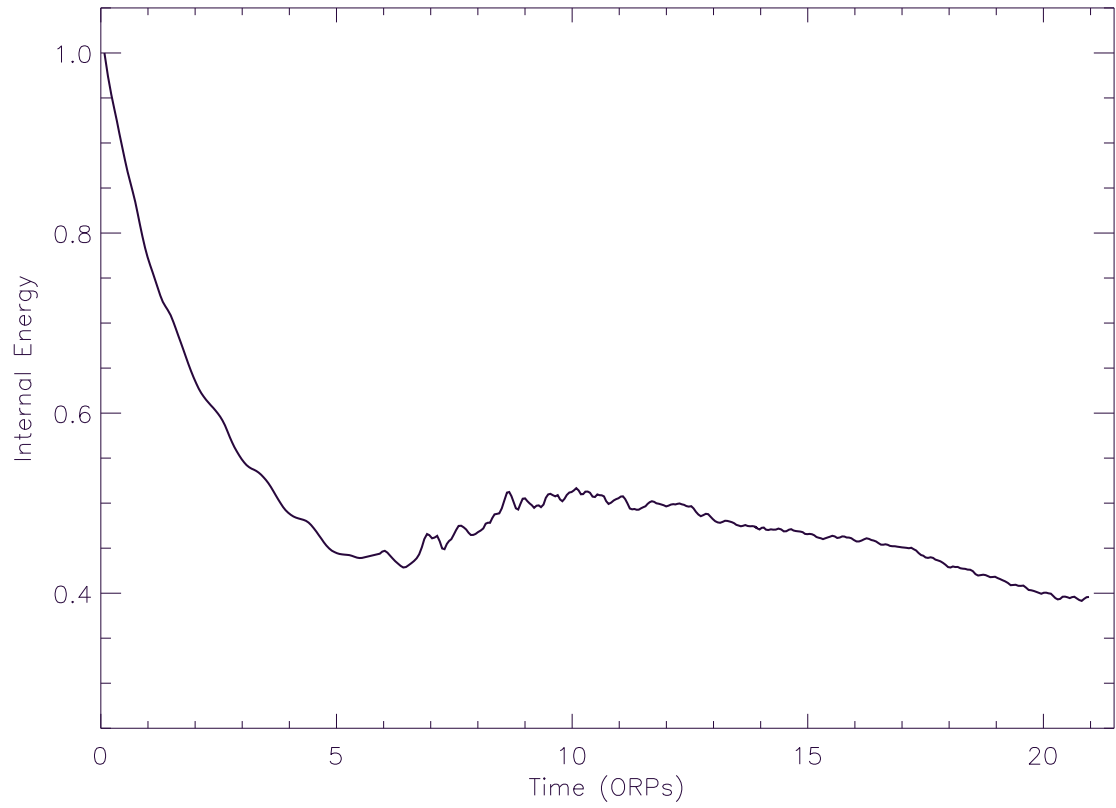


Figure 5.5: Total disk internal energy normalized to the initial value of the *BASELINE* simulation. The phases of evolution can be seen in the various components. The initial drop occurs in the axisymmetric phase, the increase occurs during the burst, followed by some variations in the transition phase and a slow decline in the asymptotic phase.

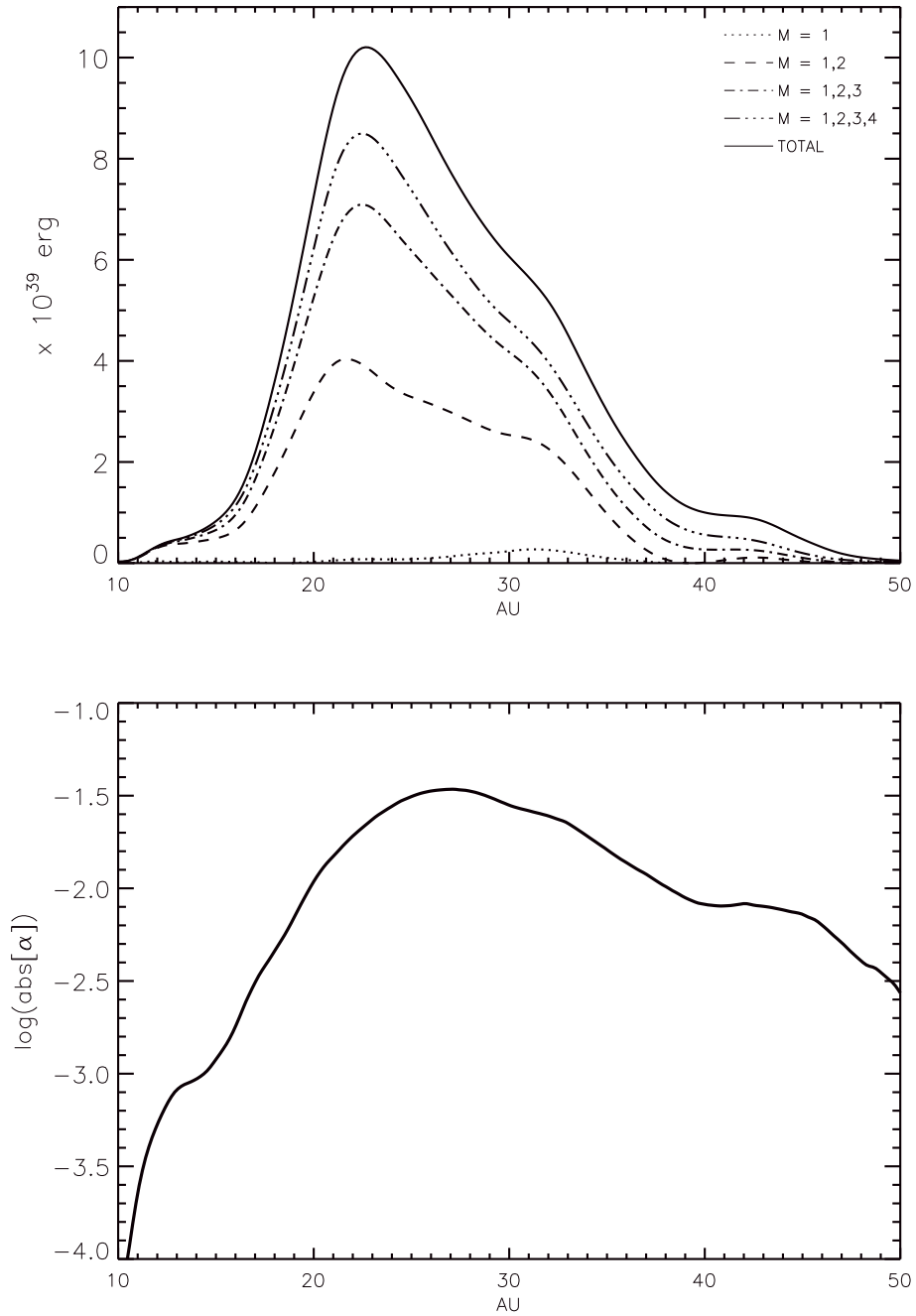


Figure 5.6: Torque profiles (top) and α profiles (bottom) averaged from 14 to 21 ORPs for the BASELINE simulation. Total torques are shown as well as contributions from sums of various m -values.

the cooling times stayed roughly constant around 3 – 3.5 ORPs, while elsewhere in the disk the cooling times were increasing as the disk evolved. This region is key since it is the area corresponding to the corotation radius of the dominant low-order modes in the disk. Figure 5.7 displays the periodograms for the $m = 1 - 4$ modes of the BASELINE simulation. One can observe clear broad stripes of power in the $m = 2, 3$ and 4 periodograms around a pattern speed of 1.3/ORP; additionally several strong clumps of power are evident in $m = 1$. These stripes of power have corotation radii ranging from 26 – 29 AU. This radial range corresponds to the range over which the cooling times did not change and the Toomre Q remained constant in the asymptotic phase. Additionally, figure 5.8 shows that near this radius the mass flow was changing from inward to outward. The mass flow rate \dot{M} was zero at 20 AU. This region near corotation was, based upon these measurements, the radius of the disk closest to a steady state, as predicted by Balbus & Papaloizou (1999).

5.4 The Asymptotic Phase Simulations

To study how a GI-active disk would respond to a planet and, in turn, how the planet would be affected by the disk, I performed three simulations where I inserted a planet into a disk that was already GI-active. The planets were all inserted into the BASELINE disk at the same time, ≈ 10.54 ORPs, at a radius of 25 AU. This radius was chosen because it is near the corotation radius of the low-order global modes seen in the BASELINE simulation, as in figure 5.7. The planets were initially given a circular velocity and were inserted at $\phi = 0$. The difference between the three simulations was the masses of the planets inserted, which were $0.3 M_J$, $1 M_J$,

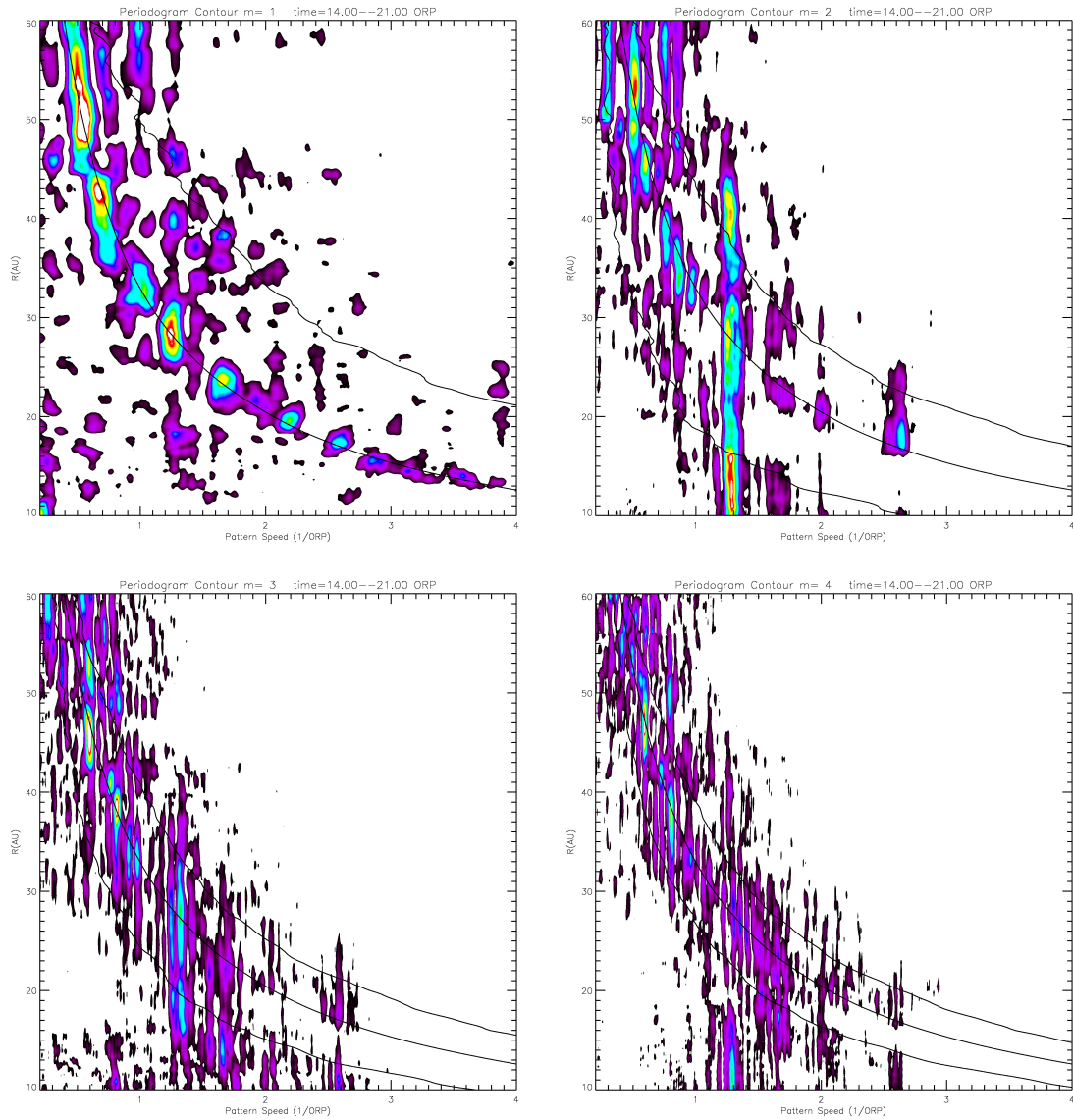


Figure 5.7: *Periodograms for the BASELINE simulation measured using data from 14 to 21 ORPs, $m = 1 - 4$ are presented here. The color scale represents relative power with purple being the smallest and red/white being the largest, in this case the relative power is the important measure as opposed to the absolute numbers. The solid lines represent the outer Lindblad resonance, corotation, and inner Lindblad resonance radii, from top to bottom, for each m -value.*

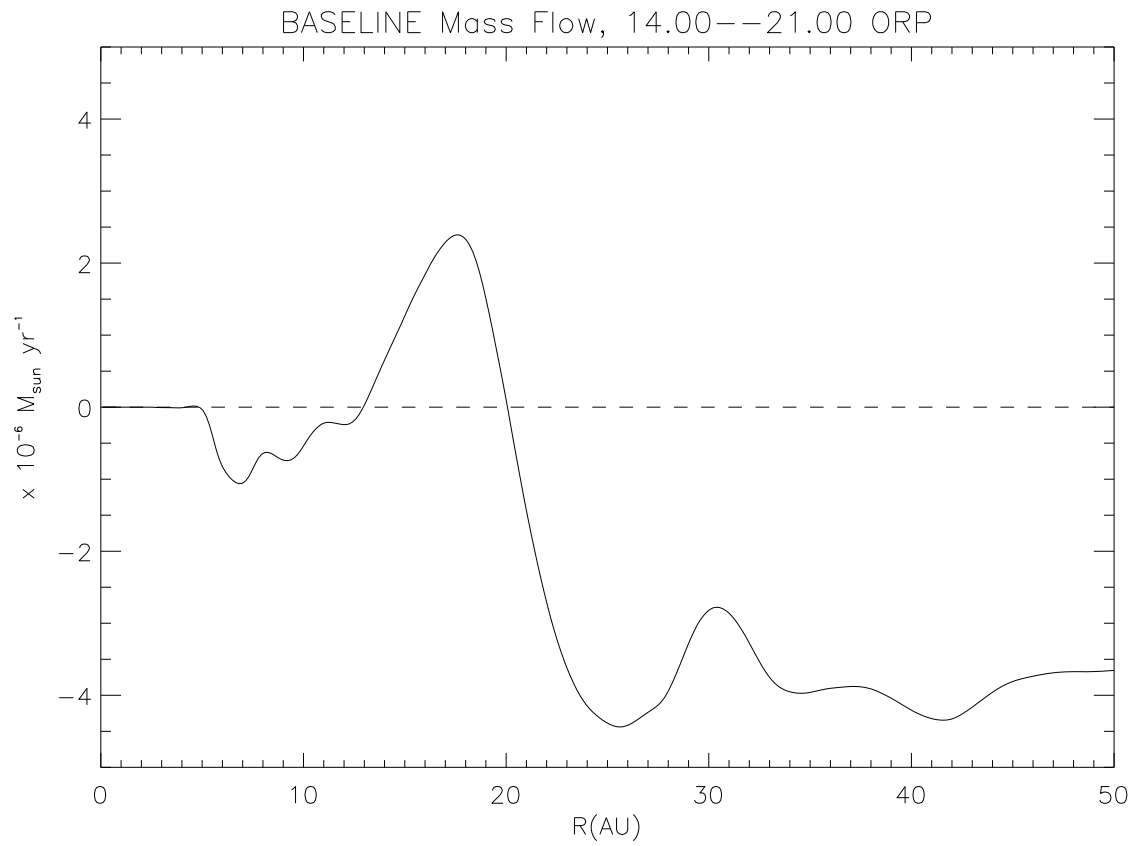


Figure 5.8: Mass transport rates in solar masses per year plotted during the asymptotic phase. The black curve represents the BASELINE simulation and the dashed line represents no mass flow. The transition from inflow to outflow occurs at 20 AU.

and $3 M_J$. The evolution of the planet's position was carried out using the algorithm described in §2.4.

I chose to study the effect of varying the planet mass for several reasons. The mass of the planet determines how strongly the planet couples to the disk and how large a gravitational influence it can have on disk structures. It is also one of the main parameters that determines type I migration rates in a laminar disk. In addition, the planet mass is the determining factor between type I and type II migration in a laminar disk. The masses I have chosen to use, namely $0.3 M_J$, $1 M_J$, and $3 M_J$, span a range of typical planet masses and also span the type I/type II migration boundary for this disk at 25 AU. It should be noted, however, that these simulations are not entirely self-consistent. Planets of these masses can only form rapidly in a GI-active disk undergoing fragmentation. As seen in the BASELINE simulation, this is not the case for this disk. However, my purpose is to study the planet-disk interaction rather than present a self-consistent scenario.

5.4.1 Effects in the Disk

Figures 5.9, 5.10, and 5.11 display the midplane densities for the 0.3JUP10ORP, 1JUP10ORP, and 3JUP10ORP simulations, respectively. A careful comparison of these snapshots to those of the BASELINE run from figure 5.3, shows that the density structures in the disk show very little difference for the 0.3JUP10ORP simulation, some slight variation in the density structures in the later stages of the 1JUP10ORP simulation and rather dramatic differences in the 3JUP10ORP simulation.

Additionally, the planet motion was very different from one planet mass to an-

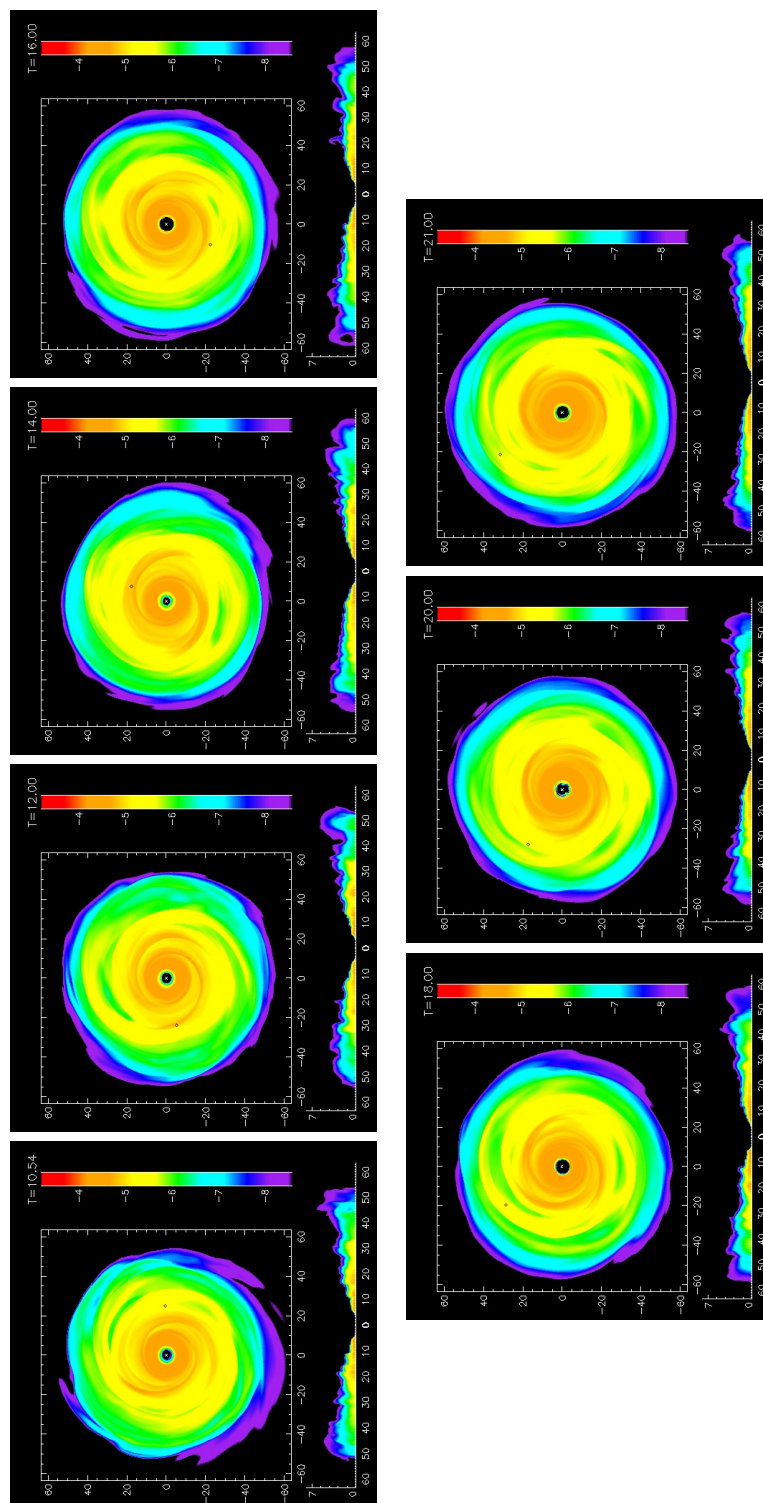


Figure 5.9: *Midplane and meridional densities in logarithmic scale for several times in the 0.3JUP10ORP simulation. The axes have units of AU and the time is given in ORPs in the upper right of each panel. The series starts at $t = 10.54$ ORPs and proceeds left to right and top to bottom to the end of the simulation at ≈ 21 ORPs. The black diamond in each of the panels indicates the location of the planet.*

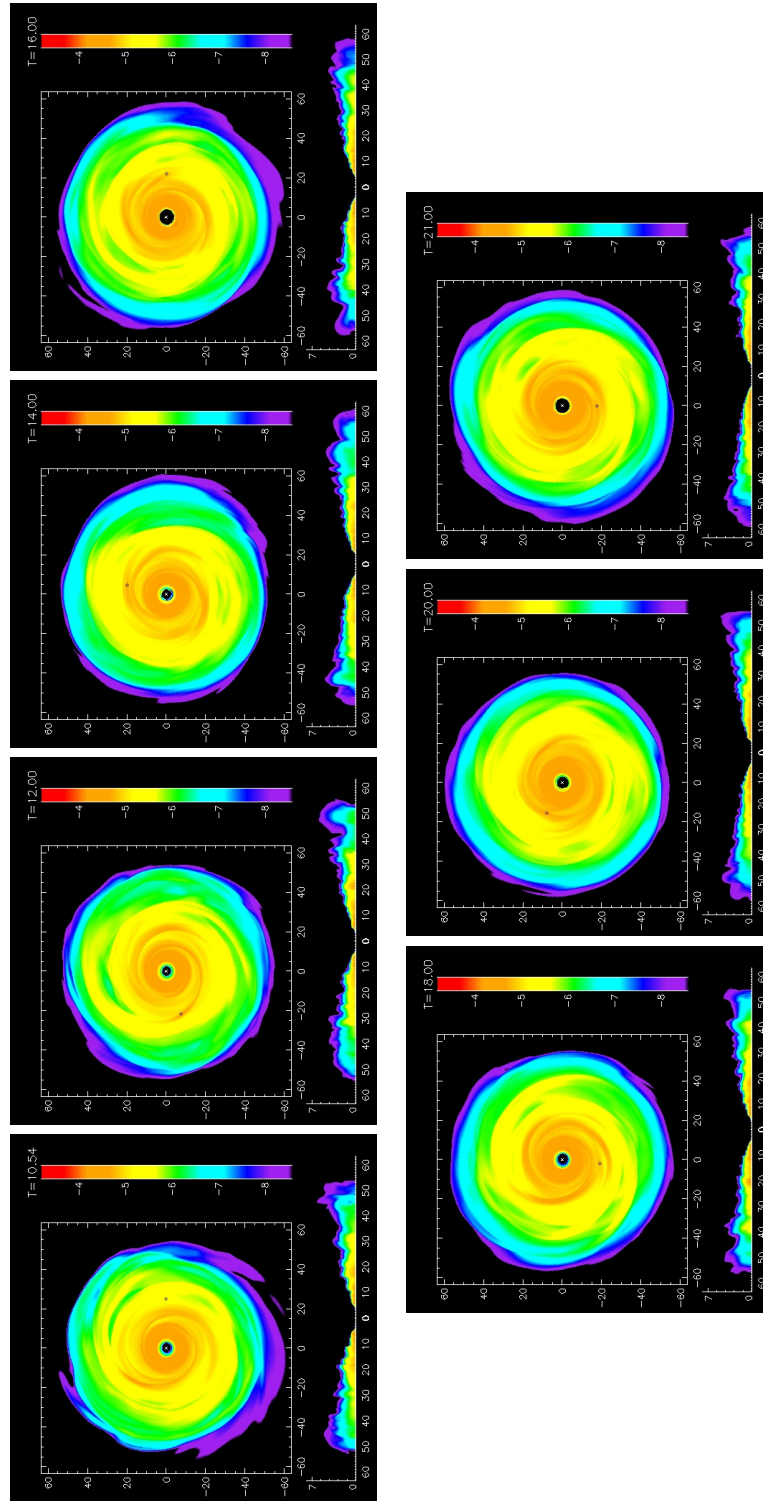


Figure 5.10: Midplane and meridional densities in logarithmic scale for several times in the 1JUP10ORP simulation. The axes have units of AU and the time is given in ORPs in the upper right of each panel. The series starts at $t = 10.54$ ORPs and proceeds left to right and top to bottom to the end of the simulation at ≈ 21 ORPs. The black diamond in each of the panels indicates the location of the planet.

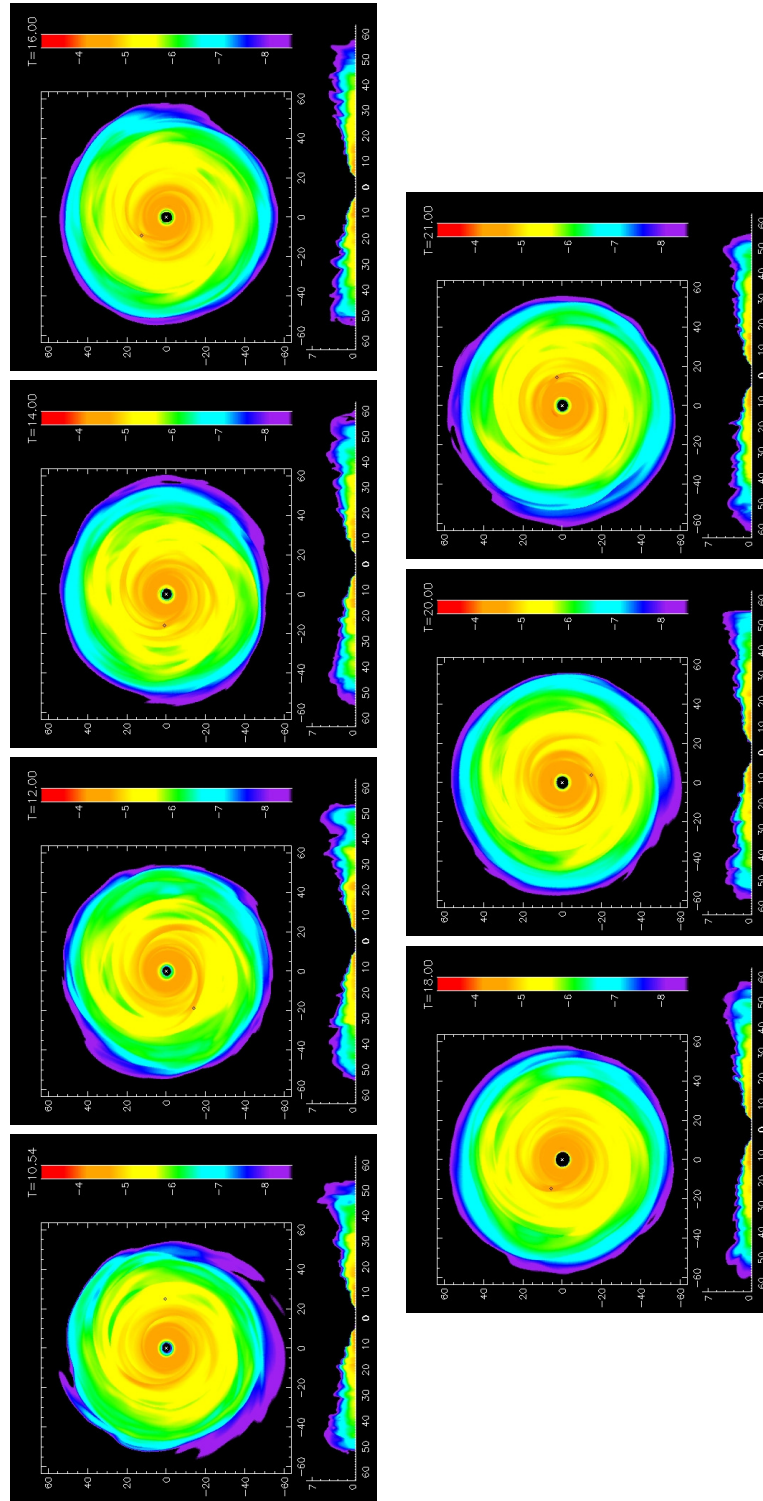


Figure 5.11: *Midplane and meridional densities in logarithmic scale for several times in the 3JUP10ORP simulation. The axes have units of AU and the time is given in ORPs in the upper right of each panel. The series starts at $t = 10.54$ ORPs and proceeds left to right and top to bottom to the end of the simulation at ≈ 21 ORPs. The black diamond in each of the panels indicates the location of the planet.*

other. In the 0.3JUP10ORP simulation, the planet migrated outward from its original radius of 25 AU. Both the planets in the 1JUP10ORP and 3JUP10ORP simulations migrated inward, but the planet motion in the 1JUP10ORP simulation was much more sporadic, because the planet did not disrupt the disk structures very much and in turn was more heavily influenced by them. The 3JUP10ORP motion was much steadier as it migrated inward and disrupted disk structures as it passed through them. In all cases the planets tended to follow the spiral arms in the disk and spent most of the time in the spiral arms. The planets tended to be overtaken by the spiral arms and then “ride” the spiral arm inward. This can be seen most clearly in animations showing the evolution of the midplane density. Animations for all seven simulations from this chapter can be viewed at the [Indiana University Scholar Works Archive](http://hdl.handle.net/2022/12960) (permanent URL <http://hdl.handle.net/2022/12960>).

Upon examining the Toomre Q values and column-wise cooling times for each of the simulations, I found a similar pattern. The Toomre Q values and column-wise cooling times were nearly indistinguishable from those in figure 5.2 for the 0.3JUP10ORP and 1JUP10ORP simulations. However, the 3JUP10ORP simulation showed dramatic differences as can be seen in figure 5.12. In the BASELINE simulation, the cooling times increased in the 10 – 20 AU range much more than they did in regions beyond 25 AU. This resulted in a steep gradient in cooling times from 20 – 30 AU. It is also in this region that one can see a “bump” develop in the Toomre Q values, and the disk was more stable in this region. This feature is not present at the same location in figure 5.12. Although the cooling times did not increase as dramatically in the 3JUP10ORP simulation as in the BASELINE simulation, there is still an noticeable increase in cooling time in figure 5.12. This also resulted in a

l_{max}	$\langle A_\Sigma \rangle$	$\langle A_{2-7} \rangle / \langle A_\Sigma \rangle$
BASELINE	1.43	0.59
0.3JUP	1.42	0.60
1JUP	1.44	0.58
3JUP	1.46	0.58

Table 5.1: Temporally and spatially averaged summed and relative amplitudes for each of the simulations with planets injected at $t = 10$ ORPs and the BASELINE simulation. All values are averaged over the time interval from 14 to 21 ORPs. The $\langle A_m \rangle$ quantities are averaged from 5 AU to the outer edge of the grid.

steep gradient, however the gradient occurred in the 15 – 20 AU region. One can also see that a “bump” similar to the one in the BASELINE Toomre Q is present over this region in the Toomre Q plot.

The differences between the different masses can also be seen in the total internal energy. Figure 5.13 shows the evolution of the internal energy for each of the simulations compared to the BASELINE run. One can see that the 0.3JUP10ORP and 1JUP10ORP simulations have minimal variation from the BASELINE run in the evolution of their internal energy. On the other hand, the 3JUP10ORP simulation has a dramatic increase in the internal energy compared to the other runs. One possible explanation is that as the more massive planet migrates inward and disrupts the existing density structures, it also heats the disk, resulting in a increased total internal energy. However, more investigation is required to confirm this hypothesis.

Although the density structures, cooling times, and internal energies show a distinct difference between the 3JUP10ORP and the BASELINE, 0.3JUP10ORP, and 1JUP10ORP simulations, the spectrum of non-axisymmetric amplitudes $\langle A_m \rangle$ are nearly identical for all of the simulations. When I plotted the $\langle A_m \rangle$ spectrum of the simulations with planets from 14 – 21 ORPs to compare with the bottom panel

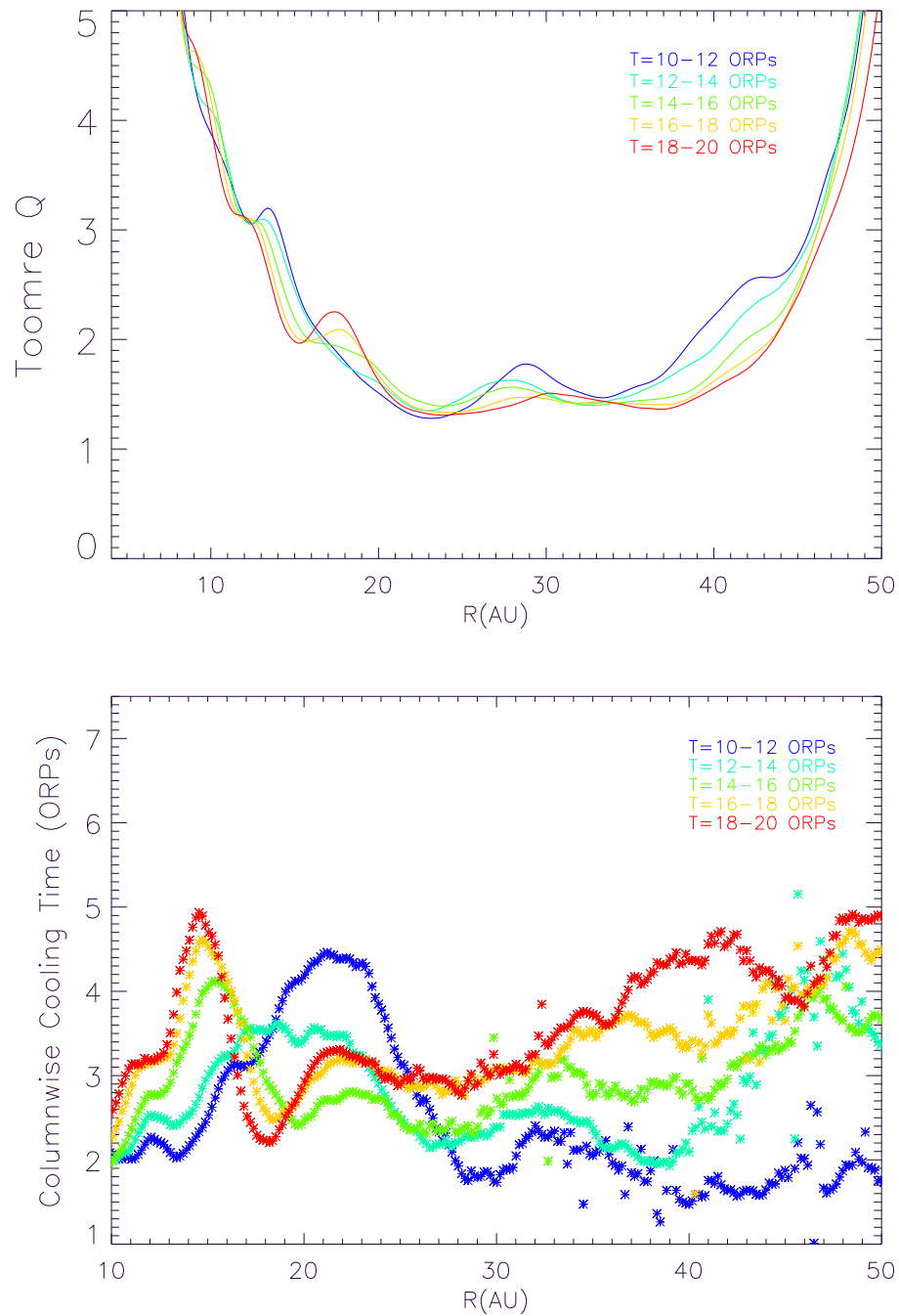


Figure 5.12: Plots show the midplane Toomre Q distribution (top) and column-wise cooling times (bottom) for a range of times throughout the asymptotic phase of the 3JUP10ORP simulation. Cooling times are calculated using equation (5.6). Values are averaged over several 2 ORP intervals.

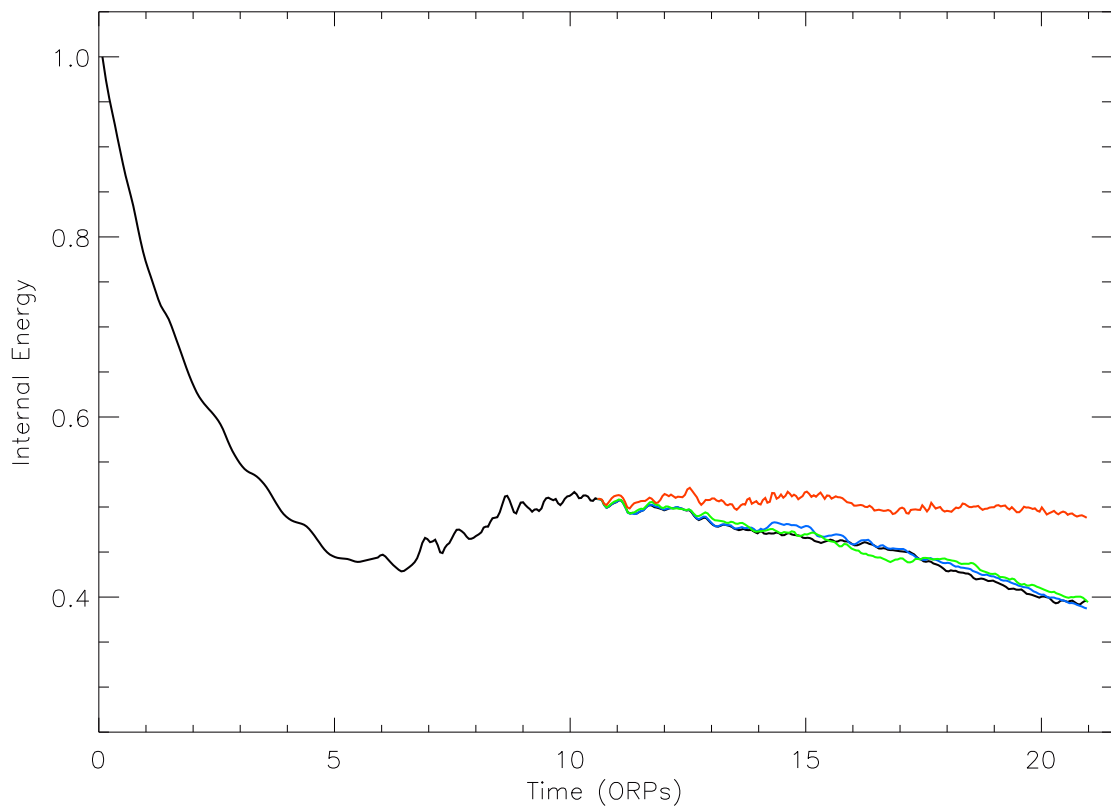


Figure 5.13: Total disk internal energy normalized to the initial value of the *BASELINE* simulation. The simulations with planets included at $t = 10$ ORPs have been included and normalized to the initial value of the *BASELINE* simulation. The *0.3JUP10ORP* (blue) and *1JUP10ORP* (green) simulations follow a similar trajectory to the *BASELINE* simulation throughout the asymptotic phase. However, the *3JUP10ORP* (red) simulation varies substantially due to the internal energy generated by the planet's motion.

of figure 5.4, the spectra all fell within the RMS fluctuations of the BASELINE simulation. This can also be seen in table 5.1, where the summed values of the non-axisymmetric amplitudes and the fractional amplitude in low-order modes differ by at most 3%. The fact that these amplitudes are so similar indicates that the presence of a planet has little effect on the overall strength of non-axisymmetric disturbances, i.e., the $\Delta\rho/\rho$, due to GIs. This is in agreement with the Toomre Q values which indicate that, over the GI active region, there is little variation in the Q values (see figures 5.2 and 5.12), and therefore the strength of GIs.

On the other hand, the $3 M_J$ planet did affect the coherence of non-axisymmetric structures. As noted in §3.1.3, the effectiveness of GIs in transporting mass in a disk is dependent on both the strength of the GIs and the coherence of the non-axisymmetric structures they produce. The investigation of the non-axisymmetric amplitudes in the preceding paragraphs tends to indicate that the strength of the GI activity is not greatly affected by the presence of a planet. However, when I examined the torques produced in the disk it was obvious that the mass transport rates were greatly reduced for the most massive planet, indicating that the presence of a planet can have a strong effect on the coherence of the spiral structures produced by GI activity. Figure 5.14 shows the total and component torque profiles averaged from 14 – 21 ORPs for the BASELINE, 0.3JUP10ORP, 1JUP10ORP, and 3JUP10ORP simulations. Clearly, the inclusion of a 0.3 or 1 M_J planet has a very small effect on the overall torque. The 0.3 M_J planet did cause the peaks of the torque to be shifted to slightly larger radii and enhanced the $m = 3$ torque over the $m = 2$ torque slightly. Additionally, the 1 M_J planet caused an overall decrease of the torque for all m values, but this variation was quite small i.e., $< 10\%$. In fact, even the shape

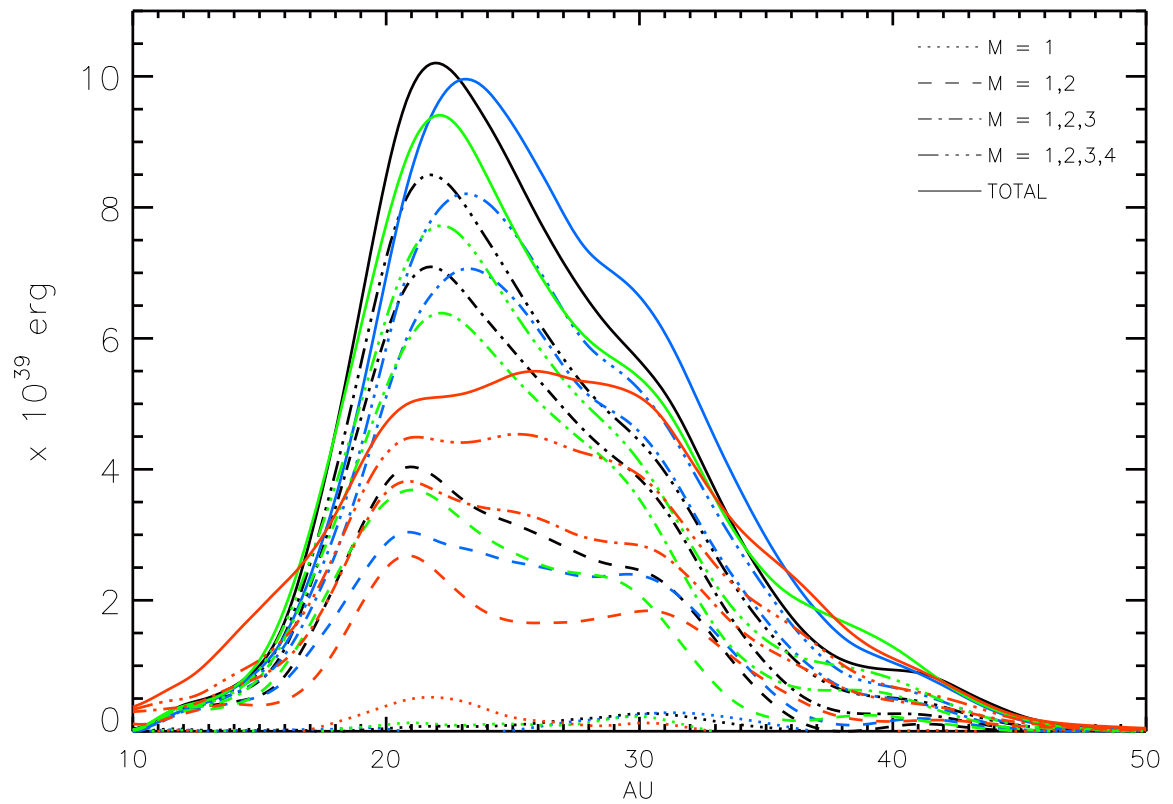


Figure 5.14: Profiles of the disk self-torque averaged from 14 to 21 ORPs for the BASELINE (black), 0.3JUP10ORP (blue), 1JUP10ORP (green), and 3JUP10ORP (red) simulations. Total torques are shown as well as contributions from sums of various m -values. The 3JUP10ORP simulation shows the strongest deviation from the BASELINE simulation.

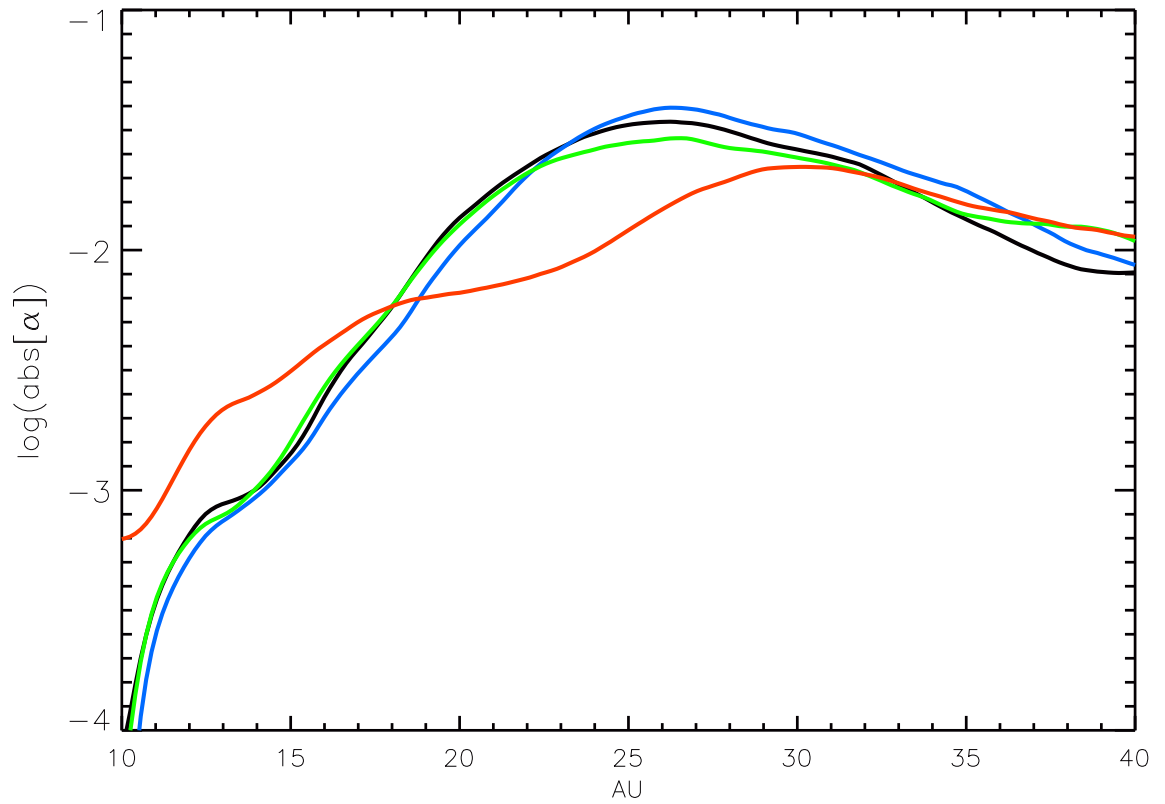


Figure 5.15: Effective Shakura-Sunyaev α -values computed for the *BASELINE* (black), *0.3JUP10ORP* (blue), *1JUP10ORP* (green), and *3JUP10ORP* (red) simulations averaged over the asymptotic phase from 14 to 21 ORPs.

of the torque profiles for both of these simulations remained largely unchanged from the BASELINE simulation for all m values. Because the torque profiles for these disks were so similar and the disk structure was largely the same, the α profiles are also very similar as can be seen in figure 5.15.

The $3 M_J$ planet presented a much different case. As one can see in figure 5.14, not only did the magnitude of the torque decrease dramatically for all m values over a large range of radii, but the fundamental shape of the torque profile changed as well. Instead of a sharp peak in the profile, one sees a broad plateau. This change in the profile was most dramatic for $m > 2$ with the greatest difference in the torque for $m = 3$. Obviously, such a large decrease in the torque resulted in a dramatic decrease in the α values, as can be seen in figure 5.15. The difference in the torque profile and α can be attributed to two main causes. First, the low-order modes are less coherent overall, and secondly, the corotation radius of the low-order coherent modes has been moved to larger radii. To study these drivers, one must examine the low-order periodograms.

Figure 5.16 shows the $m = 1 - 4$ periodograms for the 3JUP10ORP simulation from 14 – 21 ORPs. The solid lines in figures 5.7 and 5.16 represent the outer Lindblad resonance, corotation, and inner Lindblad resonance radii (see §1.3.3.2 for an explanation of Lindblad resonances). When compared to the periodograms from the BASELINE simulation (see figure 5.7), the stripes of power for the $m = 2, 3$, and 4 modes appear thinner and have a lower contrast to the surrounding regions of power. In addition the corotation radius of these stripes is $\sim 29 - 30$ AU, compared to corotation radii of $26 - 29$ AU for the BASELINE simulation. This results in the spreading of the torque peak seen in figure 5.14.

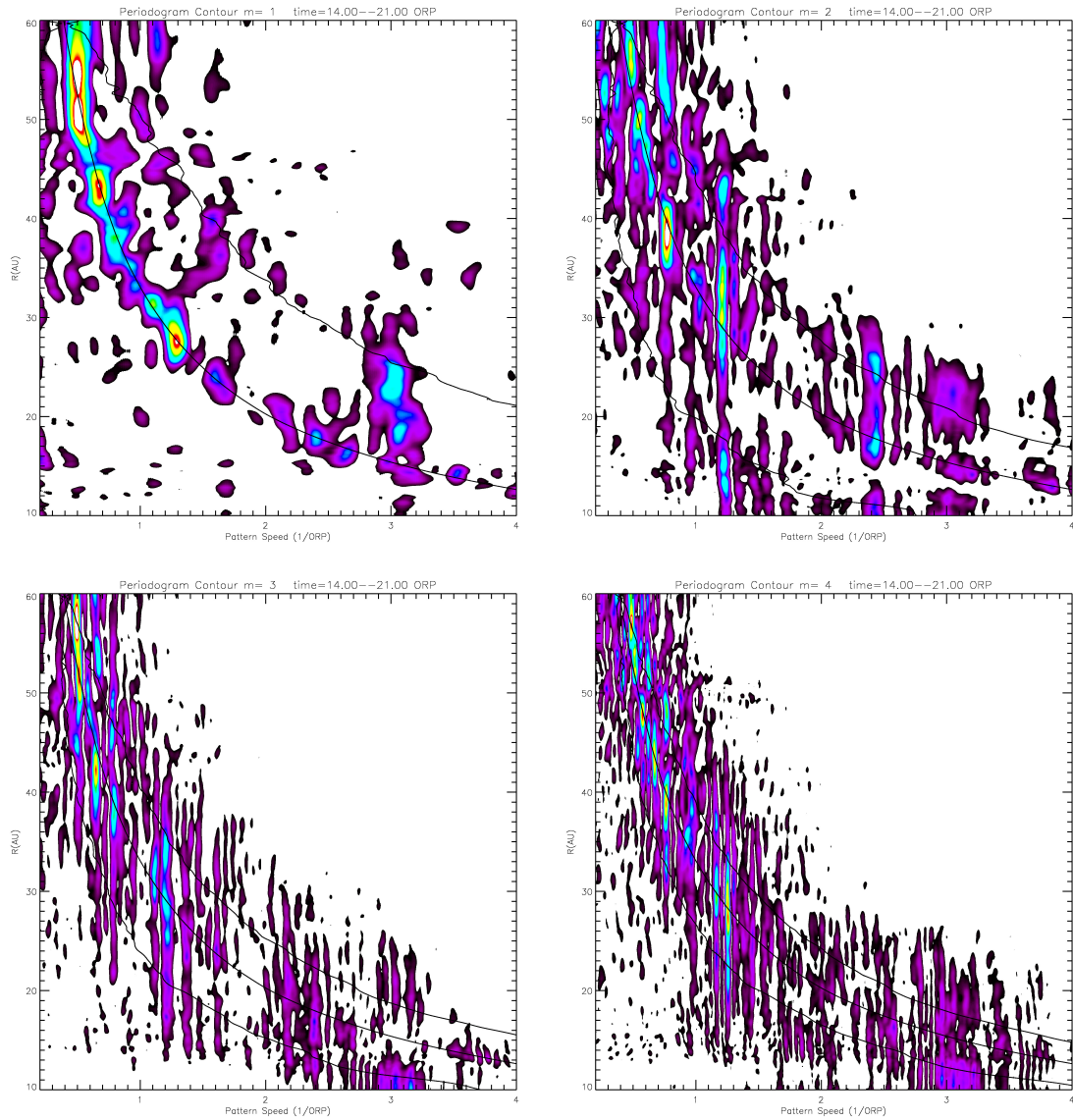


Figure 5.16: *Periodograms for the 3JUP10ORP simulation measured using data from 14 to 21 ORPs, $m = 1 - 4$ are presented here. The color scale represents relative power with purple being the smallest and red/white being the largest, in this case the relative power is the important measure as opposed to the absolute numbers. The solid lines represent the outer Lindblad resonance, corotation, and inner Lindblad resonance radii, from top to bottom, for each m -value.*

5.4.2 Planet Motions

Of course, studying how the insertion of the planets affects the disk dynamics and structure of the GIs is only half of the story. The GI activity in the disk can play an important role in the migration of the planet compared to what its migration pattern would be in a laminar disk. In §5.2 I explained what linear migration theory would predict for a planet’s motion in a laminar disk. However, for the GI active disks into which these planets were inserted, the outcome was quite different. Figure 5.17 displays the radial motion of each of the planets as well as the semi-major axis for each orbit. I measured an orbit as successive crossings of $\phi = 0$, although this is not strictly accurate because the line of apsides of the planet’s orbit precesses throughout the evolution. The orbits were nearly circular and had a very slow rate of precession when viewed in animations, so the computation of the semi-major axis and eccentricity should be reasonably accurate. For a given orbit, the semi-major axis was computed by

$$a = \frac{r_{\max} + r_{\min}}{2}, \quad (5.7)$$

where r_{\max} is the planet’s maximum distance from the star and r_{\min} is the planet’s minimum distance from the star for a given orbit. The eccentricity is calculated by

$$e = \frac{r_{\max}}{a} - 1. \quad (5.8)$$

One can see that the motion of the planets differed dramatically, with the $0.3 M_J$ planet actually moving outward from 25 to 40 AU over the course of the simulation. All of the planets moved significantly in radius in a short period of time, ~ 10 ORP

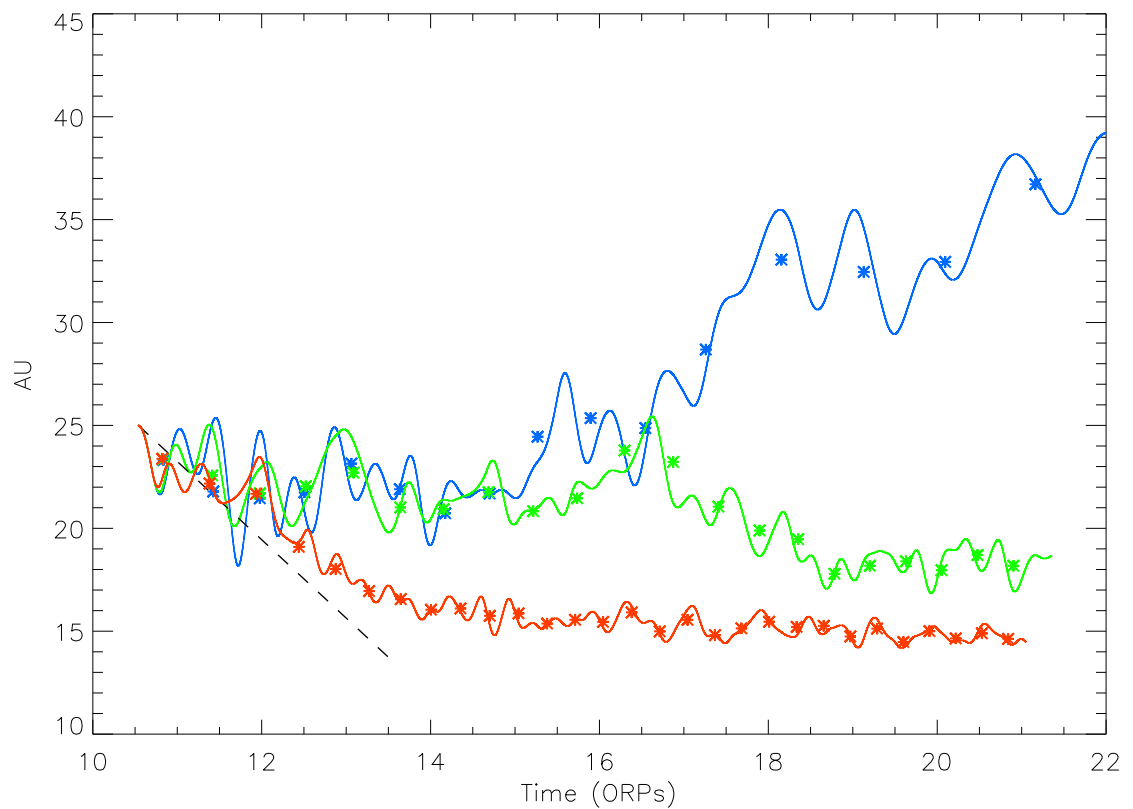


Figure 5.17: Plot of the radial positions of the planets in the 0.3JUP10ORP (blue), 1JUP10ORP (green), and 3JUP10ORP (red) simulations. The lines represent the radial position at each time while the diamonds show the semi-major axis for each orbit centered at the temporal midpoint of the orbit. The black dashed line represents the type I estimated migration rate from equation (5.5) for a $1 M_J$ planet and using the average of the two rates from section 5.2.

or 2140 years; in agreement with the type I migration timescales, but significantly shorter than type II migration timescales estimated in §5.2. By examining the animations available at the [Indiana University Scholar Works Archive](#), I determined that the orbit of the $0.3 M_J$ was heavily influenced by the GI structures in the disk causing it to make several rapid changes in radius when it encountered spiral structures produced by the GIs. One such instance can be seen between 17 and 18 ORPs. The animations also show that the orbit of the $1 M_J$ planet was similarly affected by GI structures, however not to the extent that the $0.3 M_J$ planet was. The spiral structures caused the planet to move in and out in radius as it encountered spiral arms. One example can be seen near 16.5 ORPs. Finally, the orbit of the $3 M_J$ planet was largely unaffected by the GI structures. As I outlined in the previous sections the planet had a much greater effect on the disk structures. One can compare the migration patterns to the type I estimate for a $1 M_J$ planet from §5.2 and see that even though the planets migrated rapidly, they did not move as fast as the type I estimate.

Another interesting characteristic of the migration pattern for the $1 M_J$ and $3 M_J$ planets was that they more or less ceased inward migration at a radius of 18 AU and 15 AU, respectively. Although changes in the migration rate can be caused by pressure, entropy, or surface density gradients in the disk ([Paardekooper & Papaloizou 2009](#)), I hypothesize that the inward migration was halted by interaction with GI spiral structures. My evidence for this claim is twofold. First, the animation of the $3 M_J$ planet (available at the [Indiana University Scholar Works Archive](#)) clearly shows the planet confined to the base of a spiral structure beginning around 15 – 16 ORPs. The $1 M_J$ planet is less clear cut, but it also moves from the base of one spiral

structure to another beginning around 18 ORPs. By “base” of a spiral structure I mean the leading inner end of a trailing spiral.

The second piece of evidence comes from the periodograms. One can see in figure 5.16 that the ILR of the major $m = 2$ mode for the $3 M_J$ case is located at ≈ 17 AU. Inside the ILR the mode damps and becomes less effective at transporting angular momentum (Lubow & Ogilvie 1998), causing the planet migration to stall. A similar situation can be seen in figure 5.18 for the major $m = 3$ mode for the $1 M_J$ simulation. Again, the $1 M_J$ case is less clear cut, because there are three distinct stripes of power, but the stripes of power have ILRs ranging from 18.5 AU to 20.5 AU. The $1 M_J$ planet also has a larger amount of jitter around 18 AU after it stops its inward migration, probably owing to the fact that the ILR of the major $m = 3$ modes were spread over a larger radial range.

The eccentricity of the planet orbits followed a similar pattern to their radial migration. Figure 5.19 plots the eccentricity of each of the orbits whose semi-major axes are shown in figure 5.17. All the planets began on a roughly circular orbit; however due to assumptions in calculating the circular velocity, i.e., assuming the disk mass was a point mass located at the grid center, the planets began with a small eccentricity ≈ 0.07 . In a laminar disk, the transfer of angular momentum between the disk and planet would act to regularize the orbit and drive the eccentricity to zero (Ward & Hahn 1998, 2003; Goldreich et al. 2004). However, the $0.3 M_J$ planet shows a marked increase in orbital eccentricity as its trajectory is altered by the spiral structures caused by GIs. Commensurate with their masses, the 1 and $3 M_J$ planets showed less jitter in their eccentricity, but there is still a significant amount of variation for the $1 M_J$ planet. The $3 M_J$ planet had the most regularized orbit as

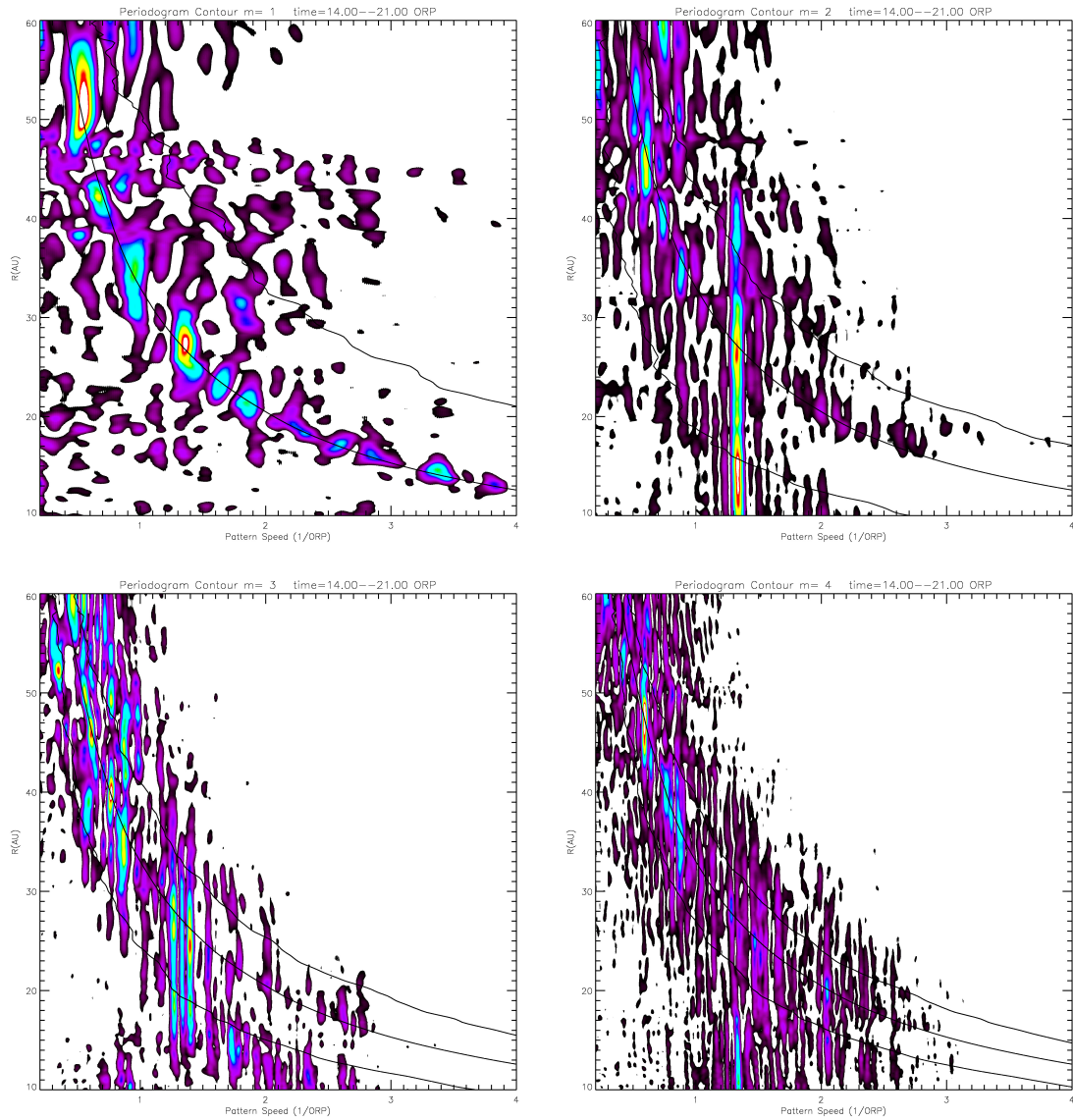


Figure 5.18: *Periodograms for the 1JUP10ORP simulation measured using data from 14 to 21 ORPs, $m = 1 - 4$ are presented here. The color scale represents relative power with purple being the smallest and red/white being the largest, in this case the relative power is the important measure as opposed to the absolute numbers. The solid lines represent the outer Lindblad resonance, corotation, and inner Lindblad resonance radii, from top to bottom, for each m -value.*

it migrated inward.

To compare the planet migration timescales in GI-active disks to the type I and type II migration timescale estimates, I computed the average angular momentum per orbit $\langle j_{pl} \rangle$ for each of the planets as well as the average torque on the planet $\langle T_{pl} \rangle = \left\langle \frac{j_{pl}}{dt} \right\rangle$. For each orbit, I then computed an estimate of the timescale for inward migration,

$$\tau_{mig} = \frac{-\langle j_{pl} \rangle}{\langle T_{pl} \rangle}. \quad (5.9)$$

In figure 5.20 the τ_{mig} values from equation (5.9) are plotted for each of the orbits of the 0.3JUP10ORP, 1JUP10ORP, and 3JUP10ORP simulations displayed in figure 5.17. Also plotted are the type I migration timescale estimates calculated at 10.5 ORPs. I have plotted the center of the range from §5.2. The type II estimates were an order of magnitude larger and would not fit on the plot. Negative τ_{mig} values indicate outward migration.

Obviously, the migration rates in the GI active disk were not consistent with type I or type II migration. It should be noted that the concept of type II migration probably does not apply in any of these cases because even the most massive planet I used, $3 M_J$, showed no sign of opening a gap. Gap formation criteria are probably different in GI-active disks. The major disparity with the type I predictions was the direction of migration. The median migration timescales were -21 ORPs for the $0.3 M_J$ planet from a distribution of 17 orbits, -12 ORPs for the $1 M_J$ planet from a distribution of 22 orbits and, 15 ORPs for the $3 M_J$ planet from a distribution of 30 orbits. I used the median rather than average values because there were a few outliers in each of the simulations with very large positive or negative timescales, representing

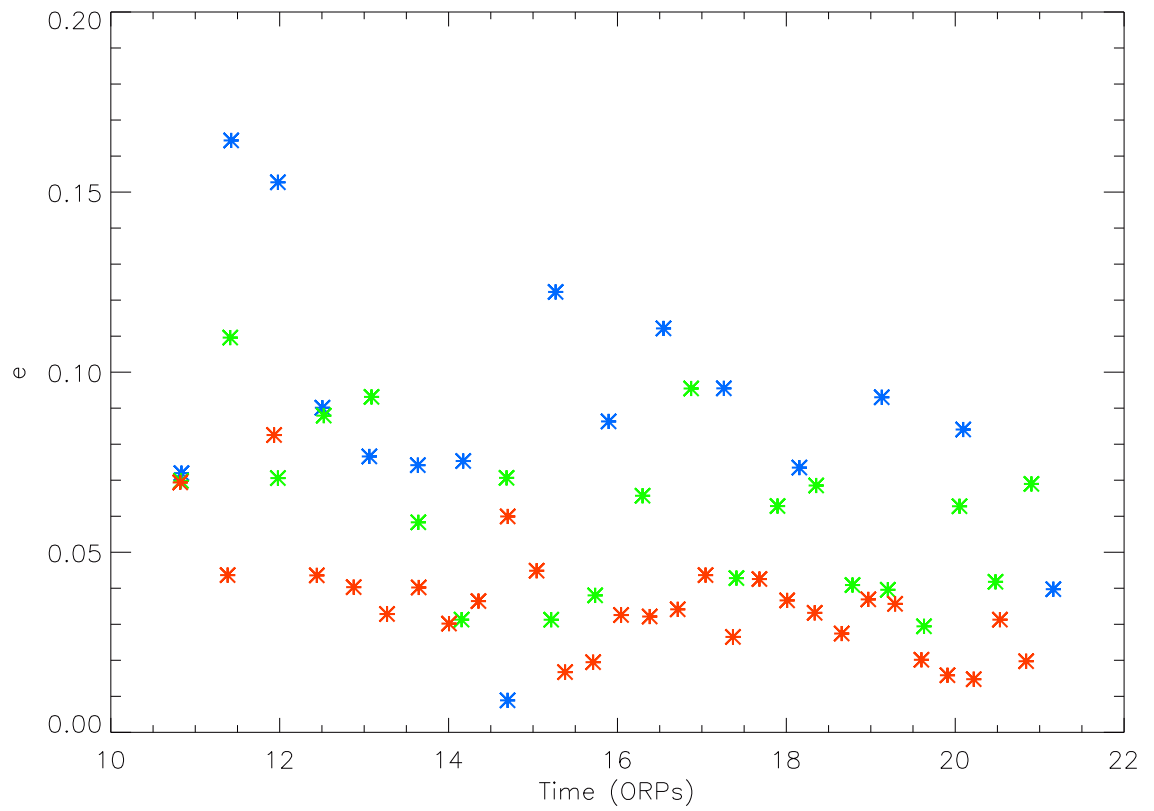


Figure 5.19: *Plotted are the eccentricities for each of the orbits plotted in figure 5.17. The $0.3M_J$ planet is shown in blue, the $1M_J$ planet is shown in green, and the $3M_J$ planet is shown in red.*

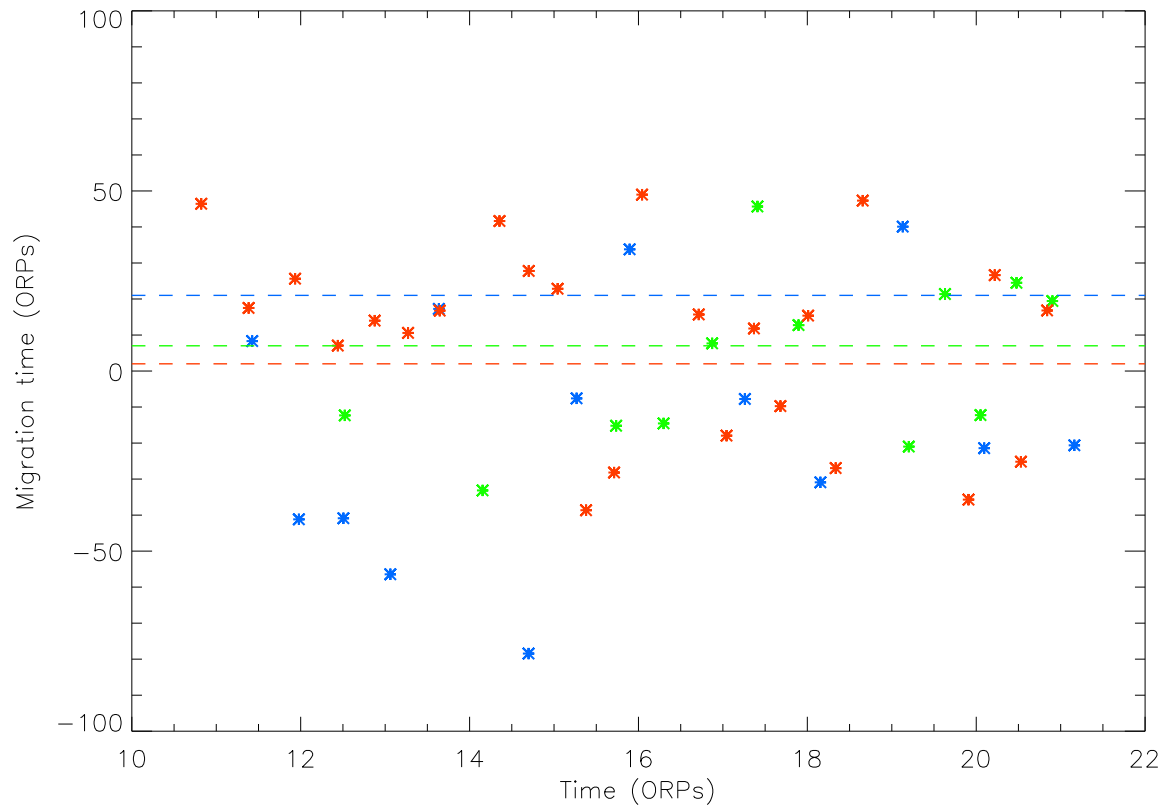


Figure 5.20: The migration timescales τ_{mig} are plotted for each of the orbits in figure 5.17. The 0.3JUP10ORP simulation is shown in blue, the 1JUP10ORP simulation is shown in green, and the 3JUP10ORP simulation is shown in red. The dashed lines indicate the estimated type I migration timescales for each of the planets at its starting radius of 25 AU. Negative values indicate outward migration

orbits in which the migration rate was very small. These few orbits tended to skew the average migration timescales, but I found the median measurement to give a more accurate representation of the data. I also computed average migration rates, by averaging $1/\tau_{mig}$, and the variance of the rates. These rates were $-0.017/\text{ORP}$ (-59 ORPs), $-0.0005/\text{ORP}$ (-1960 ORPs), and $0.023/\text{ORP}$ (43 ORPs) and the variances were 0.004 , 0.004 , and 0.003 for the $0.3 M_J$, $1 M_J$, and $3 M_J$ planets, respectively. The numbers in parentheses are the migration times that correspond to the given rates. Again, negative values indicate outward migration. The relatively large variances, for the $0.3 M_J$ and $1 M_J$ ($> 25\%$) indicate that the jitter in the planet's motion due to GI activity played a large role in the planet's migration. The variance for the $3 M_J$ is still substantial (13%) but indicative that the planet exhibited relatively less jitter from GIs when compared to the other two planet masses. Finally, to further illustrate the jitter caused by GI activity, I computed the average of the absolute value of the migration rates to give an indication of the average instantaneous rate of jitter. These rates were $0.050/\text{ORP}$ (20 ORPs), $0.051/\text{ORP}$ (20 ORPs), and $0.047/\text{ORP}$ (21 ORPs) for the $0.3 M_J$, $1 M_J$, and $3 M_J$ planets, respectively. Again, the numbers in parentheses are the migration times corresponding to the given rates.

5.5 The Initial Disk Simulations

The simulations presented in the previous section focus on the interaction of a planet and a GI-active disk. In order to study how the presence of a planet might affect the onset of GIs, I performed several simulations in which a planet was embedded in

an initial equilibrium disk before GIs had a chance to grow. I used the same initial disk as in the BASELINE simulation, which was marginally stable. I performed three simulations with planet masses $0.3 M_J$, $1 M_J$, and $3 M_J$. The planets were all inserted at a radius of 25 AU and $\phi = 0$. This radius was chosen for comparison to the asymptotic phase simulations. The planets were all initially given an approximate circular velocity as described in §5.1.1.

5.5.1 Effects in the Disk

Figures 5.21, 5.22, and 5.23 show several snapshots of the midplane and meridional densities for the 0.3JUP0ORP, 1JUP0ORP, and 3JUP0ORP simulations, respectively. For the purpose of comparison, the times for many of the snapshots are roughly equivalent to times used for the BASELINE simulation in figure 5.3. There are several obvious differences that can be seen from the density maps, these differences are also evident in the animations, which can be viewed at the [Indiana University Scholar Works Archive](#).

First, the burst of GI activity starts sooner in the simulations with planets. By comparing the panels in which the instabilities first appear, the second panel in figure 5.3 and third panels in figures 5.21, 5.22, and 5.23, one can see that spiral structure is evident by 5 ORPs in the baseline simulation and by 3.5 ORPs in the planet simulations. Furthermore, as the planet mass is increased, the onset of GIs occurs sooner. Comparing the 3.5 ORP snapshot (third panel) of the simulations with planets, one can see that for increased planet mass the GIs are more developed at the same simulation time.

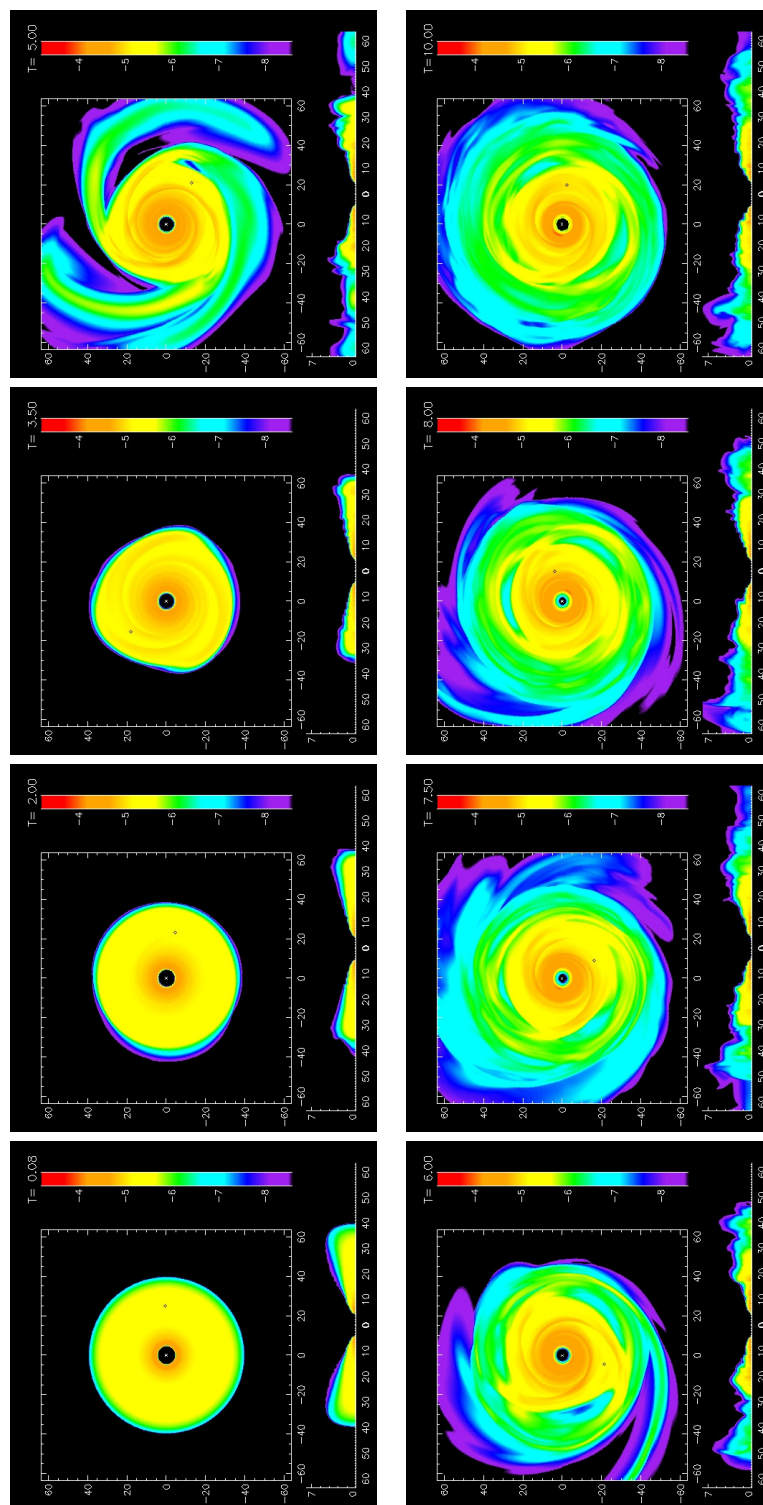


Figure 5.21: Midplane and meridional densities in logarithmic scale for several times in the $0.3JUP0ORP$ simulation. The axes have units of AU and the time is given in ORPs in the upper right of each panel. The series starts at $t = 0.08$ ORPs and proceeds left to right and top to bottom to the end of the simulation at ≈ 10 ORPs. The black diamond in each of the panels indicates the location of the planet.

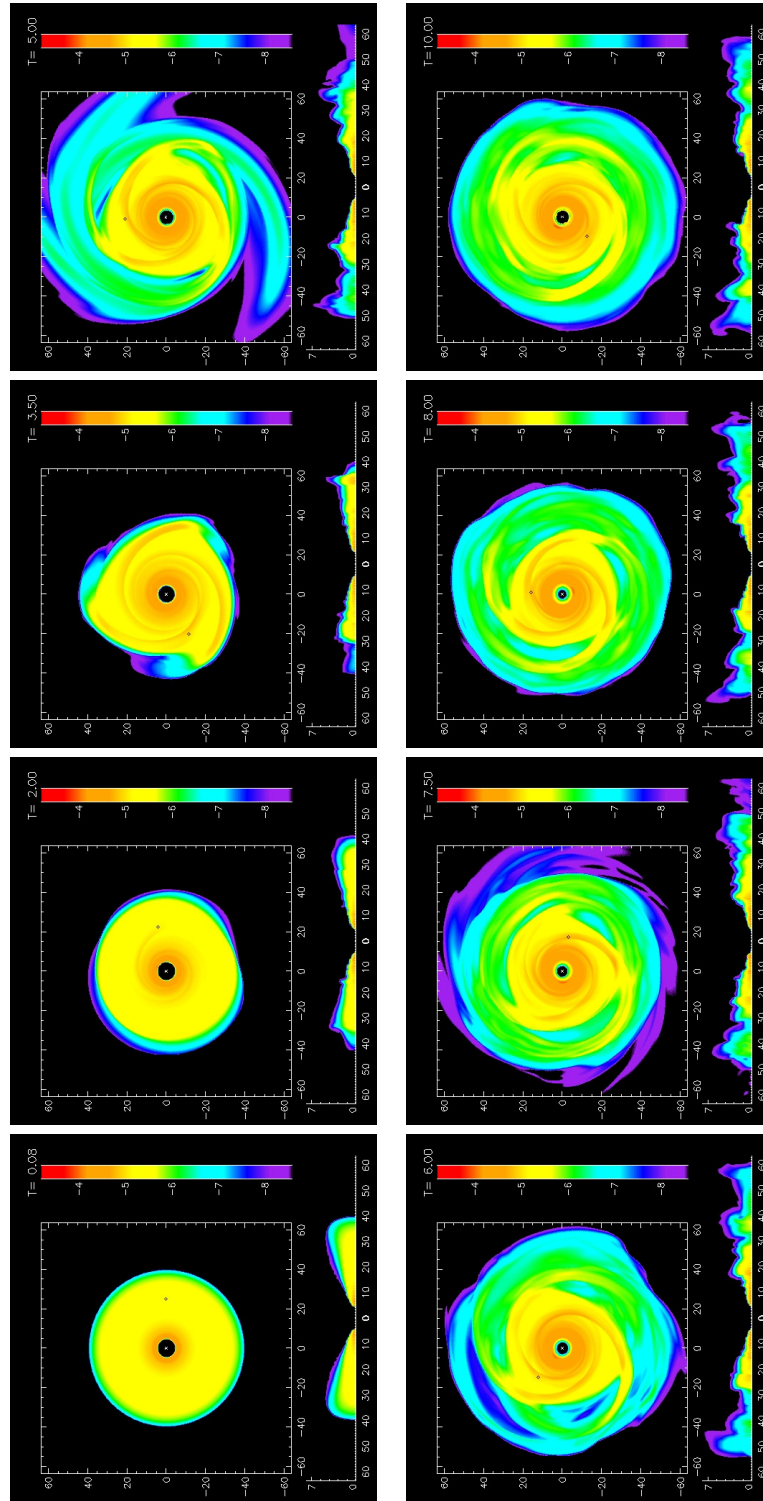


Figure 5.22: Midplane and meridional densities in logarithmic scale for several times in the 1JUP0ORP simulation. The axes have units of AU and the time is given in ORPs in the upper right of each panel. The series starts at $t = 0.08$ ORPs and proceeds left to right and top to bottom to the end of the simulation at ≈ 10 ORPs. The black diamond in each of the panels indicates the location of the planet.

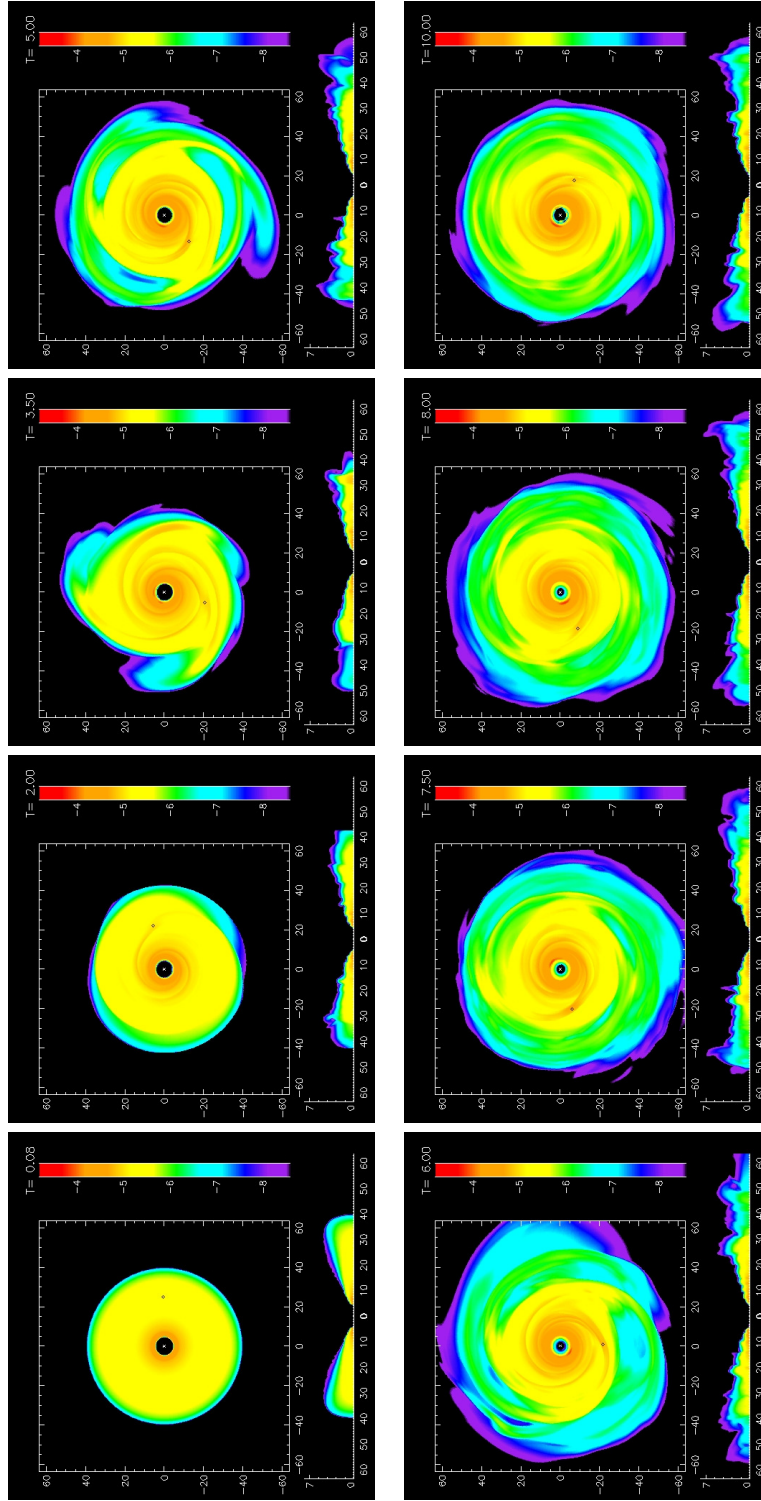


Figure 5.23: Midplane and meridional densities in logarithmic scale for several times in the 3JUP0ORP simulation. The axes have units of AU and the time is given in ORPs in the upper right of each panel. The series starts at $t = 0.08$ ORPs and proceeds left to right and top to bottom to the end of the simulation at ≈ 10 ORPs. The black diamond in each of the panels indicates the location of the planet.

Second, the addition of a planet changes the dominant mode in the burst phase. One can see that the burst in the BASELINE simulation was dominated by four- and five-armed spirals in figure 5.3. This is also reflected in the A_m versus time plot in figure 5.4. In contrast, the burst phase of the simulations with planets was dominated by three-armed spirals, seen in the third and fourth panels of figures 5.21, 5.22, and 5.23. Also, figure 5.24 shows the growth of non-axisymmetric amplitudes for each of the simulations with planets. One can clearly see that the non-axisymmetric structure grows more rapidly than in figure 5.4 and is dominated by $m = 3$.

Another interesting feature of these simulations is that the disks with $0.3 M_J$ and $1 M_J$ planets were much more radially extended than the BASELINE and 3JUP0ORP disks during the burst phase and the time just after the burst. To investigate this further, I plotted the average disk self-torques from 6 to 10 ORPs. I did not use times during the initial onset of the burst in the simulations with planets to avoid skewing the average with extremely large torques. However, this could not be avoided for the BASELINE simulation because the burst phase occurs later. This contamination from the early burst phase is evident in the torque plots (see figure 5.25), because the BASELINE simulation has an overall torque that is larger than the other simulations. One key feature of figure 5.25 is the depressed torque values for the 3JUP0ORP simulation, which is consistent with less expansion of the disk in this case.

Another noteworthy feature of the disk self-torque is the sum of $m = 1, 2$ and 3 for the 0.3JUP0ORP and 1JUP0ORP simulations. These curves are similar to the BASELINE simulation in shape and magnitude, which means that the post-burst torques were as large as the BASELINE torques with the early burst included.

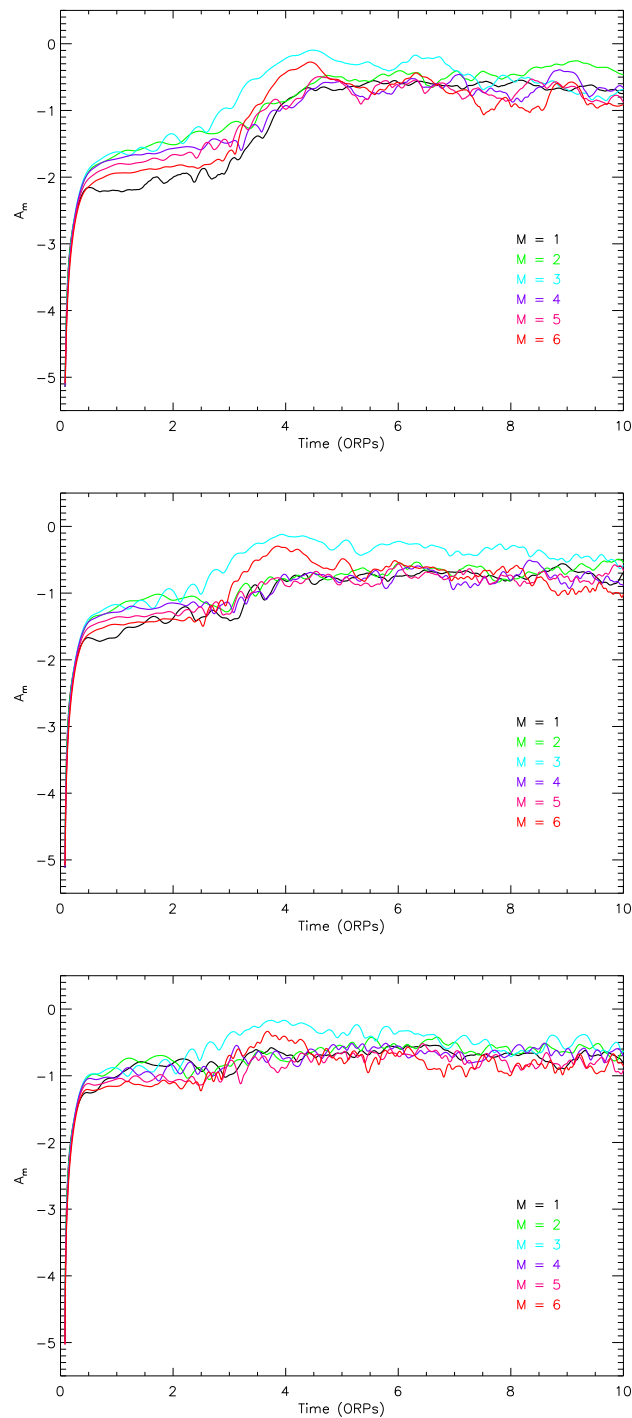


Figure 5.24: Each panel shows the Fourier components A_m as a function of time for $m = 1 - 6$. The $0.3JUP0ORP$, $1JUP0ORP$, and $3JUP0ORP$ simulations are shown from top to bottom. The amplitudes are shown from the initial models through the asymptotic phase. Contribution to the A_m components is only calculated for $\varpi > 15AU$ due to contamination from a spurious $m = 1$ signal.

Furthermore, the curve representing the sum of the torque from the $m = 1$ and 2 modes is smaller for the 0.3JUP0ORP simulation and dramatically smaller for the 1JUP0ORP simulation when compared to the BASELINE simulation. This means that the torque from the $m = 3$ mode was significantly larger in the simulations with $0.3 M_J$ and $1 M_J$ mass planets, and the torque from the $m = 2$ mode was significantly smaller.

The 0.3JUP0ORP and 1JUP0ORP simulations had a $m = 3$ non-axisymmetric structure that was significantly stronger, i.e., larger non-axisymmetric amplitude (see figure 5.24) compared to the BASELINE simulation (see figure 5.4). Although the 3JUP0ORP simulation also had stronger $m = 3$ non-axisymmetric structure, one can see in the animations (available at the [Indiana University Scholar Works Archive](#)) that as the $3 M_J$ planet passed through a spiral arm it significantly disrupted it, resulting in a loss of coherence and therefore weaker torques. My hypothesis is that the inclusion of the planet caused there to be more non-axisymmetric amplitude concentrated in the $m = 3$ mode, rather than the $m = 4$ and 5 modes as in the BASELINE simulation. This, in turn, caused there to be a greater transfer of angular momentum in the disk during the burst, which, caused a greater radial extension of the disks. However, the $3 M_J$ planet was so massive that it disrupted the $m = 3$ mode as it was growing, resulting in less angular momentum transfer from this mode, and a smaller radial extension. Clearly, the presence of a massive planet in a marginally unstable equilibrium disk can dramatically affect the onset and evolution of GIs in the disk.

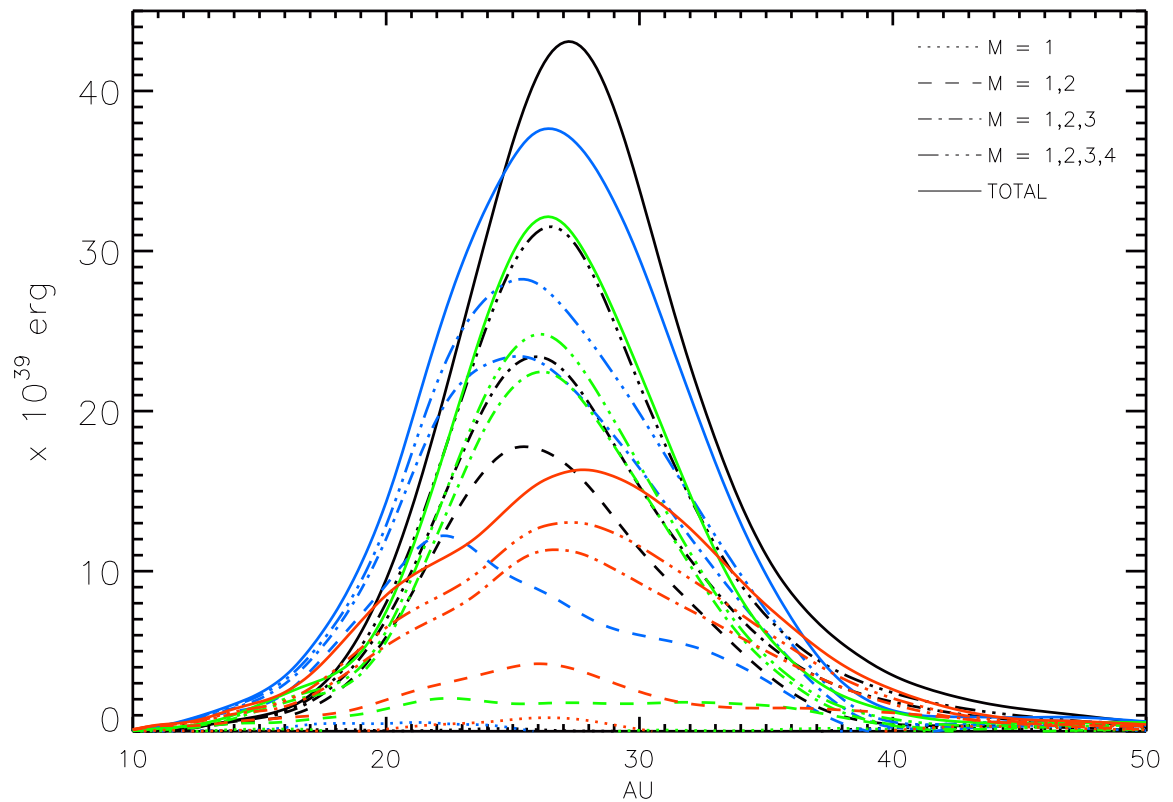


Figure 5.25: Disk self-torque profiles averaged from 6 to 10 ORPs for the BASELINE (black), 0.3JUP0ORP (blue), 1JUP0ORP (green), and 3JUP0ORP (red) simulations. Total torques are shown as well as contributions from sums of various m -values. The 3JUP0ORP simulation shows the strongest deviation from the BASELINE simulation.

5.5.2 Planet Motions

As with the asymptotic phase simulations, I analyzed the motions of the planets for each of the initial disk simulations. Unlike the asymptotic phase simulations, the disks with planets were initially nearly laminar, so one might expect them to follow the migration patterns predicted by laminar migration theory. In fact, the planets do roughly follow the predicted pattern as can be seen in figure 5.26. This figure shows the radial position of each of the planets from 0 – 10 ORPs and the semi-major axis of each orbit, as computed by counting successive crossings of $\phi = 0$ (see §5.4.2). At the beginning of the simulations, before the GIs have had a chance to develop, the planets migrated inward at rates roughly corresponding to their masses. The $0.3 M_J$ planet moved inward more slowly than the other two planets and the $1 M_J$ planet migrated at a slightly slower, but nearly the same rate as the $3 M_J$ planet. The type I migration rate estimate from §5.2 is plotted as a dashed line for comparison.

However, once the burst of GI activity began, the motion of the planets deviated significantly from their original trajectories. The burst caused the planets to move inward (see the 4.5 – 6 ORP stretch of time in figure 5.26). Following the initial burst (6 – 10 ORPs), the $3 M_J$ planet tended to move radially in a somewhat random fashion while the $1 M_J$ planet continued to migrate inward, but stopped at ≈ 17 AU. There appeared to be little dependence on planet mass in these behaviors. With the asymptotic phase simulations, the $3 M_J$ showed the least jitter in radius due to GI activity, but that does not seem to be the case here. Beginning around 6.5 ORPs, the $0.3 M_J$ planet interacted strongly with an $m = 2$ pattern that grew in the disk after the burst. At this time, the radial excursion of each of the $0.3 M_J$ planet's

orbits increased dramatically, at the same time that the $m = 3$ mode declined and an $m = 2$ mode began to dominate (see figure 5.24). The planet interacted strongly with this $m = 2$ mode (see panels 6, 7, and 8 of figure 5.21), which caused the eccentricity of its orbit to increase dramatically as can be seen in figure 5.27. This interaction can be hard to detect using only the panels of figure 5.21; however, it is quite evident in the animations available at the [Indiana University Scholar Works Archive](#).

Figure 5.27 shows the evolution of eccentricities for each of the planet simulations. For the first several ORPs of evolution while the disks were nearly axisymmetric, the eccentricity remained quite small. However, at the start of the burst phase, around 3.5 ORPs, the eccentricities increased as the planets interacted with the GIs. Although this increase was measurable for $1 M_J$ and $3 M_J$, it was not particularly large with typical eccentricities being $\lesssim 0.1$. The $0.3 M_J$ planet was an exception. Its eccentricity increased rapidly at 6.5 ORPs due to its strong interaction with an $m = 2$ spiral structure. Clearly, the action of GIs can have a noticeable effect on planet eccentricities. With GIs as a possible mechanism of increasing the orbital eccentricity of a planet, this could help explain the relatively large median eccentricity, $e = 0.27$ (Eggenberger et al. 2004), observed in extrasolar planets. Perhaps with a longer baseline of simulation time, all of the planets would interact as strongly with a non-axisymmetric structure as the $0.3 M_J$ planet did.

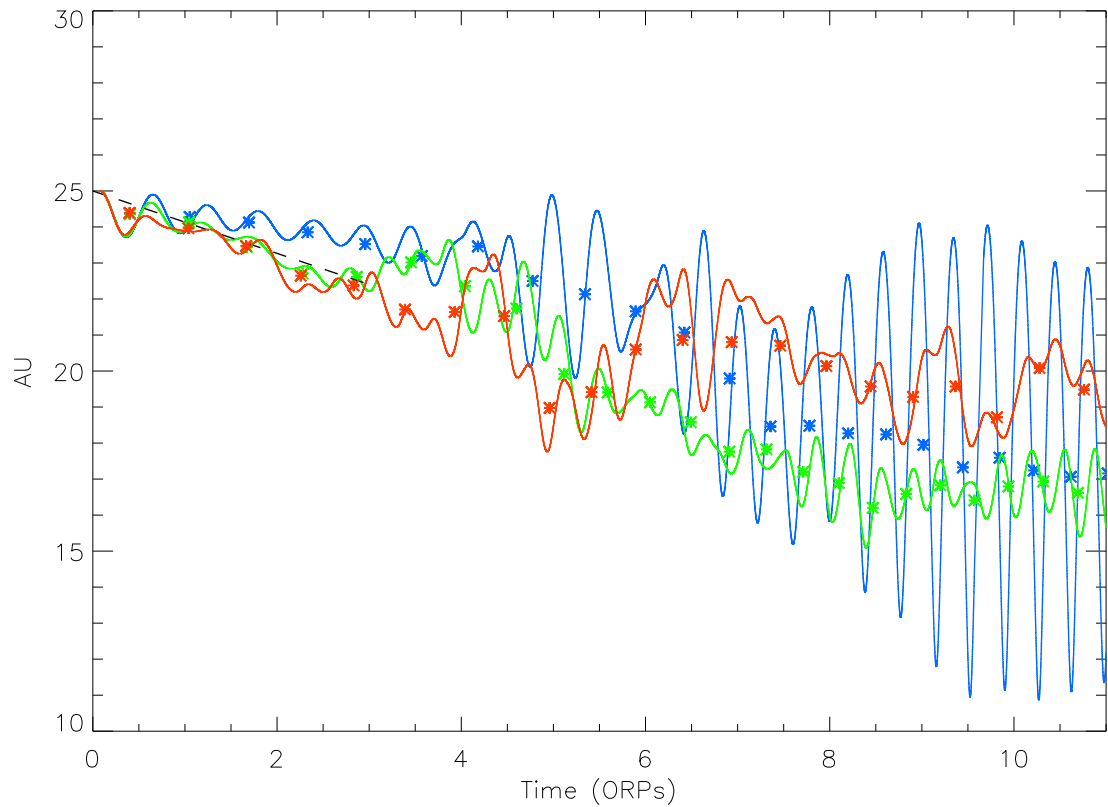


Figure 5.26: Plot of the radial positions of the planets in the 0.3JUP0ORP (blue), 1JUP0ORP (green), and 3JUP0ORP (red) simulations. The lines represent the radial position at each time while the diamonds show the radius of the semi-major axis for each orbit centered at the temporal midpoint of the orbit. The black dashed line represents the type I estimated migration rate from equation (5.5) for a $1 M_J$ planet.

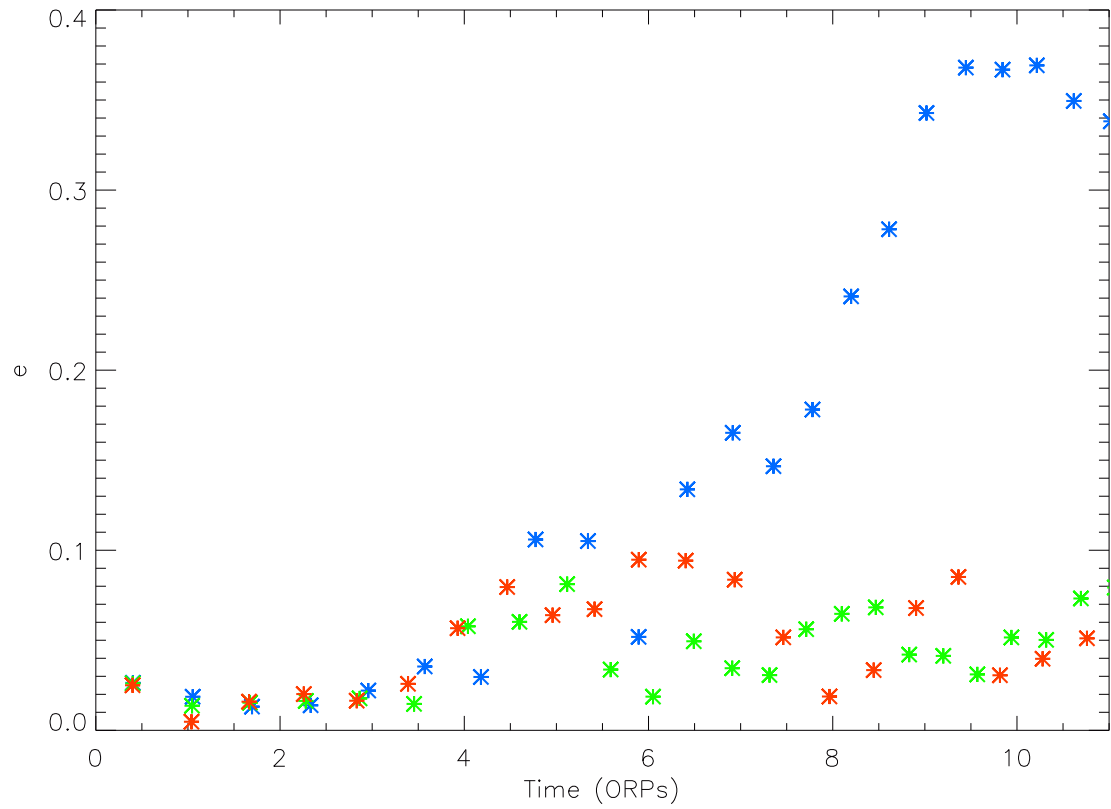


Figure 5.27: *Plotted are the eccentricities for each of the orbits plotted in figure 5.26. The $0.3M_J$ planet is shown in blue, the $1M_J$ planet is shown in green, and the $3M_J$ planet is shown in red.*

5.6 Conclusions

In comparing these two series of simulations with planets, I have shown that planets in a GI-active disk can strongly influence the organization, strength and other general characteristics of GIs including the onset of instability and dominant burst modes. I have also shown that GIs can have a large impact on the motion of a planet in a GI active disk, in some cases even reversing the direction of migration predicted by laminar disk theory. Additionally, I have found that GIs can increase, in some cases dramatically, the eccentricity of a planet's orbit. A clear distinction between type I and type II migration was not seen in any of the simulations I performed. In no case did a gap form around the planet, and I was unable to detect even the beginnings of gap formation.

Clearly, these simulations have only scratched the surface of possibilities for interactions between GIs and planets. There are a multitude of other parameters to be explored beyond planet mass and insertion time, and those two parameters have themselves not been exhaustively explored with the simulations I have presented. Even with this modest initial investigation, I have shown that the interactions between planets and GIs are significant both for the evolution of the planet and for the disk it is embedded in.

Chapter 6

Conclusion

*You may be **a** doctor. But I'm **the** Doctor.
The definite article, you might say.
– Doctor Who, *Robot**

In this dissertation, I have sought to answer several key questions regarding the evolution of gravitationally unstable protoplanetary disks. I have addressed the interplay between gravitational instabilities (GIs) and several different input parameters, GIs and stellar motion, and GIs and planetary migration. Overall I performed and analyzed twenty protoplanetary disk simulations in an attempt to answer several major questions:

- How do the following affect GI onset and evolution?
 - Surface density
 - Azimuthal resolution
 - Equation of state
 - Initial random perturbation
- What is the interplay between GI activity and stellar motion?
- How do GIs affect planet migration?

- Can planets or protoplanets trigger GIs?
- How does the presence of a planet or protoplanet affect the onset or characteristics of GIs?

In this chapter I summarize the answers to these and other questions I have uncovered throughout this work. I also present some ideas for future directions of research and end with some concluding remarks.

6.1 Key Findings

The studies I conducted have resulted in a number of interesting conclusions, which I detail below. The key findings for the field of planet formation and protoplanetary disks are mainly contained in chapter 5. Namely, by including planets in GI-active disk simulations, I was able to show that GIs can cause a planet to migrate radially outward even though the theory of type I migration in laminar disks indicates that the planet should migrate inward. Additionally, I have shown that GIs have the potential to dramatically increase the eccentricity of an orbiting planet, which could help explain the relatively large eccentricities observed in known exoplanets. Preliminary results from chapter 5 also show that it may be possible for a planet to cease its inward migration near the inner Lindblad resonance of a dominant mode in a GI-active disk.

6.1.1 Physical and Numerical Conditions

In chapter 3 I explored the effects of varying a host of numerical and physical parameters on the evolution of GI active disks. I analyzed several disks with different initial surface density profiles, specifically $\Sigma \propto \varpi^{-1/2}$, $\Sigma \propto \varpi^{-1}$, and $\Sigma \propto \varpi^{-3/2}$. I found that, in a general sense, the initial surface density profile does not have a large effect on the onset, evolution, and outcome of GIs in a protoplanetary disk. However, there were several noticeable differences. In particular, as the initial surface density profile steepens, the onset of the instability is delayed, and the GI activity in the burst phase is measurably weaker. This, in turn, results in smaller mass transport rates during the burst and smaller $\langle A_m \rangle$ amplitudes. All of the disks ended up with an outer disk surface density profile $\propto \varpi^{-5/2}$, corresponding to a disk with nearly constant Toomre Q and constant specific entropy.

I also presented several simulations with varied azimuthal resolution. I found that, for non-fragmenting disks in the asymptotic phase of evolution, the non-axisymmetric amplitude of low-order modes decreases as the azimuthal resolution increases. This, in turn, causes the disk torque and the effective gravitational α to decrease in the GI-active region. I saw a shift of non-axisymmetric amplitude from low-order modes to high-order modes as I increased the azimuthal resolution. As higher-order modes became available with the increasing resolution, non-axisymmetric amplitude shifted to those modes. This is evident in the changing $\langle A_{2-7} \rangle / \langle A_\Sigma \rangle$ presented in table 3.3. However, also evident in table 3.3, is the fact that the total non-axisymmetric amplitude $\langle A_\Sigma \rangle$ is largely unaffected by the variation in azimuthal resolution. I found that, for the disk I studied, an azimuthal resolution of $l_{max} = 512$ is likely

sufficient to measure the disk torque and effective gravitational α accurately. The effective gravitational α I measured in the $l_{max} = 512$ disk is in agreement with the predictions made by [Gammie \(2001\)](#) based on a local balance of heating and cooling.

Further, in chapter 3 I presented a study on the cooling time fragmentation limit for two different adiabatic indices. I performed these simulations to compare with the SPH simulations of [Rice et al. \(2005\)](#) that were cooled with a $t_{cool}\Omega = \text{constant}$. I found that disks with global cooling times $t_{cool} = 0.6$ and $t_{cool} = 1$ will fragment for $\gamma = 7/5$ and $\gamma = 5/3$, respectively. I estimated a critical $t_{cool}\Omega$ below which fragmentation occurred based on the radius at which fragments first appeared and found, $t_{cool}\Omega = 11 - 12$ for $\gamma = 7/5$ and $t_{cool}\Omega = 6 - 7$ for $\gamma = 5/3$, in rough agreement with [Rice et al. \(2005\)](#).

Finally, in chapter 3 I presented three simulations comparing the amplitude of the initial random perturbation given to the disks. I found that disks with larger amplitude perturbations have GI amplitudes that began to grow sooner but less rapidly. This is due to the fact that the larger perturbation prevented the formation of a dense, cool, low Q ring that can cause a violent outburst of GI activity in the outer disk.

6.1.2 Stellar Motion

To answer the question of the interplay between GIs and stellar motion, I performed a simulation that freed the central star by using the indirect potential method. I compared this to an otherwise identical simulation with the star artificially fixed to the center of the simulation grid. I found that, in contrast to the findings of [Rice](#)

[et al. \(2003a\)](#), the motion of the central star in response to the action of the GIs can be significant, as much as 0.24 AU in the simulation I performed. The motion of the star and the periodicity of the GIs are clearly related as can be seen in [table 4.1](#); however, there is a complex interaction between the disk and star which cannot be completely characterized without further study. Even though the stellar motion and its effect on the disk was measurable, it did not dramatically change the overall evolution of the GIs. Quantities such as gravitational torques and Fourier amplitudes varied by at most a few tens of percent. Simulations without stellar motion included are certainly still valid, although, in general, stellar motion should be included if possible.

6.1.3 Planetary Migration

In [chapter 5](#) I presented two series of simulations with planets inserted into the initial equilibrium disk or into an already GI-active disk near the beginning of the asymptotic phase. I compared both series to a baseline simulation without planets. I found that the inclusion of planets strongly affected the GIs in all of the initial disk simulations and in the asymptotic phase simulation with a $3 M_J$ planet included. The interaction between the planet and GIs scaled with the mass of the planet. In the cases where the planets were inserted into the initial disk, I found that the presence of a planet caused the onset of GIs to occur sooner and affected which mode was dominant during the burst phase.

The GI active disks also had a dramatic effect on the motion of the planets. The migration rates measured for some of the planets inserted in the asymptotic phase

were very different than those predicted by laminar migration theory. Additionally, some planets actually migrated outward, possibly by following the spiral patterns generated by the GIs. Although outward migration may be possible under certain conditions in a laminar disk (Paardekooper et al. 2010), the conditions are much more restrictive than those under which I found outward migration. In addition to affecting migration rates and directions, I found that GIs can drastically increase the eccentricity of a planet orbit, as in the 0.3JUP0ORP simulation.

6.2 Future Work

There are many ways to extend the work presented in this dissertation. Further resolution studies could be preformed to augment the results from §3.4, such as going to still higher azimuthal resolution and studying the effect of varied ϖ and z resolution. Several additional studies can be conducted with the current planet simulation capabilities of the CHYMERa code, i.e., a single massive planet. By varying the radius at which the planets are included, I could see how corotation and the inner and outer Lindblad resonances of the dominant GI modes affect planet motion. The code can also be used to study highly unequal-mass close binaries surrounded by a circumbinary disk. I have already performed one simulation along these lines, and the preliminary results are quite exciting.

Several improvements could be made to the code to increase its capabilities in the study of embedded planets. The simplest such improvement would be to allow for multiple massive planets to be included at once in a disk simulation. One would need to account for the planet-planet interactions, and so the number of planets

would need to be kept small as the cost of the force calculation is $O(N^2)$. However, investigations of systems with two or three planets in a GI active disk could prove to be quite interesting. Further improvements would entail including particles of different size regimes from small dust grains that basically stay entrained in the gas flows, to meter-sized boulders that are maximally affected by gas drag, through kilometer-sized bodies and on to planets. This would require significant extensions to the currently existing code, namely, accurately determining the gas drag coefficients. Currently available routines could be incorporated (Boley & Durisen 2010), but transitioning from one size regime to another could present significant difficulties.

6.3 Final Remarks

Certainly questions abound throughout the field of astrophysics and even in the tiny niche of gravitational instabilities in protoplanetary disks. There are many lifetimes worth of research needed in order to complete our understanding of young stellar systems, gas giant planet formation, and the role that GIs play in shaping them. I have been privileged to dedicate several years of my professional life to the study contained in this dissertation, and I hope to continue to tackle these and other interesting questions for many years to come. Obviously, the final word on the theory of gas giant planet formation and gravitational instabilities in protoplanetary disks is in the distant future, but hopefully my work has shed some light on the subject, answered a few questions, and raised many more. The conclusion of this work is more of a beginning than an end, hopefully a beginning to new realms of discovery. Perhaps we will never fully understand planet formation, but in the words

of Emerson, “Life is a journey, not a destination.”

References

- Adams, F. C., Lada, C. J., & Shu, F. H. 1987, *ApJ*, 312, 788
- Adams, F. C., Ruden, S. P., & Shu, F. H. 1989, *ApJ*, 347, 959
- Andre, P., Ward-Thompson, D., & Barsony, M. 1993, *ApJ*, 406, 122
- Armitage, P. J., Livio, M., & Pringle, J. E. 2001, *MNRAS*, 324, 705
- Balbus, S. A. & Hawley, J. F. 1997, in *Astronomical Society of the Pacific Conference Series*, Vol. 121, IAU Colloq. 163: *Accretion Phenomena and Related Outflows*, ed. D. T. Wickramasinghe, G. V. Bicknell, & L. Ferrario, 90–+
- Balbus, S. A. & Papaloizou, J. C. B. 1999, *ApJ*, 521, 650
- Barnes, J. E. & Hut, P. 1989, *ApJS*, 70, 389
- Boley, A. C. 2007, PhD thesis, Indiana University
- . 2009, *ApJL*, 695, L53
- Boley, A. C. & Durisen, R. H. 2008, *ApJ*, 685, 1193
- . 2010, *ApJ*, 724, 618
- Boley, A. C., Durisen, R. H., Nordlund, Å., & Lord, J. 2007a, *ApJ*, 665, 1254
- Boley, A. C., Hartquist, T. W., Durisen, R. H., & Michael, S. 2007b, *ApJL*, 656, L89
- Boley, A. C., Hayfield, T., Mayer, L., & Durisen, R. H. 2010, *Icarus*, 207, 509
- Boley, A. C., Mejía, A. C., Durisen, R. H., Cai, K., Pickett, M. K., & D’Alessio, P. 2006, *ApJ*, 651, 517
- Boss, A. P. 1997, *Science*, 276, 1836
- . 1998a, *Nature*, 393, 141

- . 1998b, *ApJ*, 503, 923
- . 2000, *ApJ*, 536, L101
- . 2003, *ApJ*, 599, 577
- . 2005, *ApJ*, 629, 535
- . 2007, *ApJL*, 661, L73
- Brandenburg, A., Nordlund, A., Stein, R. F., & Torkelsson, U. 1995, *ApJ*, 446, 741
- Cabot, W. & Pollack, J. B. 1992, *Geophysical and Astrophysical Fluid Dynamics*, 64, 97
- Cai, K. 2006, PhD thesis, Indiana University
- Cai, K., Durisen, R. H., Boley, A. C., Pickett, M. K., & Mejía, A. C. 2008, *ApJ*, 673, 1138
- Cai, K., Durisen, R. H., Michael, S., Boley, A. C., Mejía, A. C., Pickett, M. K., & D'Alessio, P. 2006, *ApJL*, 636, L149
- Cameron, A. G. W. 1978, *Moon and Planets*, 18, 5
- Cassen, P. & Moosman, A. 1981, *Icarus*, 48, 353
- Chambers, J. E. 2009, *Annual Review of Earth and Planetary Sciences*, 37, 321
- Chandrasekhar, S. 1960, *Radiative transfer* (Dover)
- Channell, P. A. & Scovel, C. 1990, *Nonlinearity*, 3, 231
- Chen, C. H. & Kamp, I. 2004, *ApJ*, 602, 985
- Clarke, C. J. 2009, *MNRAS*, 612
- Clarke, C. J., Harper-Clark, E., & Lodato, G. 2007, *MNRAS*, 381, 1543
- Cossins, P., Lodato, G., & Clarke, C. J. 2009, *MNRAS*, 393, 1157
- D'Angelo, G., Kley, W., & Henning, T. 2003, *ApJ*, 586, 540

- D'Angelo, G. & Lubow, S. H. 2008, *ApJ*, 685, 560
- Davis, S. W., Blaes, O. M., Hirose, S., & Krolik, J. H. 2009, *ApJ*, 703, 569
- Decampli, W. M., Cameron, A. G. W., Bodenheimer, P., & Black, D. C. 1978, *ApJ*, 223, 854
- Dodson-Robinson, S. E., Veras, D., Ford, E. B., & Beichman, C. A. 2009, *ApJ*, 707, 79
- Durisen, R. H., Boss, A. P., Mayer, L., Nelson, A. F., Quinn, T., & Rice, W. K. M. 2007, in *Protostars and Planets V*, B. Reipurth, D. Jewitt, and K. Keil (eds.), University of Arizona Press, Tucson, 951 pp., 2007., p.607-622, ed. B. Reipurth, D. Jewitt, & K. Keil, 607–622
- Durisen, R. H., Cai, K., Mejía, A. C., & Pickett, M. K. 2005, *Icarus*, 173, 417
- Eggenberger, A., Udry, S., & Mayor, M. 2004, *A&A*, 417, 353
- Eisner, J. A. & Carpenter, J. M. 2006, *ApJ*, 641, 1162
- Flower, D. R., Pineau Des Forêts, G., & Walmsley, C. M. 2006, *A&A*, 449, 621
- Flower, D. R. & Watt, G. D. 1984, *MNRAS*, 209, 25
- Forgan, D., Rice, K., Stamatellos, D., & Whitworth, A. 2009, *MNRAS*, 172
- Fromang, S. & Papaloizou, J. 2007, *A&A*, 476, 1113
- Fuente, A., Martín-Pintado, J., Rodríguez-Fernández, N. J., Rodríguez-Franco, A., de Vicente, P., & Kunze, D. 1999, *ApJL*, 518, L45
- Gammie, C. F. 1996, *ApJ*, 457, 355
- . 2001, *ApJ*, 553, 174
- Goldreich, P., Lithwick, Y., & Sari, R. 2004, *ApJ*, 614, 497
- Goldreich, P. & Tremaine, S. 1980, *ApJ*, 241, 425
- Greene, T. P., Wilking, B. A., Andre, P., Young, E. T., & Lada, C. J. 1994, *ApJ*, 434, 614

- Guan, X., Gammie, C. F., Simon, J. B., & Johnson, B. M. 2009, *ApJ*, 694, 1010
- Guillot, T. 2010, in *EAS Publications Series*, Vol. 41, *EAS Publications Series*, ed. T. Montmerle, D. Ehrenreich, & A.-M. Lagrange, 355–365
- Hachisu, I. 1986, *ApJS*, 61, 479
- Haghighipour, N. & Boss, A. P. 2003b, *ApJ*, 598, 1301
- Haisch, Jr., K. E., Lada, E. A., & Lada, C. J. 2001, *ApJL*, 553, L153
- Hartmann, L. 1998, *Accretion Processes in Star Formation* (Cambridge University Press)
- Hartmann, L., Calvet, N., Gullbring, E., & D’Alessio, P. 1998, *ApJ*, 495, 385
- Hawley, J. F., Gammie, C. F., & Balbus, S. A. 1995, *ApJ*, 440, 742
- . 1996, *ApJ*, 464, 690
- Helled, R., Podolak, M., & Kovetz, A. 2006, *Icarus*, 185, 64
- . 2008, *Icarus*, 195, 863
- Helled, R. & Schubert, G. 2008, *Icarus*, 198, 156
- Horne, J. H. & Baliunas, S. L. 1986, *ApJ*, 302, 757
- Hubickyj, O., Bodenheimer, P., & Lissauer, J. J. 2005, *Icarus*, 179, 415
- Hut, P., Makino, J., & McMillan, S. 1995, *ApJL*, 443, L93
- Ida, S. & Lin, D. N. C. 2008, *ApJ*, 673, 487
- Imamura, J. N., Durisen, R. H., & Pickett, B. K. 2000, *ApJ*, 528, 946
- Jayawardhana, R., Hartmann, L., & Calvet, N. 2001, *ApJ*, 548, 310
- Johnson, B. M. & Gammie, C. F. 2003, *ApJ*, 597, 131
- Kant, I. & Jaki, S. L. 1981, *Universal natural history and theory of the heavens* (Scottish Academic Press)

- Kenyon, S. J. & Hartmann, L. 1987, *ApJ*, 323, 714
- Kley, W. & Crida, A. 2008, *A&A*, 487, L9
- Korycansky, D. G. 1999, *MNRAS*, 310, 110
- Kuiper, G. P. 1951, in *50th Anniversary of the Yerkes Observatory and Half a Century of Progress in Astrophysics*, ed. J. A. Hynek, 357–+
- Lesur, G. & Longaretti, P. 2007, *MNRAS*, 378, 1471
- Lin, D. N. C. & Papaloizou, J. 1979a, *MNRAS*, 188, 191
- . 1979b, *MNRAS*, 186, 799
- . 1986, *ApJ*, 307, 395
- Lin, M. & Papaloizou, J. C. B. 2010, *MNRAS*, 405, 1473
- Lodato, G. & Rice, W. K. M. 2004, *MNRAS*, 351, 630
- . 2005, *MNRAS*, 358, 1489
- Lomb, N. R. 1975, *MNRAS*, 172, 639
- Lubow, S. H. & Ogilvie, G. I. 1998, *ApJ*, 504, 983
- Lynden-Bell, D. & Kalnajs, A. J. 1972, *MNRAS*, 157, 1
- Lynden-Bell, D. & Pringle, J. E. 1974, *MNRAS*, 168, 603
- Masset, F. S. & Papaloizou, J. C. B. 2003, *ApJ*, 588, 494
- Mayer, L., Lufkin, G., Quinn, T., & Wadsley, J. 2007, *ApJL*, 661, L77
- Mayer, L., Quinn, T., Wadsley, J., & Stadel, J. 2004, *ApJ*, 609, 1045
- Mayor, M. & Queloz, D. 1995, *Nature*, 378, 355
- Mejía, A. C. 2004, PhD thesis, Indiana University
- Mejía, A. C., Durisen, R. H., Pickett, M. K., & Cai, K. 2005, *ApJ*, 619, 1098

- Militzer, B., Hubbard, W. B., Vorberger, J., Tamblyn, I., & Bonev, S. A. 2008, *ApJL*, 688, L45
- Mizuno, H. 1980, *Progress of Theoretical Physics*, 64, 544
- Nelson, A. F., Benz, W., & Ruzmaikina, T. V. 2000a, *ApJ*, 529, 357
- Nelson, R. P. & Papaloizou, J. C. B. 2003, *MNRAS*, 339, 993
- . 2004, *MNRAS*, 350, 849
- Nelson, R. P., Papaloizou, J. C. B., Masset, F., & Kley, W. 2000b, *MNRAS*, 318, 18
- Noh, H., Vishniac, E. T., & Cochran, W. D. 1992, *ApJ*, 397, 347
- Norman, M. L. & Winkler, K.-H. A. 1986, in *NATO Advanced Research Workshop on Astrophysical Radiation Hydrodynamics*, ed. K.-H. A. Winkler & M. L. Norman (D. Reidel Publishing Co., Boston, MA), 187
- Osterbrock, D. E. 1962, *ApJ*, 136, 359
- Paardekooper, S., Baruteau, C., Crida, A., & Kley, W. 2010, *MNRAS*, 401, 1950
- Paardekooper, S. & Mellema, G. 2006, *A&A*, 459, L17
- Paardekooper, S. & Papaloizou, J. C. B. 2009, *MNRAS*, 394, 2283
- Padgett, D. L., Brandner, W., Stapelfeldt, K. R., Strom, S. E., Terebey, S., & Koerner, D. 1999, *AJ*, 117, 1490
- Papaloizou, J. C. B. & Nelson, R. P. 2005, *A&A*, 433, 247
- Papaloizou, J. C. B., Nelson, R. P., Kley, W., Masset, F. S., & Artymowicz, P. 2007, in *Protostars and Planets V*, ed. B. Reipurth, D. Jewitt, & K. Keil, 655–668
- Pepliński, A., Artymowicz, P., & Mellema, G. 2008a, *MNRAS*, 386, 164
- . 2008b, *MNRAS*, 386, 179
- . 2008c, *MNRAS*, 387, 1063
- Pickett, B. K. 1995, PhD thesis, Indiana University

- Pickett, B. K., Cassen, P., Durisen, R. H., & Link, R. 1998, *ApJ*, 504, 468
- Pickett, B. K., Durisen, R. H., & Davis, G. A. 1996, *ApJ*, 458, 714
- Pickett, B. K., Mejía, A. C., Durisen, R. H., Cassen, P. M., Berry, D. K., & Link, R. P. 2003, *ApJ*, 590, 1060
- Pickett, M. K. & Durisen, R. H. 2007, *ApJL*, 654, L155
- Pollack, J. B., Hubickyj, O., Bodenheimer, P., Lissauer, J. J., Podolak, M., & Greenzweig, Y. 1996, *Icarus*, 124, 62
- Rafikov, R. R. 2005, *ApJL*, 621, L69
- . 2007, *ApJ*, 662, 642
- . 2009, *ApJ*, 704, 281
- Rice, W. K. M., Armitage, P. J., Bate, M. R., & Bonnell, I. A. 2003a, *MNRAS*, 338, 227
- . 2003b, *MNRAS*, 339, 1025
- Rice, W. K. M., Armitage, P. J., Wood, K., & Lodato, G. 2006, *MNRAS*, 373, 1619
- Rice, W. K. M., Lodato, G., & Armitage, P. J. 2005, *MNRAS*, 364, L56
- Rice, W. K. M., Lodato, G., Pringle, J. E., Armitage, P. J., & Bonnell, I. A. 2004, *MNRAS*, 355, 543
- Ryu, D. & Goodman, J. 1992, *ApJ*, 388, 438
- Safronov, V. S. & Zvjagina, E. V. 1969, *Icarus*, 10, 109
- Saumon, D. & Guillot, T. 2004, *ApJ*, 609, 1170
- Scargle, J. D. 1982, *ApJ*, 263, 835
- Shakura, N. I. & Syunyaev, R. A. 1973, *A&A*, 24, 337
- Shannon, C. 1984, *Proceedings of the IEEE*, 72, 1192

- Shu, F. H., Tremaine, S., Adams, F. C., & Ruden, S. P. 1990, *ApJ*, 358, 495
- Simon, J. B. & Hawley, J. F. 2009, *ApJ*, 707, 833
- Slattery, W. L., Decamp, W. M., & Cameron, A. G. W. 1980, *Moon and Planets*, 23, 381
- Stamatellos, D. & Whitworth, A. P. 2008, *A&A*, 480, 879
- . 2009, *MNRAS*, 392, 413
- Sternberg, A. & Neufeld, D. A. 1999, *ApJ*, 516, 371
- Stone, J. M. & Balbus, S. A. 1996, *ApJ*, 464, 364
- Tanaka, H., Takeuchi, T., & Ward, W. R. 2002, *ApJ*, 565, 1257
- Tohline, J. E. 1980, *ApJ*, 235, 866
- Toomre, A. 1964, *ApJ*, 139, 1217
- Toomre, A. 1981, in *Structure and Evolution of Normal Galaxies*, ed. S. M. Fall & D. Lynden-Bell, 111–136
- Tuckerman, M., Berne, B. J., & Martyna, G. J. 1992, *The Journal of Chemical Physics*, 97, 1990
- van Leer, B. 1979, *Journal of Computational Physics*, 32, 101
- Vorobyov, E. I. 2009, *ApJ*, 692, 1609
- . 2010, *New Astronomy*, 15, 24
- Vorobyov, E. I. & Basu, S. 2006, *ApJ*, 650, 956
- . 2008, *ApJL*, 676, L139
- Ward, W. R. 1997, *Icarus*, 126, 261
- Ward, W. R. & Hahn, J. M. 1998, *AJ*, 116, 489
- . 2003, *AJ*, 125, 3389

Weidenschilling, S. J. 1977, MNRAS, 180, 57

Williams, H. A. 1988, PhD thesis, AA(Louisiana State Univ., Baton Rouge.)

Yang, S. X. 1992, PhD thesis, Indiana University

Yorke, H. W., Bodenheimer, P., & Laughlin, G. 1993, ApJ, 411, 274

Yoshida, H. 1990, Phys. Lett. A, 150, 262

Zhu, Z., Hartmann, L., & Gammie, C. 2010, ApJ, 713, 1143

Zhu, Z., Hartmann, L., Gammie, C., & McKinney, J. C. 2009, ApJ, 701, 620

Scott Michael

Indiana University
University Information Technology Services
2711 E. Tenth St.
Bloomington, IN 47408-2671
(812) 856-0197
scamicha@indiana.edu

2711 E. Tenth St.
Bloomington, IN 47408-2671
(812) 856-0197

EDUCATION

- ◇ **Indiana University**, Bloomington, IN.
 - ▷ Ph.D. in Astrophysics, April 2011.
Research Advisor: Richard H. Durisen
 - ▷ M. A. in Astronomy, August 2004.
- ◇ **Indiana University**, South Bend, IN.
 - ▷ B. S. in Physics, May 2002
 - ▷ B. S. in Applied Mathematics, May 2002

SKILLS

- ◇ Proficient in programming C, C++, Fortran77, Fortran95, IDL
- ◇ Proficient in parallel programming techniques using both OpenMP and MPI
- ◇ Extensive experience in program profiling and optimization
- ◇ Extensive experience with distributed data sets and networked file systems including NFS, GPFS and Lustre
- ◇ Experience in project design, planning, implementation and management
- ◇ Experience in programming Perl, Python, Visual Basic, CUDA, C#, Ruby
- ◇ Experience in administering AIX, Unix, Linux, MS-DOS, MS-Windows
- ◇ Experience in administering, installing and configuring for multi-processor/GPU-processor hardware

WORK

- ◇ **Senior Analyst/Programmer**

January 2009-present

EXPERIENCE

Indiana University Information Technology Services
High Performance Applications Group
Supervisor: Robert Henschel
Responsibilities:

- ▷ Participate in project planning, formulating objectives, preparing proposals.
- ▷ Perform systems studies to include feasibility, conceptual design, cost/benefit analysis, development and implementation planning.
- ▷ Code computer programs; develop program module test procedures, generate required test data files, and execute testing procedures.
- ▷ Perform systems integration and testing, present final test results, and obtain agreement and approval.
- ▷ Design, develop and implement scientific software in a HPC environment.

HONORS AND AWARDS ◇ NASA Earth and Space Science Fellow, 2007-2008

◇ Indiana Space Grant Fellow, 2007

◇ Indiana Space Grant Fellow, 2005

◇ Indiana University South Bend Honors Scholarship recipient, 1998

RESEARCH INTERESTS Hydrodynamics, Numerical Techniques/Modeling, Theoretical Astrophysics, Parallel Programming Techniques, Planet Formation, Protoplanetary Disk Evolution, Magnetohydrodynamical Turbulence

RESEARCH PROJECTS ◇ **Indiana University** Supervisor: Richard H. Durisen

Effects of varied initial conditions on protoplanetary disk evolution **2003-present**

Modeling magnetorotational instability with alpha disk prescription **2003-present**

Effects of gravitational instabilities on planetesimal growth **2004-present**

Optimization and parallelization of hydrodynamics codes **2004-present**

◇ **Indiana University** Supervisor: Stuart Mufson

Search for possibility of ground based calibrations of SNAP. **2002-2003**

PEER-REVIEWED PUBLICATIONS **Michael, S.**, Steiman-Cameron, T., Durisen, R. H., Boley, A. (2011) Convergence Studies of Mass Transport in Disks with Gravitational Instabilities. I. The Constant Cooling Time Case, ApJ, Submitted

Michael, S., Knezek, P., Stobie, E., Henschel, R., Simms, S. (2010) A Revolutionary New Paradigm for the Reduction and Analysis of Astronomical Images. eScience 2010; IEEE Computer Society Press, USA.

Michael, S., Durisen, R. H. (2010). Stellar Motion Induced by Gravitational Instabilities in Protoplanetary Discs. MNRAS, 406, 279

Henschel, R., **Michael, S.**, Simms, S. (2010). A Distributed Workflow for an Astrophysical OpenMP Application. Challenges of Large Applications in Distributed Environments 2010; ACM: Chicago, IL

Michael, S., Simms, S., Breckenridge, W. B., Smith, R., Link, M. (2010). A Compelling Case for a Centralized Filesystem on the TeraGrid. Teragrid 2010; ACM: Pittsburgh, PA

Boley, A. C., Hartquist, T. W., Durisen, R. H., **Michael, S.** . (2007). The Internal Energy for Molecular Hydrogen in Gravitationally Unstable Protoplanetary Disks. ApJL, 656, 89

Cai, K., Durisen, R. H., **Michael, S.**, Boley, A. C., Mejía, Pickett M. K., D'Alessio, P. (2006). The Effects of Metallicity and Grain Size on Gravitational Instabilities in Protoplanetary Disks. ApJL, 636, 149

REFERENCES Stephen Simms
Data Capacitor Project Manager
2711 E. Tenth St
Bloomington, IN 47405
(812) 855-7211

Richard H. Durisen
Professor of Astronomy
727 E. Third St
Bloomington, IN 47405
(812) 855-6921

Katherine Rhode
Professor of Astronomy
727 E. Third St
Bloomington, IN 47405
(812) 855-6925

Robert Henschel
Manager, High Performance Applications
University Information Technology Services
2711 E. Tenth Street
Bloomington, IN 47408
(812) 856-7411